ANODIC SECTIONING AND ION BOMBARDMENT STUDIES WITH METALS

ANODIC SECTIONING AND ION BOMBARDMENT STUDIES WITH METALS

by

MULK RAJ ARORA, B. Tech.(Hons.), M.Sc.

A Thesis
Submitted to the School of Graduate Studies
in Partial Fulfilment of the Requirements
for the degree
Doctor of Philosophy

McMaster University

February 1974

© Mulk Raj Arora 1974

DOCTOR OF PHILOSOPHY
(Metallurgy and Materials Science)

McMASTER UNIVERSITY
Hamilton, Ontario

TITLE: Anodic Sectioning and Ion Bombardment Studies with Metals

AUTHOR: Mulk Raj Arora, B.Tech. (I.I.T., Bombay)
M.Sc. (McMaster University)

SUPERVISOR: Professor R. Kelly

NUMBER OF PAGES: xviii, 260

SCOPE AND CONTENTS:

In this dissertation, the principles of anodic sectioning have been discussed and satisfactory anodic sectioning methods have been developed for V, Mo, Nb and Ta. In addition, W has been reconsidered. It will emerge that the use of suitable non-aqueous electrolytes permits the formation of impurity-containing (doped) anodic films which have enhanced solubility, thus permitting anodic sectioning.

Thicknesses of film-formed and metal-removed have been determined separately using a conventional gravimetric method for anodizations at ≥ 10 volts. In the thin-film region (≤ 100 Å), new methods of determining small thicknesses, based on ion-range-profiles, have been developed leading to a sensitivity which is suggested to be as good as, if not better than, ellipsometry.

The stoichiometry of the anodic films has been inferred from the thickness calibrations of metal-removed and film-formed, and the matter has been further investigated for V, Mo and W using reflection electron diffraction. The results

were that the films are V_2O_5, MoO_3 and WO_3 respectively. Examination of as-formed films showed that thin anodic films on V, Mo, Ta and W are crystalline with likely stoichiometries $H_6V_4O_{12}$, MoO_3, Ta_2O_5 and WO_3, whereas all thick films (and also the thin films on Nb) are amorphous in nature.

The sectioning methods developed here have been used in determining the range profiles of 5-40 keV Kr^{85} in polycrystalline metals and evidence is presented to show that the stopping process involved the usual mixture of random and channeled ion trajectories.

Similar work on range profiles in amorphous anodic films on V has also been pursued with the main result being that the film properties were found to vary as the bombardment dose increased. The properties include solubility (decreased with dose), sputtering coefficient (decreased with dose from ~44 to ~12 atoms/ion) and stoichiometry (progressed from V_2O_5 to V_2O_3 to VO). These results suggest that all ion bombardment work with oxides must be accompanied by structural investigation, and in particular makes suspect some of the previous work on sputtering coefficients, especially that with Nb_2O_5, WO_3 and TiO_2.

ACKNOWLEDGMENTS

The author sincerely appreciates the interest, continuous guidance and encouragement of his supervisor Professor R. Kelly throughout the course of this work, and also for his many valuable criticisms and suggestions during the preparation of this thesis.

The author also wishes to thank Drs. Smeltzer, Davies, Naguib and Young for their valuable comments at various critical stages of the work. Thanks are also extended to the staff and graduate students of the Department of Metallurgy and Materials Science for their helpful discussions and comments.

Thanks are due to Mrs. H. Kennelly for her cheerful skill and patience in typing the manuscript and to Messrs. D. S. Hodgson and Fred Smith for their technical assistance.

This project was supported by grants from the Defence Research Board and National Research Council of Canada to Professor R. Kelly and by the Ontario Government and McMaster University to the author.

TABLE OF CONTENTS

		Page
CHAPTER 1	INTRODUCTION	1
CHAPTER 2	ANODIC OXIDATION PART I - BACKGROUND	14
	2.1.1 Verwey's Model	15
	2.1.2 Mott and Cabrera's Model	19
	2.1.3 Young's Generalized Model	22
	2.1.4 Generalized Model	24
	2.2 Certain Inadequacies of the Above Models	25
	2.3 Recent Theories Incorporating an E^2 term	28
	2.3.1 General	28
	2.4 Mechanism of Anodic Oxidation	31
	2.4.1 General	31
	2.4.2 Ion Transport Number	31
	2.4.3 Influence of Nature of Electrolyte on Anodization Behaviour	34
	2.4.4 Sources of O_2^- in the Anodic Film	38
	2.5 Limiting Film Thickness	39
	2.5.1 General	39
	2.5.2 Chemical Limitation	39
	2.5.3 Electrochemical Limitation	40
	2.5.4 Electrical Breakdown	41
CHAPTER 3	ANODIC SECTIONING PART II - FILM FORMATION	45
	3.1 General	45
	3.2 Anodization of V, Mo and W	48

Page

3.2.1 General 48

3.2.2 Anodizing Step 49

3.2.3 Effect of Stirring 50

3.3 Constant-Current Characteristics 52

3.3.1 Film Growth 52

3.3.2 Anodizing Efficiency 58

3.3.3 Film Formation Rate 61

3.4 Anodizing Characteristics When Both Current and Voltage are Fixed 63

3.4.1 General 63

3.4.2 Effect of Current Density 64

3.4.3 Anodizing Efficiency When Both Current and Voltage are Preset 66

3.5 Anodization of Nb and Ta 68

3.5.1 General 68

3.5.2 Role of Doping in Anodozihg 70

3.5.3 Loss During Anodizing 71

3.5.4 Properties of Anodic Films 73

3.5.5 Anodizing Efficiency 77

3.6 Summary 78

CHAPTER 4 ANODIC SECTIONING PART III - FILM REMOVAL AND THICKNESS CALIBRATIONS 80

4.1 General 80

4.2 Dissolution End-Points 84

4.2.1 General 84

4.2.2 Determination of Dissolution End-Points 84

Page

4.3 Thickness Calibrations 99

4.3.1 General 99

4.3.2 Effect of Electrode Spacing 99

4.3.3 Calibrations for Thick Films 100

4.3.4 Deduction of Film Stoichiometries 106

4.4 Calibrations for Thin Films 109

4.4.1 General 109

4.4.2 Metal-Removal Thicknesses 110

4.4.3 Film Thickness at Low Voltages 118

4.5 Effect of Radiation Damage on Thickness Calibrations 124

4.6 Summary 125

CHAPTER 5 CHARACTERIZATION OF ANODIC FILMS 129

5.1 General 129

5.2 Background 130

5.2.1 Ta 130

5.2.2 Nb 131

5.2.3 W, V and Mo 132

5.3 Experimental Results and Discussion 133

5.3.1 General 133

5.3.2 Anodic Films As-Formed 134

5.3.3 Thermally Crystallized Films in Air 142

5.3.4 Thermally Crystallized Films in Vacuum 151

5.4 On the Occurrence of V_6O_{13} and MoO_2 156

5.5 Summary 161

Page

CHAPTER 6 RANGE PROFILES - BACKGROUND 163

6.1 Potential Application of Anodic Sectioning 163

6.2 Range Profiles 165

6.2.1 General 165

6.2.2 Advantages and Disadvantages of Ion Implantation 166

6.3 LSS Theory 168

6.3.1 General 168

6.3.2 Stopping Processes 168

6.3.3 Range Concepts 170

6.3.4 Outline of LSS Theory 173

6.3.5 Corrections 177

6.3.6 Range Straggling 181

6.4 Constructing Range Profiles 182

6.4.1 Differential Profiles 182

6.4.2 Integral Profiles 183

6.5 Crystal Lattice Effects on Ranges 186

6.5.1 General 186

6.5.2 Channeling 187

6.5.3 Factors Affecting Channeling 191

6.5.4 Supertails 195

6.5.5 Z_1 Oscillations 196

6.6 Summary 198

Page

CHAPTER 7 APPLICATIONS OF ANODIC SECTIONING (PART I): RANGE PROFILES 200

7.1 General 200

7.2 Experimental 201

7.2.1 General 201

7.2.2 Surface Preparation 201

7.2.3 Bombardment and Counting Techniques 202

7.3 Results and Discussion 202

7.4 Evidence for Channeling 211

7.4.1 Effect of Radiation Damage 211

7.4.2 Use of Amorphous Targets 211

7.4.3 Dose Effects 212

7.5 Estimation of Corrosion Rates 216

7.6 Analytical Forms for Range Profiles 218

7.7 Summary 219

CHAPTER 8 APPLICATIONS OF ANODIC SECTIONING (PART II): SPUTTERING 221

8.1 General 221

8.2 Factors Affecting a Sputtering Coefficient 223

8.2.1 Ion Energy 223

8.2.2 Target Material 225

8.2.3 Incident Ion 225

8.2.4 Ion Dose 227

8.3 Theories of Sputtering 228

8.3.1 Theory of Rol, Fluit and Kistemaker 228

8.3.2 Sigmund's Theory 229

Page

8.4 Experimental Results and Discussion 233

8.4.1 General 233

8.4.2 Variable Dissolution Rates 233

8.4.3 Structural Investigation 234

8.4.4 Estimation of Sputtering Coefficients 238

8.5 Summary 242

CHAPTER 9 SUMMARY AND SUGGESTIONS FOR FURTHER RESEARCH 244

9.1 Summary 244

9.2 Future Work 249

REFERENCES 251

LIST OF ILLUSTRATIONS

FIGURE NO.	TITLE	Page
1-1	Representative depth distributions of dopant for an initially channeled ion beam	2
1-2	Deviation from the Arrhenius-type curve for self-diffusion of Zr and Nb.	3
1-3	Activity Profiles for diffusion of Nb into mono- and polycrystalline Ta	5
1-4	Activity-vs-time curves serving to determine the rate of dissolution of Nb_2O_5	7
1-5	Concentration vs penetration distance profile for the diffusion of Co in Au	8
1-6	Concentration vs penetration distance profile for the diffusion of Ni in Au	9
2-1	Potential energy of mobile ions vs distance with and without field	16
2-2	Potential energy vs distance for ion entering oxide from the metal	21
2-3	Corrosion in Hf of films formed in 1% Na_2SO_4 and 80% H_2SO_4	32
2-4	Distribution of activity in Ta discs	32
3-1	Effect of stirring on film growth at constant current	51
3-2	Constant current film growth kinetics for V at various current densities	53
3-3	Constant current film growth kinetics for Mo at various current densities	54
3-4	Constant current film growth kinetics for W at various current densities	55
3-5	Initial intercept as a function of current density	57
3-6	Variation of $\frac{dV}{dt}$ with current	59

Page

3-7	Relation between log $(\frac{dV}{dt})$ and log I	62
3-8	Effect of initial current density over the 'anodizing end-point' for V	65
3-9	Typical current-time plots at 50 volts with initial current of 2.0 mA/cm^2	67
3-10	Relation between metal dissolution and anodizing time for V and Mo	69
3-11	Typical voltage-time and current-time curves for aqueous and non-aqueous electrolytes in the anodization of Nb and Ta	76
4-1	Dissolution of 15 volt and 30 volt films of V and Mo in 0.1% KOH as inferred by loss of radioactivity	86
4-2	Typical dissolution end-point for V	88
4-3	Typical dissolution end-point for Mo	89
4-4	Typical dissolution end-point for W	90
4-5	Typical dissolution end-points for Nb with films formed in a 4:1 mixture of H_2SO_4 and HNO_3	91
4-6	Activity vs time curves serving to determine the rate of dissolution of anodic Nb_2O_5 in 40% HF saturated with NH_4F.	92
4-7	Activity vs time curves serving to determine the rate of dissolution of anodic Nb_2O_5 in a 68% HNO_3 solution held at 120°C	92A
4-8	Dissolution behaviour of anodic films of Nb formed in an electrolyte containing diethyl sulphate and H_2SO_4	94
4-9	Dissolution behaviour of anodic films of Ta formed in an electrolyte containing diethyl sulphate and H_2SO_4	95
4-10	Duplex nature of anodic films of Nb formed in sulphate-based electrolyte	96
4-11	Dissolution of anodic film of Nb formed in sulphate-based electrolyte when exposed to 10% KOH for 12 minutes and then to saturated KOH	97

		Page
4-12	Thickness vs anodizing voltage relation for V	101
4-13	Thickness vs anodizing voltage relation for Mo	102
4-14	Thickness vs anodizing voltage relation for W	103
4-15	Thickness vs anodizing voltage relation for Nb using conc. H_2SO_4 as the electrolyte	105
4-16	Thickness vs anodizing voltage relation for Nb using sulphate-based electrolyte	107
4-17	Thickness vs anodizing voltage relation for Ta using sulphate-based electrolyte	108
4-18	Integral depth distributions in V	111
4-19	Integral depth distributions in Mo and W	114
4-20	Integral depth distributions in Nb and Ta	115
4-21	Variation of $f(\xi_1)$ with ξ	122
4-22	Relation between oxide thickness of V and the quantity $erf^{-1}[1-2C^{int}(x)]$	123
5-1	Electron diffraction patterns of as-formed thick anodic films	135
5-2	Reflection-electron-diffraction patterns of as-formed thin anodic films	136
5-3	Reflection-electron-diffraction patterns of air-heated anodic films	144
5-4	Reflection-electron-diffraction patterns of vacuum-heated anodic films	155
6-1	Theoretical nuclear and electronic stopping-power based on the LSS theory	169
6-2	Typical range profiles	172
6-3	Range parameters as functions of mass ratio $\frac{M_2}{M_1}$	18[illegible]

Page

		Page
6-4	Theoretical differential and integral range profiles of Kr^{85} in amorphous Mo in linear scale	184
6-5	Theoretical integral range profile of Kr^{85} in amorphous Mo in the usual logarithmic form	185
6-6	Schematic representation of ion trajectories for axial channeling showing variation in trajectories with (a) angle of incidence, and (b) impact position	189
6-7	The experimental range profile of 500-keV K^{42} ions injected at 27°C along the <111> direction in W	190
6-8	Effect on range profile of (a) target temperature, (b) ion dose, and (c) misalignment and surface disorder	192
6-9	Plot of total stopping cross-section S vs $E^{1/2}$ for well-channeled Xe ions injected into W along the <100> direction	194
6-10	Z_1 dependence of the electronic stopping power, Se, in W for well-channeled ions	197
7-1	Target arrangement	203
7-2	Range profiles of Kr^{85} in polycrystalline V at various energies	204
7-3	Range profiles of Kr^{85} in polycrystalline Mo at various energies	205
7-4	Range profiles of Kr^{85} in polycrystalline Nb	207
7-5	Range profiles of Kr^{85} in polycrystalline Ta	208
7-6	Range profiles of Kr^{85} in polycrystalline W	209
7-7	Range profiles for Kr^{85} in anodized V	213
7-8	Effect of varying ion dose on range profiles of Kr^{85} in polycrystalline Mo	214

		Page
7-9	Effect of prebombardment on range profiles of Kr^{85} in polycrystalline Mo	217
8-1	Collisions leading to sputtering process	222
8-2	Variation of the sputtering yield with ion energy	224
8-3	Variation of the sputtering yield with atomic number of the target for 400 eV noble gas ions	226
8-4	Variation of the sputtering yield with atomic number of the incident ions for Cu, Ag and Ta.	225
8-5	Variation of α with mass ratio in the elastic collision region	231
8-6	Effect of ion bombardment on anodic films of V at various doses	235
8-7	Effect of 40-keV Kr ion bombardment on the dissolution behaviour of 12-volt anodic film of V.	239

LIST OF TABLES

Table No.		Page
3-1	Values of k and (i_2+i_3) for V, Mo and W	60
3-2	Film formation current efficiency at constant currents	60
3-3	Values of 'a' and 'b'	61
3-4	Estimation of E_d values for V, Mo and W	63
3-5	Determination of anodic efficiency from Faraday calculations	66
3-6	Loss during anodizing for Nb, Ta and W	72
3-7	Film and anion weight ratios for Nb, Ta and W	73
3-8	Comparison of $\frac{dV}{dt}$ values for aqueous and non-aqueous electrolytes	75
3-9	Anodizing efficiencies determined from coulombic and gravimetric data	77
4-1	Assumptions involved in determining metal-removal thicknesses	85
4-2	Stripping times for Nb and Ta in sat. KOH	98
4-2A	Anodizing breakdown voltages for Nb and Ta	104
4-3	Deduction of film scoichiometries from thickness calibrations	109
4-4	Metal-removal thicknesses for low anodizing voltages for V	113
4-5	Metal-removal thicknesses for low anodizing voltages for Mo and W	116
4-6	Metal-removal thicknesses for low anodizing voltages for Nb and Ta	117
4-7	Determination of thin-film thicknesses using ellipsometry	118

Page

4-8	Results of transmission experiments	120
4-9	Effect of radiation damage on thickness calibrations of V and Mo	125
4-10	Minimum and maximum metal-removal thicknesses for a single sectioning	128
5-1	Thickness vs voltage slopes at low and high voltages	134
5-2	Electron diffraction data for as-formed anodized V	138
5-3	Electron diffraction data for as-formed anodized Mo	139
5-4	Electron diffraction data for as-formed anodized W	140
5-5	Electron diffraction data for as-formed anodized Ta	141
5-6	Crystallization temperatures of anodic films on V, Mo and W	143
5-7	Air-heating of anodic film on V at 425°C	145
5-8	Air-heating of anodic film on Mo at 400°C	147
5-9	Air-heating of anodic film on W at 425°C	149
5-10	Thermodynamic calculations of possible oxidation/reduction processes	152
5-11	Vacuum heating of anodic film on V at 300°C	157
5-12	Vacuum heating of anodic film on Mo at 300°C	158
5-13	Vacuum heating of anodic film on W at 425°C	159
6-1	Projected ranges with and without electronic stopping	170
6-2	Values of ε, ρ and k for incident Kr^{85}	178
7-1	Comparison between experimental median projected range, R_m, and the expected mean projected range, $\langle R_p \rangle_{LSS}$, for V and Mo	206

		Page
7-2	Comparison between experimental median projected range, R_m, and the expected mean projected range, $\langle R_p \rangle_{LSS}$, for Nb, Ta and W	206
7-3	Summary of comparison between R_m and $\langle R_p \rangle_{LSS}$	210
7-4	Comparison of R_m and $\langle R_p \rangle_{LSS}$ for Mo for various doses at 10-keV	215
7-5	Rate of metal corrosion in saturated KOH solution	216
8-1	Reduced nuclear stopping cross-section $s_n(\varepsilon)$	232
8-2	Dissolution rate as a function of ion dose	236
8-3	Electron diffraction data for V_2O_3	237
8-4	Electron diffraction data for VO	237
8-5	Sputtering coefficients for anodized V as a function of dose.	241

CHAPTER 1

INTRODUCTION

The pioneer work of Güntherschulze and Betz (1937) initiated much of the present day interest in the formation of anodic films. Such films have been used extensively in the capacitor industry for over fifty years, with other important uses being in microcircuitry (McLean, 1960) and in thin-film technology (Wilcox et al., 1960). More recently, major indirect uses have emerged for anodic films in the fields of ion-implantation, radiation damage, low-temperature diffusion, etc. These new uses all centre around the possibility of anodic sectioning.

A great amount of work is being carried out on ion-implantation of metals and semiconductors. A major problem in such studies is that a detailed knowledge of the depth distribution of the ions is required. For example, with implanted semiconductors the depth distribution directly determines the junction depth (R_j), peak impurity concentration depth (R_p), and base width (w) (Dearnaley, 1970) as shown schematically in figure 1-1, and indirectly determines the depth of amorphization (Lam and Kelly, 1970). A more fundamental reason for measuring depth distributions of ions is to provide accurate experimental data to test the theoretical predictions of such groups as those of Lindhard or Sigmund or Winterbon

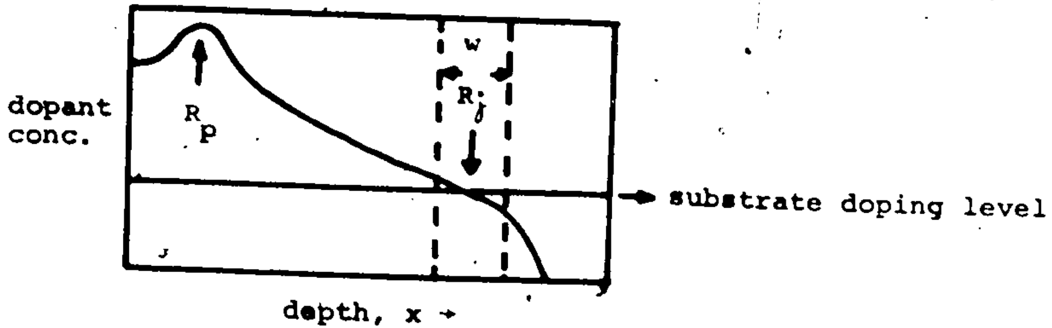

Fig. 1-1 Representative depth distribution of dopant for an initially channeled ion beam. R_p corresponds to the peak dopant concentration, R_j to the depth at which the junction is located and 'w' is the base width.

on the slowing down behaviour of ions in solids. However, in the energy range below 1 MeV, experimental data have until now been obtainable only with a limited number of target materials. This is mainly due to the difficulties involved in accurately measuring the extremely small depths of penetration: for example, the projected mean range of 40 keV As ions in silicon, according to the LSS theory (Lindhard, Scharff and Schiøtt, 1963), is about 271 Å (Johnson and Gibbons, 1970).

A closely related problem is that of determining diffusion profiles under extreme conditions involving small thicknesses. For example, the self-diffusion coefficients in the bcc metals Ti, Nb, U and Zr have been found to have two components (LeClaire, 1965) as shown in figure 1-2. In the case of another bcc metal V, Lundy et al. (1964) and Peart (1965) seem to disagree on the extent of the anomaly

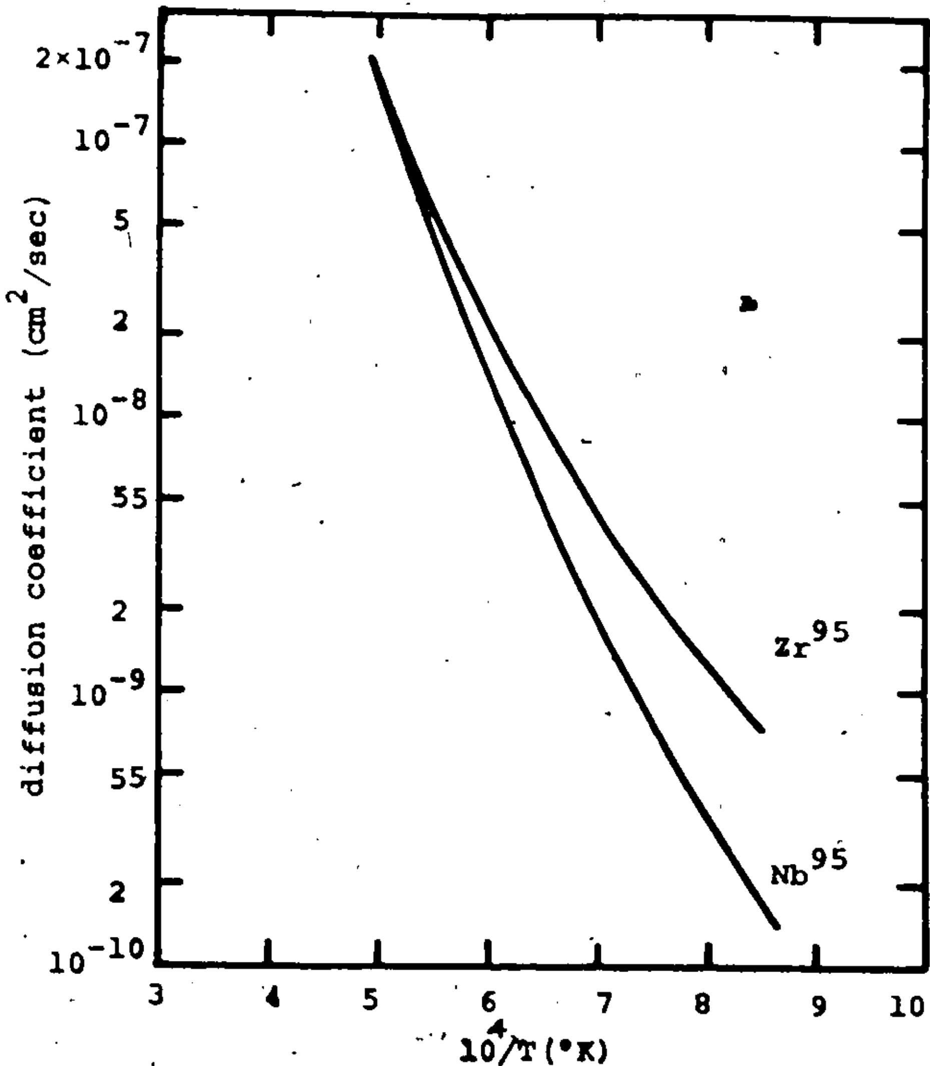

Fig. 1-2 Deviation from the Arrhenius-type curve for self-diffusion of Zr and Nb (after LeClaire, 1965).

at lower temperatures ($\leq$ 1500°C) though Lundy et al. regard their results only as being preliminary. There has therefore been recent interest in extending diffusion measurements with vanadium and other bcc metals to the lowest possible temperatures (Pawel and Lundy, 1965), thence in using an extremely precise sectioning technique. As an example for comparing the various methods conventionally employed to determine self-diffusion coefficients, use of lathe sectioning permits measurements of D down to about 10^{-13} cm^2/sec, chemical etching enables one to go to about 10^{-15} - 10^{-16} cm^2/sec, whereas anodic sectioning (where possible) permits measurements to about 10^{-18} - 10^{-19} cm^2/sec. In addition, Pawel and Lundy (1965) point out that when measurements are made using polycrystalline specimens, the concentration profile due to lattice diffusion is restricted to a rather shallow zone, and the "tails" of these curves entirely reflect the behaviour of the short-circuiting paths, as shown in figure 1-3. Thus, according to these authors, the high sensitivity of anodic sectioning can be utilized to study the characteristics of lattice diffusion in the near surface region at low temperatures. The present work will be seen to open up this possibility for a total of four previously unstudiable bcc metals (V, Nb, Ta, Mo), with only W being previously studiable.

The previous statement could perhaps be qualified in that both Nb and Ta allowed the mechanical stripping of

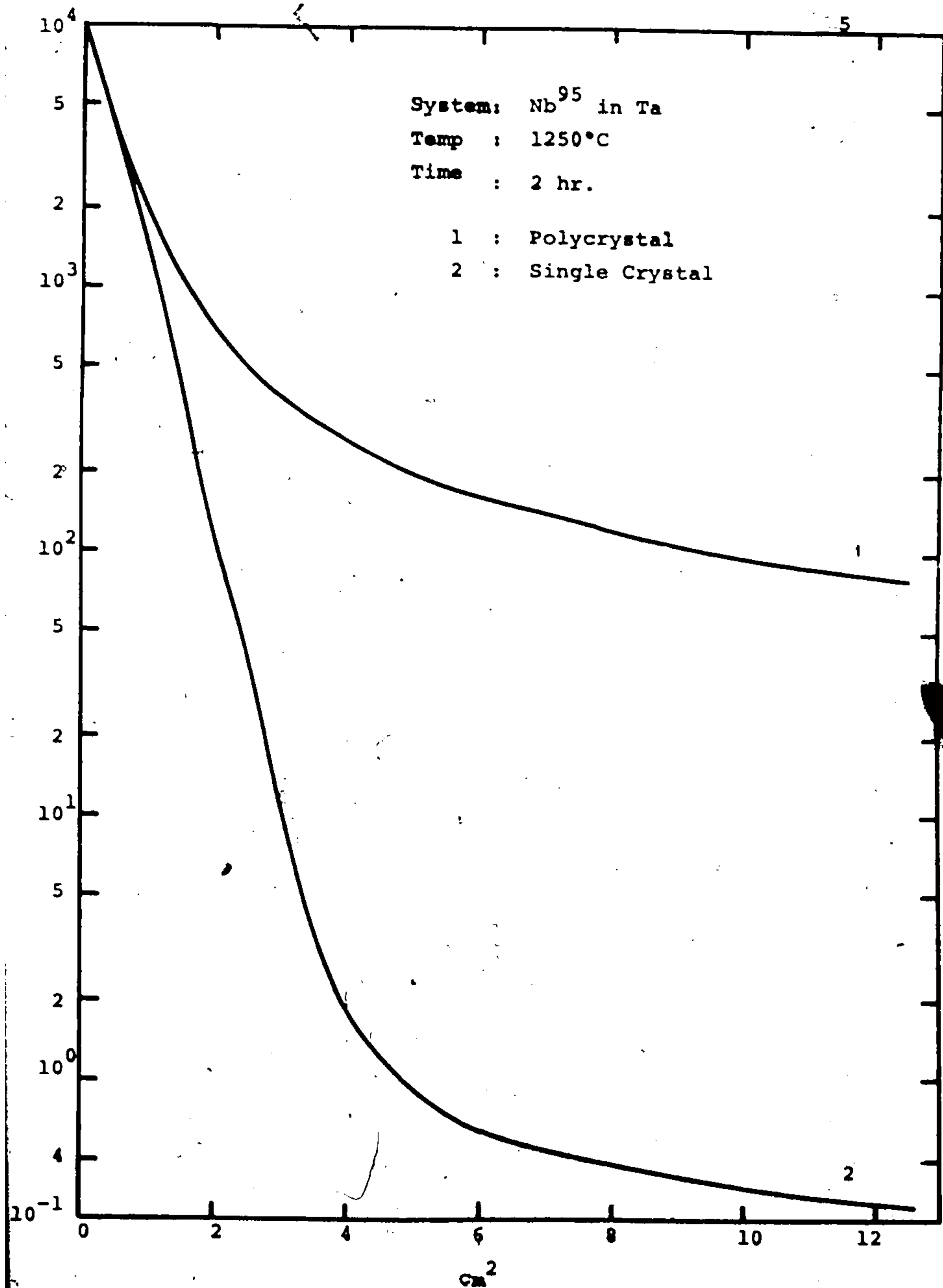

Fig. 1-3 Activity profiles for diffusion of Nb^{95} into mono- and polycrystalline Ta after 2 hr at 1250°C (After Pawel and Lundy, 1965)

anodic films (Pawel, 1965). This procedure is fairly cumbersome, however, and in addition fails for films thinner than about 200 Å. Moreover, Nb permitted an imperfect form of anodic sectioning (Lam, 1971). This imperfection lay in the stripping step as shown in figure 1-4. Indeed, such stripping behaviour is typical with any unperfected form of anodic sectioning and hence is the type of result that formed one of the major experimental hurdles in the present work.

In still other work, anomalous near-surface diffusion behaviour has been detected for noble metals (Styris and Tomizuka, 1963; Mortlock, 1968; Lundy and Padgett, 1968) such that the impurity diffusion rate in the surface region (0.2-0.5 μ) was found to be roughly one thousandth of that in the bulk material. Results obtained for cobalt in gold and nickel in gold are shown in figures 1-5 and 1-6. Only at sufficiently large depths are the diffusion rates found to be normal. Mortlock (1969) has tentatively attributed such anomalous behaviour to the Gibbs adsorption effect but the nature of forces behind such behaviour is still not known exactly. Similar anomaly is also expected to occur close to internal surfaces such as grain boundaries. It is perhaps worth noting that, in spite of their rather different behaviours in gold, both cobalt and nickel have virtually the same Goldschmidt atomic diameter so that elastic forces alone cannot account for the results. Clearly, much more work needs to be done in order to adequately explain the observations.

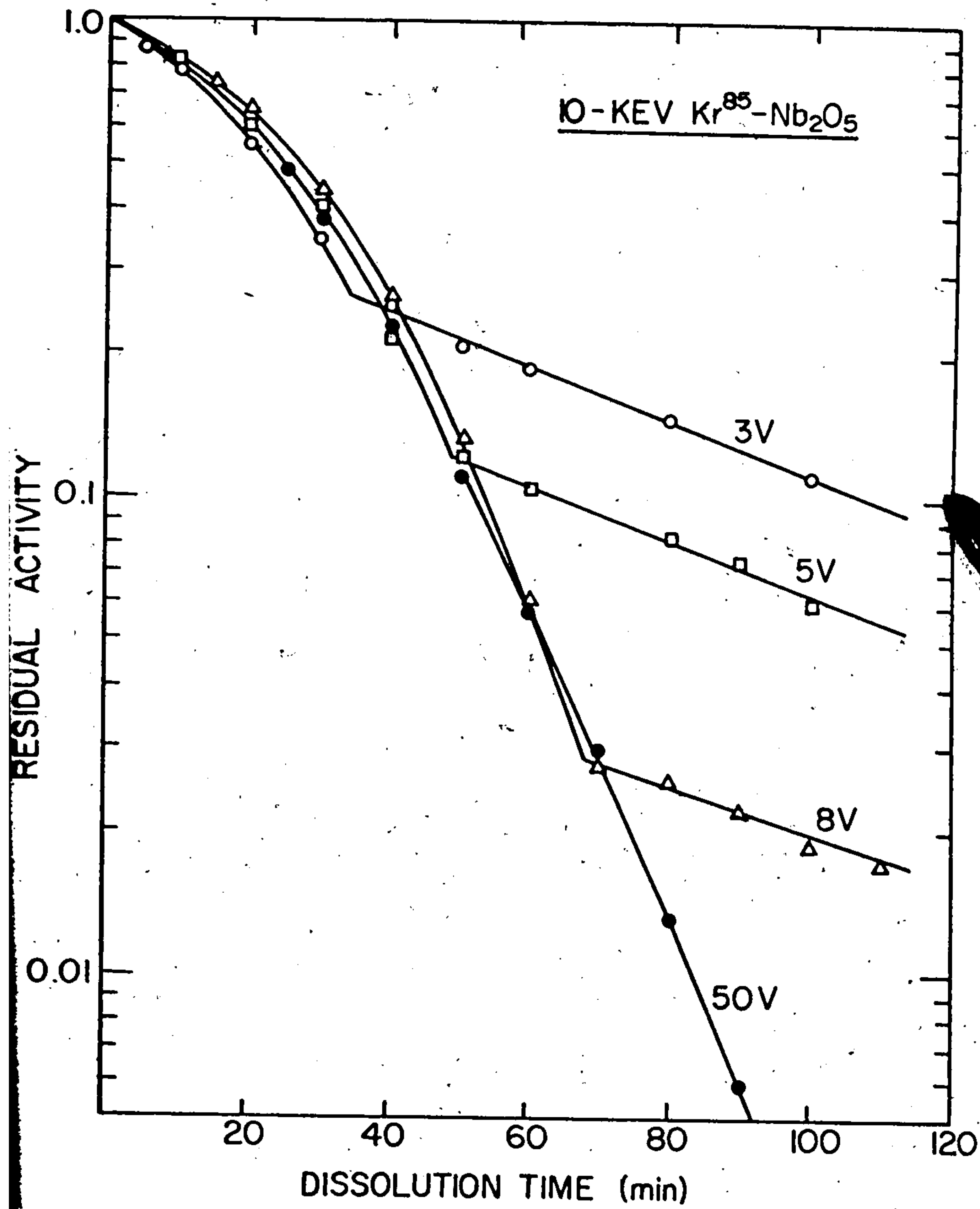

Fig. 1-4 Activity-vs-time curves serving to determine the rate of dissolution of anodic Nb_2O_5 in a solution of 40% HF saturated with NH_4F.

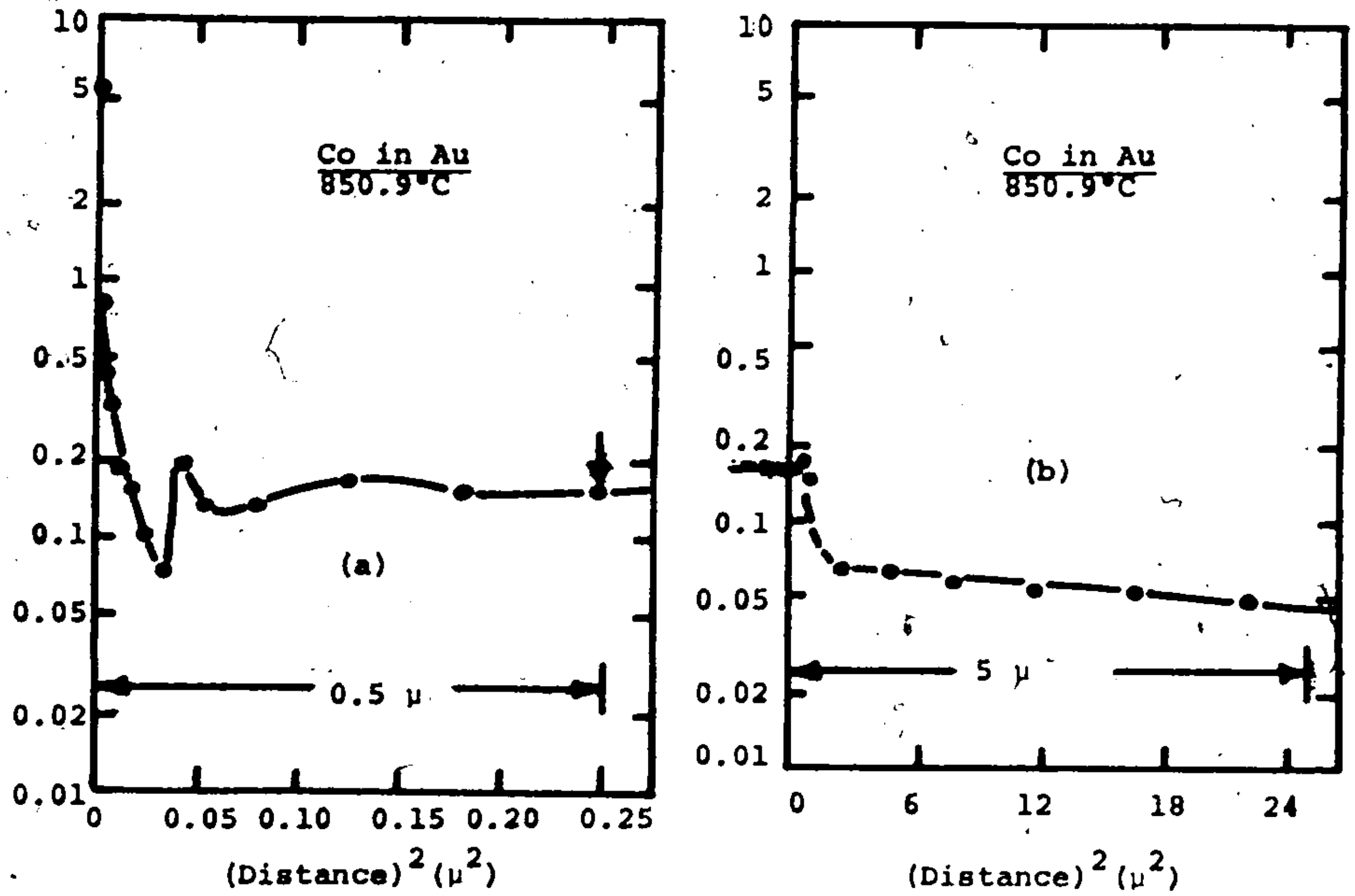

Fig. 1-5 Concentration vs penetration distance profile for the diffusion of ^{60}Co in Au (a) in the near-surface region (b) excluding the part of the near-surface region

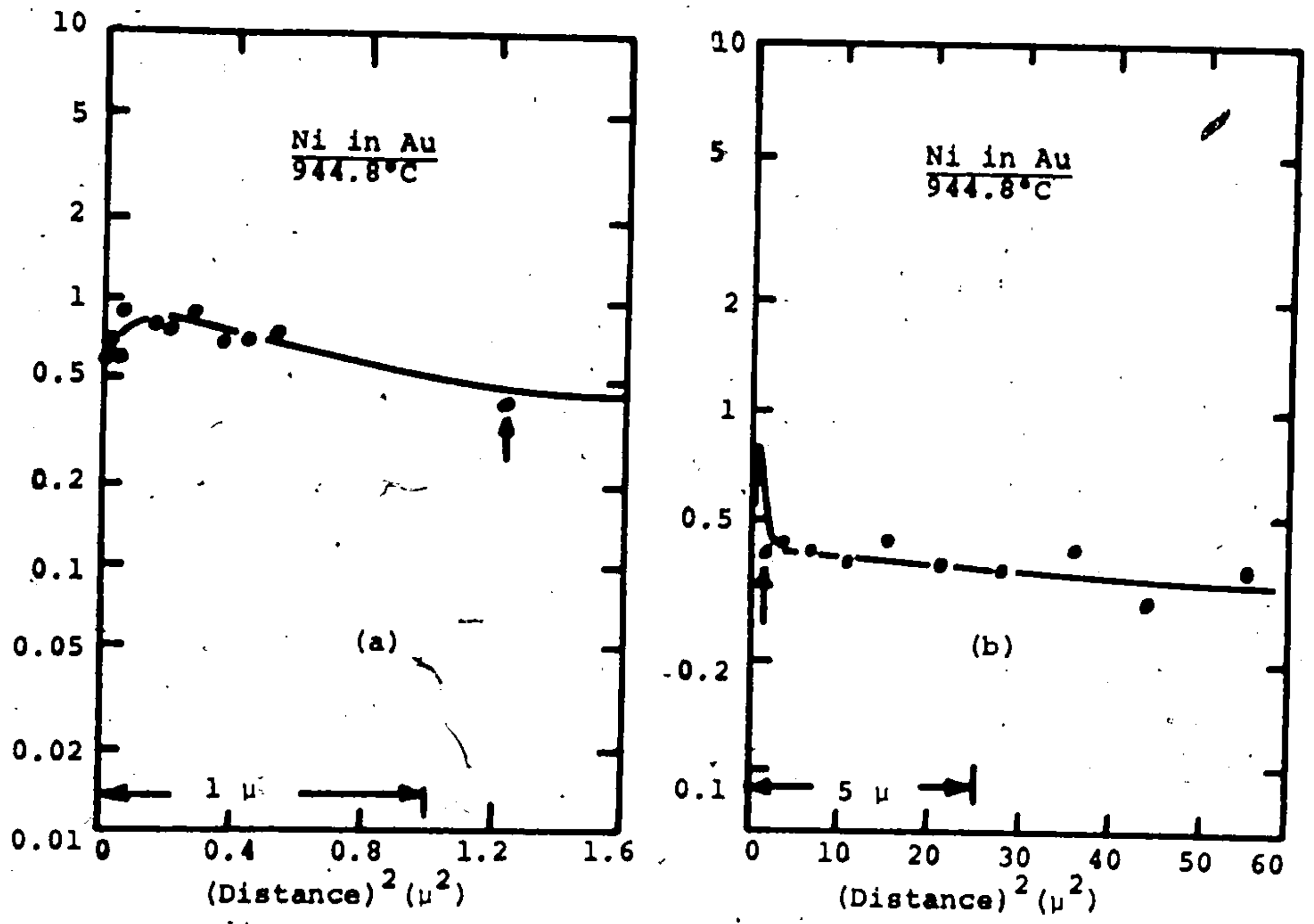

Fig. 1-6 Concentration vs penetration distance profile for the diffusion of ^{63}Ni in Au (a) in the near-surface region, and (b) excluding the part of the near-surface region.

Since the depths involved in such studies will be only about 0.2-0.5 μ, sectioning techniques which permit the removal of thin (≤ 100 Å) uniform layers from the surfaces of metals have to be developed.

Several possibilities have been explored with a view to removing thin uniform films from the surfaces of solids in a precise and reproducible manner based on physical, chemical, and electrochemical means. For example, Andersen and Sørensen (1969) have demonstrated that well-defined halide films can be formed and stripped from silver and copper. Vibratory polishing (Whitton, 1965) and sputtering (Kelly, 1968a) are nearly universally applicable. However, the most sensitive sectioning method probably still remains that based on the use of anodic films, namely that generally known as anodic sectioning.

In anodic sectioning, use is made of the fact that when anodic oxidation is carried out at constant voltage, then within a few minutes the film thickness approaches an almost constant value and the resulting film is extremely uniform (Charlesby, 1951). If such films can be removed without affecting the substrate, then it should be possible to remove uniform layers of metal, with thicknesses down to 10-20 Å. Whitton (1969), while discussing the preparation of completely damage-free target surfaces for heavy-ion channeling, proton scattering etc., concluded that of all the methods available for target preparation, such as mechanical

polishing, spark erosion, acid etching, vibratory polishing, electropolishing, and anodic sectioning, the last one, namely anodic sectioning, produces perhaps the most damage free and uniform surface. The only problem with anodic sectioning is that each substance has to be investigated separately and the method has till now been fully perfected only for two metals [Al (Davies et al., 1960) and W (McCargo et al., 1963)] and partly perfected for only a further five [Ag (Lam et al., 1972a), Au (Whitton and Davies, 1964), Cu (Lam et al., 1972b), Nb (Lam, 1971) and Si (Schmidt and Michel, 1957; Dubrovskii et al., 1962, Wilkins, 1968)].

In this dissertation, the principles of perfect anodic sectioning will be described for the first time for four new metals (V, Mo, Nb and Ta) and, in addition, improvements will be suggested for the sectioning of W. It will emerge that, with a suitable choice of electrolyte, doped anodic films (and not pure oxides) may be formed on metals which have desirable chemical properties, thus leading to anodic sectioning. It will also be seen that anodic sectioning, whose main advantage over other methods lies in the possibility of its extreme resolution, normally does not yield satisfactory results in the thin-film range (≤ 100 Å) using conventional methods of calibration. To overcome such difficulties, new techniques of determining small thicknesses, based on ion depth distributions, have been developed, leading to a resolution which is suggested to be as good as, if not

better than, that of ellipsometry.

The nature of the anodic films on V, Mo and W has been inferred from the metal and film thickness data and has been further investigated using reflection-electron-diffraction microscopy. Rather unexpected results have been obtained for the composition of the vacuum heat-treated anodic films of V and Mo, namely that the stoichiometries are V_6O_{13} and MoO_2. A knowledge of the composition of these films, besides permitting the estimation of anodizing efficiency, is closely relevant to the synthesis of oxides with interesting electrical properties but which cannot be formed conveniently by other means.

As another major topic, the use of sectioning techniques is described in connection with determining the depth distributions of energetic Kr^{85} ions in V, Mo, W, Nb and Ta at high doses, and the effect of prebombarding specimens with inactive Kr ions on the distribution profiles has been studied in the 5-40 keV range. The main result here was that all behaviour was as expected, i.e., the stopping process involved the usual mixture of random and channeled trajectories; this result is similar to that obtained for W by other workers but is, in contrast, different from that obtained for alkali halides which show too much channeling. Another, and a more novel, topic studied concerns the rather elusive quantity, the sputtering coefficient at low doses. This has been esti-

mated using both the structural information and the depth distribution profiles and a rather startling result of 'S' lying in the region 44±9 atoms/ion has been observed.

Due to the interdisciplinary nature of this investigation, a general review of the present state of knowledge is given separately for each of the following topics: the anodic oxidation of metals, structure of anodic films, and range profiles of energetic ions in solids. In the next chapter, therefore, we start with a review of the anodic oxidation of metals.

CHAPTER 2

ANODIC OXIDATION

PART I - BACKGROUND

Most metals are thermodynamically unstable at room temperature in contact with oxygen at atmospheric partial pressure and should tend to form oxide until prevented by kinetic considerations. This leads to oxide thicknesses of about 50 Å (Hass, 1947; 1957). If the oxide-coated metal is made the anode of an electrolytic cell, then if the oxide is a poor electronic conductor and the electrolyte does not attack the oxide, the applied voltage sets up an electrostatic field in the oxide (or increases the already existing field) and produces a continued growth of the film by causing metal and/or oxygen ions to migrate through the film. Thus, the growth of anodic film is basically a problem in the ionic conductivity of oxides at high fields combined with complications due to the processes occurring at the metal/oxide and oxide/electrolyte interfaces. Many of the phenomena were established semi-quantitatively by Güntherschulze and Betz (1937), though during the past forty years, our understanding of anodic films has advanced greatly. Since excellent reviews already exist on the subject [Hoar,

1959; Young, 1961; Vermilyea, 1963; Dignam, 1972, etc.], a complete review is not attempted for individual metals and only some of the classical theories of anodic oxidation are discussed. Some additional relevant information such as the mechanism of film growth and parameters that limit the final film thickness are also discussed. All the classical theories of anodic oxidation are based on the assumption of an idealized, homogeneous, and a parallel-sided film which is free from flaws.

2.1.1 Verwey's Model:

Verwey (1935) made the following assumptions additional to those stated above:

(i) Metal ions at interstitial sites are the mobile entity. (This is now known to be a highly restrictive assumption and will be discussed later.)

(ii) All interstitial ions are equivalently placed as regards their ease of movement. (This is again only an approximation since there must be a range of site types, jump distances, and potential barriers due to the amorphous nature of most anodic oxides.)

(iii) No interstitial ion blocks the path of another.

(iv) The concentration of mobile species corresponds to electroneutrality of the bulk oxide.

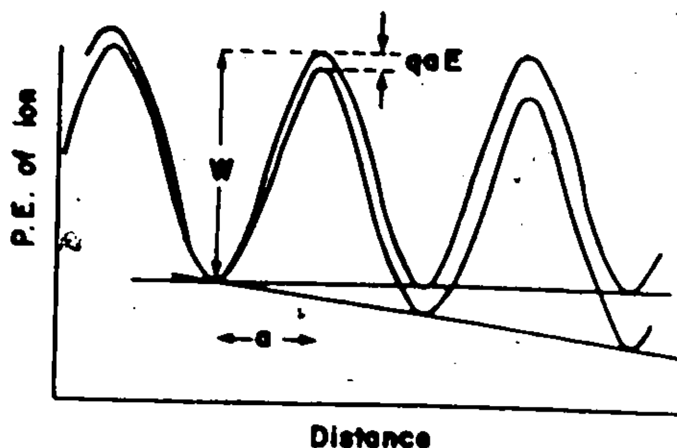

Fig. 2-1 Potential Energy (P.E.) of mobile ions vs. distance with and without field.

The governing equation is derived by picturing the ions as acquiring sufficient energy from thermal agitation plus the applied field to jump the potential energy barrier and thus reach the next site. It is assumed here that the rate-determining step involves overcoming the barriers in the bulk oxide and not the barrier at the metal/film interface.

In the absence of an electric field, the number of ions jumping in any direction is given, in units of $\frac{\text{ions}}{\text{cm}^2\text{-sec}}$, by

$$i = 2an\nu \exp[-(\frac{W}{KT})]$$

where a = activation distance, equivalent to half-jump distance,

ν = frequency of vibration of interstitial ion, including a factor of the type $\exp(\frac{\Delta s}{R})$,

n = number of mobile ions per unit volume of the oxide.

In the presence of an electric field, the flux of the mobile ions will be greater in the direction of the field,

due to the lower potential barrier, as compared to the flux against the field. This will result in a net flux of ions in the direction of the field, thence in the observed current

$$i = \vec{i} - \overleftarrow{i} \quad \text{ions/cm}^2\text{-sec.}$$

where

$$\vec{i} = 2an\nu\exp[-(\frac{W-qaE}{kT})]$$
$$\overleftarrow{i} = 2a\{n + 2a(\frac{\partial n}{\partial x})\}\nu\exp[-(\frac{W+qaE}{kT})] \qquad (2\text{-}1)$$

$\frac{\partial n}{\partial x}$ = concentration gradient of the mobile ions.

q = charge of mobile ion.

Then, the current becomes

$$\begin{aligned} i &= \vec{i} - \overleftarrow{i} \\ &= 4an\nu\exp[-(\frac{W}{kT})]\sinh(\frac{qaE}{kT}) - 4a^2\nu\,\frac{\partial n}{\partial x}\,\cdot \\ &\quad \cdot \exp[-(\frac{W+qaE}{kT})] \end{aligned} \qquad (2\text{-}2)$$

Or, with the substitutions

$$A = 2an\nu\exp[-(\frac{W}{kT})] \quad \text{and} \quad B = \frac{qa}{kT}$$

$$i = 2A\sinh(BE) - 2A\cdot\frac{a}{n}\,\frac{\partial n}{\partial x}\exp(-BE).$$

<u>Low-Field Limit</u>:

For $(BE) \ll 1$, we have $\sinh(BE) \approx (BE)$ and $\frac{W}{kT} \gg BE$, and therefore obtain

$$\begin{aligned} i &= \text{constant}\cdot E - \text{constant}\cdot\frac{\partial n}{\partial x} \\ &= \sigma\cdot E - D_o\cdot\frac{\partial n}{\partial x} \end{aligned} \qquad (2\text{-}3A)$$

where σ is the Ohms law conductivity and D_o is the diffusivity according to Fick's first law.

High-field Limit:

At the other extreme, we have $BE >> 1$, so that $\overrightarrow{i}$ becomes much greater than $\overleftarrow{i}$, to the order of 10^{10} times, and so

$$i \equiv \overrightarrow{i} = A \exp(BE). \qquad (2\text{-}3B)$$

It is of interest to examine the Verwey model numerically and determine whether one of (2-3A) or (2-3B) is always valid under anodic oxidation conditions. Rewriting equation (2-2), we have for the general expression for ionic current,

$$i = 4a\nu\exp[-(\frac{W}{kT})]\{n\cdot\sinh(\frac{qaE}{kT}) - a\exp[-(\frac{qaE}{kT})]\frac{\partial n}{\partial x}\}$$

$$= C\{n\sinh[\frac{qaE}{kT}] - a\exp[-(\frac{qaE}{kT})]\frac{\partial n}{\partial x}\}$$

where C stands for $4a\nu\exp[-(\frac{W}{kT})]$. Two terms will be recognized:

$$\text{field-assisted term} = C\cdot n\cdot\sinh[\frac{qaE}{kT}] \qquad (2\text{-}4)$$

and

$$\text{diffusion term} = C\cdot a\exp[-(\frac{qaE}{kT})]\cdot\frac{\partial n}{\partial x}. \qquad (2\text{-}5)$$

To maximize the diffusion term, we assume that there is a maximum possible concentration gradient, i.e.,

$n = n$ at $x=0$, i.e., at the metal/film interface

$= 0$ at $x=2a$, i.e., one atomic layer away.

Then, $$a\cdot\frac{\partial n}{\partial x} = \frac{n}{2}$$

and the ratio of relative contributions to the current due to the field-assisted and diffusion terms is given by

$$\frac{\text{Field-assisted term}}{\text{Diffusion term}} = \frac{2\sinh(\frac{qaE}{kT})}{\exp[-(\frac{qaE}{kT})]} \; .$$

Under typical operative conditions of anodic oxidation, we can assume values for the various parameters as follows:

$E^* \geq 3\times10^6$ volts/cm ; $a \approx 1.5$ Å ;

$q = 2$ if oxygen mobile ;

$kT = \frac{1}{40}$ eV at room temperature

The result is that the ratio of current contributions for $q=2$, is as follows,

$$\frac{\text{Field-assisted term}}{\text{Diffusion term}} = \frac{2\sinh(3.6)}{\exp(-3.6)}$$

$$= 1360$$

such that field-assisted migration dominates over the diffusion term to an extreme extent and, moreover, the ionic current will always be the same as for high fields, i.e.,

$$i = A\exp(BE) \; . \qquad (2\text{-}3)$$

2.1.2 Mott and Cabrera's Model:

Mott and Cabrera (1947, 1948-9) took into consideration the surface space charge at the metal/film** interface.

---

*The estimate for E is based on the common observation that anodic oxide films have a thickness which is less than about 35 Å/volt.

**We prefer the use of "anodic film" to "anodic oxide" because, under certain circumstances, the product of anodic oxidation is not a pure oxide but contains anionic contributions from the electrolyte (Amsel, 1969).

The field strength in the oxide will change, according to Poisson's equation, only if volume space charge is present. Such a change in field strength is given, in e.s. units, by

$$\frac{\partial E}{\partial x} = \frac{4\pi\rho}{\varepsilon}$$

where ρ is the volume space charge density and ε is the dielectric constant.

The net volume space charge is due to the inequality between the positive space charge due to the mobile ions (we note again the restrictive assumption of an interstitial carrier!) and the negative space charge due to the conjugate non-mobile species (electronic space charge would tend to be swept away at such high fields).

If the volume space charge density is not too great, then the change in the field across the film, a function of the total charge present in the film, must be small for a thin enough film, i.e., the field is a constant to a first approximation. Moreover, the current will be controlled only by the rate of entry of ions into the film provided, as assumed by Mott and Cabrera, two conditions are satisfied: (a) the film is thin and (b) the first barrier to be surpassed by ions entering the film is sufficiently higher than the later barriers, as shown in figure 2-2. The current across the entrance barriers is given by

Fig. 2-2

Potential Energy vs. distance for ion entering oxide from the metal, with applied field.

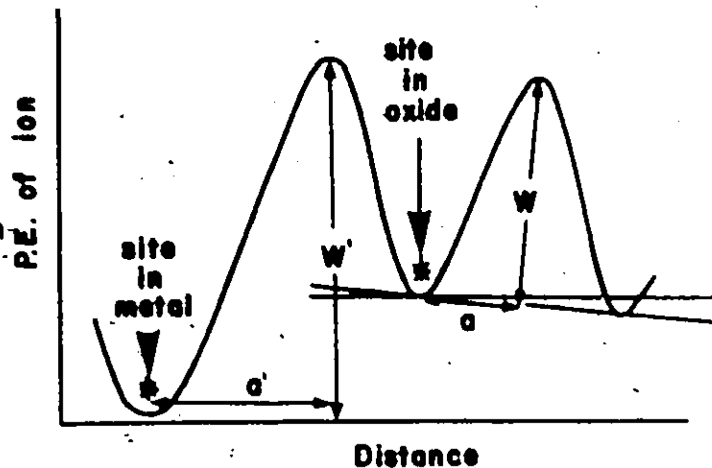

$$i = n'\nu' \exp[-(\frac{W'-qa'E}{kT})] \qquad (2\text{-}6A)$$

where n' is the concentration of ions per cm^2 at the interface and primes are used to identify parameters associated with the entrance barrier. The concentration, n, of ions within the film is not fixed. It adjusts itself, in the steady state, until the current within the film, assuming high fields, namely

$$i = 2an\nu \exp[-(\frac{W-qaE}{kT})], \qquad (2\text{-}6B)$$

just equals that across the entrance barrier. We thus obtain the result

equation (2-6A) = equation (2-6B).

This leads to $n = n_o$

where

$$n_o = \frac{(n'\nu')^{\frac{a}{a'}}}{2a\nu} \exp[(\frac{W - \frac{aW'}{a'}}{kT})] i^{(1-\frac{a}{a'})} \quad . \qquad (2\text{-}7)$$

2.1.3 Young's Generalized Model:

This is a general treatment with the above two models as the limiting cases. In deriving it, Young (1959) generalized the treatment of Dewald (1955).

Assume that the concentration of mobile metal ions in the electrically neutral film is p. The space charge due to the conjugate non-mobile species is thus (-pq) where q is the charge on the metal ions. Then, Poisson's equation gives

$$\frac{\partial E}{\partial x} = \frac{4\pi q}{\varepsilon}\,(n-p)$$

where (n-p) is the number of mobile ions per unit volume in excess to those required for electrical neutrality and $n = n(x)$ is, as before, the actual concentration of mobile metal ions in the film during anodization. The current at point x in the film is

$$i = 2an\nu\ \exp[-(\frac{W-qaE}{kT})]\,. \qquad (2\text{-}8)$$

Under steady-state conditions, it follows that $i \neq i(x)$. However, we must anticipate that both n and E vary with x. Writing $B = \frac{qa}{kT}$, we have

$$\frac{\partial i}{\partial x} \propto [\frac{\partial n}{\partial x} + nB\,\frac{\partial E}{\partial x}] = 0\ .$$

Substituting for $\frac{\partial E}{\partial x}$ from Poisson's equation leads to the result

$$\frac{\partial n}{\partial x} + nB\,\frac{4\pi q}{\varepsilon}\,(n-p) = 0.$$

Integrating, we get

$$n(x) = p[1-(1 - \frac{p}{n_o})\exp(-\frac{4\pi qpBx}{\varepsilon})]^{-1} , \qquad (2-9)$$

where n_o is the value of $n(x)$ at $x = 0$ as given by equation (2-7). Substituting for $n(x)$ in equation (2-8), we get

$$E(x) = E_o + \frac{1}{B} \ln\{p^{-1}[n_o-(n_o-p)\exp(-\frac{4\pi qpBx}{\varepsilon})]\} \qquad (2-10)$$

where E_o, equal to $(\frac{W}{qa} + \frac{1}{B} \ln \frac{i}{2an_o\nu})$, is the value of $E(x)$ at $x=0$ and given by equation (2-6A). $n(x)$ and $E(x)$ are thus both determined.

Equation (2-9) reduces to Mott's relation (i.e., $E = E_o$) for small x and to Verwey's relation for large x (i.e., $E = \frac{W}{qa} + \frac{1}{B} \ln \frac{i}{2ap\nu}$). The field thus changes with thickness at first but eventually becomes constant at Verwey's value.

Young (1961) suspected that the physical limitation that a film cannot be less than one unit cell thick may mean that the film may never be thin enough for Mott's model to be applicable to anodic oxidation. In Mott's model, the current through the anodic film is controlled only by the rate of entry of ions into the film. Thus, one expects the oxidation rate to depend on the crystal orientation. However, Masing and Young (1962) using Bi, Wales (1963) and Zwerdling and Sheff (1960) using Ge, and Whitton and Davies (1964) using Au did not observe any dependence of the oxidation rate on crystal orientation. On the other hand, Mott's case is tentatively supported by the results of Dewald (1957), who has found a

dependence of oxidation rate of InSb on the crystal orientation at low fields, though such dependence was not observed at high fields. Likewise, Young (1959) points out that as the metal ions leave the metal to enter the anodic film, they leave vacancies in the metal lattice which may result in a local misfit, causing the outer 2-3 layers of metal to become effectively amorphous. Such an effect, Young thinks, would depend on current density since diffusion within the metal would tend to repair such damage at low currents. If, however, such an amorphousness exists, it would tend to remove, or diminish, differences between kinetics on different crystal faces which are expected by the Mott's model.

2.1.4 Generalized Model

Writing down the expressions for ionic currents thus far discussed, we have:

Verwey's model: $$i = 2an\nu \exp\left(\frac{-W}{kT}\right)\exp\left(\frac{qaE}{kT}\right) \quad (2\text{-}1)$$

$$= A_1 \exp B_1 E$$

Mott-Cabrera model: $$i = n'\nu' \exp\left[-\left(\frac{W' - qa'E}{kT}\right)\right] \quad (2\text{-}6A)$$

$$= A_2 \exp B_2 E$$

Young's model: $$i = 2an\nu \exp\left[-\frac{W}{kT}\right]\exp\left(\frac{qaE}{kT}\right) \quad (2\text{-}8)$$

$$= A_3 \exp B_3 E$$

[Note: n is a function of x in eqn. (2-8)].

The difference between these models lies in the interpretation of A and B though we note that all models result in the same form for the relation between i, E and T, i.e.,

$$i = A_i \exp B_i E \qquad (2\text{-}11)$$

where $B_i \propto \frac{1}{T}$.

Hence, the experimental data are independent of the model for the particular models so far discussed and should give a simple voltage vs. time behaviour at constant current. This in turn means that there is no valid experimental distinction between these models.

2.2 Certain Inadequacies of the Above Models:

All the above models predict for the steady-state current

$$i = A \exp BE \qquad (2\text{-}11)$$

where $B \propto \frac{1}{T}$. In connection with equation (2-11), the following anomalies have been found:

(i) In the case of zirconium, the parameters A and B have been found by Young (1959) to depend on the thickness of the anodic film. Similar data for Ta, Nb, Bi, Ti etc. do not show any such anomaly for films thicker than about 100 Å. This suggests either that the anodic film on Zr is inhomogeneous or that Zr anodizes in accord with another model such as the two-barrier model of Dewald (1955). The difficulty with this model, however, as pointed out by Dignam (1965) is that it requires six disposable constants to define steady-state behaviour (Young's

generalized model involves at least seven disposable constants) and agreement with data of limited scope, such as is available for Zr, is almost inevitable regardless of the validity of the model. But more important, such an effect has been observed only with Zr.

(ii) Equation (2-11) leads to the conclusion that the Tafel slope, $\frac{\partial E}{\partial \ell n I}$, is proportional to T but independent of E. Vermilyea (1953), however, found that for Ta, the Tafel slope was independent of T. Later experiments of Young (1960) were fitted by replacing (W-qaE) by $(W-|\alpha|E + |\beta|E^2)$ to account for the variation of Tafel slope with field strength at a given temperature. Similar anomalies were also observed by Young (1956) for Nb and by Dignam et al. (1965) for Al. Sufficiently accurate data are not available for other valve metals.

(iii) Vermilyea (1957) also carried out transient experiments. He changed the field rapidly from a given initial value, under which steady-state conditions had been set up, and observed the immediate value of the ionic current at the new field. He assumed that in this case the change in current was solely due to a change in velocity of whatever mobile species were present, with no change occurring in their concentrations. He found that under these conditions the relation $\left(\frac{\partial E}{\partial \ell n I}\right)_{transient} \propto T$, which is expected from the above models, was not ob-

served, with the slope in fact decreasing slightly with increasing temperature. Similar measurements of Young (1961b) could, once again, be described by the empirical substitution $(W-|\alpha|E + |\beta|E^2)$ in the equation for ion mobility in place of $(W-qaE)$. This implies that the Tafel slope depends on E at constant T.

We recall, at this point, that all the above models ignored the amorphous nature of most anodic films. Young (1960) assumed a range or distribution of parameters 'a' and 'W', associated with an amorphous film but still could not justify the quadratic term in E. Later, Young (1963) suggested that the quadratic term may be explained in terms of an increase in the activation energy with increasing electrostriction. As the electrostriction, i.e., the film compression on applying a field, is proportional to E^2, this explanation predicts a quadratic term of the correct sign. Unfortunately, from the estimates given by Young and later discussed by Dignam (1964), it seems that the influence of electrostriction is below the limit of detection and hence does not serve much useful purpose.

(iv) In all the above models, it was assumed that only the metal ions are mobile. However, the tracer work of Davies et al. (1965) indicates that at least with Ta,

Nb, Al and W, both ions are not only mobile, but the transport numbers of both ions are also comparable. These results have, since then, been confirmed by Randall et al. (1965) for Nb and Ta, and by Pringle (1973) for Ta. The fact that both ions are mobile during the film growth process to comparable extents over a wide range of currents presents considerable difficulties to these models. The main difficulty is that any model with independent metal and oxygen ion mobilities would be expected to display a rapid change with field in the ratio of the two currents unless there existed fortuitously close similarities between the activation energies and activation distances, which is quite unlikely to occur with more than one metal.

2.3 Recent Theories Incorporating an E^2 term:

2.3.1 General: In the previous section, certain inadequacies of the classical theories of anodic oxidation were discussed. For example, it was shown that a major drawback of the classical theories lies in their inability to explain the Tafel slope behaviour of the experimental results. It was then pointed out that such anomalies could be removed by assuming the activation energy to be of the form:

$$W(E) = W - |\alpha| \cdot E + |\beta| E^2 . \qquad (2\text{-}12)$$

Recently, Dignam (1964), Christov (1963), Christov and Ikonopisov (1969) and Ibl (1967) have derived expressions which have the form of eqn. (2-12). Dignam's approach consists

of expressing the potential curve in the absence of external field with three types of functions, namely a clipped parabolic, a cosine and a Morse function, and found that the Morse function fitted the data best. He then extended his derivation, based on the Morse function, to his model of anodic film growth based on a mosaic structure. He considered that the oxide, in spite of being nominally amorphous, is composed of very small crystallites, or polymeric units, and that there are two types of ionic movements, one within a polymeric unit, and the other from one unit to another. On this basis, he is able to consistently explain almost all the anomalies described previously, including the comparable transport numbers of the metal and oxygen ions.

But Young and Zobel (1966) and Christov and Ikonopisov (1969) do not agree with Dignam's use of the Morse function. According to them, the Morse function does not represent the periodic variation of ion potential in the film and therefore is not acceptable from the physical standpoint. (Their view is probably incorrect as Morse functions with empirically determined coefficients have repeatedly given good results for solids (Jackson, 1973)). Moreover, by using the non-periodic clipped parabolic function, with a fixed barrier peak as assumed by Dignam, the quadratic term arising from the shifting of the potential minimum proves to be too small. Therefore, they think that the agreement found by Dignam with experimental results cannot be regarded as sufficient justification for his model.

In their approach, Christov (1963) and Christov and Ikonopisov (1969) assume a parabolic approximation of the ion potential only in the region of its maximum, with no hypothesis being made about the entire barrier shape. When large fields are applied, such as in the case of anodic oxidation, two types of shifts occur: firstly, the barrier top gets shifted with respect to its original position, and secondly the initial equilibrium position of the ion itself becomes displaced. The former corresponds to the shift occurring in Dignam's treatment whereas the latter is an additional shift tending to increase the quadratic term in E, an effect which is in the right direction. Christov and Ikonopisov also point out that expressions of the type given by eqn. (2-12) are valid only when the variations in field are not very large. In wider field ranges, they expect higher order terms, as perhaps happens in the case of electrolytic deposition of silver (Déspic, 1960).

Though the model of Christov and Ikonopisov predicts the existence of a term quadratic in E with minimum assumptions, it is unable to cope with the comparable ionic mobilities of the metal and oxygen ions. This problem may perhaps best be overcome by combining their treatment in getting E^2 term with the mosaic model of Dignam which explains the transients and the comparable cationic and anionic mobilities.

2.4 Mechanism of Anodic Oxidation

2.4.1 General: In the previous sections, we have discussed the various models of anodic oxidation. There are two basically different models, that of "internal control" of Verwey (1935) and of "interfacial control" by Mott and Cabrera (1947, 1948-9). These were generalized into a "dual-control" model, first by Dewald (1955) and then by Young (1959). However, these classical models were found to be inadequate in explaining various experimental observations, especially with regard to the behaviour of the Tafel slope, i.e. $\frac{\partial E}{\partial \ln I}$. Dignam (1964), Christov (1963), Christov and Ikonopisov (1969), and Ibl (1967), separately, put forward theories which explained the experimental behaviour much better.

But none of these models described the mechanism, i.e., the mode of ion transport, by which the anodic film grows. The classical models assumed that cations were the only mobile entity, as interstitials, whereas the later models of Dignam, Christov and Ibl made no such assumption.

2.4.2 Ion Transport Number: Vermilyea (1954), in his work on anodization of Ta in aqueous and non-aqueous electrolytes, first formed an anodic film in aq. 1% Na_2SO_4, then further formed the film in 80% H_2SO_4, and finally dissolved the duplex film in HF. The results are shown in Fig. 2-3 and lead one to conclude that the film grows at the electrolyte/film interface,

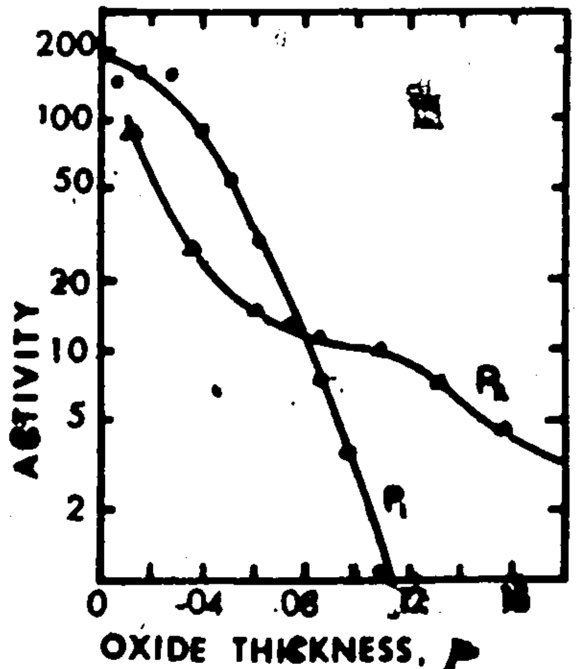

Fig. 2-4 Distribution of activity in Ta discs - P_1 without oxidation and P_2 after anodic oxidation.

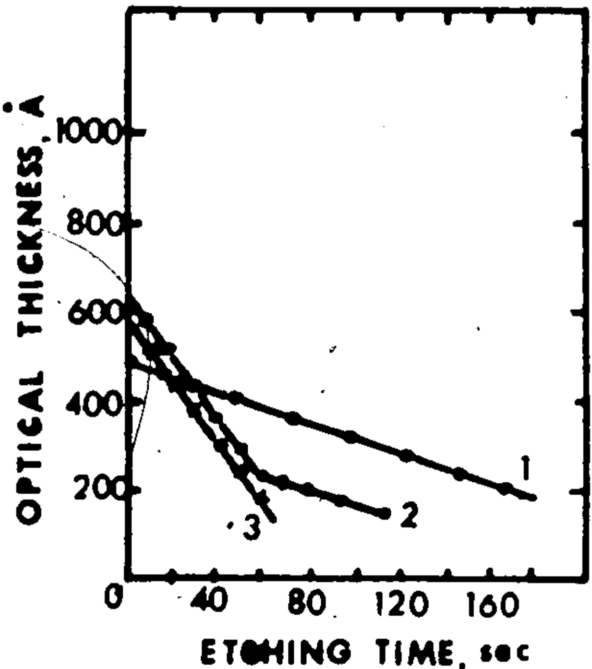

Fig. 2-3 Corrosion in HF of films formed in 1% Na_2SO_4 and 80% H_2SO_4 (after Vermilyea, 1954).

so that Ta ions were the only mobile species when anodized in concentrated H_2SO_4.

Verkerk et al. (1958) sputtered radioactive Ta on a clean Ta disc and heat-treated it. They then determined the profile of radioactive Ta in the disc with and without anodization and their results are shown in Fig. 2-4. They concluded that Ta ions were mobile but their transport is neither governed by pure vacancy mechanism, nor by a pure interstitial mechanism. Cheseldine (1964), using a sequence of non-aqueous (formic acid) and aqueous (dil. H_2SO_4) electrolytes, found that in the case of Ta the rapidly dissolving part of the film, formed during the first anodization in non-aqueous electrolyte, was sandwiched between the two less soluble films, i.e., both Ta and oxygen ions move during anodic oxidation.

Concerning the anodization of Al, Lewis and Plumb (1958) used marker experiments and Amsel and Samuel (1962) used O^{18} as tracer in their studies on the ion transport mechanism, and both groups concluded that the anodic film growth in Al proceeds by metal ion migration.

In their now classical work, Davies et al. (1965) used β-ray spectroscopy and a radiotracer technique to study the mode of ion transport in the anodic oxidation of Al, Nb, Ta, W, Hf, and Zr. They introduced trace amounts of Xe^{125} in thin anodic layers of the metals under investigation, measured the mean depth of the Xe^{125} atoms, anodized the metal foils

further and again determined the mean depth of Xe^{125} atoms. They concluded that both, metal and oxygen, are mobile during film growth on Al, Nb, Ta, and W, but in Zr and Hf only oxygen ions moved. There seemed an obvious conflict with the previous results on Al and Ta (except those by Cheseldine) but Davies et al. reinterpreted the results of previous studies and concluded that there was no basic disagreement and that both species were indeed mobile in the cases of Al, Nb, Ta and W whereas only oxygen was mobile in Zr and Hf anodic oxidation when aqueous electrolytes are used.

2.4.3 Influence of Nature of Electrolyte on Anodization Behaviour:

The formation of highly insulating anodic films is possible in the case of about 20 elements and many data exist on the subject. In most investigations on the formation kinetics and properties of anodic oxide films, it has been tacitly assumed that the film formed is a pure metal oxide and little attention has been directed until recently to the role that the electrolyte plays in the film growth and in the film properties. In recent years, it has been demonstrated in anodization of several metals that the electrolyte may play a decisive role in determining the kinetics and the film properties. To arrive at the knowledge of the mechanism and the optimal conditions of anodic film formation, it is necessary to know, among other things, the role of the electrolyte, the sources of oxygen in the anodic film, etc. Some of the important effects of electrolyte are considered below

and the sources of oxygen will be considered in the next section.

Solubility Effect: While it has long been known that metals such as Nb and Ta may be anodized in nearly all electrolytes, there are other materials which will anodize only in some particular solutions. Thus, with Ge (Zwerdling, 1960; Wales, 1963), V (Keil and Salomon, 1965, 1968), Mo (present work) and Sn (Giani, 1971), anodic films fail completely to grow in aqueous solutions and electrolytes based on non-aqueous solvents have to be used. Therefore, the choice of electrolyte not only affects the nature of anodic growth but may also determine whether any growth at all would be observed due to the solubility problem.

Doping Effect: In aqueous electrolytes, the anodic films on Nb, Ta, Al, etc. are pure metal oxides (see for example Young, 1961). In his work on Ta, Vermilyea (1954) demonstrated that films formed in H_2SO_4 were inhomogeneous so that the outer portion dissolved in HF at a much faster rate than the inner portion with the inner layer behaving like pure Ta_2O_5. Randall et al. (1964) used sulphuric and phosphoric acids as electrolytes and found massive incorporation of sulphur and phosphorous in the anodic films. They concluded that the inhomogeneity in the anodic films on Ta was chemical in nature due to the presence of sulphur and phosphorous, i.e., the anodic films were doped. Essentially similar results were

obtained by Amsel et al. (1969) while using H_2SO_4 solutions. The extent of doping was found to depend on the concentration of H_2SO_4 and H_3PO_4 solutions. Even with dilute acids as electrolytes, some incorporation of foreign material was found in the anodization of Al [Plumb, 1958; Bernard and Randall, 1961], Nb [Randall et al.,1965] and Si [Schmitt and Owen, 1964].

One of the effects of doping is that the thickness at any given voltage, for a given current density, is smaller [Young, 1960; Vermilyea, 1954], i.e., the potential necessary to form a film of a given optical thickness increases markedly with the concentration of sulphuric acid. Further, Vermilyea (1954), Randall et al. (1964) and Smyth et al. (1966) observed that the interface between doped and undoped films moves towards the metal/film interface as the concentration of H_2SO_4 or H_3PO_4 increases, i.e., the amount of film formed as a result of oxygen ion migration decreases with increased acid concentration. Thus, it appears that the presence of dopants in the film reduces the field-assisted mobility of oxygen. Since for Ta and Nb the anodic films formed in concentrated H_2SO_4 and H_3PO_4 are optically thinner than those formed in aqueous electrolytes, the flow of both Ta ions and oxygen ions may be retarded due to doping provided the refractive index of the film has not changed too drastically. Smyth et al. (1966), however, think that the oxygen ion current is restricted to a much greater extent.

As described earlier, most doped anodic films in Ta have enhanced solubility as compared with the pure Ta_2O_5 films. This fact has proved to be of paramount importance leading to the successful anodic sectioning of Nb and Ta (to be described later). It must, however, be kept in mind that doping does not necessarily lead to enhanced film solubility since the anodic films formed in concentrated H_3PO_4 have a solubility rate in HF smaller than that of the normal Ta_2O_5 films.

Stoichiometry Effect: Another important, though totally unrelated, effect of the electrolyte is on the electronic conductivity of anodic films formed on Nb and Ta. Vermilyea (1965) found that when as little as 0.01% H_2O_2 was added to dilute acids (e.g., 1% HNO_3 or 1% H_2SO_4), the electronic conductivity of films formed on Nb and Ta decreased by several orders of magnitude. Nb also shows a similar effect, to a lesser extent, with the additions of small amounts of $HClO_4$. This effect may be correlated with the result of Janninck and Whitmore (1962) who found that Nb_2O_{5-x} [where x may be as small as 0.05] has a much greater electronic conductivity than pure Nb_2O_5. Addition of a strong oxidizing agent such as H_2O_2 or $HClO_4$ would tend to remove the slight non-stoichiometry of the anodic oxide (if any), an effect which is quite consistent with the experimental results.

2.4.4 Sources of O_2 in the Anodic Film

The problem of the origin of oxygen in anodic films has not been extensively studied till recently. Most authors have concluded that the only source of oxygen is water. Kover and Musselin (1968), using the nuclear reactions $O^{16}(d,p)O^{17}$ and $O^{18}(p,\alpha)N^{15}$, show that water is the main oxidizing agent for Ti, Nb and Ta. In their initial study, Amsel et al. (1969) found that most of the oxygen came from water when Ta was anodized in aqueous solutions of H_2SO_4, H_3PO_4 and HNO_3. In a more detailed study on the anodization of Ta and Si in organic solvents, Croset et al. (1971), using a three-compartment cell (to isolate the anodic and cathodic compartments), found that (in an electrolyte consisting either of N-methylacetamide containing 0.4% H_2O or of an aqueous solution with 0.4% KNO_3) nearly 0.5 mole/Faraday of water was formed at the anode, 80% of which was destroyed at the cathode. From their studies, they concluded that 88±3% of the oxygen in oxides came from water, and about 10.6±1% oxygen came from the salt; they also concluded that the direct incorporation of nitrogen-containing anions accounted for less than 0.6% of the oxygen in SiO_2 and less than 2.4% in Ta_2O_5. They suggest that the protons which are produced at the anode by the following reactions:

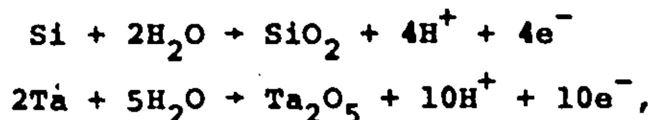

$$Si + 2H_2O \rightarrow SiO_2 + 4H^+ + 4e^-$$

$$2Ta + 5H_2O \rightarrow Ta_2O_5 + 10H^+ + 10e^-,$$

could react with the nitrate ions of the salt near the surface of anode to loosen up the oxygen-nitrogen bonds by the mechanism:

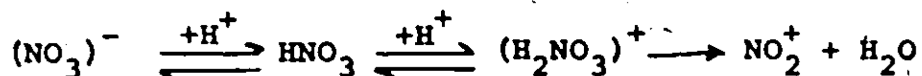

$$(NO_3)^- \underset{}{\overset{+H^+}{\rightleftharpoons}} HNO_3 \overset{+H^+}{\rightleftharpoons} (H_2NO_3)^+ \longrightarrow NO_2^+ + H_2O$$

As a result, the water just formed would react immediately with the anode to form oxide. Croset et al. also suggest that the primary reaction at the cathode is probably given by

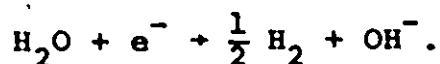

$$H_2O + e^- \rightarrow \frac{1}{2} H_2 + OH^-.$$

2.5 Limiting Film Thickness

2.5.1 General: As a consequence of the laws of ion transport, the thickness of barrier anodic films increases, in general, linearly with the potential across the film. The ultimate thickness of the anodic film may be limited by three phenomena which may be broadly classified as "chemical", "electrochemical", and "electrical". The chemical limitation is associated with film dissolution, the electrochemical limitation with oxygen evolution, while the electrical limitation generally occurs when the film has grown quite thick and electronic avalanche occurs.

2.5.2 Chemical Limitation: The chemical effect is basically quite trivial. If the anodic film is chemically unstable in the electrolyte, it will dissolve during film formation. If the dissolution rate is comparable to the formation rate, films

may never grow to large thicknesses, i.e., the film thickness is then limited.

2.5.3 <u>Electrochemical Limitation</u>: Oxygen is evolved when the potential of an electrode exceeds 1.23 volts on the hydrogen scale. In practice, however, a noticeable rate of oxygen evolution proceeds only at 1.5 - 2.0 volts due to the large overvoltages being required. If the anodic film contains pores, then oxygen will continue to be evolved rapidly at about 1.5 - 2.0 volts (Vermilyea, 1963). But even when the pores do close, oxygen may still be evolved if electrons can somehow be transported through the film (as when the film has a non-zero electronic transport number). In either case, the result is that the potential across the film would not rise, and the film growth would thus be limited. The anodic reaction would then be

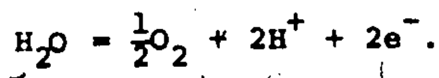

$$H_2O = \frac{1}{2}O_2 + 2H^+ + 2e^-.$$

What happens when the film is a poor electronic conductor? Now the field can rise to a value sufficient to move ions through the film, and the film would apparently continue to grow.

But the picture is still not complete. Even a film which is a poor electronic conductor must meet two requirements. The first is that the band gap should, in general, be greater than about 3 eV, and second that the film thickness should be $\gtrsim$ 20 Å at the oxygen evolution potential. The reason is that the electric fields involved in the anodic film growth are

extremely high (10^6 - 10^7 volts/cm) such that electron tunneling becomes a distinct possibility. For example, with band gap of 2 eV and a field of 10^7 volts/cm, the distance that is required to move an electron at the top of the valence band at constant energy to an empty state in the conduction band is only 20 Å, and tunneling should occur fairly easily. Similarly, when the film thickness is less than 20 Å at the oxygen evolution potential, the band gap should be even greater than ∿ 3 eV otherwise the anodic film growth cannot be supported without much current being consumed in oxygen evolution via tunneling.

Provided oxygen evolution can be avoided, the film thickness can reach several thousand angstrom units. However, even in the most ideal cases, oxygen must eventually be evolved. This high-voltage breakdown is discussed next as "electrical breakdown".

2.5.4 Electrical Breakdown: When barrier anodic films are grown at constant current, their potentials increase almost linearly with time until, at a particular voltage, there is a sharp deflection in the voltage-time curve, which may be accompanied by sparks across the film so that voltage oscillates without rising any further. In other systems, such as Ti and Zr (Yahalom, 1971), the galvanostatic potential behaviour does not show any sharp deflection point; in such cases, the rate of potential rise is found to be characteristically low, which tends to decrease still further with time as the

potential gradually reaches the sparking level. Films formed in such systems are partly crystalline at any stage of their formation (Yahalom, 1973) and oxygen evolution accompanies film growth.

The experiments of Yahalom and Zahavi (1971) have demonstrated that a relation exists between the electrical breakdown and the electrolyte. They first anodized Ta in concentrated sulfate solution to beyond the breakdown voltage till the film was crystalline; the specimen was then transferred to a dilute sulfate solution and the anodizing resumed. They found that film formation continued at normal kinetics until the voltage reached the breakdown value characteristic of the latter electrolyte. They then conducted a similar experiment in the reverse sequence by first forming the film to large thicknesses (above the limit for the concentrated electrolyte) in the dilute electrolyte (but before breakdown) and resuming it in a concentrated solution. Breakdown occurred instantly in the second electrolyte despite the soundness and the purity of the film formed in the first stage. This elegant experiment rules out any hypothesis based on the argument that the incorporation of foreign anions causes brittleness of the film to facilitate the breakdown. It also makes an important distinction between the cause and effect problem of breakdown and crystallization. Some authors (see for example Lakhiani, 1960) believe that breakdown is caused

by the film crystallization. As has been shown by Yahalom and Zahavi (1971), however, the crystalline film formed in concentrate sulfate solution, could be further anodized at its normal kinetics, to its characteristic breakdown voltage in a dilute sulfate solution, i.e., the film crystallinity had almost no effect over the anodic behaviour.

During galvanostatic anodization, breakdown does not seem to occur until a certain thickness of film has been formed. Such a critical-thickness effect has been demonstrated even more forcefully in connection with potentiostatic anodizing of Al (Yahalom (1973), where the field decreases as the film thickens until breakdown eventually occurs.

One possible interpretation of the need for a critical film thickness for breakdown to occur is that internal stresses, which increase with film thickness, finally cause the film to fracture. The film/electrolyte interface in this argument would then determine the surface energy of the oxide and hence the necessary stress for brittle fracture.

Another interpretation involves the formation of an electron avalanche in the film (Kawamura, 1953). In this instance, electrons are accelerated by the field to an energy at which they can make ionizing collisions with the oxide lattice. If a critical size avalanche is needed for film breakdown, then a critical film thickness is required and the role of the film/electrolyte interface probably involves

the availability of the number of electrons for such process.

Based on all this information, Yahalom (1973) concludes that the mechanism of electrical breakdown involves two stages. In the first stage, sporadic electron discharges, perhaps initiated by tunnelling, may develop into short-lived avalanches; this may cause localized heating in oxides such as TiO_2, ZrO_2, and Ta_2O_5 (field crystallization). When the film thickness approaches a critical thickness, the small-scale discharges develop into large-scale sustained avalanches. The critical thickness, besides permitting a sufficient number of collision generations, also serves to bring about sufficient Joule heating as required to increase local conductivity both in the film and in the adjacent electrolyte; this heat may also trigger additional electron emission at the interface. Thus, for a given metal, with high natural oxide conductivity and good donor properties of the electrolyte, film breakdown may occur at smaller thicknesses. Crystallization of the film would now be said to be only one of the by-products of the breakdown and not its cause.

CHAPTER 3

ANODIC SECTIONING

PART II - FILM FORMATION

3.1 General:

As already pointed out at the beginning of Chapter 2, reaction films on metals and semiconductors are formed due to thermodynamic instability in the surrounding environment. Anodic films constitute a special class of reaction films which are electrochemically formed with the aid of an electric field. The growth of anodic films permits much greater freedom with regard to the driving force E (related to current passing through the film) which may either be varied at will or be kept constant, and the environment (i.e. the electrolyte). The influence of the electrolyte was described in the previous chapter as being such that either pure or doped anodic films may be formed, while to some extent even the electronic properties of the films could be varied. Among the characteristics of anodic films as opposed to other reaction films, one might also mention their uniformity and reproducibility.

Though the anodization of many metals and semiconductors has been studied to date, the substances that come closest to exhibiting perfect anodic behaviour are Ta, Nb, and Al. Most work, especially of a quantitative nature such as testing the models (as outlined in sections 2.1-2.3) or studying the mechanism

of anodic oxidation (section 2.4), has therefore been done with these three metals. It has been mentioned earlier that there is now a growing interest in the removal of extremely thin films from the surfaces of solids (≤ 100 Å thick). Davies et al. (1960), in their pioneering work on Al, described a two-step process of anodic film formation and its removal without significant attack on the underlying metal. Such a process is known as "anodic sectioning" and has been found to be the most precise, sensitive and reliable of all sectioning methods available. Davies and his co-workers subsequently studied W (McCargo, 1963), Si (Davies, 1964), and Au (Whitton, 1964), though only in the case of W was the sectioning procedure fully satisfactory.

With ion implantation studies, as has been mentioned earlier, anodic sectioning plays an important role. However, with procedures perfected only for Al and Si (mass region 30) and W and Au (mass region 190), a big gap obviously remains in the region of intermediate masses. As a further point, there is a great current interest in extending information on self-diffusion in bcc metals to very low temperatures due to the anomalous behaviour found with V, Ti, Zr, and U. Therefore, for the present work, four bcc metals three of which have intermediate masses were chosen: V (mass 51), Nb (mass 93), Mo (mass 96), and Ta (mass 181). Work was also undertaken on W, in part for the sake of comparison, and in part to extend the already existing sectioning procedure.

Other groups have also been active, and therefore it is probably well to emphasize that sectioning procedures have recently been described by Lam for Ag (1972a), Cu (1972b) and Nb (1971). However we do not regard this new work as detracting from the importance of what is presented here, in view of the fact that the new procedures were, so to say, "imperfect". In fact, considering all the available information, one can summarize as follows:

Al, W : satisfactory sectioning available

Ag, Cu: imperfect sectioning since current remains constant at a fixed voltage

Au : imperfect since current remains constant at a fixed voltage and the current efficiency is low (∿ 2%)

Nb : imperfect since dissolution-end-point is unsatisfactory

Si : imperfect since the current efficiency is low (1-2%) and the thickness calibration depends on the electrolyte.

The two steps of anodic sectioning are considered separately. In this chapter, the first part consisting of film formation which includes the experimental set-up, followed by the work on kinetics of film formation, will be described. The second part, with emphasis on the film removal and thickness calibrations, will be described in the next chapter.

3.2 Anodization of V, Mo and W:

3.2.1 General: Various authors (see for example Johansen et al., 1957; Wood and Pearson, 1967) have consistently failed to form insulating, protective anodic films on V in aqueous electrolytes, though Young (1961) suggested that anodic films on V may be formed in non-aqueous electrolytes. Subsequently, Keil and Salomon (1965, 1968) established what is still the only known electrolyte that will support the growth of insulating anodic films on V. They, as well as Keil and Ludwig (1971), established the basic electrochemical properties of the anodic films on V, e.g., that anodization was close to 100% in efficiency, that the anodic current obeyed the expected exponential law, and that the film had a stoichiometry similar to VO_2.

On anodic polarization in alkaline solutions, Mo dissolves to form molybdates (for references, see Young, 1961). Lavrenko et al. (1963) have anodized Mo in a solution of saturated boric acid but it appears that they used conditions of anodic polishing. In addition, Ikonopisov (1972) has suggested that the high potential drop that Lavrenko et al. (1963) observed in their study may have been due to the high-resistance diaphragm between the two electrodes. Wood and Pearson (1967) and Menzies (1969) were quite unable to form protective anodic films on Mo. Very recently, however, Mo has been successfully anodized in an electrolyte based on a glycol-borate mixture (Ikonopisov, 1972, 1973) but the data available are limited in nature.

W, on the other hand, is readily anodized and has been studied in comparatively great detail. Güntherschulze and Betz

(1937) and Boosz (1957) studied anodic film formation on W from the kinetic point of view. McCargo et al. (1963) anodized W in an aqueous solution of KNO_3(0.4M) and HNO_3(0.04M), while more recently, Ammar and Khalil (1971) have studied the anodic behaviour of W in other acidic media. The latter pointed out that stirring and higher formation temperatures increased the rate of film dissolution, but that the film growth otherwise followed an exponential growth law (i.e., $i = A \exp(BE)$).

3.2.2 Anodizing Step: Polycrystalline specimens, with dimensions of 20×15×0.1 mm and with a purity claimed to be 99.98% were used with all the three metals. They were cleaned using a sequence of petroleum ether, dilute nitric acid, and distilled water, and were anodically sectioned at least twice at 50 volts (sectioning details in the next chapter). The electrolyte used was similar to that proposed by Keil and Salomon (1965), namely glacial acetic acid such that each liter of solution contained 0.02 moles of $Na_2B_4O_7 \cdot 10H_2O$ and 1.0 mole of additonal water. In the case of V and Mo, freshly formed anodic films were found to be rather unstable in ambient atmosphere so that they would change interference colours when exposed to air. They were therefore stabilized by either dipping them in glacial acetic acid and then drying using filter paper or by using a jet of compressed air immediately after their withdrawal from the electrolyte. Once stabilized, they could be stored in a desiccator indefinitely. Such problems did not arise with W.

The electrolyte was not protected from air and due to its hygroscopic nature, it tended to pick up moisture. Therefore, it was discarded after 8 to 10 anodizings or 2 hrs, whichever came first. The cathode used was either a Pt cylinder with an inside diameter of 2.5 cm or a 2.5×2.5 cm Pt foil spaced 0.8-1.0 cm from the specimen, the choice depending on whether the experiment was concerned with both sides of the specimen (e.g., a gravimetric calibration or a kinetic measurement) or only one side (e.g., a depth distribution). All anodizings were carried out at 25±1°C with a power supply such that limits to both the current and voltage could be preset (Hewlett-Packard Model 6186B). Voltages refer to the total voltage drop from the anode to cathode, being uncorrected for the ohmic drop in the electrolyte (this correction is not important when the current is allowed, as in the thickness calibration, to fall).

Above 10-15 volts, the presence of the anodic films on these metals could be detected visually, and their uniformity verified, by means of the brilliant interference colours that occur.

3.2.3. <u>Effect of Stirring</u>: Galvanostatic measurements on V and Mo with stirred and unstirred electrolytes showed that stirring affects the rate of film growth in such a manner that the charging curves (voltage vs. time) are lowered (figure 3-1). Such an effect was found to increase with increased stirring and decreased current density. Similar effects have also been found to occur with Bi (Ammar, 1971a) and W. (Ammar, 1971b) and may be

Fig. 3-1 Effect of stirring on film growth at constant current

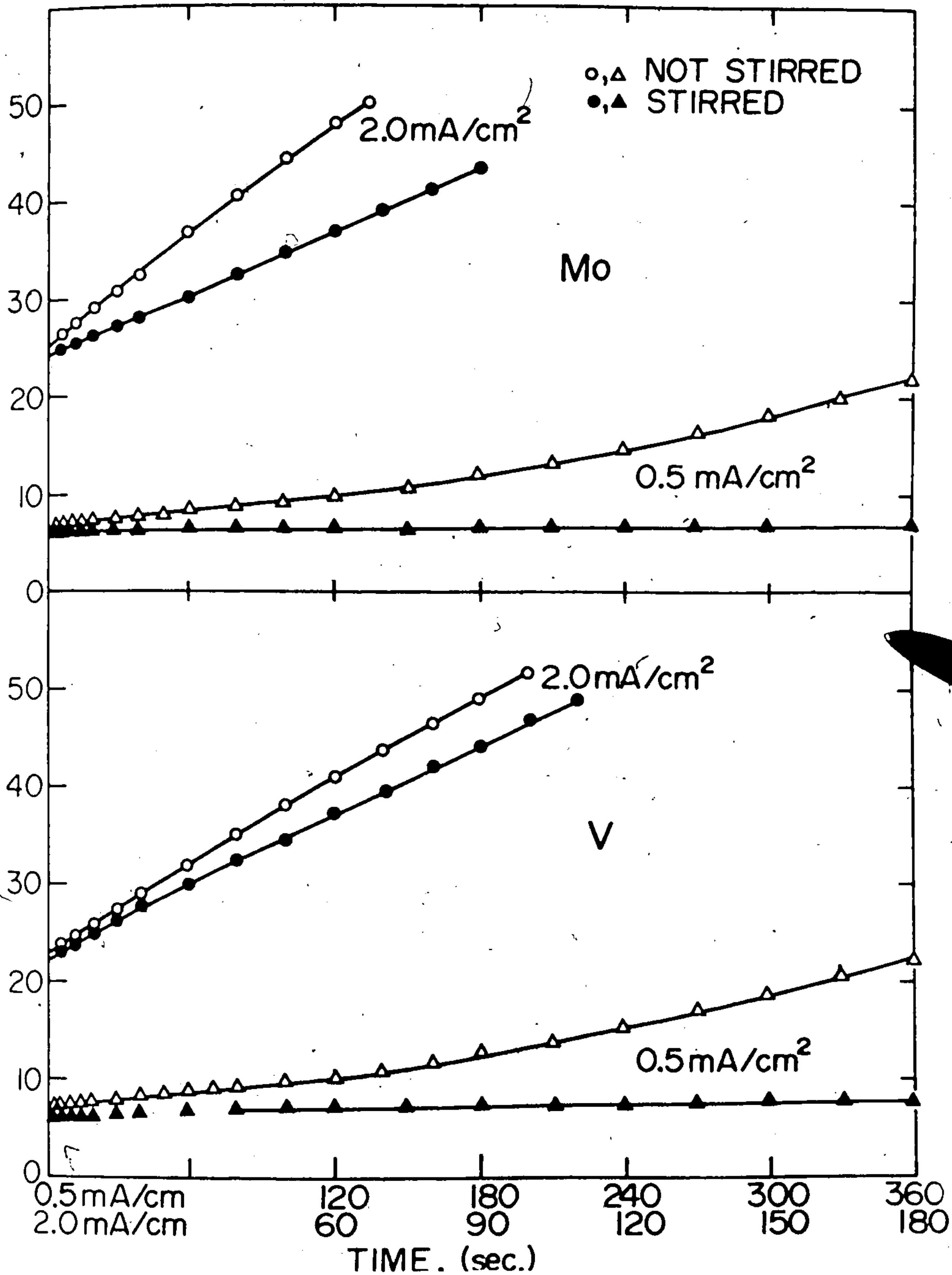

o,△ NOT STIRRED
●,▲ STIRRED
2.0mA/cm²
Mo
0.5 mA/cm²
2.0mA/cm²
V
0.5mA/cm²
0
10
20
30
40
50
0.5mA/cm
2.0mA/cm
120
60
180
90
240
120
300
150
360
180
TIME. (sec.)

explained in terms of stirring preventing the dissolved film from accumulating near the anode surface. At high current densities ($\geq$ 1.5 mA/cm^2), stirring is less successful in removing all the dissolved anodic film from the area close to electrode surface so that very soon the metal is surrounded by a high concentration of dissolved film and further dissolution is hindered. At medium current densities ($\sim$1.0 mA/cm^2) due to the smaller rate of film formation, it is assumed that a greater fraction of the dissolved film can be transported away from near the electrode surface by stirring and as a result the V-t curves are concave upwards. At still lower currents ($\leq$ 0.5 mA/cm^2), even the random motion due to thermal energy (in the absence of stirring) is sufficient to transport much of the dissolved film away from the anode, and a prominent induction period (or even no film formation at all) is thus observed. Such problems did not arise with W. It will be shown later (section 3.3.3) that these differences in the film properties, with V and Mo representing one type of behaviour and W representing another, have a significant effect on the kinetics.

In order to avoid the undesirable, and indeed basically trivial, effects as described above, all anodizings were subsequently carried out in unstirred electrolytes.

3.3 Constant-Current Characteristics

3.3.1: Film Growth: Film growth curves were obtained with a potentiometric recorder at various current densities, and are shown in figs. 3-2 to 3-4. When the film growth commenced,

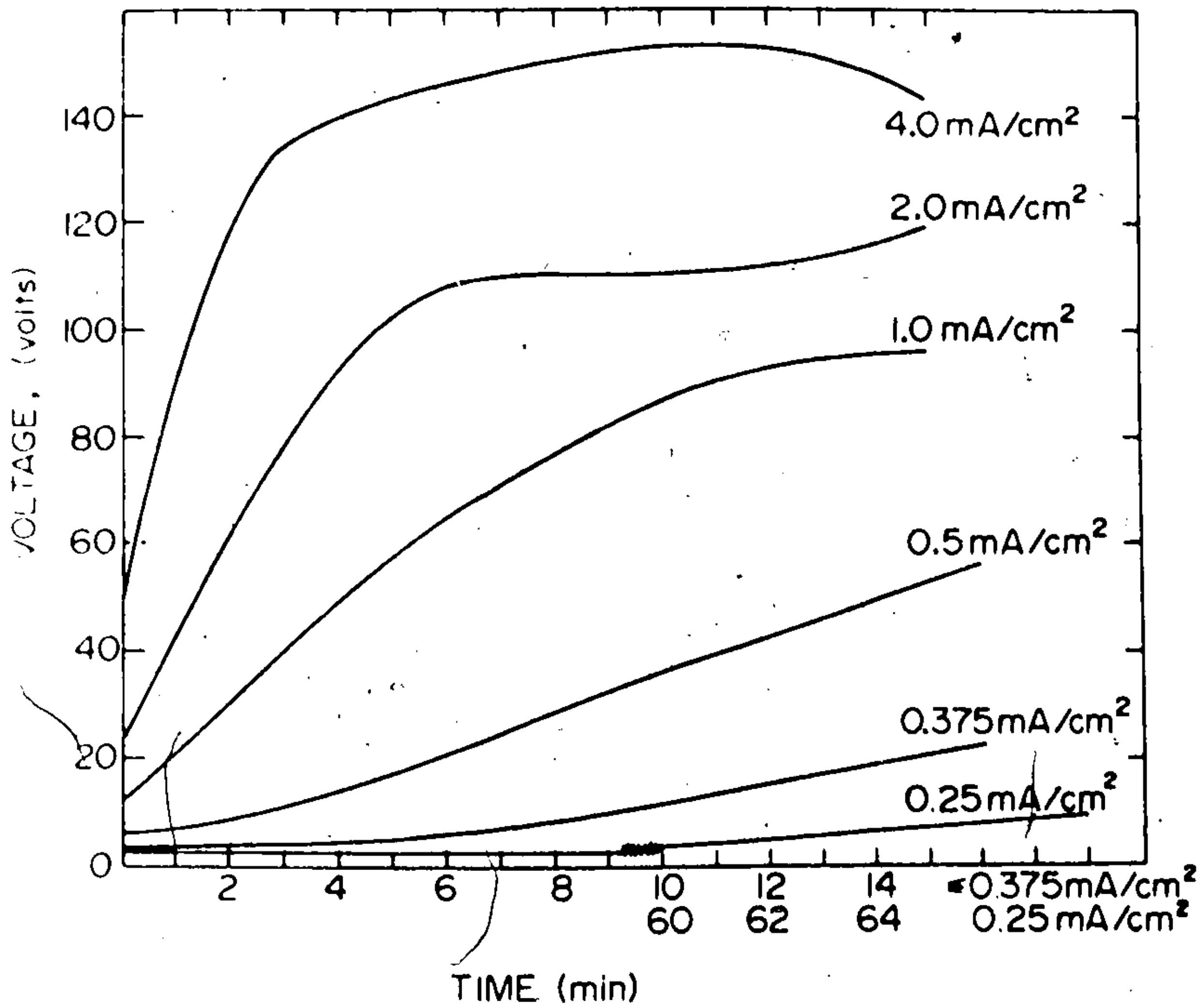

Fig. 3-2 Constant current film growth kinetics for V at various current densities

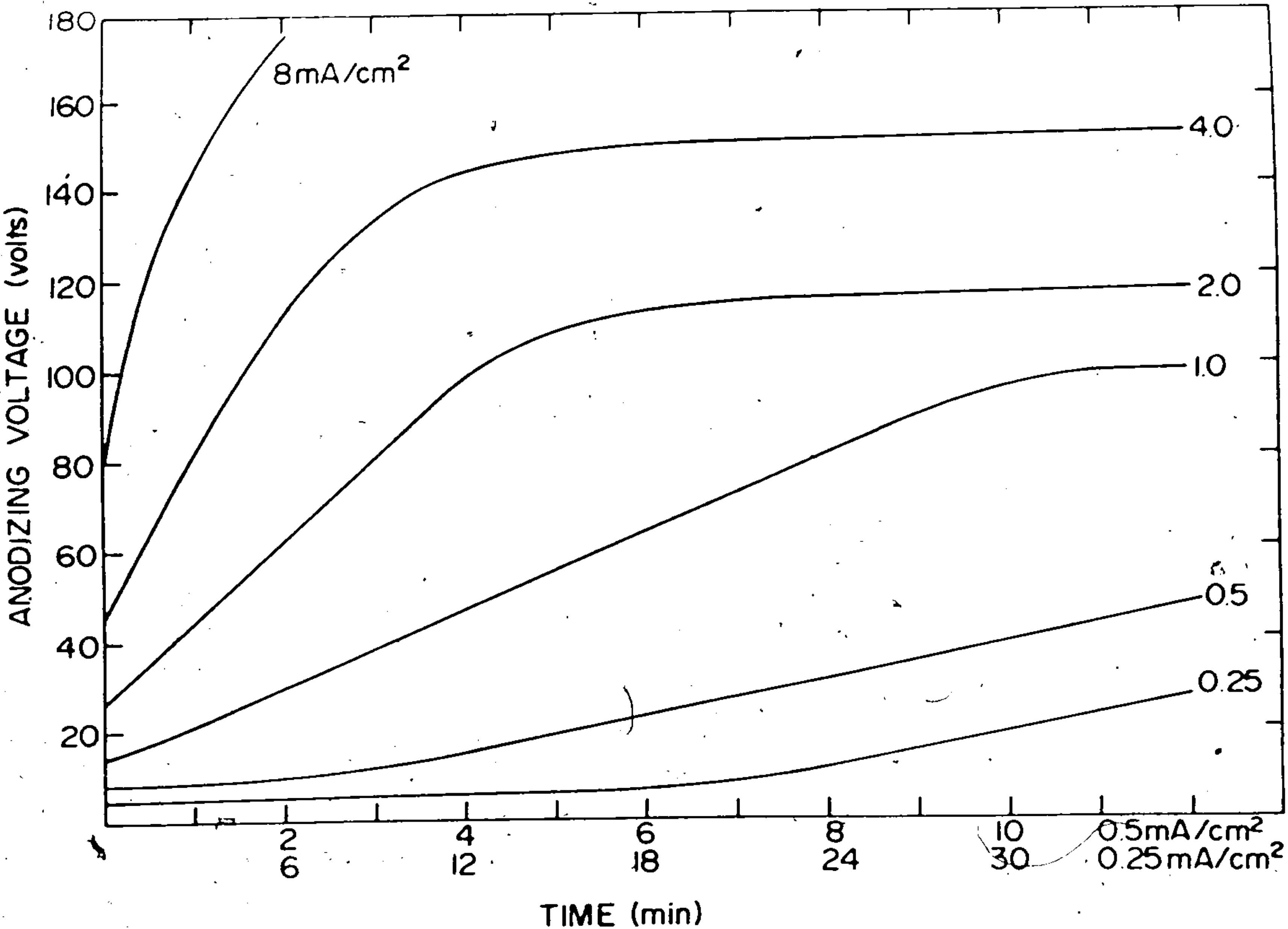

Fig. 3-3 Constant current film growth kinetics for Mo at various current densities

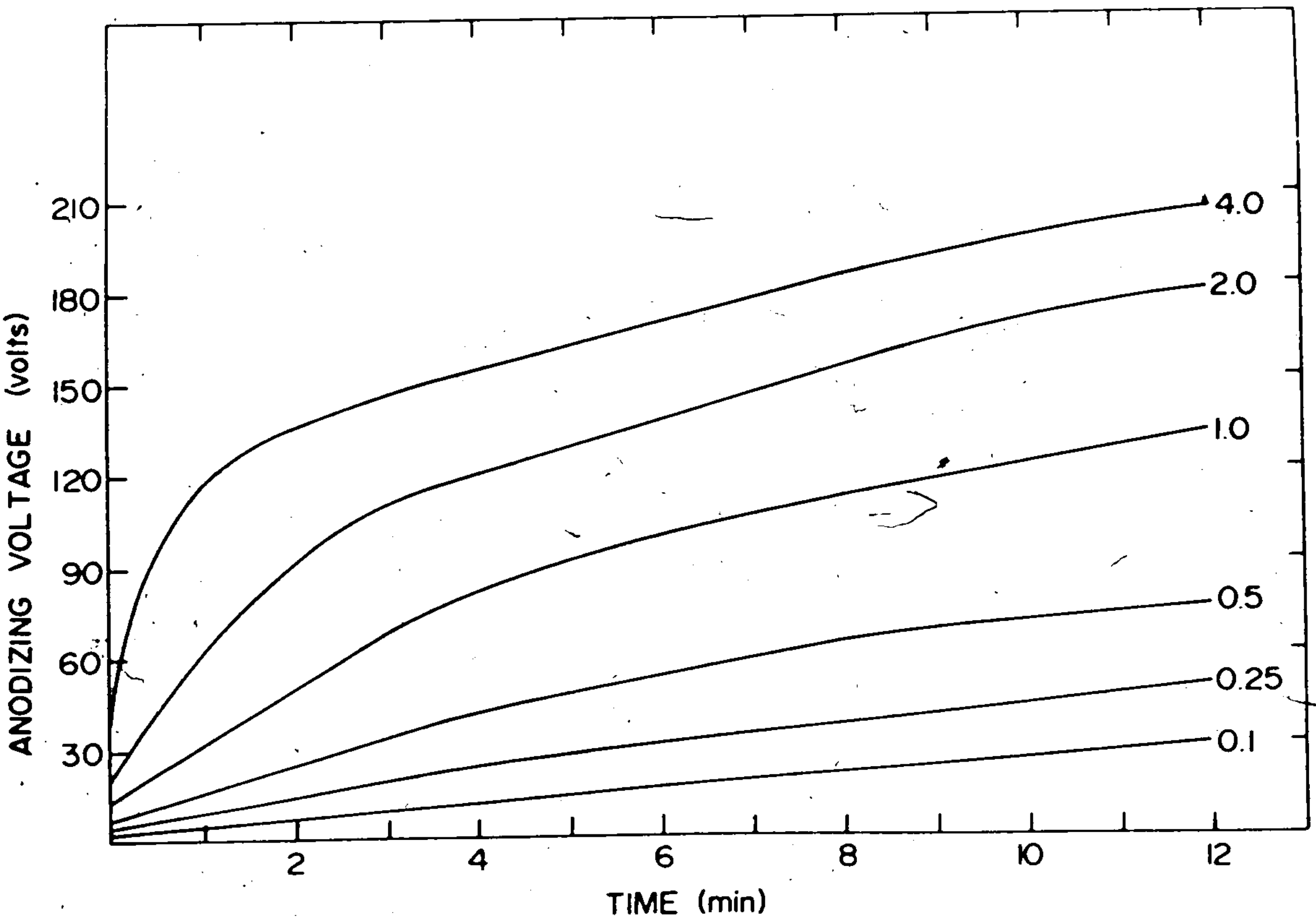

Fig. 3-4 Constant current film growth kinetics for W at various current densities

the anode potential first rose sharply. This transient may be attributed to the ohmic potential drop across the anodizing solution since, as shown in fig. 3-5, it is essentially linear with current density. As stated above, either an upward concaveness or an induction period is observed at low currents ($\lesssim$ 0.5 mA/cm^2) in case of V and Mo. After this induction period for V and Mo, and from the very beginning for W, there followed a period of gradual and almost linear rise of potential. When a critical value of the potential is reached, however, a breakdown process occurs when the potential begins to show an erratic behaviour by either oscillating or by rising reluctantly. This behaviour was accompanied by gas evolution (assumed to be oxygen) and occasional sparks, and soon the films lost their brilliant interference colours and gradually became dull gray in appearance.

In the region just before the breakdown voltage, the V-t curves departed from linearity. Similar behaviour has also been observed in the cases of Ti and Zr by Yahalom and Zahavi (1971) who explained it as being due to the partly crystalline nature of anodic films on Ti and Zr and the simultaneous oxygen evolution accompanying the film growth. In the case of V, Mo and W, the films retained their amorphous nature even at the breakdown voltage, and the departure from the linear rise of potential at constant current must therefore be due only to evolution of oxygen.

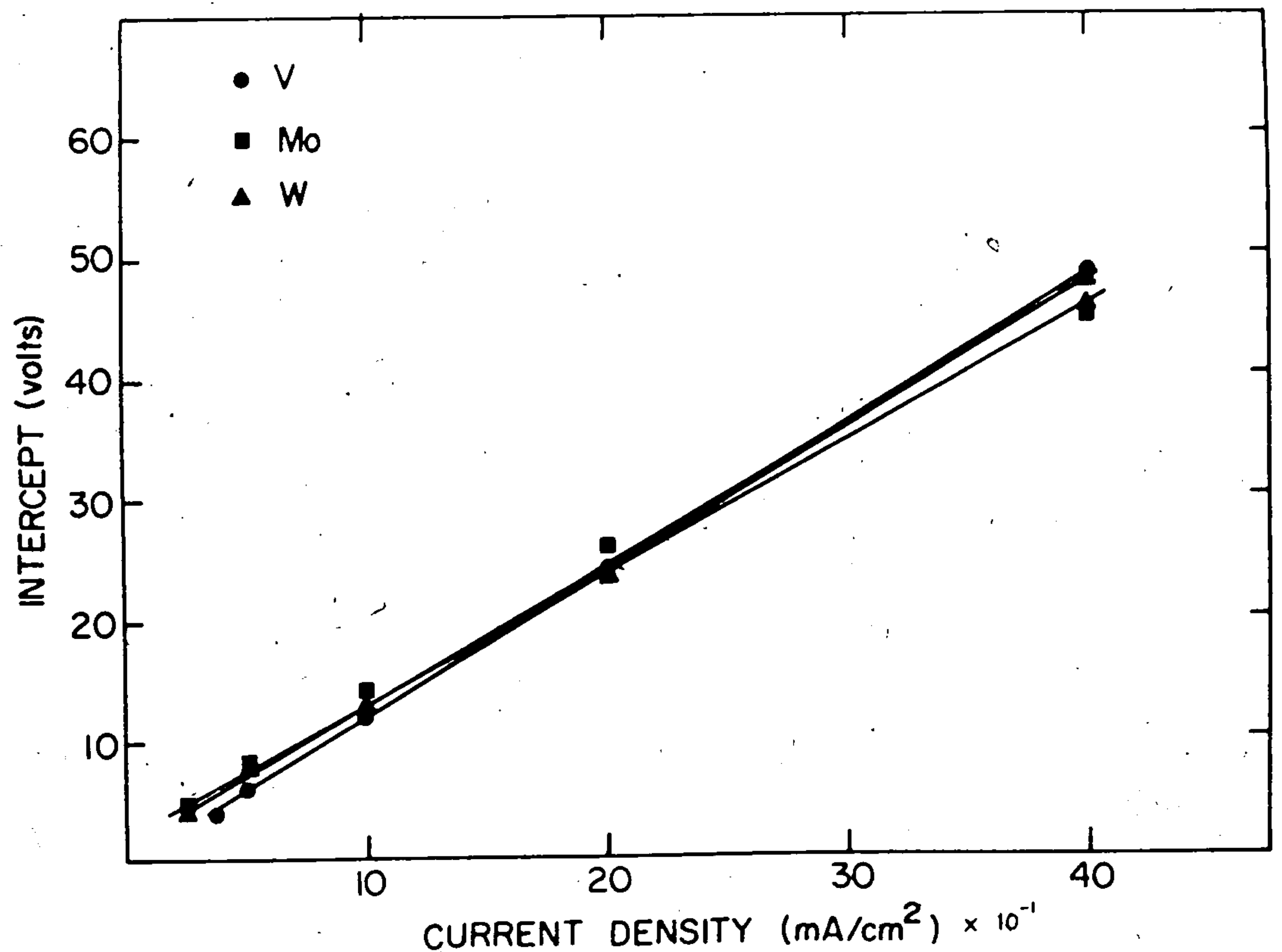

Fig. 3-5 Initial intercept as a function of current density

3.3.2 Anodizing Efficiency: The rate of potential rise at constant current may be written as

$$\frac{dV}{dt} = \frac{i_1 M E_d}{z F \rho} \qquad (3\text{-}1)$$

where i_1 = ionic current density, amp/cm^2

t = anodizing time, sec

V = potential, volts

z = number of Faradays (F) required to form the formula weight in grams of the film (M)

ρ = film density, g/cm^3

$E_d = \frac{dV}{dx} \approx \frac{\Delta V}{\Delta x}$ = differential field across the film, volts/cm.

The applied current density, I, may be considered to have three additive components, ionic (i_1), electronic (i_2) and that part of current leading to film dissolution (i_3). Therefore, the applied current can be expressed as

$$I = i_1 + i_2 + i_3 .$$

The term $\frac{ME_d}{zF\rho}$ in eqn. (3-1) is apparently independent of thickness and voltage since $\frac{dV}{dt}$ is found to be independent of time to the first approximation (figs. 3-2 to 3-4); it is also largely independent of current density in view of the linearity of $\frac{dV}{dt}$ with I (fig. 3-6). If we in addition assume that the low conductivity of the electrolyte, i.e. the non-uniformity of the films formed at constant current, is not a significant effect, then eqn. (3-1) may be rewritten as

$$\frac{dV}{dt} = ki_1 = k(I-i_2-i_3) \qquad (3\text{-}2)$$

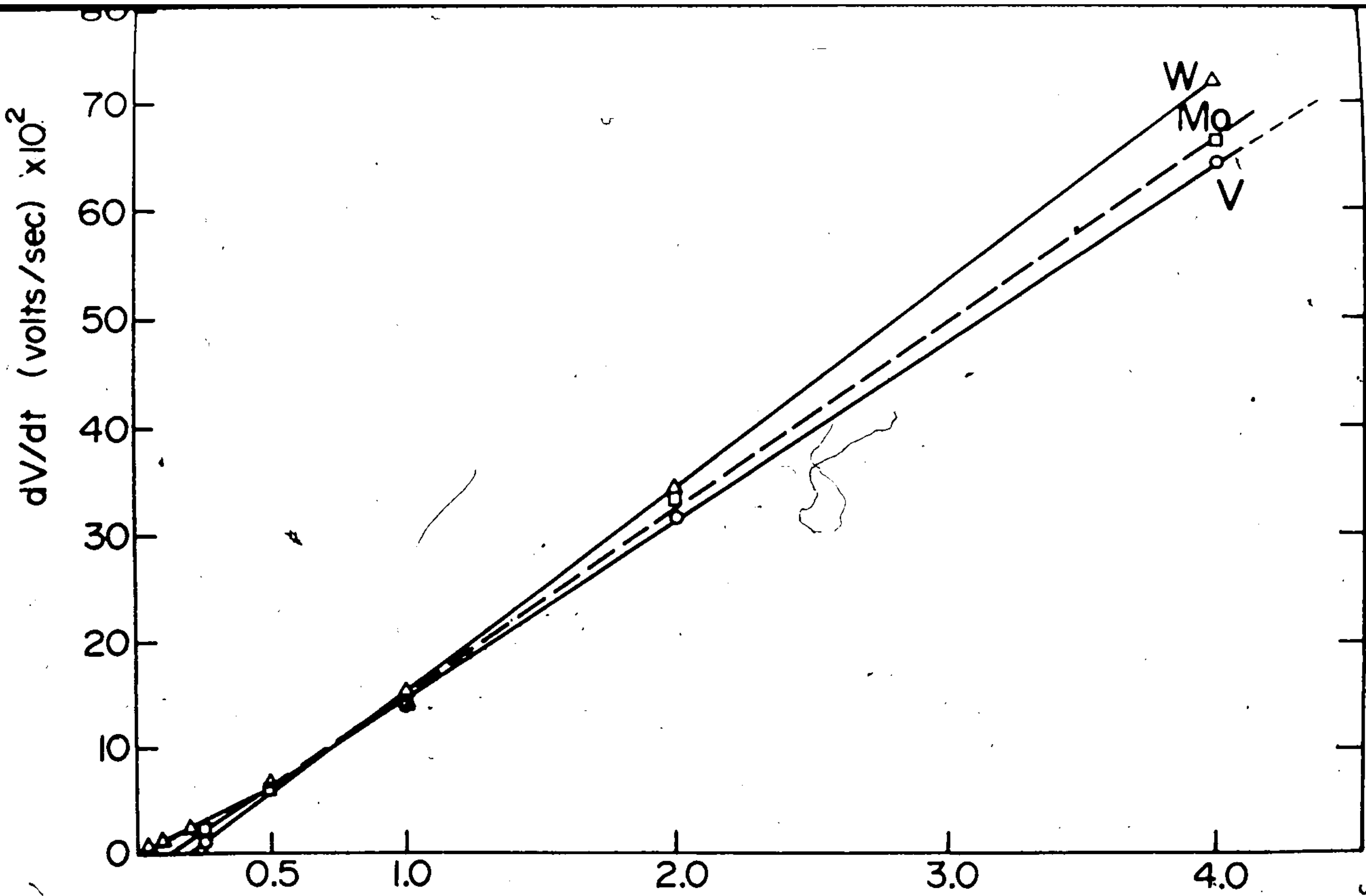

Fig. 3-6 Variation of $\frac{dV}{dt}$ with current

where $$k = \frac{ME_d}{zF\rho} .$$

Using the data of fig. 3-6, the results of Table 3-1 have been deduced.

Table 3-1

Values of k and (i_2+i_3) for V, Mo and W

	V	Mo	W
k, $\frac{\text{volts-cm}^2}{\text{amp-sec}}$	165	170	380
(i_2+i_3), $\frac{\text{mA}}{\text{cm}^2}$	0.106	0.102	0.095

From the values of (i_2+i_3) so deduced, the current efficiency at constant current, namely $\eta = \frac{i_1}{I}$, for film formation may be inferred, with results as in Table 3-2.

Table 3-2*

Film Formation Current Efficiency at Constant Currents

I, $\frac{\text{mA}}{\text{cm}^2}$	$\eta = \frac{i_1}{I}$		
	V	Mo	W
0.25	0.58	0.59	0.62
0.50	0.79	0.80	0.81
1.0	0.89	0.90	0.905
2.0	0.95	0.95	0.95
4.0	0.97	0.975	0.98

*The values of (i_2+i_3) were taken from Table 3-1.

Note that an anodized efficiency, η, deduced this way necessarily increases with current, as has also been observed for other metals (for references, see for example Young, 1961).

3.3.3 Film Formation Rate: Johansen et al. (1957) have related the film formation rate to an empirical expression of the form

$$\frac{dV}{dt} = a(I)^b \qquad (3\text{-}3)$$

where I is the applied current, and 'a' and 'b' are constants. Such an expression fits the kinetic data (in the linear V-t region) in case of V, Mo and W, as shown in fig. 3-7. It is found that the curves are almost identical for V and Mo, a result which is not surprising since both have shown a similar behaviour with regards to film stability, induction periods at low formation currents, etc. The values of 'a' and 'b' are calculated from eqn. (3-3) for V in volts, t in sec and I in amp/cm^2, and are given in Table 3-3 which also shows some selected values as obtained

Table 3-3

Values of 'a' and 'b'

	a	b	Reference
V	316	1.12	Here
Mo	316	1.12	Here
W	670	1.10	Here
W	39000	1.57	Ammar and Salim (1971)
Bi	245	1.20	Ammar and Khalil (1971)
Ti	1440	1.26	Ammar and Kamal (1971)

Fig. 3-7 Relation between $\log(\frac{dV}{dt})$ and $\log I$

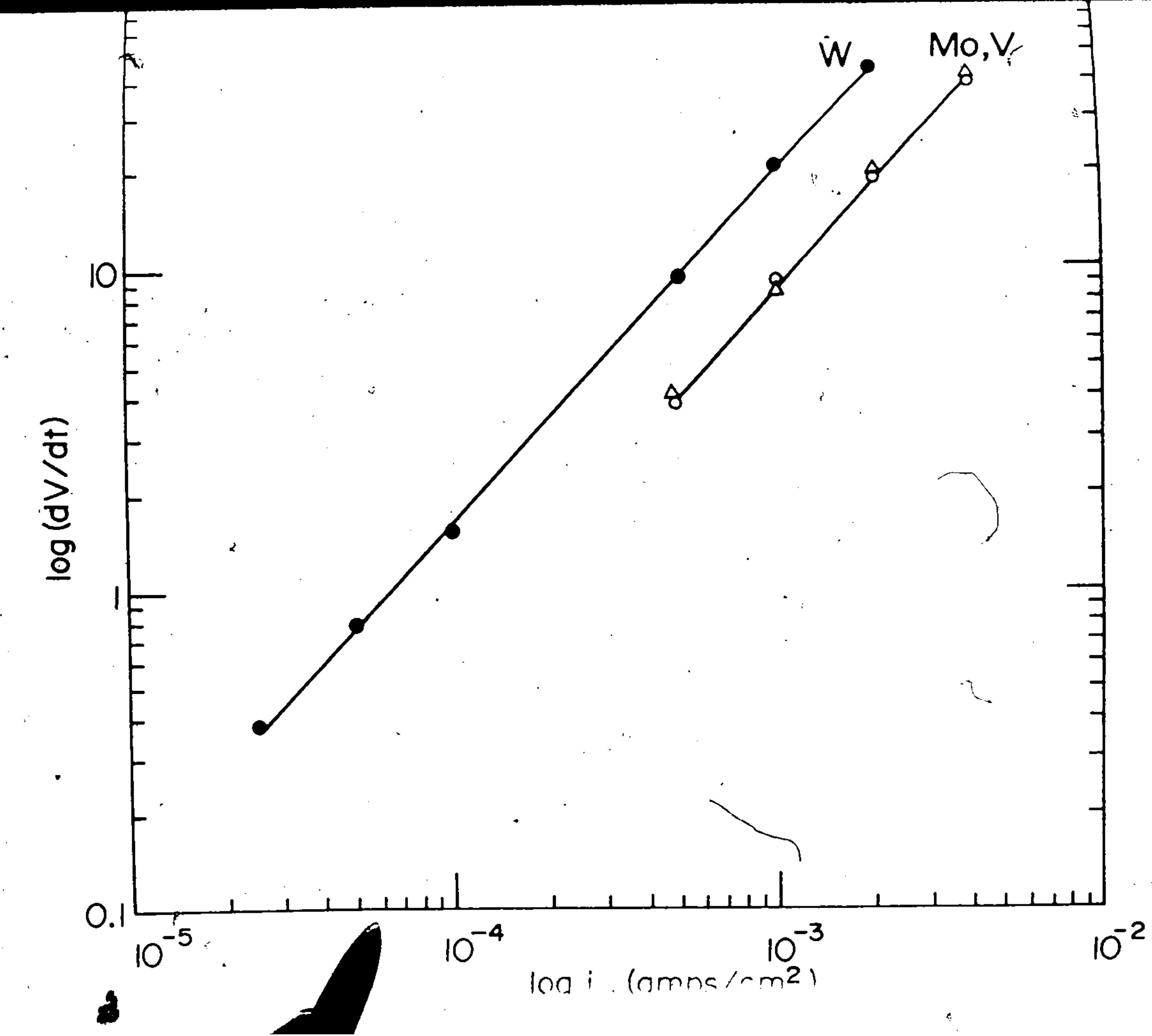
W
Mo, V
log(dV/dt)
10
1
0.1
10^{-5}
10^{-4}
10^{-3}
10^{-2}
log i (amps/cm^2)

by other workers. A value of $b \approx 1$ is expected for anodizing at unit efficiency and the anodic behaviour of V, Mo and W may thus be concluded to be close to having such efficiency. Eqn. (3-3) is highly empirical, however, and we suggest that its use has little other justification.

3.3.4 E_d Determinations: The differential field across the anodic film, E_d, may be obtained by combining eqns. (3-1) and (3-2) provided one can make suitable assumptions about the values of M, z, and ρ. The results so obtained are given in Table 3-4.

Table 3-4

Estimation of E_d values for V, Mo and W

Metal	z	M	ρ, g/cm^3	$\frac{M}{zF\rho}$, $\times 10^5$	E_d, $\times 10^{-6}$ volts/cm
V	5	91	<3.36	>5.61	<2.94
Mo	6	144	<4.69	>5.30	<3.20
W	6	232	<7.16	>5.58	<6.80

3.4 Anodizing Characteristics When Both Current and Voltage are Fixed

3.4.1 General: Anodizing at constant current alone, without letting the current drop when a given voltage is reached is not necessarily acceptable when a uniform anodic film is desired, especially when the electrolyte has low conductivity. The reason is basically trivial, namely that at constant current the field near the edges of specimens is initially higher than

in the central part, leading to thicker films at the edges; uniform films are, however, obtained when the current is allowed to drop. To determine the optimum conditions for producing uniform anodic films, the effect of current density was investigated under conditions when both current and voltage were preset.

3.4.2 Effect of Current Density: In these experiments, the nature of the "anodizing end-point" was explored. The term "anodizing end-point" here refers to a sharp discontinuity in current when anodizing is performed with both the current and voltage preset. Thus, the voltage rises as the film grows and when the preset voltage is reached, the current abruptly begins to drop. Fig. 3-8 shows results for V in which the voltage was preset at 50 volts and the current was initially preset at various values. Simultaneously, times (marked with arrows) were noted in each case when the film became uniform in terms of its interference colours. It is seen that initial currents of 2.0 and 4.0 mA/cm^2 give excellent anodizing end-points though the lower current necessarily gives less heating. The value of 2.0 mA/cm^2 together with a total anodizing time of six minutes was accordingly chosen for subsequent work whenever uniform anodic films were desired. These conditions also gave satisfactory results with Mo and W and hence were adopted as the standard anodizing conditions for all three metals.

Fig. 3-8 Effect of initial current density over the 'anodizing end-point' for V

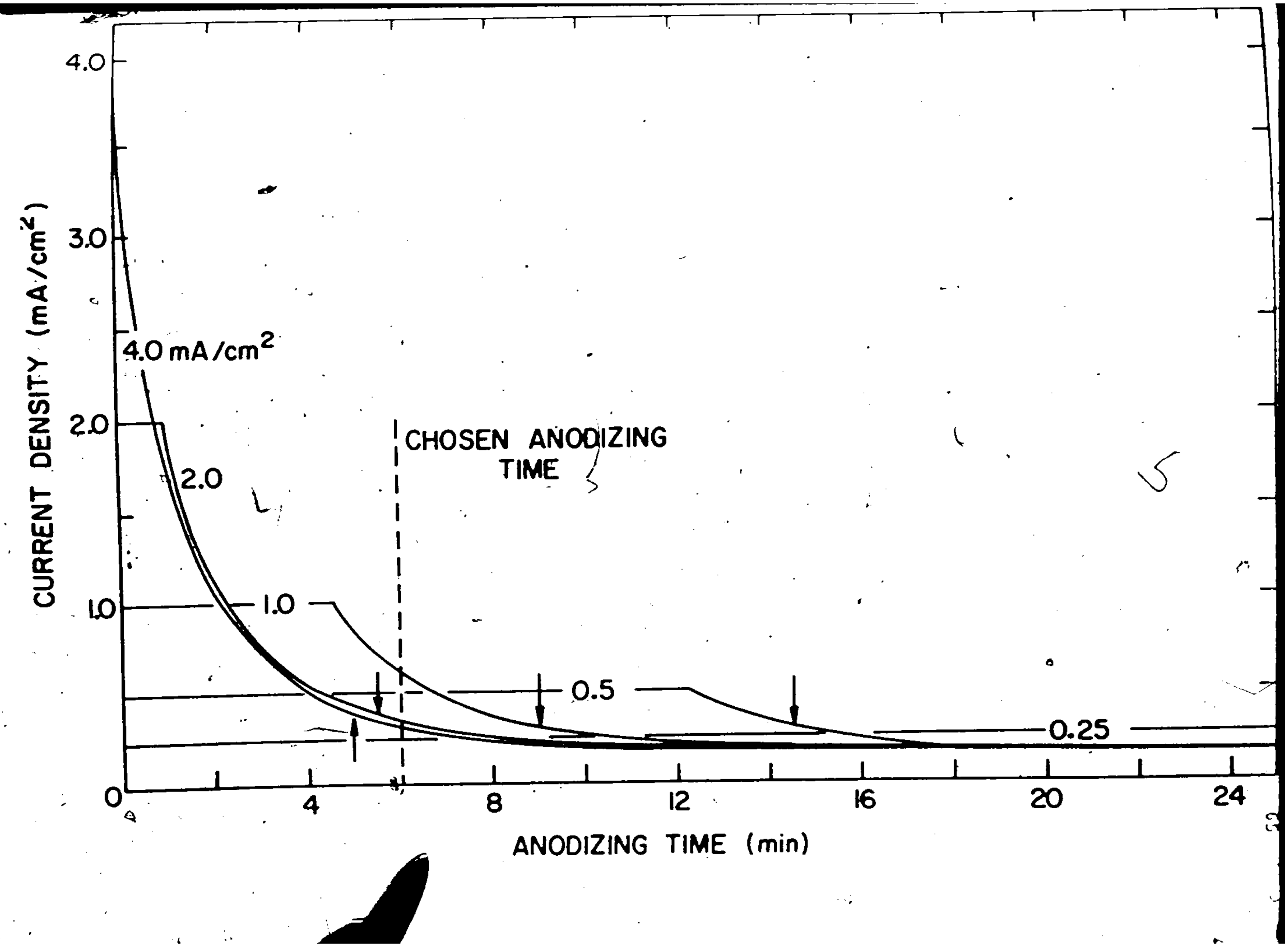
CURRENT DENSITY (mA/cm²)
4.0
3.0
2.0
1.0
0
4.0 mA/cm²
2.0
1.0
0.5
0.25
CHOSEN ANODIZING TIME
4
8
12
16
20
24
ANODIZING TIME (min)

3.4.3 Anodizing Efficiency When Both Current and Voltage are Preset:

Using the standard anodizing conditions as described above and a preset voltage of 50 volts, I-t plots were obtained as shown in fig. 3-9. These plots, when combined with the thicknesses of metal removed and film formed, as determined by the gravimetric method (to be discussed in the next chapter), enable estimates of the overall anodizing efficiency to be made. These results are given in Table 3-5 for various

Table 3-5

Determination of Anodic Efficiency from Faraday Calculations

Metal	Assumed Stoichiometry	Weight Changes, μg/cm² Faraday Calculations Film	Metal	Experimental Film	Metal	η Film	η Metal
V	V_2O_4	84.0	51.6	59.7	37.2	0.71±0.05	0.72±0.05
	V_2O_5	73.5	41.2	59.7	37.2	0.81±0.05	0.90±0.05
Mo	MoO_2	110.4	82.5	80.4	58.4	0.72±0.03	0.71±0.03
	MoO_3	82.5	55.0	80.4	58.4	0.975±0.03	1.06±0.03
W	WO_2	110.5	94.4	79.2	60.9	0.72±0.04	0.645±0.04
	WO_3	79.3	62.9	79.2	60.9	1.00±0.04	0.97±0.04

assumptions about the film stoichiometry. (It should be pointed out here that the constant-current anodizing efficiencies as given in Table 3-2 (section 3.3.2) were independent of the stoichiometry). The anodizing efficiencies will be noted to be consistently high. As far as comparison with constant-current conditions is concerned (where $\eta = 0.95$ for $I=2.0$ mA/cm²), there is a good agreement

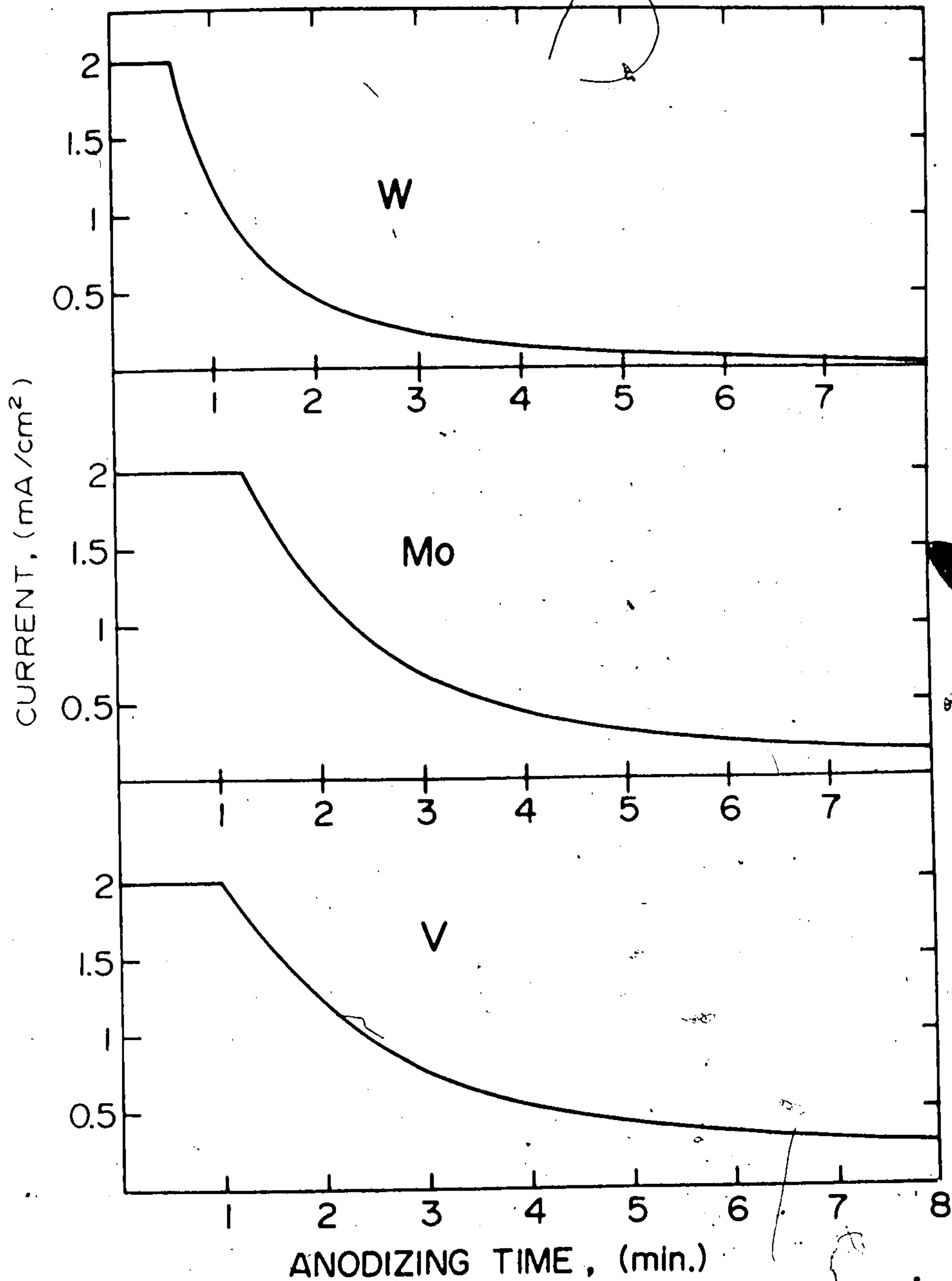

Fig. 3-9 Typical current-time plots at 50 volts with initial current of 2.0 mA/cm^2

provided the stoichiometries can be taken as V_2O_5, MoO_3 and WO_3. But if the stoichiometries are for example VO_2 (as deduced by Keil, 1968), MoO_2 and WO_2, then the new efficiencies are consistently low. It will be shown in subsequent chapters that the preferred stoichiometries are indeed V_2O_5, MoO_3 and WO_3, and thus there is no basic inconsistency in the efficiency results.

Since a non-zero value of leakage current (i_2+i_3), leading to an anodizing efficiency of less than unity, can arise both from electronic current and from dissolution, the matter of dissolution was investigated explicitly. This was done by anodizing V and Mo at 50 volts using an initial current of 2.0 mA/cm^2 with the total anodizing time varying between 6 and 60 minutes. The film thicknesses thus formed and the amounts of metal involved in each case were then determined gravimetrically (using the anodic sectioning procedures described in the next chapter). The results thus obtained are given in fig. 3-10 and may be expressed as follows:

Dissolution rate of V = $(0.3+0.696\ t_{min})$ $\mu g/cm^2$ of metal

Dissolution rate of Mo = $(-4.7+0.527\ t_{min})$ $\mu g/cm^2$ of metal.

It would seem from above results that the anodic films formed on V are more susceptible to dissolution during formation than those formed on Mo.

3.5 Anodization of Nb and Ta

3.5.1 General: In the previous sections of this chapter, the anodic behaviour of V, Mo and W has been described. It was found that V and Mo presented many problems. For example, it

Fig. 3-10 Relation between metal dissolution and anodizing time for V and Mo

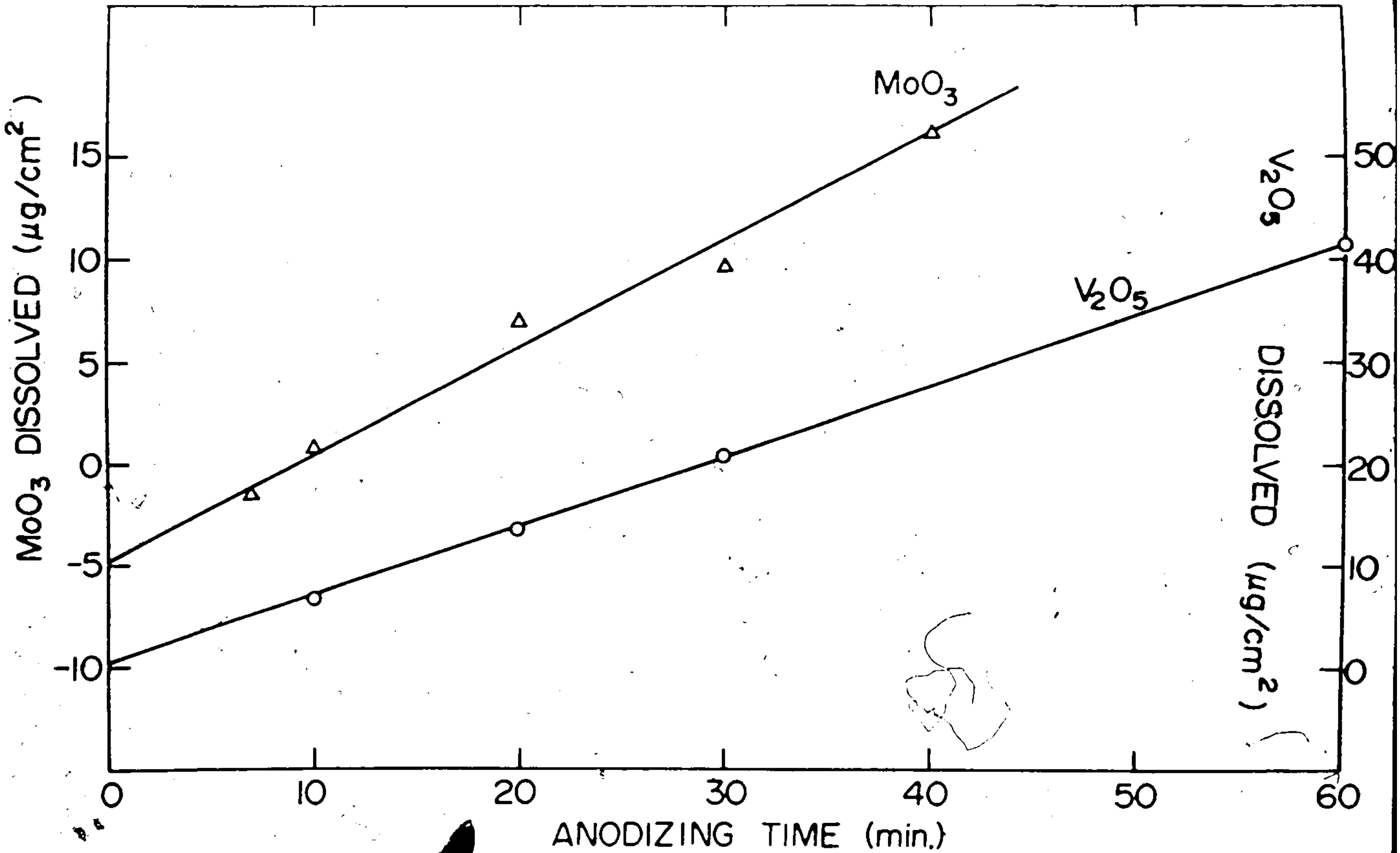
MoO3
V2O5
V2O5 DISSOLVED (μg/cm2)
MoO3 DISSOLVED (μg/cm2)
ANODIZING TIME (min.)
15
10
5
0
-5
-10
50
40
30
20
10
0
0
10
20
30
40
50
60

was not possible to form films on them in aqueous solutions; moreover, of the various non-aqueous solutions tried, only the one based on acetic acid supported film growth, and even then the freshly formed films were rather unstable and had to be stabilized by drying them immediately. Such difficulties do not arise with Nb and Ta. Indeed, it may be said that these two metals, espcially Ta, come closest to ideal behaviour, with anodization possible in almost any conducting liquid (except obviously in HF solutions due to the problem of film solubility). The major problem with these two metals, in a study on anodic sectioning, is that connected with removing the films, for these films are normally so stable that their rate of dissolution is similar to that of the underlying metal. The basic problem thus involves finding the combination of electrolyte and dissolving reagent which will yield good sectioning behaviour.

This problem will be attacked on two fronts: while keeping the dissolving reagent fixed (HF has been the favourite reagent in most previous work), the electrolyte will be changed and the behaviour studied. Alternatively, the electrolyte will be fixed and the dissolving reagent varied. The results on sectioning are given in the next chapter and we will describe here only the experiments related to film formation.

3.5.2 Role of Doping in Anodizing: The work of Vermilyea (1954), Draper (1963), Randall et al. (1965), Smyth et al. (1966) and Amsel et al. (1969) indicated an important role for non-aqueous

electrolytes. They found that the use of H_2SO_4, H_3PO_4, or a glycol-borate electrolyte leads to duplex anodic films on Nb and Ta such that the part next to metal is pure metal oxide (undoped) while the outer film contains significant amounts of anions from the electrolyte (doped). As described earlier (section 2.5.3), the doped part of the film formed in H_2SO_4 has enhanced solubility, and increasing the concentration of H_2SO_4 leads to a greater proportion of doped film such that when concentrated H_2SO_4 ($\geq$ 80%) is used, the film is entirely doped (Vermilyea, 1954). However, doped films do not necessarily have enhanced solubility since films formed in H_3PO_4 are also doped but show retarded solubility. Therefore, an electrolyte based on H_2SO_4 was chosen for subsequent work. It will be shown in the next chapter that the use of concentrated H_2SO_4 does not yield satisfactory results as regards the reproducibility and the maximum achievable thickness, and thus mixtures of diethyl sulphate and H_2SO_4 were tried (diethyl sulphate is an obvious diluent for H_2SO_4 in that it is miscible with and not attacked by H_2SO_4 except in so far as $C_2H_5 \cdot HSO_4$ is formed). A 3:1 mixture of diethyl sulphate and H_2SO_4 was found to give good results as regards the enhanced solubility of the doped film (increasing the amount of diethyl sulphate tended to retard the film solubility) and the reproducibility of film thicknesses.

3.5.3 Loss During Anodizing: It was shown in section 3.4.3 that both V and Mo dissolved significantly during anodizing.

Similar experiments were performed with W, Nb and Ta but no loss could be detected gravimetrically. A more sensitive and precise method was therefore developed for determining loss during anodizing. In this method, specimens of Nb, Ta and W were labelled with 10-keV Kr^{85} ions to a dose of 4×10^{15} ions/cm^2, the activity loss after anodizing at 10 or 25 volts was noted, and the activity loss was then interpreted as a measure of depth. To this end, the depth distribution was taken as having exponential shapes (see for example the experimental distributions of chapter 7 as well as those of Davies et al.,1963),

$$\text{integral concentration} = \exp(-\frac{x\ell n2}{R_m}) \ ,$$

where R_m is the median range. Overall results are given in Table 3-6 and show essentially zero anodizing loss.

Table 3-6

Loss During Anodizing for Nb, Ta and W

Metal	R_m^*, Å	Residual Activity	Anodizing Loss, Å
Nb	61	0.984±0.006	$\lesssim$1
Ta	54	0.994±0.008	$\lesssim$1
W	68	0.992±0.010	$\lesssim$1

* R_m values are based on the experimental range profiles as described in Chapter 7.

3.5.4 Properties of Anodic Films: When there is virtually no loss during anodizing, the doped nature of the anodic film may be verified by weighing the specimens before and after anodizing and then by removing the films using the sectioning procedures (as described in Chapter 4). This procedure leads to the ratios (observed film weight)/(expected film weight for pure oxide) and (observed anion weight)/(expected anion weight for pure oxide), with results as summarized in Table 3-7. Similar results could not be obtained for V and Mo in view of their

Table 3-7

Film and Anion Weight Ratios for Nb, Ta, and W.

Metal	Anodizing voltage, volts	observed film weight / expected film weight	observed anion weight / expected anion weight
Nb	30	1.01	1.04
	50	1.04	1.13
Ta	30	1.10	1.60
	100	1.12	1.60
W	30	1.02	1.10
	140	1.02	1.11

tendency to dissolve during anodizing. It is seen that the anodic films formed on Ta are rather heavily doped whereas those formed on Nb and W are undoped to within the precision of gravimetric measurements. The difference between doping of Ta and Nb agrees well with the results of Draper (1963) obtained in experiments with radiotracers.

Still unsettled at this point is the question as to whether the films formed on Nb and W are significantly doped. We would suggest that a sensitive though somewhat indirect criterion of doping is the value of $\frac{dV}{dt}$ for film growth at a given current density. The argument follows from the relation governing the film-forming current,

$$i = i_o \exp\{- \frac{[W-f(qa \frac{VK}{x})]}{kT}\},$$

where a more general dependence on field is assumed (Dignam, 1964) than has been used in Chapter 2. Here, 'W' is the zero-field energy barrier, 'q' is the charge of the migrating ion, 'a' is the half-jump distance and K is a factor similar to either unity as in all the work discussed in chapter 2 or else to $\frac{(\varepsilon+2)}{3}$ as when a Lorentz field (related to local field) and not a Maxwell field (related to average field) is assumed within the oxide (Dignam, 1965). If a given film-forming current is compared for two electrolytes and if 'i_o' is assumed to be roughly constant, then it follows that one can write

$$[W-f(qa \frac{VK}{x})]_1 = [W-f(qa \frac{VK}{x})]_2 \ . \qquad (3-4)$$

Doping caused by the electrolyte could affect any of the structure-dependent parameters (W,q,a,K) though we would propose the effect on K to be the most important one. Eqn. 3-4 then yields the following approximate relation

$$(\frac{VK}{x})_1 \approx (\frac{VK}{x})_2 \qquad (3-5)$$

and one concludes that if an electrolyte affects K (as by

doping) then it will also affect $\frac{V}{x}$ (thence $\frac{dV}{dt}$). An independent justification of eqn. (3-5) follows from the results of Draper (1963) and of Amsel et al. (1969), where the product CV (proportional to $\frac{V\varepsilon}{x}$) was found to be largely independent of the concentration of H_2SO_4 at a given film-forming current. Therefore, to bring out the differences in the nature of the anodic films formed in aqueous (0.2% KF for Nb and Ta, and 0.4 M KNO_3 plus 0.04M HNO_3 for W) and non-aqueous (H_2SO_4-based for Nb and Ta, and acetic-acid based for W) electrolytes, anodizations were carried out at constant currents and the $\frac{dV}{dt}$ values compared, with the results given in Fig. 3-11 and Table 3-8. If we make

Table 3-8

Comparison of $\frac{dV}{dt}$ Values for Aqueous and Non-aqueous Electrolytes

Metal	Current mA/cm^2	$\frac{dV}{dt}$, $\frac{\text{volts}}{\text{sec}}$ non-aqueous	aqueous
Nb	5.0	3.2±0.2	1.24±0.04
Ta	5.0	6.2±0.2	2.1 ±0.1
W	2.0	0.73±0.02	0.70 ±0.01

the assumption that aqueous electrolytes give undoped films, it follows that the films formed with non-aqueous electrolytes on Nb and Ta (but not W) are doped to an important extent. The large difference in $\frac{dV}{dt}$ values for aqueous and non-aqueous electrolytes has, with Ta, also been noted by Draper (1963) and by Amsel et al. (1969). It is anticipated at this stage that an indirect effect of sulphate doping will be to cause

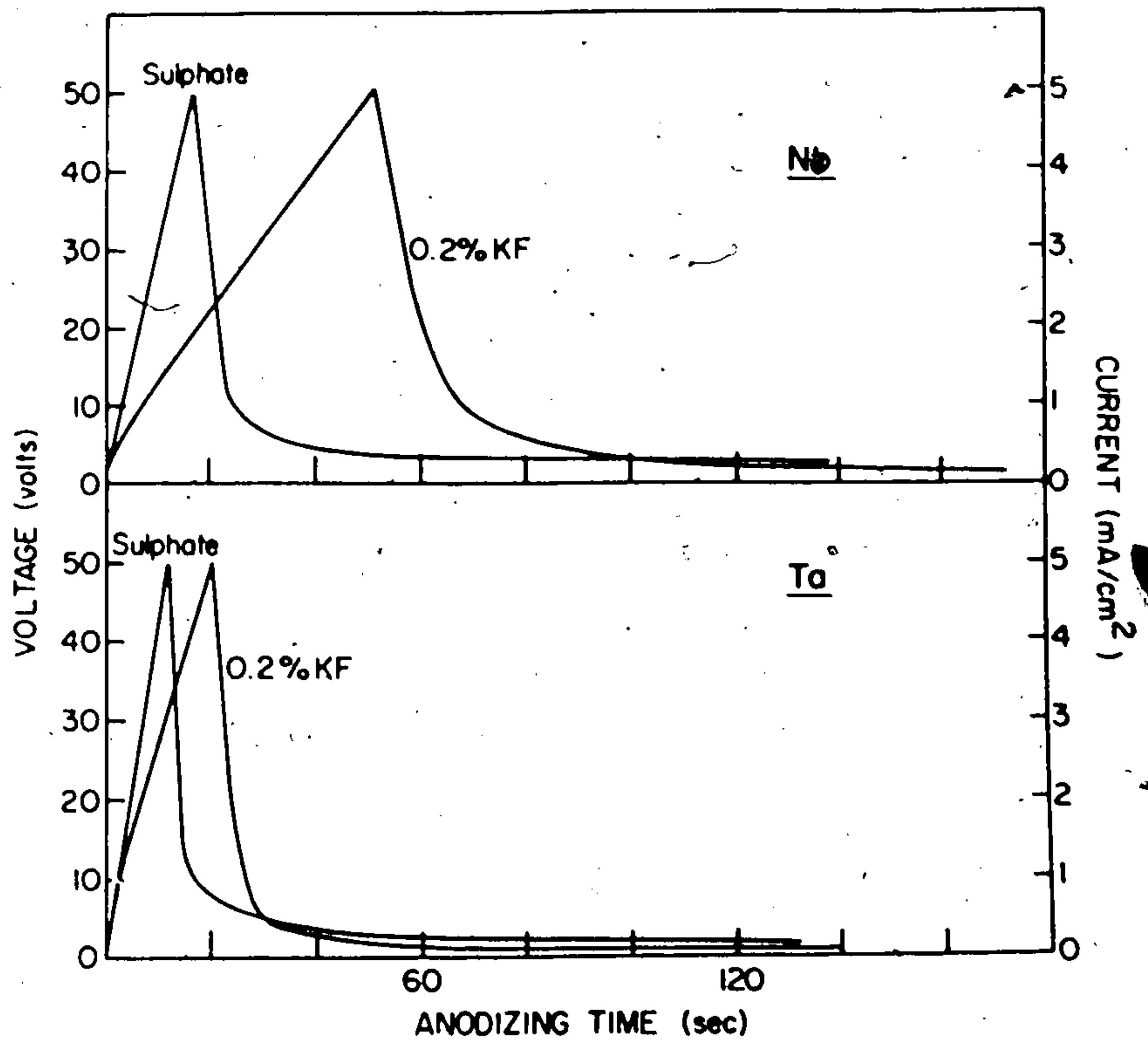

Fig. 3-11 Typical voltage-time and current-time curves for aqueous and non-aqueous electrolytes in the anodization of Nb and Ta

thinner films for the same anodization voltage. Thus, if the preset voltage is attained more rapidly due to higher values of $\frac{dV}{dt}$, a smaller amount of charge will then be passed, giving rise to thinner films. Such an effect will indeed be confirmed in the next chapter.

3.5.5 Anodizing Efficiency: Anticipating the results of gravimetric measurements from the next chapter, further information can be obtained from the voltage-time and current-time data of fig.3-11 for 50 volts. The ratio $\eta \cdot \frac{n_o}{n}$, where η is the anodizing efficiency, n_o is the expected equivalents per gram-atom (e.g. 5 with Nb and Ta) and n is the actual equivalents per gram-atom (undeterminable at this stage), follows by comparing the Coulombic values of the amount of metal removed with the gravimetric values. The results are given in Table 3-9. The efficiency of near unity for Nb

Table 3-9

Anodizing Efficiencies Determined from Coulombic and Gravimetric Data

Metal	Total Charge, C/cm^2		Weight change, μg/cm^2				$\eta \cdot \frac{n_o}{n}$	
			Calculated		Observed			
	aqueous	non-aq.	aq.	non-aq.	aq.	non-aq	aq.	non-aq.
Nb	0.253	0.142	48.8	27.4	50.3	21.4	1.03±0.02	0.78±0.03
Ta	0.143	0.108	55.1	40.8	54.1	26.9	1.01±0.03	0.66±0.01

and Ta in the aqueous electrolyte agrees with previous work of Vermilyea (1953) and Dreiner (1964) though the efficiency obtained for the sulphate-containing electrolyte disagrees with that estimated by Amsel et al. (1969). Note, however, that the latter authors inferred the relevant efficiency from a visual

search for oxygen bubbles, which is obviously not quantitative. Thus, they saw no bubbles and therefore proposed an efficiency near unity.

3.6 Summary

The anodization behaviour of V, Mo, W, Nb and Ta has been described in this chapter. It was shown that the formation of anodic films on V and Mo presented serious problems: firstly, it was not possible to form them in aqueous electrolytes, and secondly, of all the non-aqueous electrolytes tried, only an acetic-acid based electrolyte permitted the formation of films, and thirdly, even such films when freshly formed were rather unstable and could be stabilized only by drying with a filter paper or using a jet of compressed air. Moreover, at very low currents ($\leq$ 0.5 mA/cm^2), induction periods were observed in galvanostatic anodization, this effect increasing with stirring and decreasing with current density. Attempts were made to determine optimum anodizing conditions and it was found that an initial current of 2.0 mA/cm^2 with a total anodizing time of six minutes gave uniform films when the electrolyte was not stirred. Such problems were not observed with W but the same anodizing conditions were adopted for anodizing W.

In case of Nb and Ta, anodic films can be formed in almost any electrolyte but there is great difficulty in the satisfactory removal of these films. Keeping in mind the enhanced film solubility and reproducibility of film thicknesses as will be demonstrated in Chapter 4, a 3:1 mixture

of diethyl sulphate and H_2SO_4 was used for anodizing, with all the work being done using 5 mA/cm^2 as the initial current. A cylindrical Pt cathode, 2.5 cm inside diameter, was used for all five metals.

These anodizing conditions were employed in all experiments on film formation, to be described in the following chapters.

CHAPTER 4

ANODIC SECTIONING

PART III: FILM REMOVAL AND THICKNESS CALIBRATIONS

4.1 General

As has been mentioned earlier, anodic-sectioning consists of two steps:

(i) formation of an anodic film on a metal, and

(ii) its removal without significantly attacking the substrate.

The formation of anodic films on V, Mo, W, Nb and Ta has been described in the previous chapter; in the present chapter, their removal will be considered. The success of an anodic sectioning method, however, depends not only on the above mentioned two steps, but also on the precise knowledge of the metal-removal thickness; and, of course, the usefulness is extended if both metal-removal and film-formed thicknesses are available. Several methods of determining thicknesses have been developed, the more important of these being as follows:

(a) Using Faraday's Law: The total charge involved in the anodization step determines the number of moles of metal involved. One then converts this charge into metal-removal and film-formed thicknesses using Faraday's law together with appropriate assumptions regarding the anodizing efficiency, the film stoichiometry, and film density. The difficulties inherent in this approach are obvious in the case of efficiency and density,

but even the relatively simple matter of stoichiometry presents problems. One must ask whether the film is really the expected oxide (e.g. V_2O_5) or whether it is oxygen deficient (e.g. VO_2 or V_6O_{13}) and therefore has the cation in lower valence state. For example, Keil and Salomon (1968) proposed that the anodic film on V was mainly VO_2.

(b) Gravimetric Method: The weight increase of an anodized specimen as determined using a microbalance is due to the oxygen pick up, plus any adsorbed species or excess anions. This increase yields the film thickness provided one makes assumptions regarding the film density (if thickness is required in length units and not in mass units of $\mu g/cm^2$, where $\mu g/cm^2 = \frac{\mathring{A} \times \rho}{100}$ with ρ being density in g/cm^3) though is free from the problem of anodizing efficiency. Again, the film stoichiometry can be a problem while the possibility of doping takes on major importance. Indeed, presence of doping can lead to quite misleading results such as the conclusions of Vermilyea (1954), based on the weight increase and on the assumption of the film being Ta_2O_5, that the anodizing efficiency of Ta was 210%. Later experiments by Amsel et al. (1969) and others (referred to in section 2.4.3) have shown that the films were sufficiently doped to cause anomalous weight increases. This method is also unsatisfactory when the film dissolves during formation.

Similarly, the weight decrease of a specimen which is weighed, anodized, weighed, anodically sectioned and then weighed again gives directly the film-formed and the metal-removal thicknesses. There are no obvious difficulties here as

the results are independent of the properties of the film as well as of film dissolution.

(c) A.C. Capacity: For a pore-free, uniform and insulating anodic film, the A.C. capacity is given by, in e.s. units,

$$C = \frac{\varepsilon A}{4\pi x} \tag{4-1}$$

where ε is the dielectric constant, C is the capacity, and x is the thickness. With C in farads, A in cm^2, and x in angstroms, eqn. (4-1) can be written as

$$C = \frac{A\varepsilon}{x} \times 8.85 \times 10^{-6}. \tag{4-2}$$

The assumptions involved also include the fact that the film should have a uniform composition (and not, for example, be duplex in nature) and a known value of ε. For example, tabulations of ε are seldom useful, as they nearly always apply to crystalline materials rather than to amorphous ones. Moreover, the value of ε will also in principle depend strongly on doping and stoichiometry.

(d) Ellipsometry: This method requires the knowledge of optical constants of both the film and the metal. It also involves assumptions regarding the uniform film composition and the effect of interfaces on the optical constants (this effect is greatest for thin films though it is invariably ignored). The stoichiometry of the film as well as the presence of dopants could in principle be quite important as even a small oxygen deficiency or impurity content could seriously affect optical constants.

(e) Spectrophotometry: This is considered to be the most accurate method of determining film thicknesses (Young, 1961). Here, a spectrophotometer is used, together with a specular reflectance attachment to locate the wavelength of minimum reflectivity at a fixed angle of incidence. Again a knowledge of optical constants (in this case the refractive index) is necessary and stoichiometry or doping therefore present serious problems.

(f) Measurement of Step Heights: In this method, which has been applied to the thickness measurements of films on Si, multiple beam interference is used. By anodically oxidizing and etching, with use of suitable masks, one can determine the thicknesses of the reacted silicon and of the anodic film separately (Schmidt and Owen, 1964). The one paramount disadvantage here is the lack of sensitivity.

In methods (c), (d), (e) and (f), if metal-removal thicknesses are required, then the presence or absence of dissolution during anodizing becomes important.

(g) Radiotracer Method: This method gives the metal removal thickness directly. Here, the specimens are labeled with radioactivity either by an implantation or by neutron activation in a reactor, and are then anodically sectioned. With a suitable calibration, the amount of activity removed in each sectioning leads directly to the total metal removal. Moreover, it also leads to explicit estimates of metal dissolution during anodizing.

The main assumptions involved in all the above methods with regard to the metal-removal thicknesses (as distinct from film thicknesses) are summarized in Table 4-1. It is seen that a gravimetric method (sectioning) is as good as any other, especially for determining the anodizing efficiency and for estimating the extent of dissolution during film formation. It has therefore been used in the work that follows as the primary method of thickness determination (section 4.3). However, new problems enter in this method in that the substrate may be attacked during film removal. This leads to the concept of "dissolution end-point" which will be discussed next.

4.2 Dissolution End-Points

4.2.1 General: When a metal, with an anodic film on it, is placed in a reagent for dissolving the film, the reagent first attacks the film and then continues its attack on the substrate. At the film/metal interface, however, the dissolution kinetics generally change such that the film has either an enhanced or retarded solubility with respect to metal. For a satisfactory dissolution end-point, the rate of film dissolution must be much greater than that of the metal, as shown in fig. 4-1.

4.2.2 Determination of Dissolution End-Points: Specimens of V, Mo and W, after the appropriate surface preparation (section 3.2.2) were labeled with radioactive Kr^{85} and the activity was counted using a G-M counter. The specimens were then anodized, counted for activity and then alternately exposed to various dissolving reagents and counted. This procedure leads

Table 4-1

Assumptions Involved in Determining Metal-Removal Thicknesses

	Method	Anodizing Efficiency	Film Composition	Film Density	Dissolution	Optical Constants	Film Uniformity
(a)	Faraday's Law	Yes	Yes	-	-	-	-
(b)	Gravimetric	-	-	-	-	-	-
(c)	A.C.Capacity	-	Yes	-	Yes	Yes	Yes
(d)	Ellipsometry	-	Yes	-	Yes	Yes	Yes
(e)	Spectro-photometry	-	Yes	-	Yes	Yes	Yes
(f)	Step-Height	-	Yes	Yes	Yes	-	-
(g)	Radio-tracer	-	-	-	-	-	-

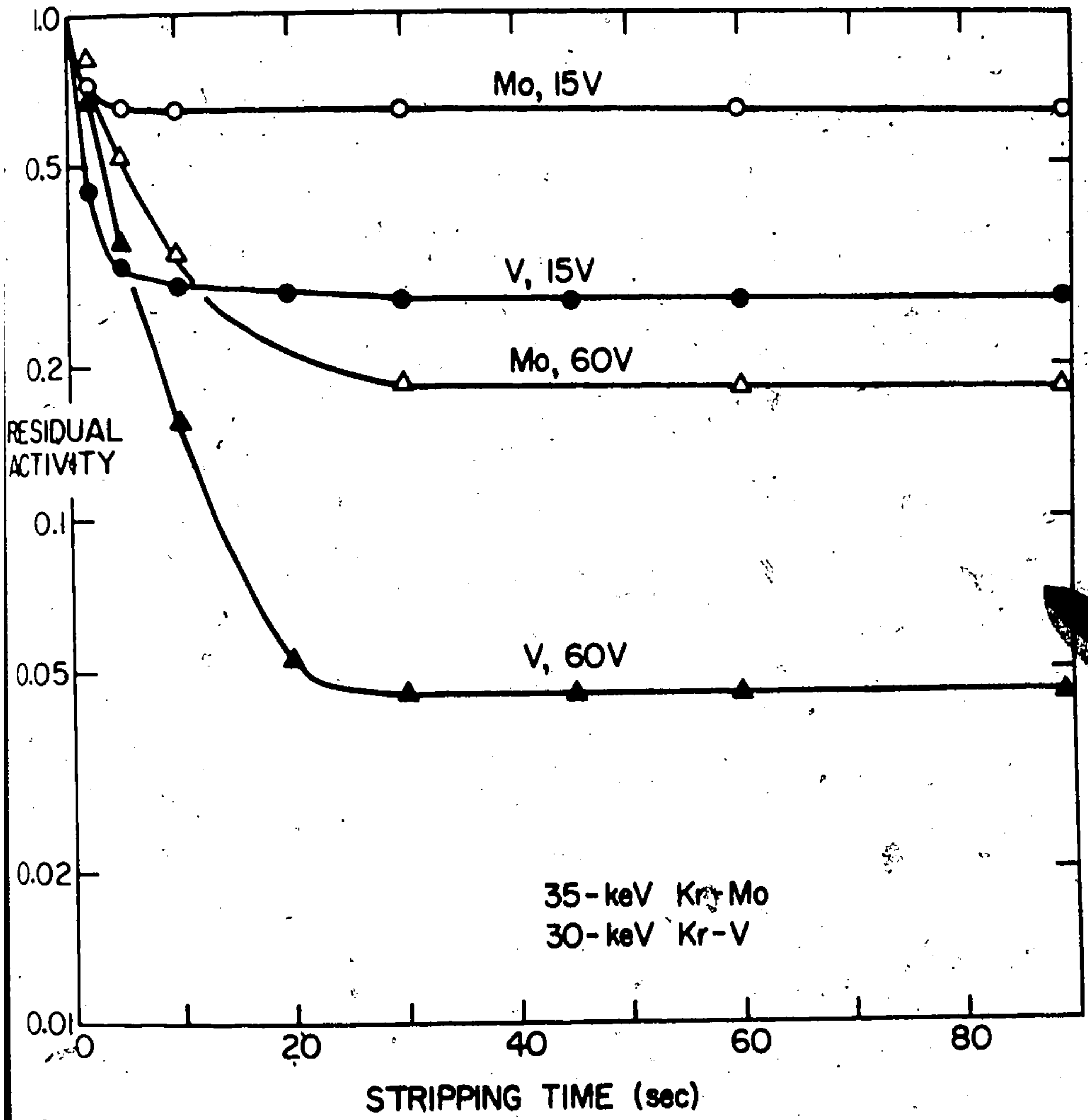

Fig. 4-1 Dissolution of 15 volt and 60 volt films of V and Mo in 0.1% KOH as inferred by loss of radioactivity.

to plots similar to that shown in fig. 4-1. The results for V, Mo and W are given in figs. 4-2 to 4-4, and show that a choice of the acetic-acid-based electrolyte and dilute KoH as dissolving reagent leads to a satisfactory dissolution end-point such that the anodic films are dissolved at a rate of ∿ 2000 Å/min whereas the attack on the metals is less than about 1 Å/min (such estimates involve the knowledge of the range profiles and anticipate the results of Chapter 7).

The behaviour of Nb and Ta was, on the other hand, not as simple. Films formed in aqueous electrolytes were extremely stable and dissolved in most solvents only at rates comparable with the metal dissolution rates, as shown for Nb in fig. 4-5. Somewhat better behaviour was found by Lam (1971) when he anodized Nb in a 4:1 mixture of H_2SO_4 and HNO_3, as shown in fig. 4-6 and 4-7. Pawel (1964) described a method in which anodic films on Nb and Ta, when formed in an aqueous solution of 0.2% KF, may be mechanically "peeled off". Such behaviour is apparently due to the presence of fluoride ions between the metal and the film and has the limitation that the films must be thicker than those formed at about 10 volts. Pringle (1972) has recently described the sectioning of anodic Ta_2O_5 such that, using HF saturated with NH_4F, the anodic film can be slowly and uniformly removed. He, however, did not describe the effect of this dissolving reagent on Ta itself.

In our own experiments, we used the above mentioned electrolytes, i.e. 0.2% KF and the 4:1 mixture of H_2SO_4 and

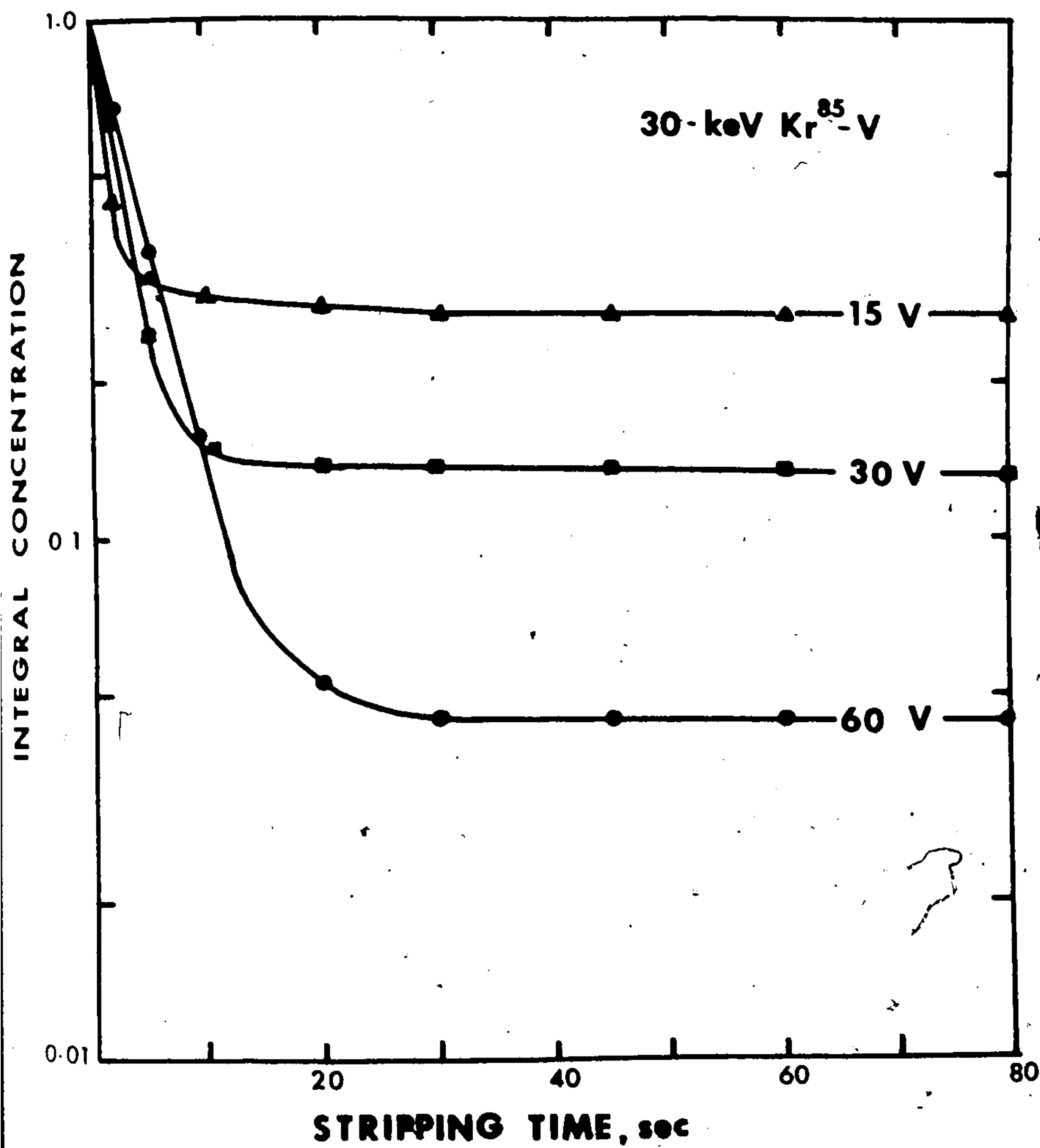

Fig. 4-2 Typical dissolution end-point for V

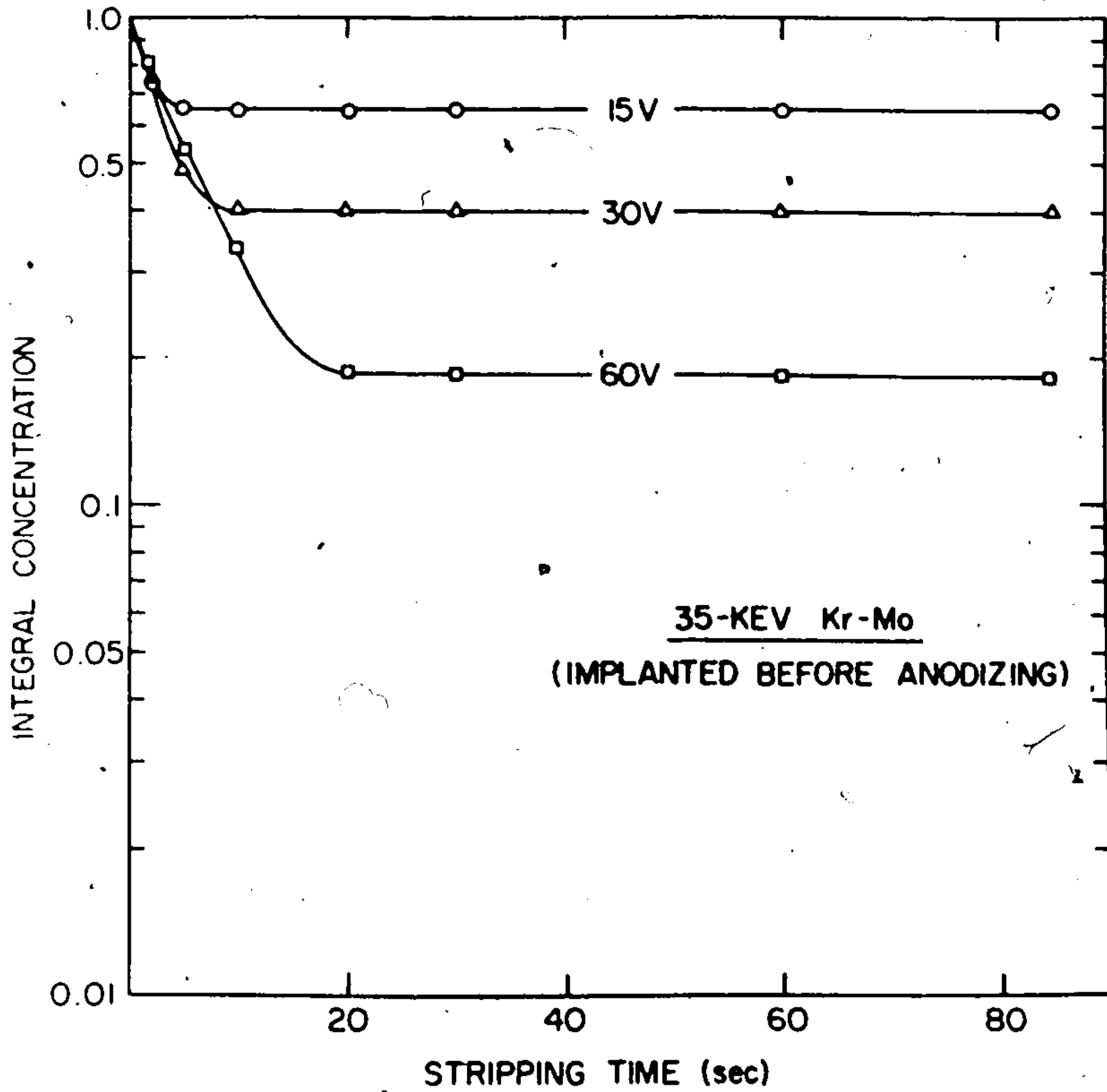

Fig. 4-3 Typical dissolution end-point for Mo

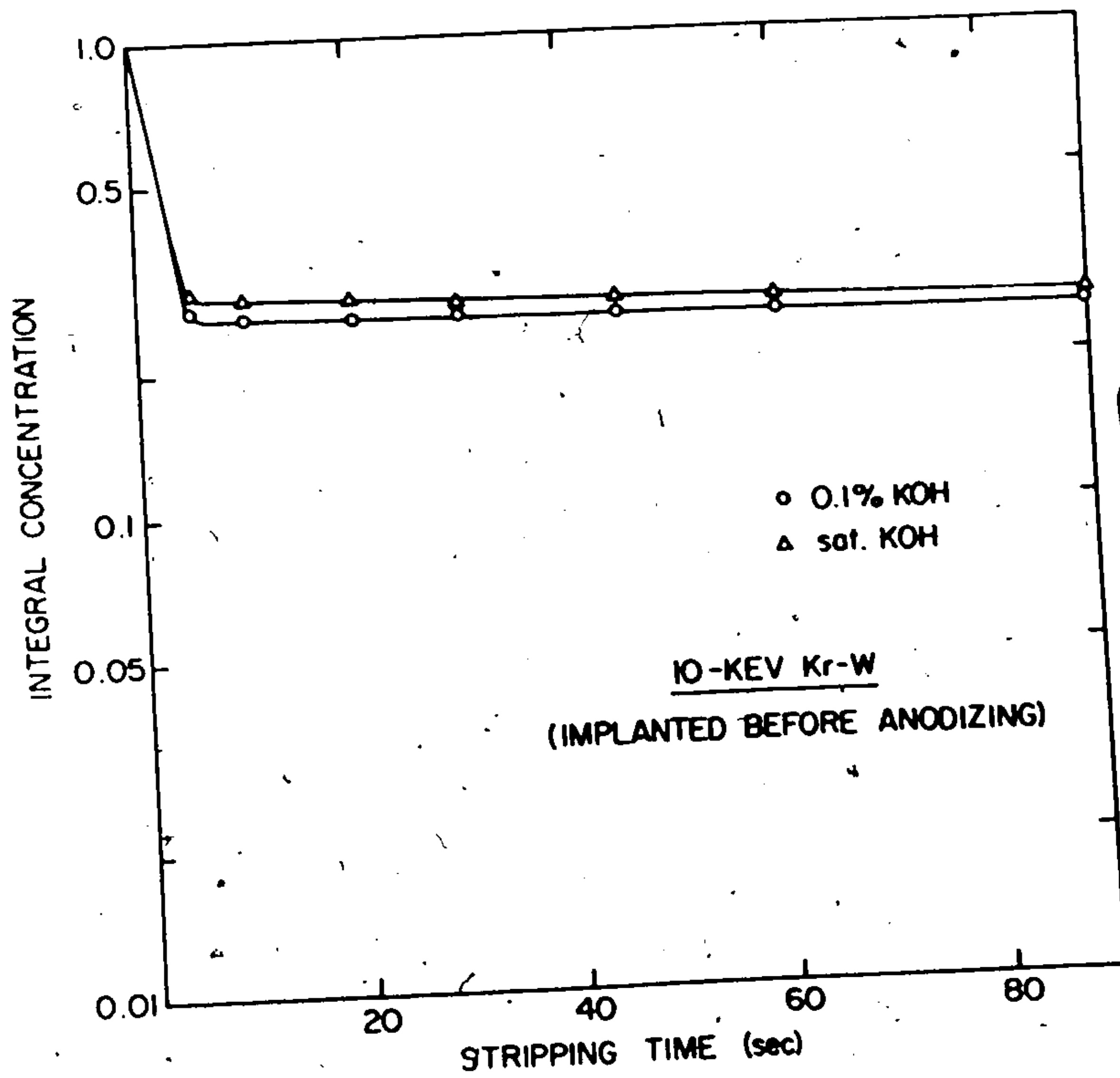

Fig. 4-4 Typical dissolution end-point for W anodized at 25 volts

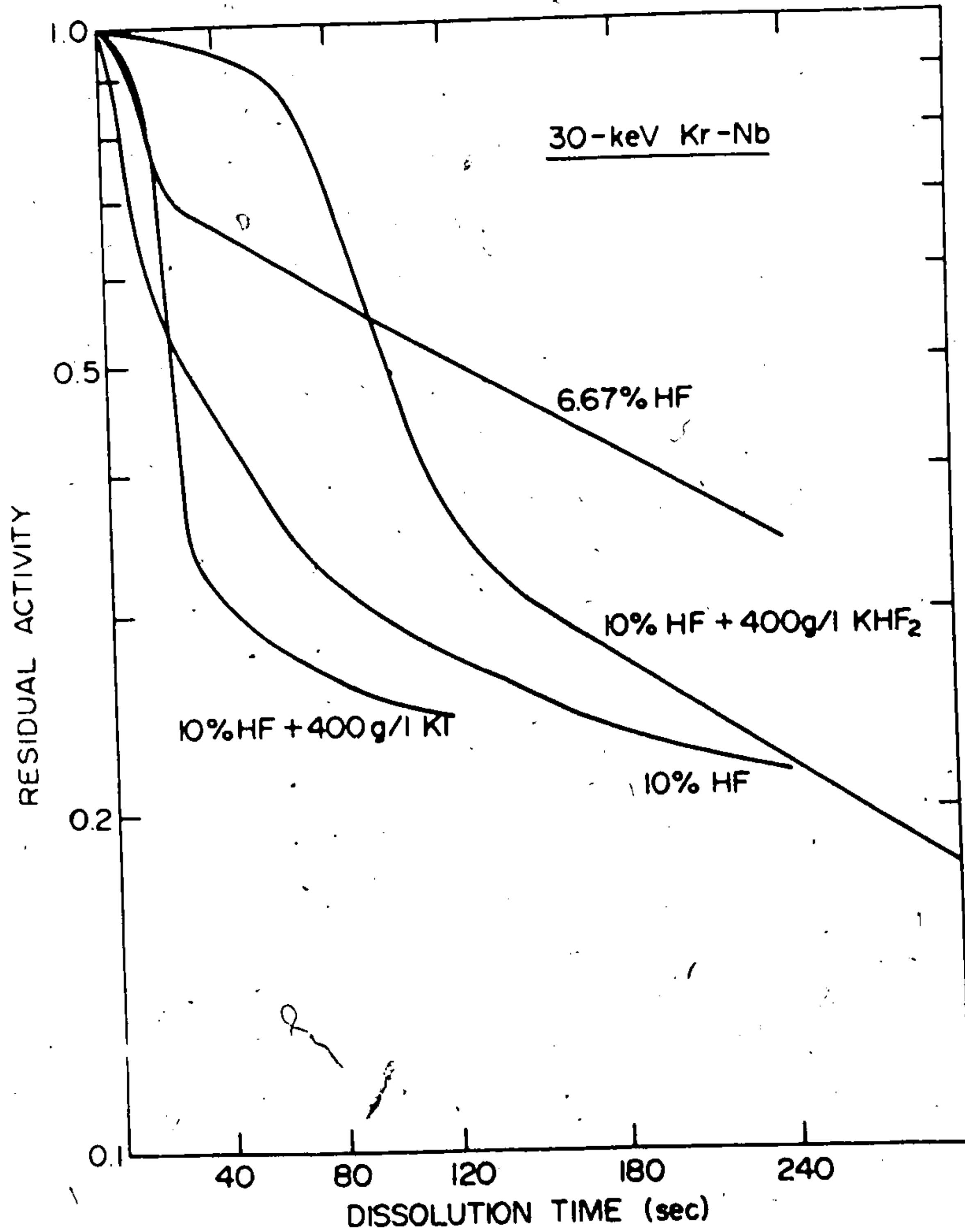

Fig. 4-5 Typical dissolution end-points for Nb with films formed in a 4:1 mixture of H_2SO_4 and HNO_3

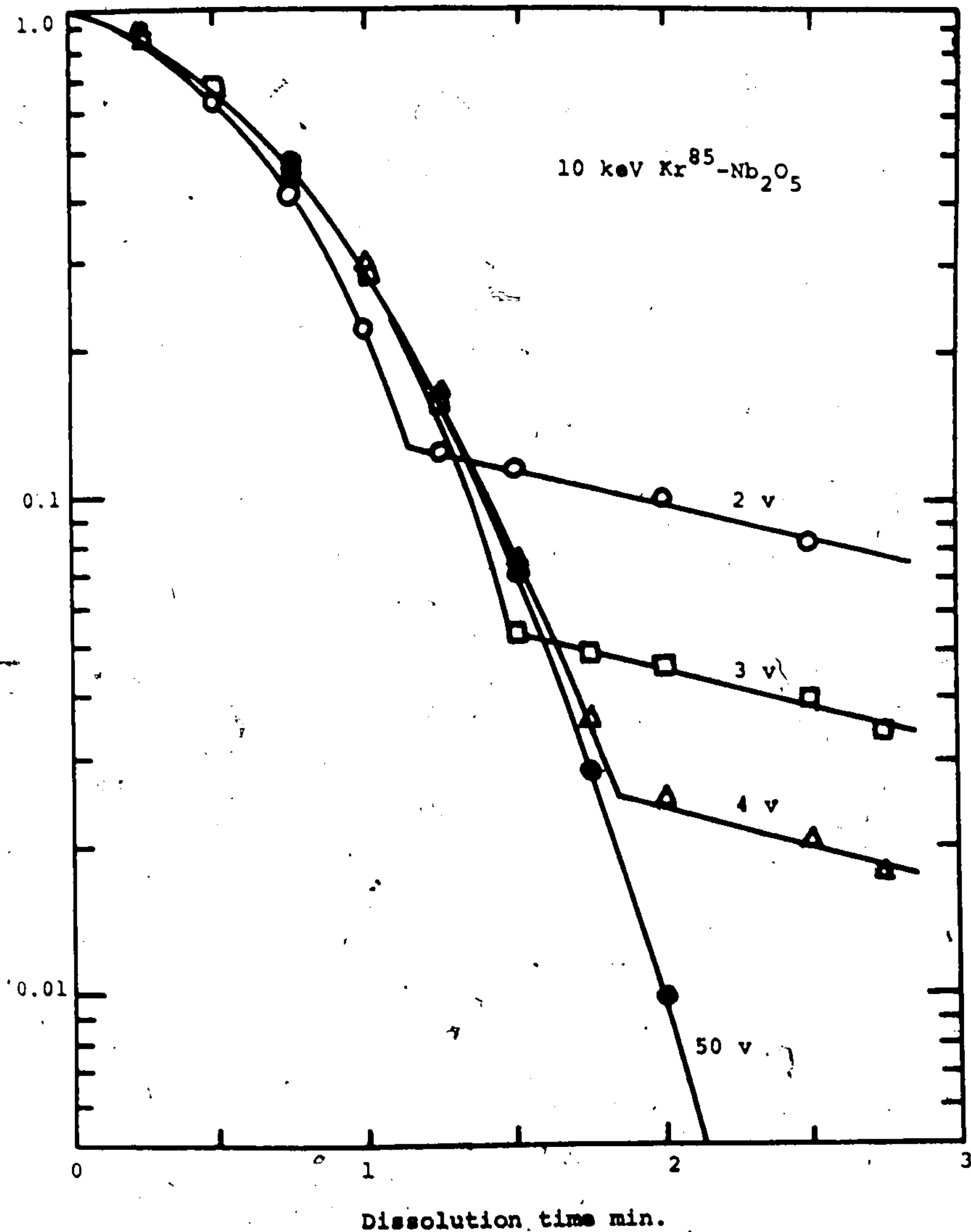

Fig. 4-6 Activity vs time curves serving to determine the rate of dissolution of anodic Nb_2O_5 in 40% HF saturated with NH_4F. Electrolyte = 0.20% KF (after Lam, 1971)

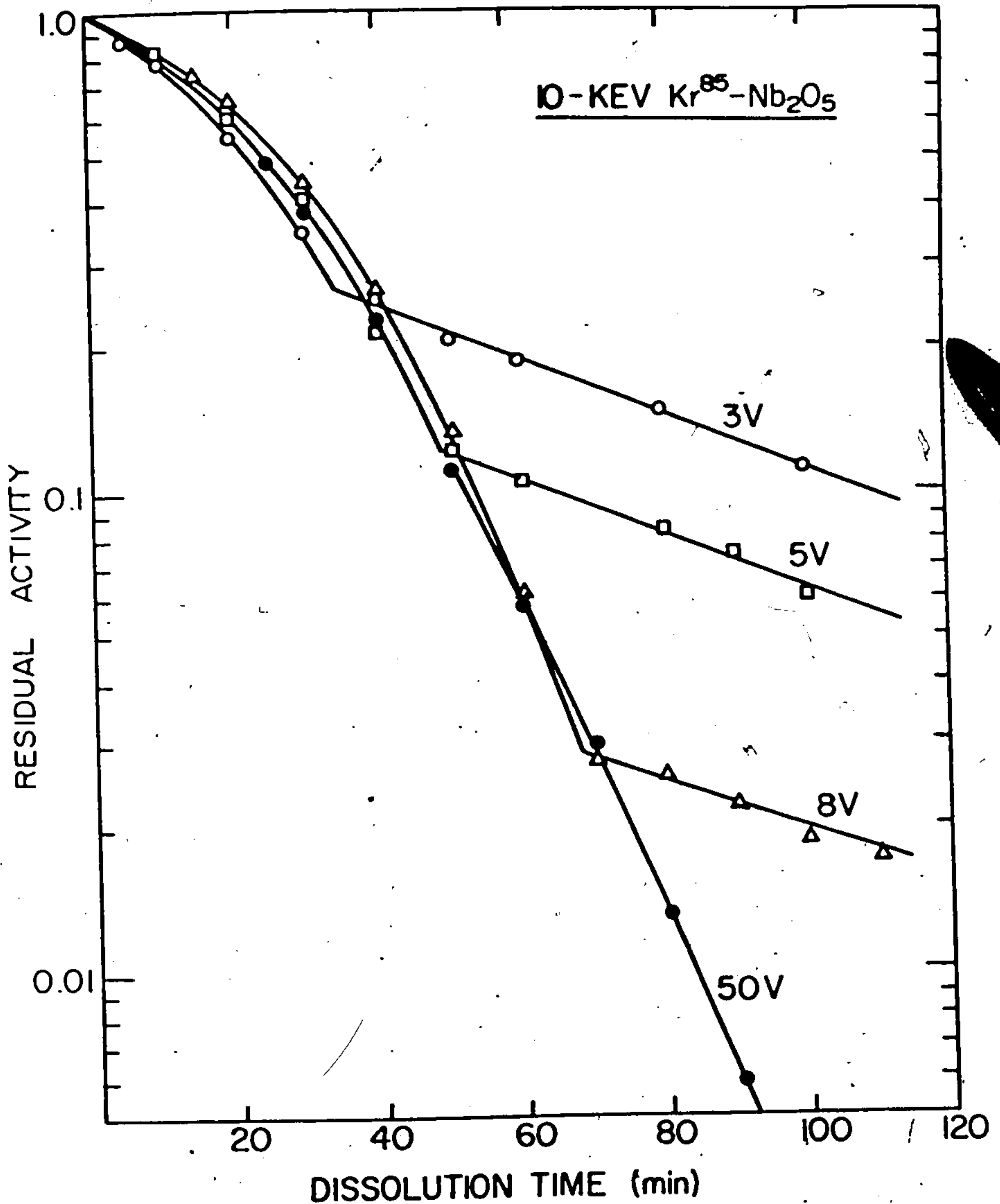

Fig. 1-4 Activity-vs-time curves serving to determine the rate of dissolution of anodic Nb_2O_5 in a solution of 40% HF saturated with NH_4F.

HNO_3, and tried various stripping solutions in an effort to achieve satisfactory sectioning. Some of the stripping solutions tried included HF of various concentrations between 6% and conc. HF (with or without additives such as NH_4F) as well as various concentrations of KOH between 1% and saturated KOH. The results were, in general, similar to those shown in fig. 4-5 and thus unsatisfactory, including for the stripping reagent used by Pringle. We have concluded from this that what is at fault is probably the use of aqueous electrolytes and we have therefore tried the use of non-aqueous electrolytes.

As described previously (sections 2.5.3 and 3.5.2) when Ta and Nb are anodized in non-aqueous electrolytes such as H_2SO_4, H_3PO_4, or glycol-borate, duplex anodic films are formed with the film next to the metal being a pure oxide and that next to the electrolyte being doped. This doped film has enhanced solubility when formed in H_2SO_4, and increasing the concentration of H_2SO_4 leads to a greater proportion of the doped film such that for $\geq$ 80% H_2SO_4, the films formed are more or less completely doped. Dissolution end-points for Nb and Ta; using the sulphate-based electrolytes (non-aqueous) are shown in figs. 4-8 and 4-9. Even with these electrolytes, of the various dissolving reagents tried, only the use of sat. KOH gave satisfactory end-points. In particular, HF or HF saturated with NH_4F led to unacceptably high metal dissolution rates.

Fig. 4-8 Dissolution behaviour of anodic films of Nb formed in an electrolyte containing diethyl sulphate and H_2SO_4

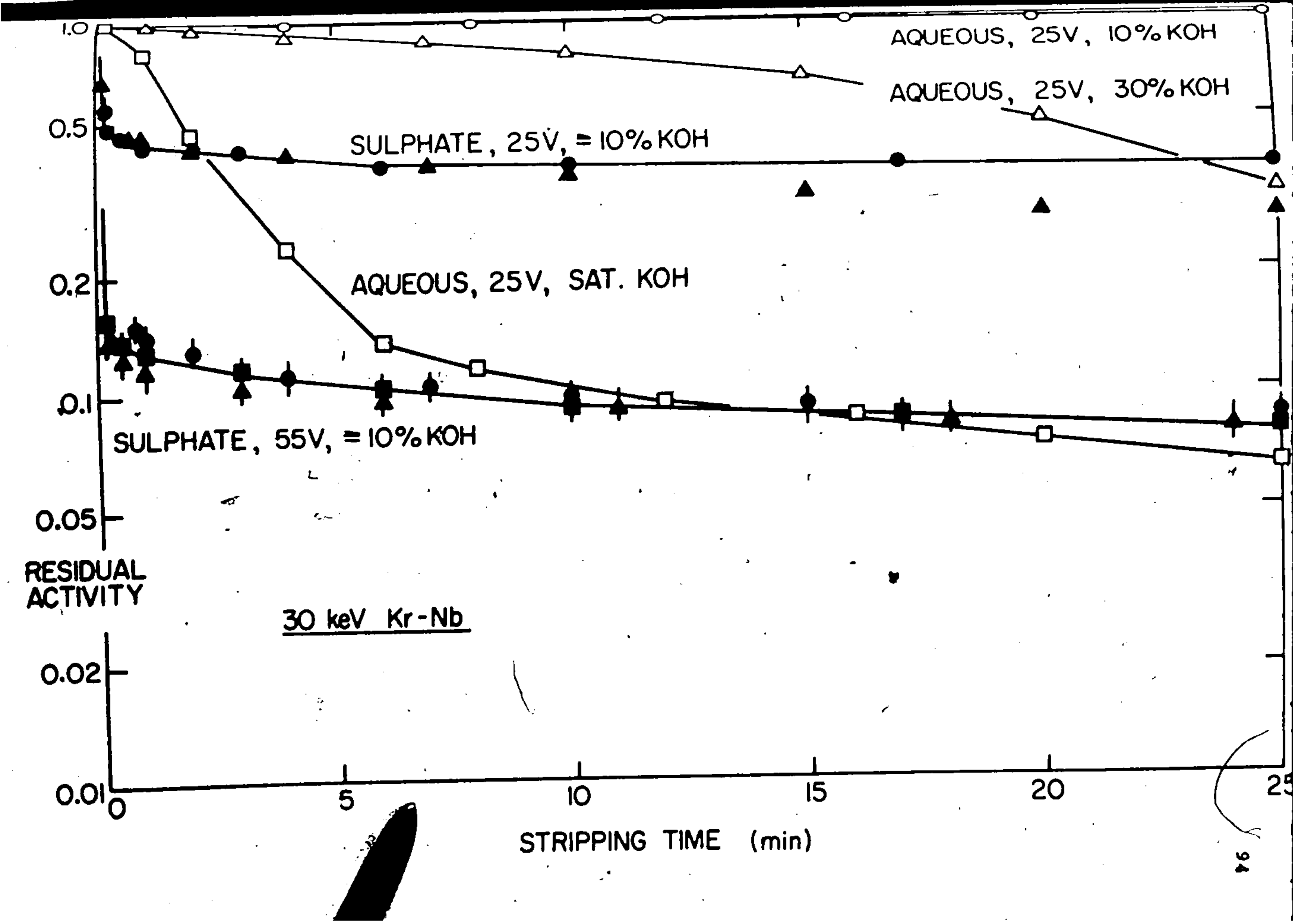
AQUEOUS, 25V, 10% KOH
AQUEOUS, 25V, 30% KOH
SULPHATE, 25V, ≈ 10% KOH
AQUEOUS, 25V, SAT. KOH
SULPHATE, 55V, ≈ 10% KOH
30 keV Kr-Nb
RESIDUAL ACTIVITY
1.0
0.5
0.2
0.1
0.05
0.02
0.01
0
5
10
15
20
25
STRIPPING TIME (min)

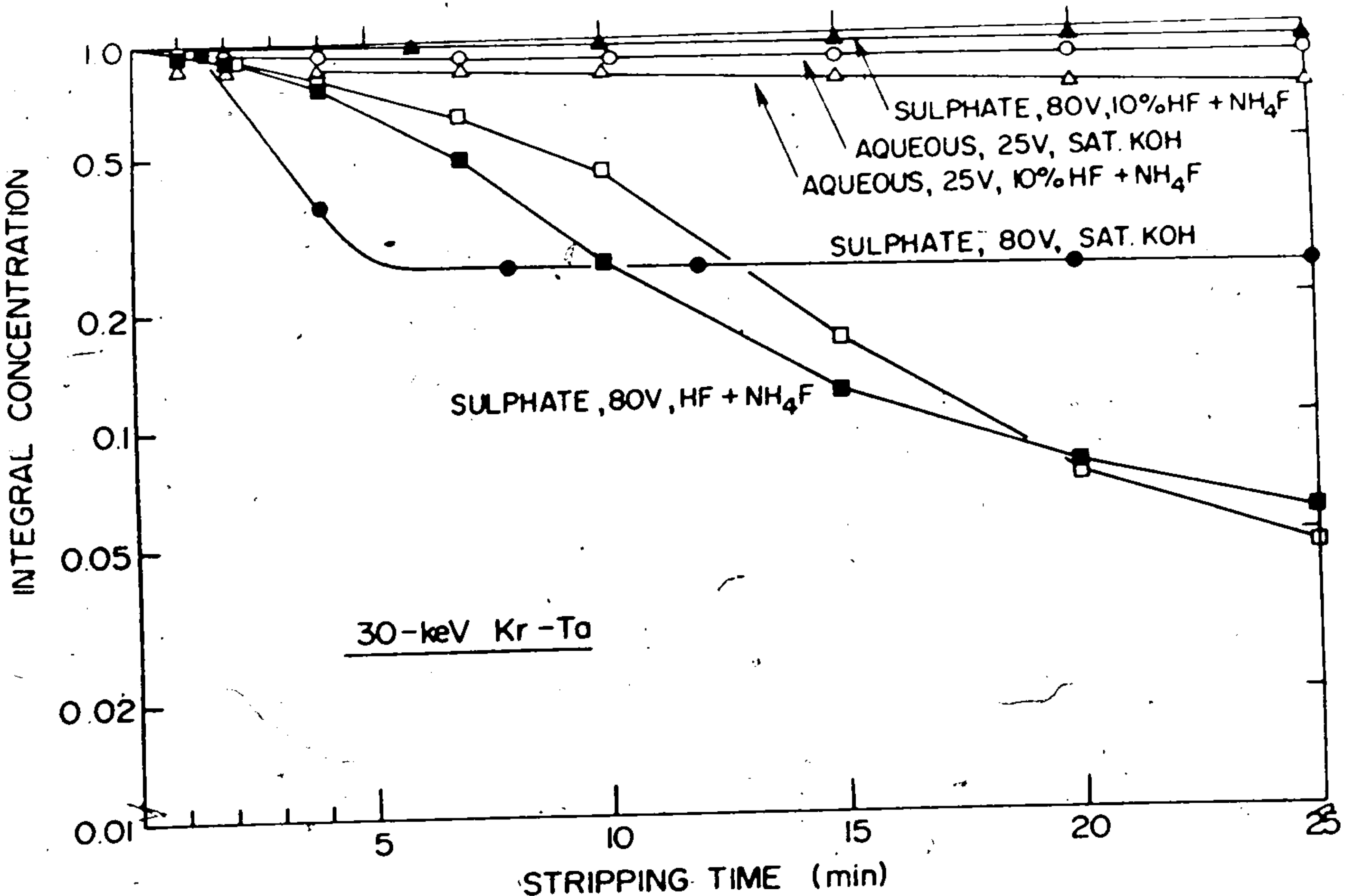

Fig. 4-9 Dissolution behaviour of anodic films of Ta formed in an electrolyte containing diethyl sulphate and H_2SO_4

It can be deduced from the data of fig. 4-8 that Nb still dissolves at about 3 Å/min in sat. KOH. The use of 10% (instead of saturated) KOH reduces the attack to about 1 Å/min but new problems arise in this case. The films on Nb are duplex, with a thin undoped part (presumably due to oxygen ion migration) and a thicker doped part (presumably due to cation and/or S migration), as shown in fig. 4-10. The undoped part of the film could be shown in two ways to have a significantly lower solubility. Firstly, the undissolved part of the film accumulated during repeated sectionings using 10% KOH until it became visible by virtue of interference colours. Secondly, the film dissolution could be shown to resume with sat. KOH, as shown in fig. 4-11. The attack rate by 30% KOH is similar to that by 10% KOH so that the use of sat. KOH as the solvent becomes imperative. The corresponding problem for Ta was not the attack on the metal by sat. KOH (about 0.4 Å/min) but rather the slowness of the film dissolution. Table 4-2 therefore includes minimum times (in minutes) for film removal in case of Ta, and maximum times (in seconds) for Nb. The latter values should be met exactly.

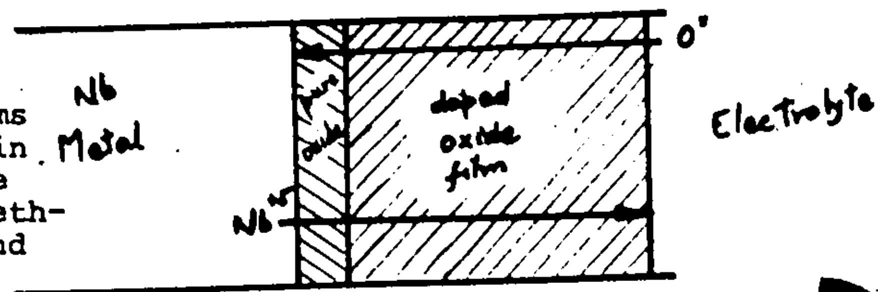

Fig. 4-10 Duplex nature of anodic films of Nb formed in an electrolyte containing diethyl sulphate and H_2SO_4.

Fig. 4-11 Dissolution of anodic film of Nb formed in sulphate-based electrolyte when exposed to 10% KOH for 12 minutes and then to saturated KOH

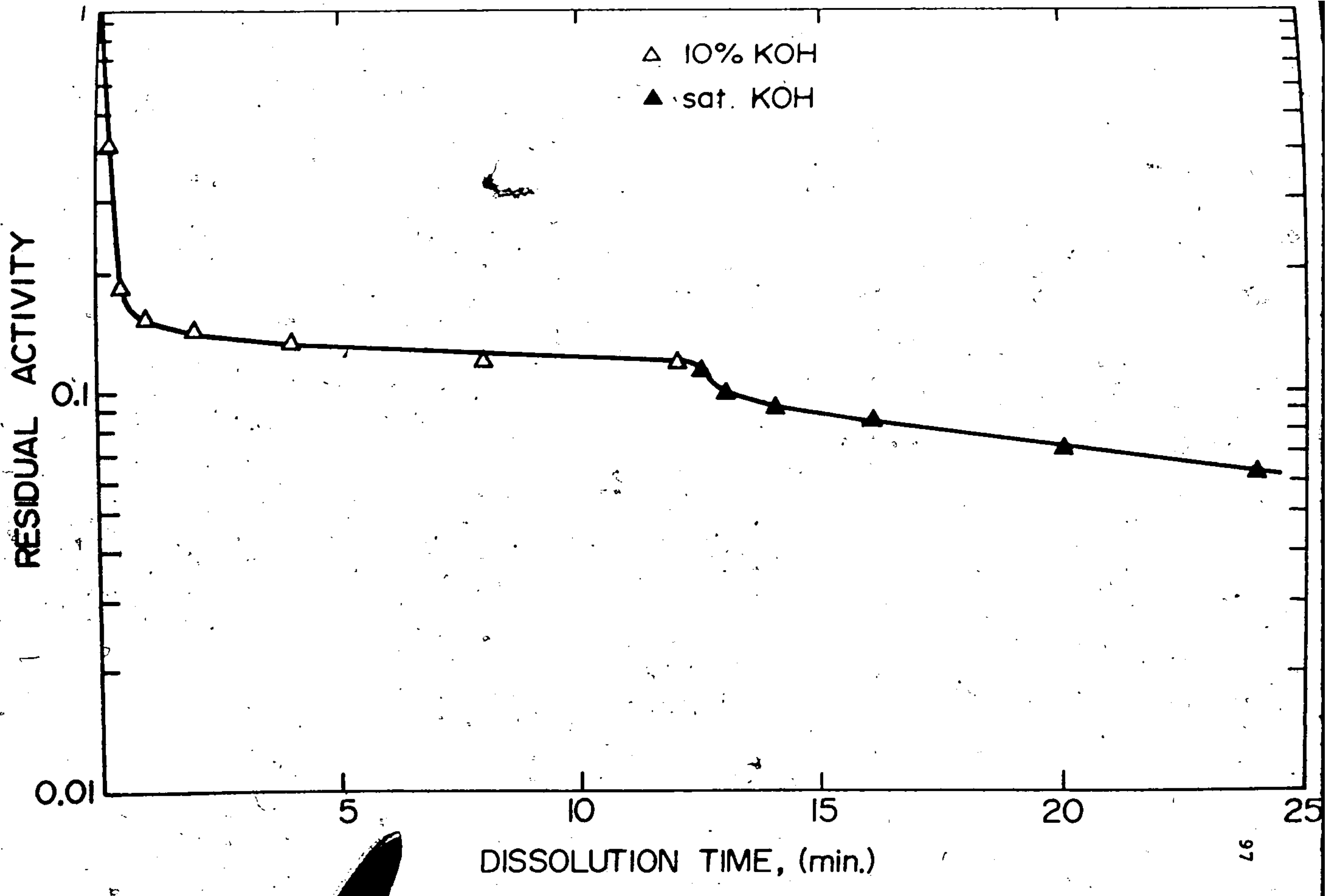
△ 10% KOH
▲ sat. KOH
RESIDUAL ACTIVITY
1
0.1
0.01
5
10
15
20
25
DISSOLUTION TIME, (min.)

Table 4-2

Stripping times for Nb and Ta in sat. KOH

Anodizing voltage	Stripping time for Nb (sec)[a]	Stripping time for Ta (min)[b]
1	5	1
3	9	2
6	14	3
10	22	5
20	30	6
30	38	8
40	45	9
60	60	11
100	...	13

[a]The recommended times for Nb should be followed exactly.

[b]The recommended times for Ta should be regarded as lower limits.

4.3 Thickness Calibrations

4.3.1 General: As described above, combinations of the acetic-acid-based electrolyte and dilute KOH as the film solvent for V, Mo and W, and the sulphate-based electrolyte and sat. KOH as the solvent for Nb and Ta lead to satisfactory dissolution end-points. Once the anodic sectioning techniques are established, the metal-removal and film thicknesses can in principle be determined gravimetrically. But a minor problem of electrode spacings was found to affect the thickness calibrations to some extent.

4.3.2 Effect of Electrode Spacing: The acetic-acid based electrolyte has a rather low conductivity and the calibrations were found to depend on the electrode spacing, initial current density and the total anodizing time. It has already been shown (section 3.4.2) that the use of an initial current of 2.0 mA/cm^2 and a total anodizing time of 6 min yields satisfactory results. On further investigation, it was found that the thickness calibrations were the same to within the experimental errors when the electrode spacing was varied between 0.5 and 1.0 cm; however, when the electrodes were 2.0 cm apart, an anodizing time of about 8 min was required for the same film thickness. With these results in mind, the anodizing conditions become: electrode spacing = 0.8-1.0 cm; initial current = 2.0 mA/cm^2; total anodizing time = 6 min; no electrolyte stirring; temperature = 25±1°C; and the use of a filter paper

or an air jet to stabilize the anodic films (on V and Mo) when a permanent film is desired (such as in thickness calibrations). Relaxing any of these conditions will to some extent invalidate the thickness calibrations for V, Mo and W which are described below. Such effects were not important in the case of Nb and Ta. The anodizing conditions used here were therefore simply an initial current of 5.0 mA/cm^2 with the current being allowed to drop for 2 min after the desired voltage was reached.

4.3.3 Calibrations for Thick Films: Since all five metals under discussion are found to have good dissolution end-point, the weights of the anodic films as well as the metal-removal weights can, at high formation voltages ($\geq$ 10 volts), be easily determined using the conventional gravimetric method. The results for V, Mo, and W are shown in figs. 4-12 to 4-14, and are, in addition represented within certain ranges as follows:

(a) V.
Weight of metal removed = (5.50+0.634 volts) μg/cm^2 for 4-100 volts

Weight of film formed = (2.20+1.15 volts) μg/cm^2 for 7.5-100 volts

(b) Mo.
Weight of metal removed = (5.90+1.05 volts) μg/cm^2 for 7.5 to 110 volts

Weight of film formed = (1.35+1.58 volts) μg/cm^2 for 10-110 volts.

(c) W.
Weight of metal removed = (5.90+1.10 volts) μg/cm^2 for 7-100 volts

Weight of film formed = (10.7+1.37 volts) μg/cm^2 for 10-100 volts.

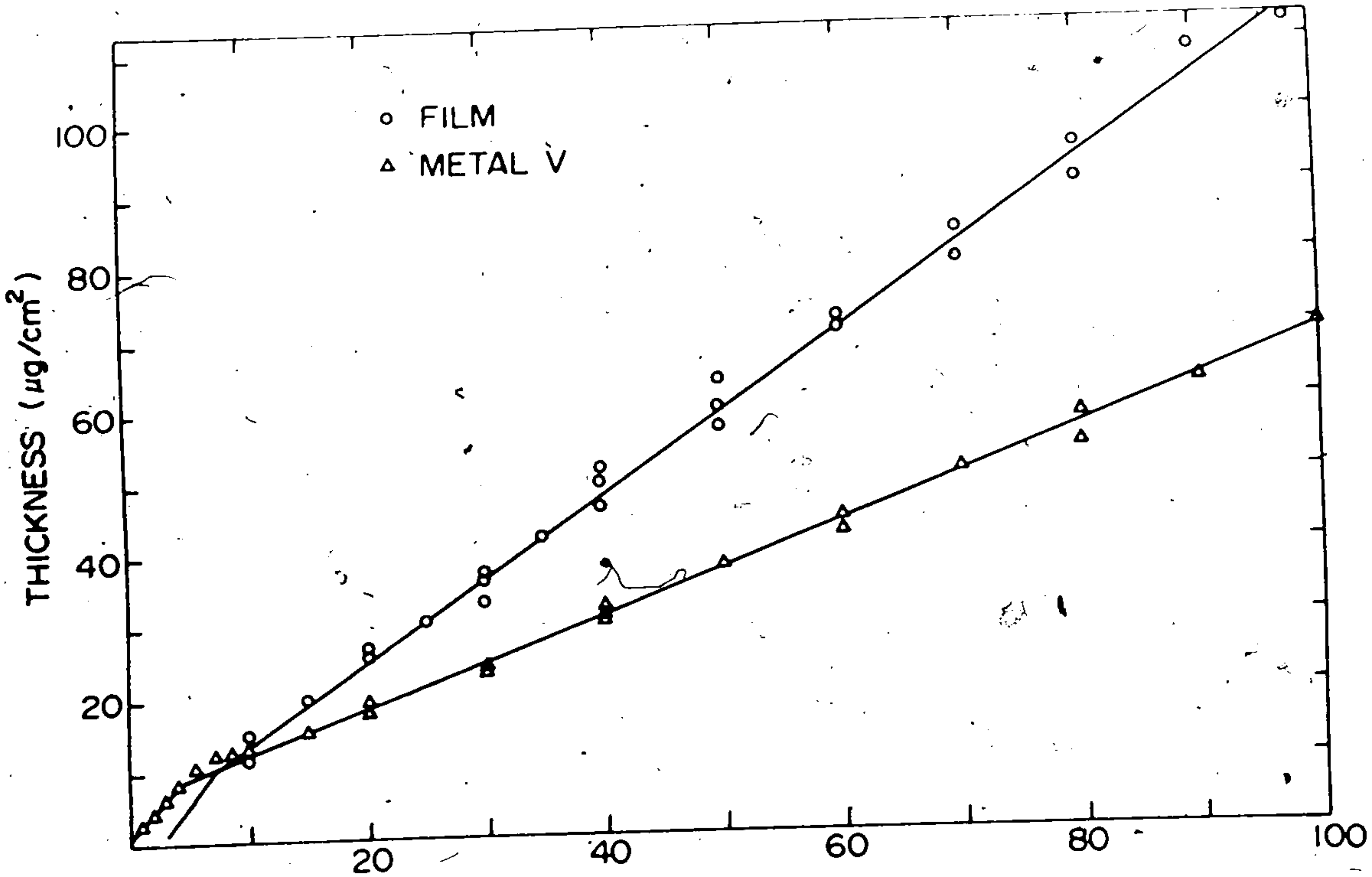

Fig. 4-12 Thickness vs anodizing voltage relation for V

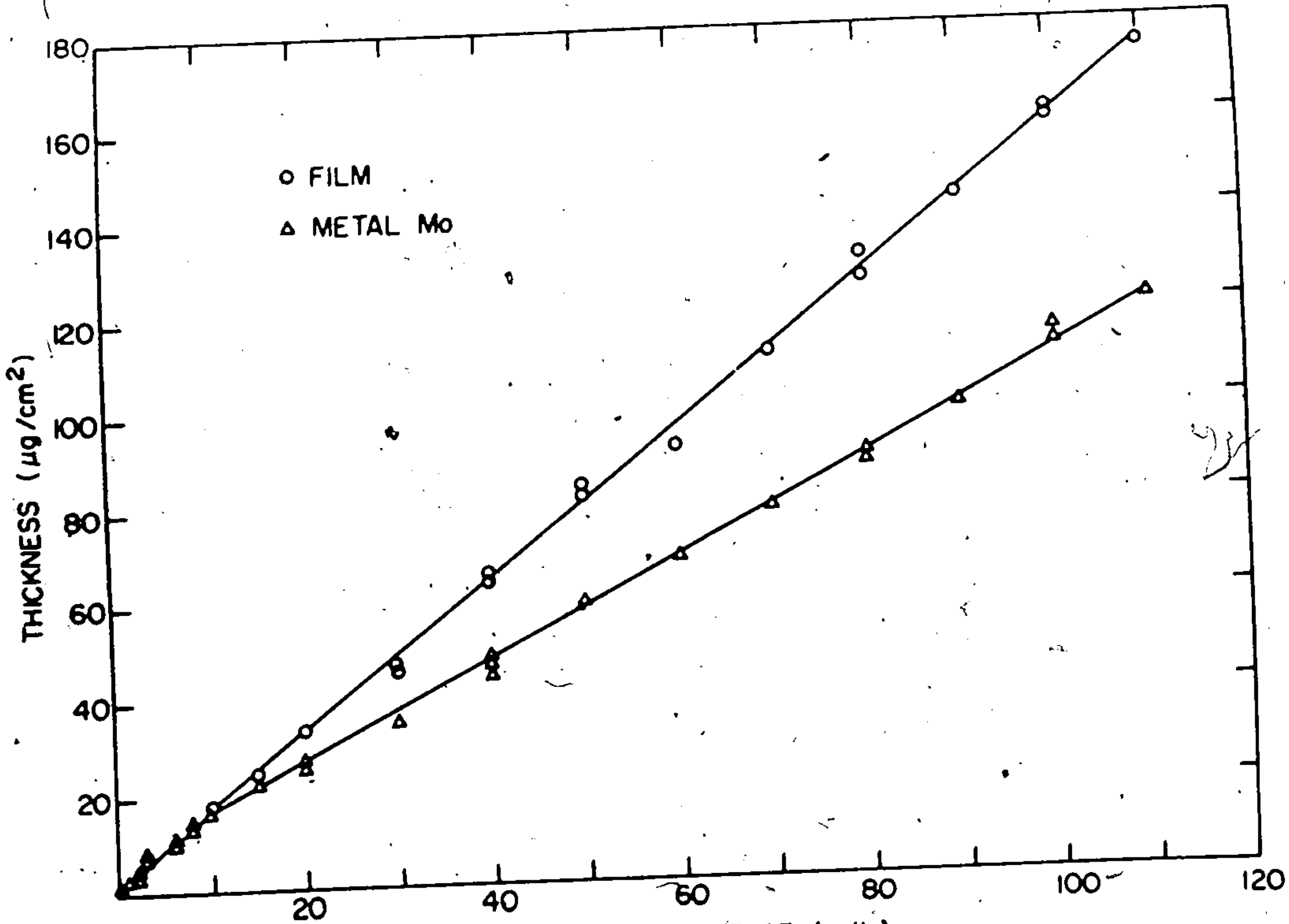

Fig. 4-13 Thickness vs anodizing voltage relation for Mo

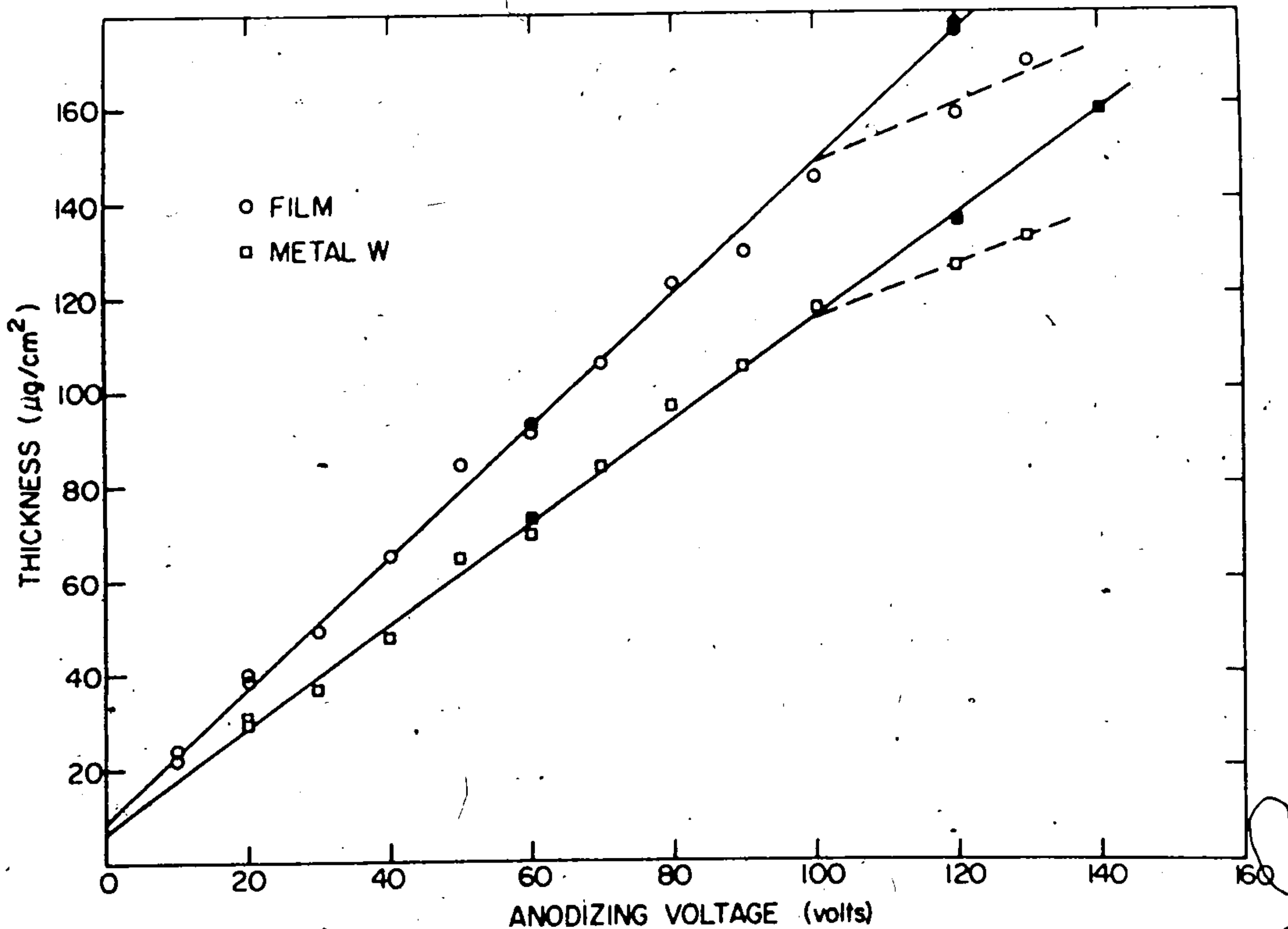

Fig. 4-14 Thickness vs anodizing voltage relation for W. Open points: 2 mA/cm^2. Closed points: 10 mA/cm^2

Further experiments showed that the calibrations for W may be extended up to 140 volts provided one uses 10.0 mA/cm^2 as the initial current density instead of 2.0 mA/cm^2. The relevant calibration remains the same as above.

Results for Nb are shown in fig. 4-15 using conc. H_2SO_4 as the electrolyte and reveal that the thicknesses for neither the metal nor the film are reproducible. Another problem also arises with conc. H_2SO_4: electrical breakdown occurs at about 45 volts. Similar problems of reproducibility did not arise with Ta but the low breakdown voltage still limited the maximum thickness achievable in a single sectioning. A series of experiments was then carried out to improve the results and it was found that a 3:1 mixture of diethyl sulphate and conc. H_2SO_4 led to much better reproducibility (with Nb) and much higher breakdown voltages (with Nb and Ta). Table 4-2A shows the results for breakdown voltages for 100% H_2SO_4, 50% H_2SO_4, and 25% H_2SO_4 as electrolytes. Subsequent work involving Nb and

Table 4-2A

Anodizing Breakdown Voltages for Nb and Ta

	Electrical Breakdown voltages, volts			Thickness Reproducibility
	100% H_2SO_4	50% H_2SO_4	25% H_2SO_4	Limit 25% H_2SO_4
Nb	∿45	∿65	∿85	∿70
Ta	∿115	∿150	∿180	∿100

Ta was therefore carried out using the 3:1 mixture of diethyl

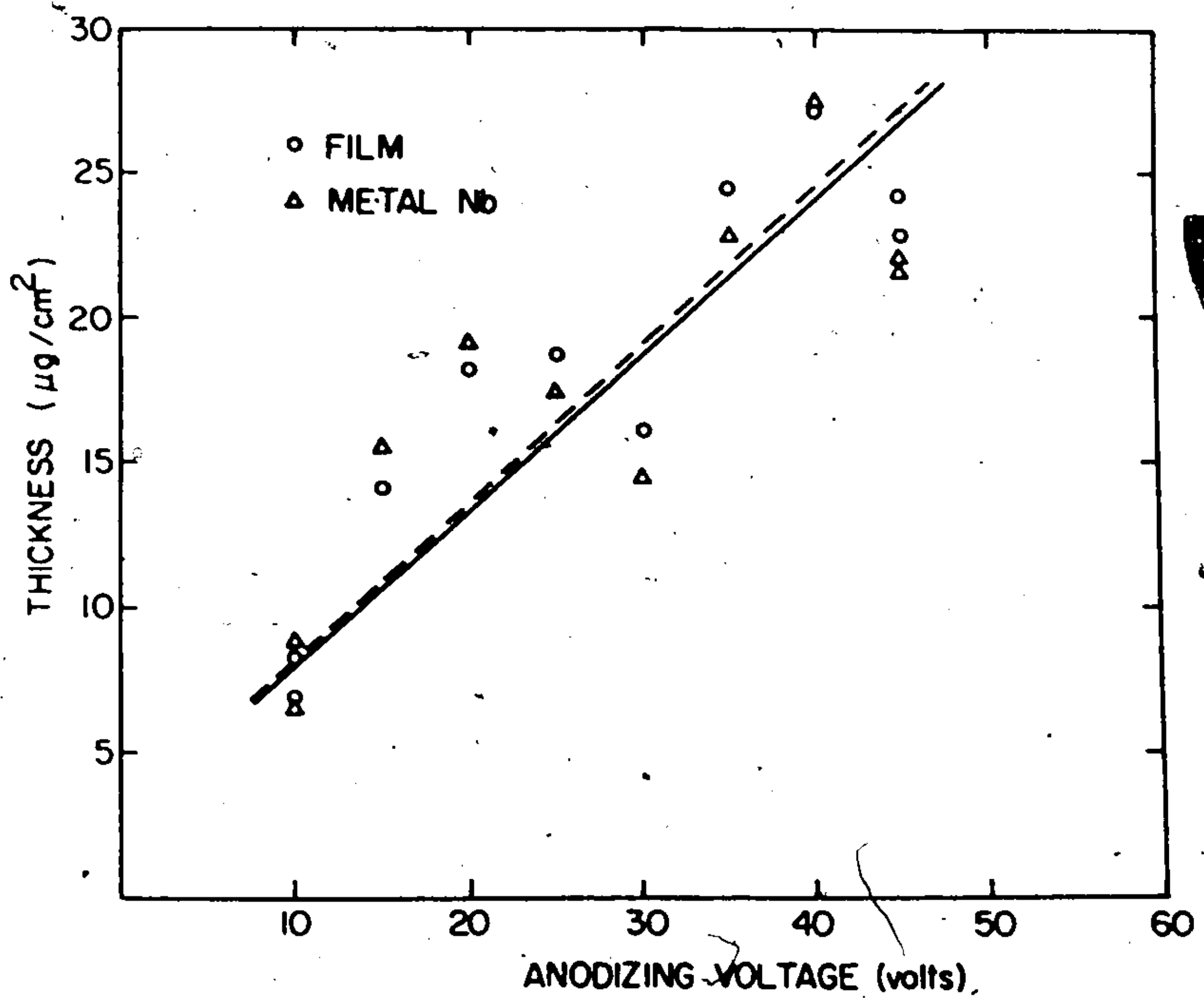

Fig. 4-15 Thickness vs anodizing voltage relation for Nb using conc. H_2SO_4 as the electrolyte

sulphate and conc. H_2SO_4. The results for thickness calibrations are shown in figs. 4-16 and 4-17, and summarized in analytical form as follows:

(d) Nb. Weight of metal removed = (1.14+0.42 volts) $\mu g/cm^2$ for 8-50 volts

Weight of film formed = (0.56+0.624 volts) $\mu g/cm^2$ for 10-50 volts

(e) Ta. Weight of metal removed = (4.03+0.455 volts) $\mu g/cm^2$ for 15-80 volts

Weight of film formed = (3.28+0.689 volts) $\mu g/cm^2$ for 10-80 volts.

It should be pointed out that the expressions (and slopes) for thickness calibrations for Nb and Ta change at voltages higher than those given in the above expressions. They are reproducible, however, up to 70 and 100 volts for Nb and Ta respectively, with values as in figs. 4-16 and 4-17.

4.3.4 Deduction of Film Stoichiometries: The thickness calibrations provide us with explicit information on the amounts of metal involved and the amounts of film formed. This information may be correlated to deduce the stoichiometries of anodic films formed. One thus considers the amount of metal removed, converts that into the amount of film which would form assuming various stoichiometries, and finally compares the result with the amount of film as determined experimentally. In view both of the interfacial potentials, as well as the fact that some metal dissolution occurs during film formation in the case of V and Mo, only the slopes involved in the thickness

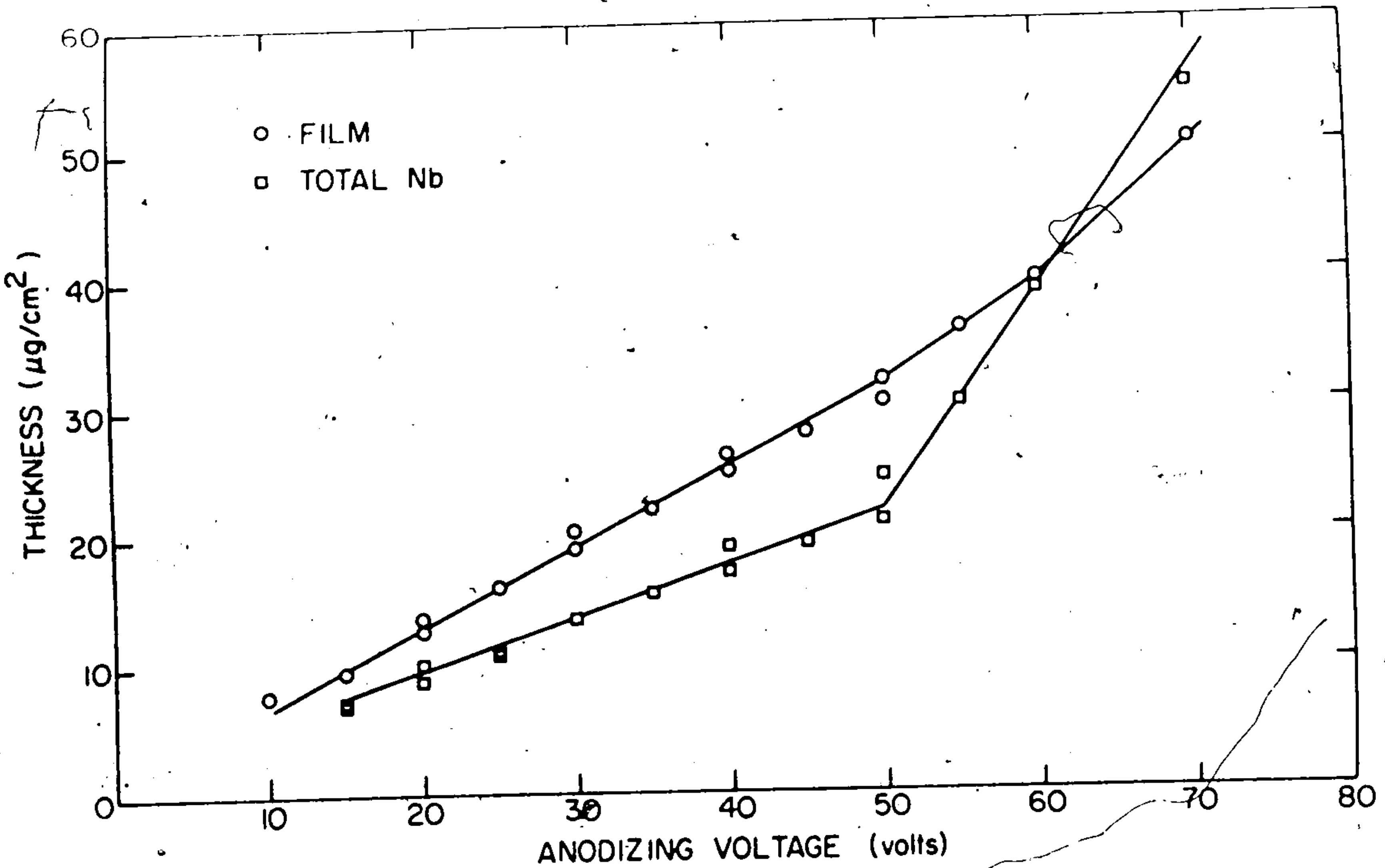

Fig. 4-16 Thickness vs anodizing voltage relation for Nb using sulphate-based electrolyte

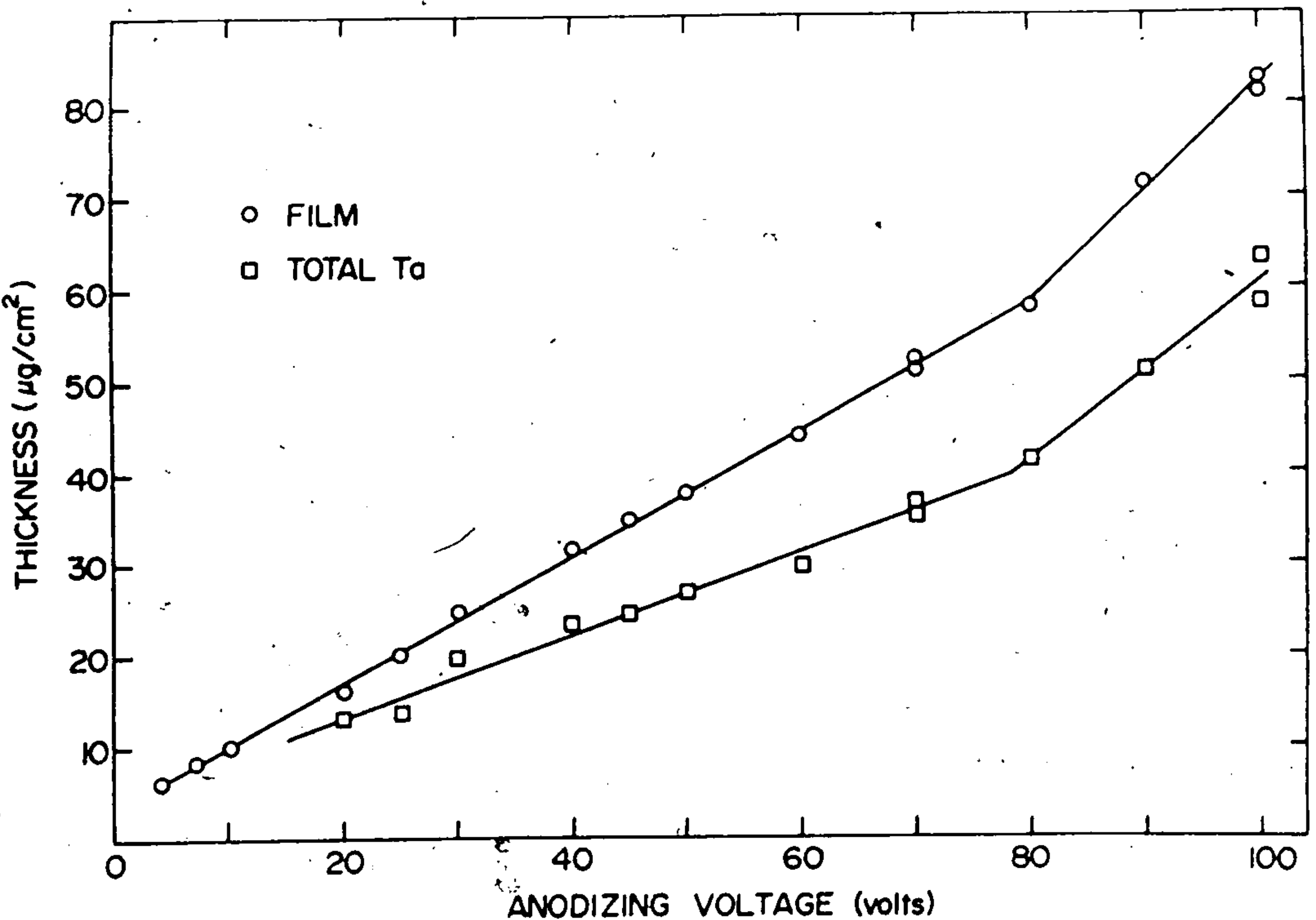

Fig. 4-17 Thickness vs anodizing voltage relation for Ta using sulphate-based electrolyte

calibrations must be considered. The results of section 4.3.3 have been analyzed and are summarized in Table 4-3. Thus, the stoichiometries inferred are respectively V_2O_5, MoO_3, WO_3, Nb_2O_5 and Ta_2O_5 with no noticeable doping of V, Mo and W, whereas Nb to some extent and Ta to a large extent show doping. The extents of doping, as deduced here, are consistent with the results of section 3.5.5 for W, Nb and Ta.

Table 4-3

Deduction of Film Stoichiometries from Thickness Calibrations

Metal	Experimental Metal Loss $\mu g/cm^2$ per volt	Film Weight as Inferred from Metal Loss $\mu g/cm^2$ per volt	Experimental Film Weight $\mu g/cm^2$ per volt	Remarks
V	0.634	if VO_2=1.03 if V_2O_5=1.13	1.15	Film likely V_2O_5, with no noticeable doping
Mo	1.05	if MoO_2=1.40 if MoO_3=1.58	1.58	Film likely MoO_3 with no noticeable doping
W	1.10	if WO_2=1.30 if WO_3=1.38	1.37	Film likely WO_3 with no noticeable doping
Nb	0.42	if NbO_2=0.565 if Nb_2O_5=0.60	0.624	Film likely Nb_2O_5 with some doping
Ta	0.455	if Ta_2O_5=0.555	0.689	Film likely Ta_2O_5 with significant doping.

4.4 Calibrations for Thin Films

4.4.1 General: An accurate knowledge of small thicknesses, $< 10\ \mu g/cm^2$, is essential to anodic sectioning, yet serious

problems arise in this region. The estimated error involved using gravimetric methods is about ± 2 μg for each weighing and this method is thus not sensitive enough to determine thicknesses below ≲ 50 Å (for example, for Mo, 50 Å ≈ 5 μg/cm^2 which for a surface area of 4 cm^2 would involve a weighing error of about 10%). Supplementary calibration methods, based on the use of radioactive labeling, have therefore been developed and will be described separately for the metal-removal and film-formed thicknesses.

4.4.2 Metal-Removal Thicknesses: Metal-removal thicknesses for 1 to 20 volts region were obtained in experiments in which thicknesses for low voltages were determined as a function of those for high voltages.

In the case of V, 66 specimens were implanted with 20-keV Kr^{85} to a dose of 5×10^5 ions/cm^2. With 3 specimens, the residual activities were determined after repeated 3-volt sectionings, the results being a true range profile (fig. 4-18, dashed), with depth expressed in units of volts. It is seen that there is no apparent discontinuity in the range profile until about 9 volts.

With another 36 specimens, the residual activities were determined after a single sectioning at various voltages. The resulting curve (fig. 4-18, solid), when interpreted in the light of the true range profile (fig. 4-18, dashed), brings out the following two features about the thickness-

Fig. 4-18 Integral depth distributions in V. Dashed: curves obtained after repeated 3-volt sectionings. Solid: curves obtained from a series of specimens, each sectioned once at a different voltage.

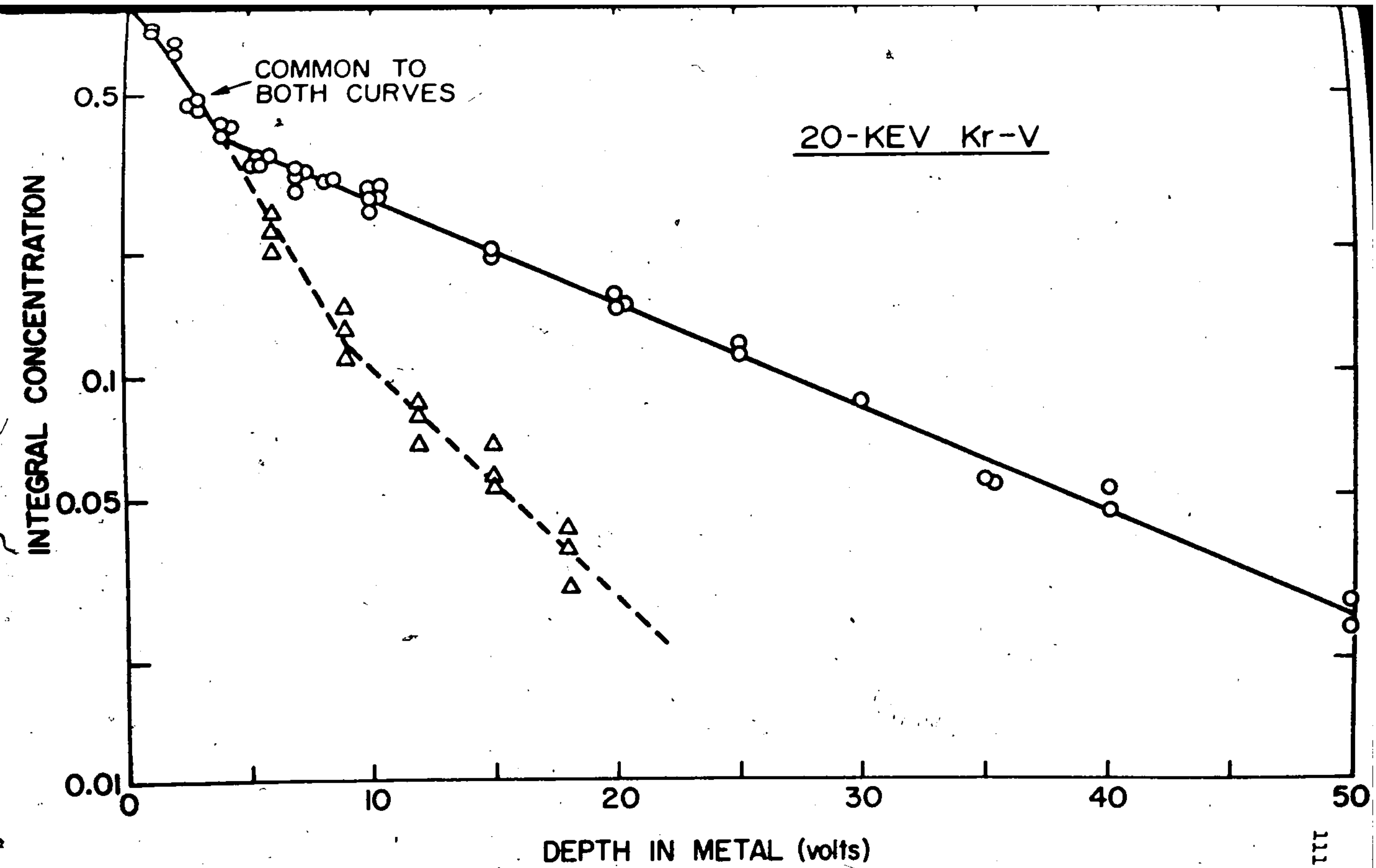
20-KEV Kr-V
COMMON TO BOTH CURVES
INTEGRAL CONCENTRATION
0.5
0.1
0.05
0.01
0
10
20
30
40
50
DEPTH IN METAL (volts)

voltage calibration:

(i) the calibration is "well-behaved" starting at about 1 volt, and

(ii) there is a discontinuity at 4±0.5 volts.

The remaining 27 specimens were then used to obtain further information. Residual activities were obtained after repeated sectionings at 1 to 15 volts. Reference to fig. 4-18 (solid) then enabled the final metal-removal thicknesses to be expressed as a function of those for higher voltages ($\geq$ 10 volts), with results summarized in Table 4-4. For example, sectioning V seven times at 1 volt led to a residual activity of 0.139 which corresponds, from fig. 4-18 (solid), to 21.4 volts. Since one sectioning at 21.4 volts removes 19.1 μg/cm^2, it follows that one 1 volt sectioning would remove $\frac{1}{7}$ (19.2) = 2.73 μg/cm^2.

Similar experiments were performed with the other four metals, and their results are given in figs. 4-19 and 4-20, as well as in Tables 4-5 and 4-6. The analytical expressions for thicknesses for all five metals can be expressed as follows:

(a) V. Metal-removal thickness = (1.82+1.45 volts) μg/cm^2 for 1 to 4 volts

(b) Mo. Metal-removal thickness = (1.46+1.75 volts) μg/cm^2 for 1 to 7.5 volts

(c) W. Metal-removal thickness = (0.35+1.33 volts) μg/cm^2 for 1 to 7 volts

(d) Nb. Metal-removal thickness = (0.82+0.462 volts) μg/cm^2 for 1 to 8 volts

(e) Ta. Metal-removal thickness = (0.79+0.641 volts) μg/cm^2 for 1 to 15 volts.

Table 4-4

Metal-removal thicknesses* for low anodizing voltages for V**

Anodizing voltage volts	Number of anodic sectionings	Integral activity	Thickness in terms of that for a single high-voltage sectioning*	Thickness per sectioning $\mu g/cm^2$
1	7	0.139	$(1/7)(x_{21.4})$	2.73
2	5	0.139	$(1/5)(x_{21.4})$	3.8
3	4	0.079	$(1/4)(x_{30.8})$	6.3
4	3	0.080	$(1/3)(x_{30.6})$	8.4
5.5	2	0.108	$(1/2)(x_{25.4})$	10.9
7	2	0.079	$(1/2)(x_{30.8})$	12.6
8.5	2	0.083	$(1/2)(x_{29.8})$	12.3
10	2	0.071	$(1/2)(x_{32.6})$	13.2
15	2	0.048	$(1/2)(x_{39.2})$	15.3

*The nomenclature "$x_{21.4}$" means "metal-removal thickness accomplished in a single sectioning at 21.4 volts".

**Specimens labeled with 20-keV Kr^{85}.

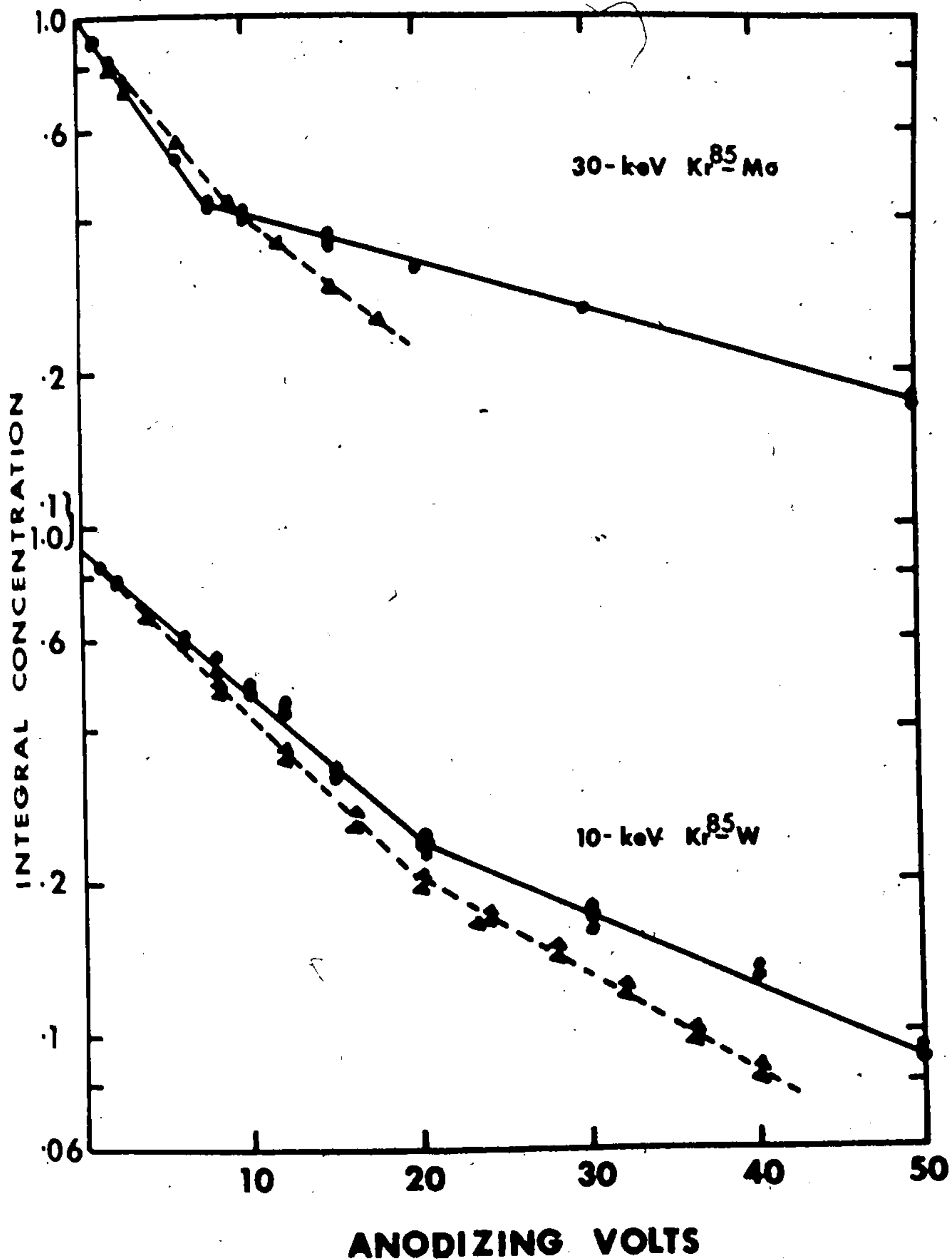

Fig. 4-19 Integral depth distributions in Mo and W. Dashed: 3-volt sectionings for Mo and 4-volt sectionings for W. Solid: each specimen sectioned once at a different voltage.

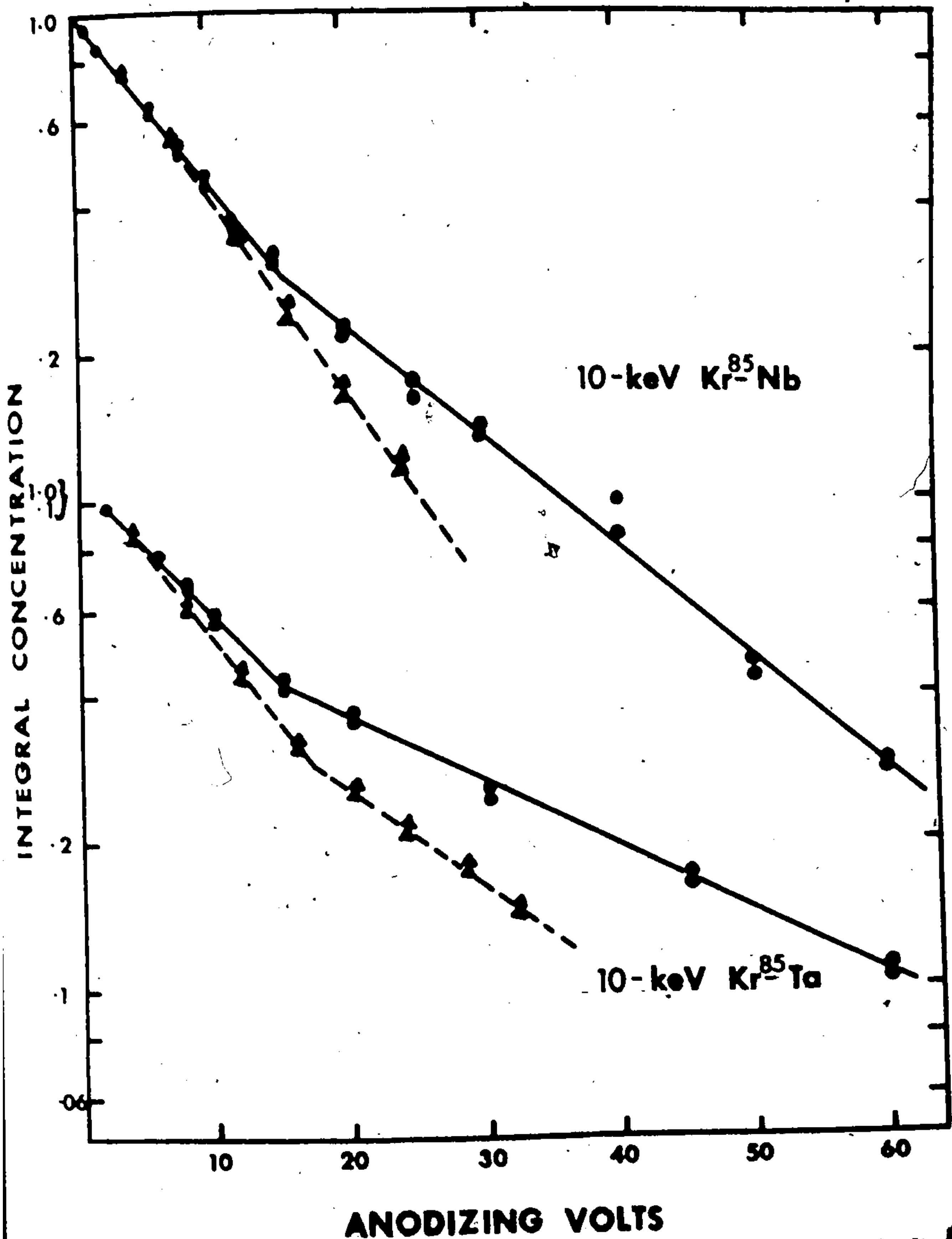

Fig. 4-20 Integral depth distributions in Nb and Ta. Dashed: 4-volt sectionings. Solid: each specimen sectioned once at a different voltage.

Table 4-5

Metal-removal Thicknesses for Low Anodizing Voltages for Mo and W

Mo

(Specimens labeled with 30-keV Kr^{85})

Anodizing Voltage volts	Sectionings	Integral concentration	Equivalent Voltage volts	Thickness per sectioning $\mu g/cm^2$
1	7	0.387	12.0	2.65
3	5	0.303	23.2	6.05
6	4	0.20	43.2	12.8
8	3	0.212	40.1	16.0
10	3	0.182	48.0	18.8

W

(Specimens labeled with 10-keV Kr^{85})

Anodizing Voltage volts	Sectionings	Integral concentration	Equivalent Voltage volts	Thickness per sectioning $\mu g/cm^2$
1	10	0.326	15.4	2.30
2	8	0.214	23.7	4.00
4	5	0.205	25.0	6.70
6	5	0.140	36.2	9.10
8	3	0.183	28.4	12.4
10	2	0.246	19.8	13.6
12	3	0.115	42.2	17.4

Table 4-6

Metal-removal Thicknesses for Low Anodizing Voltages for Nb and Ta

(Specimens labeled with 10-keV Kr^{85})

Nb

Anodizing Voltage volts	Sectionings	Integral Concentration	Equivalent Voltage volts	Thickness per sectioning $\mu g/cm^2$
1	9	0.180	24.8	1.28
2	7	0.162	26.8	1.77
4	6	0.118	32.8	2.50
6	3	0.180	24.8	3.84
8	3	0.126	31.6	4.80
10	3	0.103	35.4	5.30
12	2	0.143	29.2	6.70
15	2	0.105	35.0	7.90

Ta

Anodizing Voltage volts	Sectionings	Integral Concentration	Equivalent Voltage volts	Thickness per sectioning $\mu g/cm^2$
1	15	0.358	20.0	0.875
2	10	0.247	32.4	1.88
4	4	0.315	24.4	3.78
6	4	0.260	30.8	4.50
8	3	0.263	30.4	5.95
10	3	0.180	42.8	7.84
15	3	0.115	58.0	10.1
20	2	0.147	49.6	13.3

4.4.3 Film Thickness at Low Voltages: Two methods have been used, one based on radioactive labeling and the other on ellipsometry to indicate the possibilites that exist in determining thicknesses for very thin films. Since the main emphasis in this work is on metal removal rather than on film formation per se, the latter was not investigated in detail.

4.4.3A Using Ellipsometry: Thicknesses of anodic films formed on Mo were determined using ellipsometry. Six specimens were examined with the refractive indices assumed (Rowe, 1970) as

$$n_{Mo} = 3.14 - i\ 3.60$$

$$n_{film} = 1.55$$

The thicknesses thus obtained are as follows in Table 4-7

Table 4-7

Determination of Thin-Film Thicknesses Using Ellipsometry

Voltage	Thickness, Å	Thickness, μg/cm^{2}*
Air-formed	31±2	<1.45
4 volts	127±4	<5.95
6 volts	219±5	<10.3

*ρ assumed to be 4.69 g/cm^{3} as for crystalline MoO_3; the actual density is necessarily less if the film is amorphous MoO_3.

4.4.3B Using Radioactive Labeling: This method is related to the one described for metal-removal thickness in section 4.4.2. It may be considered as an alternative to ellipsometry but without the latter's drawbacks regarding the assumption of uniform refractive indices throughout the thickness of the film. Moreover, ellipsometry requires the knowledge of optical constants which are seldom available for anodic films and even lack for many metals (Landolt-Bornstein, 1962) . It will emerge that the method is better in principle than in practice due to the structural changes involved in the present case which were not at first appreciated. As already stated, this method was not applied in detail, with all the work being done for V alone.

Anodic films on V were formed at 2 to 15 volts and the specimens were only then labeled with 20-keV or 40-keV Kr^{85} ions to a dose of about 1.5×10^{14} ions/cm^2 (higher doses lead to a partial sputtering of the films as will be described in chapter 8). The Kr^{85} activity was now measured before and after dissolving the films in 1% KOH with results given in Table 4-8. The basis of the film thickness determination lies in assuming that the fractional activity C^{int} transmitted through an amorphous film of thickness x is given, according to amorphous stopping theory (Lindhard et al.,1963) by

$$C^{int} \approx \frac{1}{2}\,\mathrm{erfc}\left[\frac{\langle x - R_p\rangle}{2^{1/2}\cdot\langle\Delta R_p\rangle}\right]\cdot f(x)$$

$$\approx \frac{1}{2}\,\mathrm{erfc}[A'x - B'].$$

Table 4-8

Results of Transmission Experiments

Anodizing Voltage Volts	$C^{int.}$ 20-keV	$C^{int.}$ 40-keV	Mean $C^{int.}$ 20-keV	Mean $C^{int.}$ 40-keV
2	0.707;0,703	0.982;0.984	0.705	0.983
3	0.610;0.617	0.959;0.974	0.614	0.967
4	0.515;0.539;0.557	0.925;0.952;0.962	0.537	0.946
4.5	-	0.84	-	0.84
5	0.283;0.277	0.785;0.814	0.280	0.80
6	0.134;0.152	0.603;0.611;0.673	0.143	0.629
7	0.0517;0.0565	0.441;0.459	0.0541	0.45
8	0.301;0.0335	0.243;0.243;0.249	0.0318	0.245
9	0.0158;0.0183	0.166;0.169;0.175	0.017	0.170
10	0.0108;0.0111	0.089;0.105	0.010	0.0968
11	-	0.0474;0.0595	-	0.0535
12	-	0.0325;0.0353; 0.0381	-	0.0353
13	-	0.0167;0.0168	-	0.0168
15	-	0.0037;0.0038	-	0.0038

Here, $C^{int.}(x)$ stands for integral concentration at x(i.e. fractional transmission of activity beyond x), $\langle R_p \rangle$ is the mean projected range, $\langle \Delta R_p \rangle$ is the mean square projected standard deviation, and f(x) is a factor [see Kelly and Reid (1973) for its form] which has been taken here as unity. This latter simplification is seen from fig. 4-21 to be a valid approximation when $\langle (\frac{x-\langle R_p \rangle}{\langle \Delta R_p \rangle}) \rangle$ lies between -2 and +2, i.e. for (0.02<$C^{int.}$<0.98). This means that, provided the relation for film thickness at low voltages is of the type

$$x = A'' + B'' \text{ volts}$$

the fractional transmission experiments can be plotted to yield straight lines by using the relation

$$\begin{aligned} \text{erf}^{-1}[1-2\,C^{int.}(x)] &= A'x - B' \\ &= A' \cdot B'' \text{ volts} + A' \cdot A'' - B' \\ &= A \cdot \text{volts} + B \end{aligned}$$

where erf^{-1} stands for inverse error function. The results are shown in fig. 4-22 and serve to establish the fact that the thickness-voltage relationship is "well-behaved" starting at about 3 volts, that there is a discontinuity in thickness and/or range at 7.5±0.5 volts, and that the slopes are given by

$$\frac{\text{slope for} < 7.5 \text{ volts}}{\text{slope for} > 7.5 \text{ volts}} = 1.83 \pm 0.04 \ .$$

This along with the equation for higher voltages (section 4.3.3) is in principle sufficient information to allow the

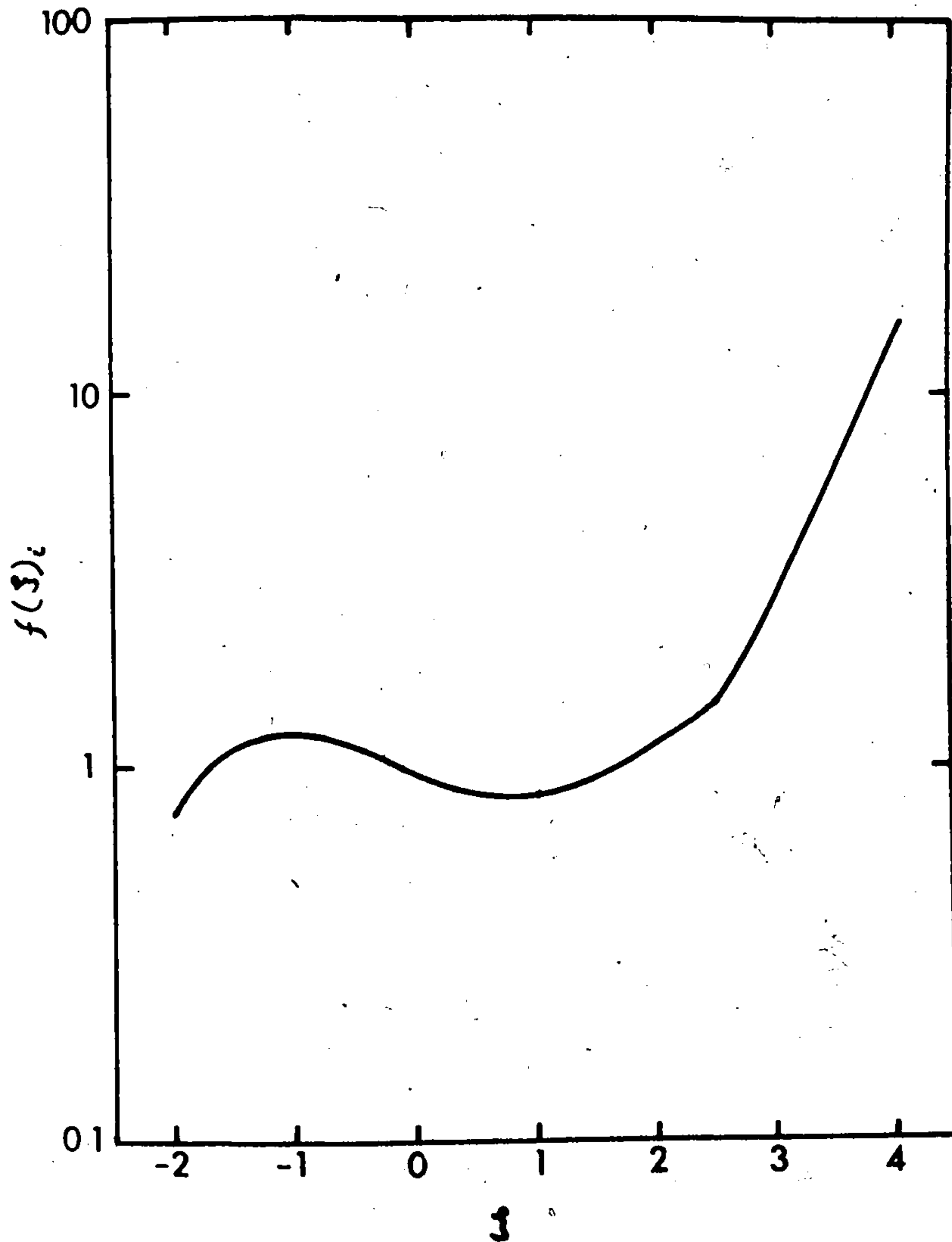

Fig. 4-21 Variation of $f(\xi)_i$ with ξ (after Reid and Kelly, 1973)

Fig. 4-22 Relation between oxide thickness of V and the quantity $erf^{-1}[1-2C^{int.}(x)]$

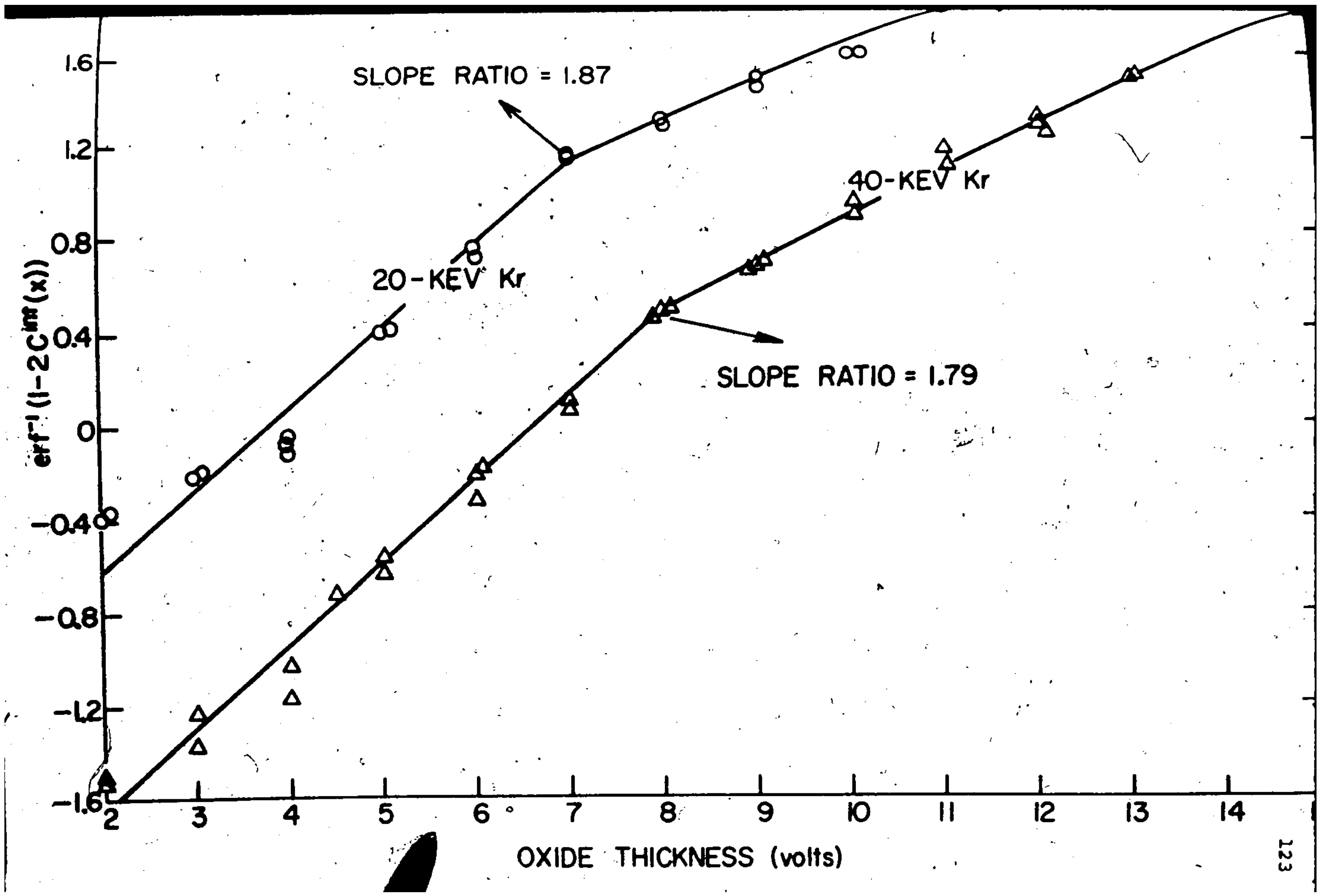
SLOPE RATIO = 1.87
20-KEV Kr
40-KEV Kr
SLOPE RATIO = 1.79
erf⁻¹ (1-2C^inf(x))
1.6
1.2
0.8
0.4
0
-0.4
-0.8
-1.2
-1.6
2
3
4
5
6
7
8
9
10
11
12
13
14
OXIDE THICKNESS (volts)

constants A^* and B^* to be determined at low voltages, the result apparently being

Film thickness for V = (-5.1+2.09 volts) μg/cm^2 for 3 to 7.5 volts

It is assumed to be obvious that the negative term does not imply a negative film thickness for a non-anodized specimen.

The problem is that, as will be shown in chapter 5, the anodic film on V is crystalline at low voltages ($\lesssim$ 7 volts). There is therefore a discontinuity in the range parameters and the present analysis fails to identify an explicit discontinuity in the thickness calibration. This is evidently a fairly general problem, applying not only to V but also at least to Mo, Ta and W, and will affect ellipsometry to a similar extent. The method may however still prove to have a unique importance - namely in pinpointing the thickness at which anodic films become amorphous.

4.5 Effect of Radiation Damage on Thickness Calibrations:

All calibrations except those involving small thicknesses of metal removal (section 4.4.2) were made with unbombarded specimens. One of the major applications of anodic sectioning is in the field of ion implantation which may require the bombardment of specimens before anodizing. To investigate whether ion bombardment causes a change in thickness calibrations of V and Mo, twelve specimens of each metal were implanted with 10-keV Kr to various doses and were then anodized at 40 volts. After making suitable corrections for the mass of the implanted Kr, it was found that, to within an uncertainty of about 5% there was no effect of the radiation

damage on the thickness calibrations (Table 4-9) except perhaps at the highest doses (4×10^{17} ions/cm^2). Such a result was also obtained by Davies et al. (1964) for Si and Anderson (1969) for Cu and is probably rather general.

Table 4-9

Effect of Radiation Damage on Thickness Calibrations of V and Mo

Kr dose	Metal Removed in a 10-volt Sectioning, μg/cm^2 V	Mo
zero	30.9±0.3	47.9±0.50
5×10^{15}	33.8±0.7	47.0±0.5
4×10^{16}	32.7±0.2	48.4±1.2
4×10^{17}	35.0±0.0	42.4±0.9

4.6 Summary:

The anodic sectioning of V, Mo, W, Nb and Ta has been described in this chapter. Conditions were established such that anodic films could be removed from the surfaces of the metals using KOH and with excellent "dissolution end-points" being obtained.

Thicknesses for metal-removal and film-formed had to be determined separately due variously to film dissolution during anodizing (V, Mo) and to the doped nature of films

(Nb,Ta). It was also found that, in the case of V and Mo, due to the instability of the anodic film combined with the low conductivity of the electrolyte used, the thickness calibrations were affected by minor details such as stirring and electrode spacing. Current and temperature variation may also have played unexpected roles, though were not studied. The use of standard anodizing conditions with respect to all these details, however, enabled quite reproducible results to be obtained.

Due to the excellent "dissolution end-points" and the ease of film removal, thickness calibrations for films formed at high voltages ($\geq$ 10 volts) were made using the direct and conventional gravimetric method. But the thin-film region ($\leq$ 10 $\mu g/cm^2$) is more important in anodic sectioning and it was in this thickness region that serious difficulties arose. A new method, using radioactive labeling, was developed such that the thicknesses of thin films could in principle be estimated as a proportion of those for thick films and the results thus obtained were quite reproducible. For film thicknesses, the method fails for an unexpected reason, however: the anodic films on V, Mo, Ta and W are crystalline at low voltages and there is therefore a discontinuity in the range parameters. In hindsight, the method is still important, however, in that it provides an enormously sensitive means for determining the thickness at which the films become amorphous. Since

the metals were bombarded with high energy ions prior to anodizing, the effect of radiation damage was also investigated for V and Mo, and no significant influence on thickness calibrations was observed for doses up to and including 4×10^{16} ions/cm^2. This result, similar to that obtained by other workers for Cu and Si, is expected to be rather general.

When this work was initiated, good anodic sectioning techniques were available for only two metals, Al and W. In this chapter, similar sectioning procedures have been described for four additional metals, V, Mo, Nb and Ta, and the behaviour of W has been reconsidered. With W, the use of an acetic-acid-based electrolyte enables sectioning up to 140 volts (metal-removal thickness ~830 Å) instead of 75 volts (~ 400 Å); similarly, much greater film thicknesses, essential for ion-transmission-experiments, are possible with the method described here. In Table 4-10 the sectioning behaviour of the six metals so far perfected is summarized.

The thickness calibrations enabled the film stoichiometries to be inferred as V_2O_5, MoO_3, WO_3, Nb_2O_5, and Ta_2O_5 and it was found that doping occurred moderately with Nb and more significantly with Ta for sulphate-based electrolytes. Results on doping obtained in this chapter were in agreement with the conclusions derived from the kinetic data of section 3.5.5 as well as with the work of Amsel et al. (1969). But the evidence on film stoichiometries as presented here (as

Table 4-10

Minimum and Maximum Metal-Removal Thicknesses for a Single Sectioning

Metal	Minimum Thickness (1) Å	Maximum Voltage Volts	Maximum Thickness Å	Reference
Al	30	400	3500	Davies (1960)
V	50	100	1200	here
Nb	15	70	650	here
Mo	30	110	1200	here
Ta	10	100	360	here
W	10	75	400	McCargo (1963)
	15	140	830	here

(1) This was taken as the metal-removal for a 1-volt sectioning.

well as in section 3.5.5) is only indirect and the more direct method of observation by electron microscopy has also been employed. The results of such studies will be described in the next chapter.

CHAPTER 5

CHARACTERIZATION OF ANODIC FILMS

5.1 General:

In previous chapters, certain assumptions were made regarding the stoichiometry of the anodic films on V, Mo, Nb, Ta and W in order to determine the current efficiency of anodization or while determining the differential field strength, E_d. In addition, we recall the change in slope that occurs in the thickness calibration which may be related either to the mechanism of film growth or to the nature of the anodic films. Thus, a knowledge of the stoichiometry of the anodic films becomes essential but these films are generally amorphous as formed and present problems in establishing their stoichiometry. Recently, the amorphous anodic films on Al (Takamura et al, 1970) and Ta (Kiharo-Morishita, 1970) have been identified as Al_2O_3 and Ta_2O_5 respectively using infra-red reflectance spectroscopy but the more widely used method has been to crystallize the anodic films, either in air or vacuum, or in an electron-microscope (implying ill-defined temperature and pressure), and then characterize them using either electron- or X-ray diffraction. In our own work, reflection-electron-diffraction has been used and work has been done on as-formed films as well as on thermally

crystallized films. But before describing that, a background will be provided for the work already done on the characterization of anodic films.

5.2 Background:

5.2.1 Ta: A large amount of work on the crystallization of anodic films on Ta is already available. Vermilyea (1953) has shown that the anodic films on Ta, whether formed in an aqueous or in a non-aqueous electrolyte, are amorphous and crystallize to orthorhombic β-Ta_2O_5 between 500-800°C in a vacuum of 10^{-5} torr. Essentially similar results were obtained by Draper and Harvey (1963c) who heated anodized Ta in air. Calvert and Draper (1962) heated the Ta anodic films in a vacuum of 10^{-5} torr and confirmed the formation of orthorhombic β-Ta_2O_5 but, in addition, they found the crystallization temperature to depend on the electrolyte. Harvey and Wilman (1961) crystallized anodized Ta in air and in a vacuum of 10^{-5} torr and found that there was no difference in the crystallization product, which they think is pseudo-hexagonal in the initial stages but finally has the orthorhombic structure of β-Ta_2O_5. In their case, Harvey and Wilman found that the observed weak lines did not correspond well with the previous data and concluded that "one or both of the hexagonal and orthorhombic structures correspond to a non-stoichiometric composition near Ta_2O_5 with a slight excess or deficiency of oxygen". Similar work on anodic films on Ta has also been

carried out by several other workers such as by Pawel and Lundy (1964), who crystallized anodized Ta in air, vacuum and in the microscope, or by Calbrick and Schwartz (1962) and Aladjem et al. (1970) who crystallized the films in the microscope and once again found the crystallized product to be β-Ta_2O_5. The consensus thus seems to be that the amorphous anodic film on Ta is Ta_2O_5 and that it yields β-Ta_2O_5 when crystallized either in air or in vacuum.

5.2.2 Nb: The anodic films formed on Nb have also been found to be amorphous (Draper and Harvey, 1963c) and to crystallize on heating in air at 590°C for 30 minutes to Nb_2O_5. Lakhiani and Shreir (1960) anodized Nb at high temperatures, $\geq$ 50°C, and found the as-formed film to be a crystalline form of Nb_2O_5. Pawel and Campbell (1964) crystallized the stripped anodic films in vacuum and in air and found the crystallized product to be Nb_2O_5 without giving any further details. Aladjem et al. (1970) crystallized the anodic films on Nb in the electron microscope and observed a pseudo-hexagonal form of Nb_2O_5 related to the low temperature γ-phase. The overall result is thus similar to Ta, namely that the amorphous anodic film on Nb is Nb_2O_5 and yields γ-Nb_2O_5 when crystallized either in air or in vacuum though requires lower temperatures than Ta_2O_5 for crystallization.

5.2.3 W, V and Mo: In the case of anodic films on W, V, and Mo, little work has been carried out with a view to characterization. Aladjem et al. (1970) crystallized anodic film removed from tungsten in an electron microscope and found the product to be made up of monoclinic WO_2 and β-$WO_{2.9}$. Lam (1971) found that the anodic film on W crystallized at about 400°C when heated in air for 15 minutes but did not identify the product. Piercy (1964) found that when the anodic film on W was about 130-160 Å thick, it was crystalline (and not amorphous as expected) with the structure being mainly WO_3 but with traces of WO_2. Thus, there is an inconsistency between the results of Aladjem et al. (1970) and Piercy (1964) regarding the stoichiometry of the anodic film on W.

With V, Keil and Salomon (1968) employed attenuated total reflectance (ATR) spectra and electron paramagnetic resonance (EPR) spectra to infer that the anodic film was close to VO_2 in composition. This result must be treated with caution, however, as the approach used was highly indirect. With Mo, only one previous work is available, namely that of Ikonopisov (1962/73) in which the initial film, when very thin, is proposed on the basis of its dark colour and the constant values of the potential (as might be expected for a semiconducting film) to be "MoO_2 or some intermediate oxide Mo_nO_{3n-1} (all of which are semiconducting and black in colour".

Beyond a critical thickness, however, this semiconducting film is argued to be converted into MoO_3 since the latter is the only oxide of Mo which is an insulator and thus would permit anodic film growth.

It is seen from the above discussion that the anodic films formed on Ta and Nb have been extensively studied and the results obtained by various workers are quite consistent. However, in the case of W, the results of Aladjem et al. (1970) and Piercy (1964) do not agree whereas reliable information is not at all available about the nature of anodic films formed on V and Mo. Thus, more work on the identification of anodic films formed on these three metals is required. Results for Nb and Ta are also considered, however, in view of the change in the thickness calibration slopes in the thin-film region as described in chapter 4.

5.3 Experimental Results and Discussion:

5.3.1 General: From the previous chapter, one can make two observations. In the calibrations of thick films (section 4.3.3), we have found both the metal-removal and film-formation thicknesses. This means that, without any significant assumptions, one can estimate the stoichiometry of the anodic films on V, Mo and W to be V_2O_5, MoO_3 and WO_3 respectively. The films on Nb and Ta are probably Nb_2O_5 and Ta_2O_5 but with significant doping, as evidenced both by the $\frac{dV}{dt}$ data (section 3.5.4) and the gravimetric data (section 4.3.4). A second point to note is the discontinuity in the thickness calibrations such that the

slopes at lower potentials are higher than those at higher voltages, as summarized in Table 5-1. The cause of such a

TABLE 5-1

Thickness vs. Voltage Slopes at Low and High Voltages

	Slope at low voltage	Slope at high voltage	Voltage of Discontinuity Volts
V	1.43	0.634	4
Mo	1.75	1.05	7.5
W	1.33	1.10	7
Nb	0.462	0.42	8
Ta	0.641	0.455	15

discontinuity in the thickness calibration, which is present to some extent in all cases under study, has to be investigated in view of a possible relation to the nature of films.

5.3.2 Anodic Films As-Formed: When thick anodic films (> 200 Å) were observed under reflection-electron-diffraction using a Philips 300 EM electron microscope, they were found to show halos, and hence were concluded to be amorphous in nature (fig. 5-1). However, when thin films (≤ 200 Å) were observed, all the metals under study except Nb, which still showed halos, had crystalline ring patterns (fig. 5-2). Such a result of thin films being crystalline is similar to that obtained by Piercy (1964) who found that the anodic films formed

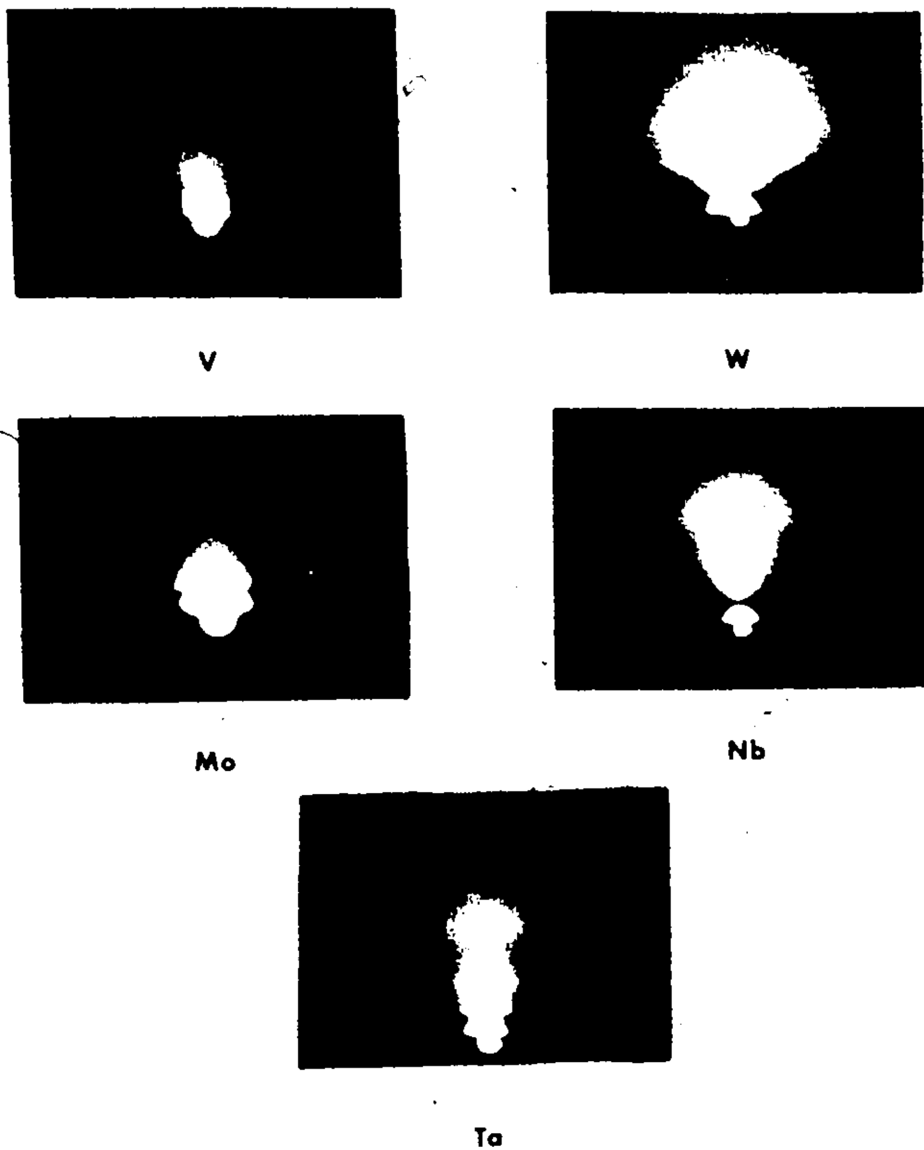

Fig. 5-1 Electron Diffraction Patterns of as-formed Thick Anodic Films (≥ 200 Å)

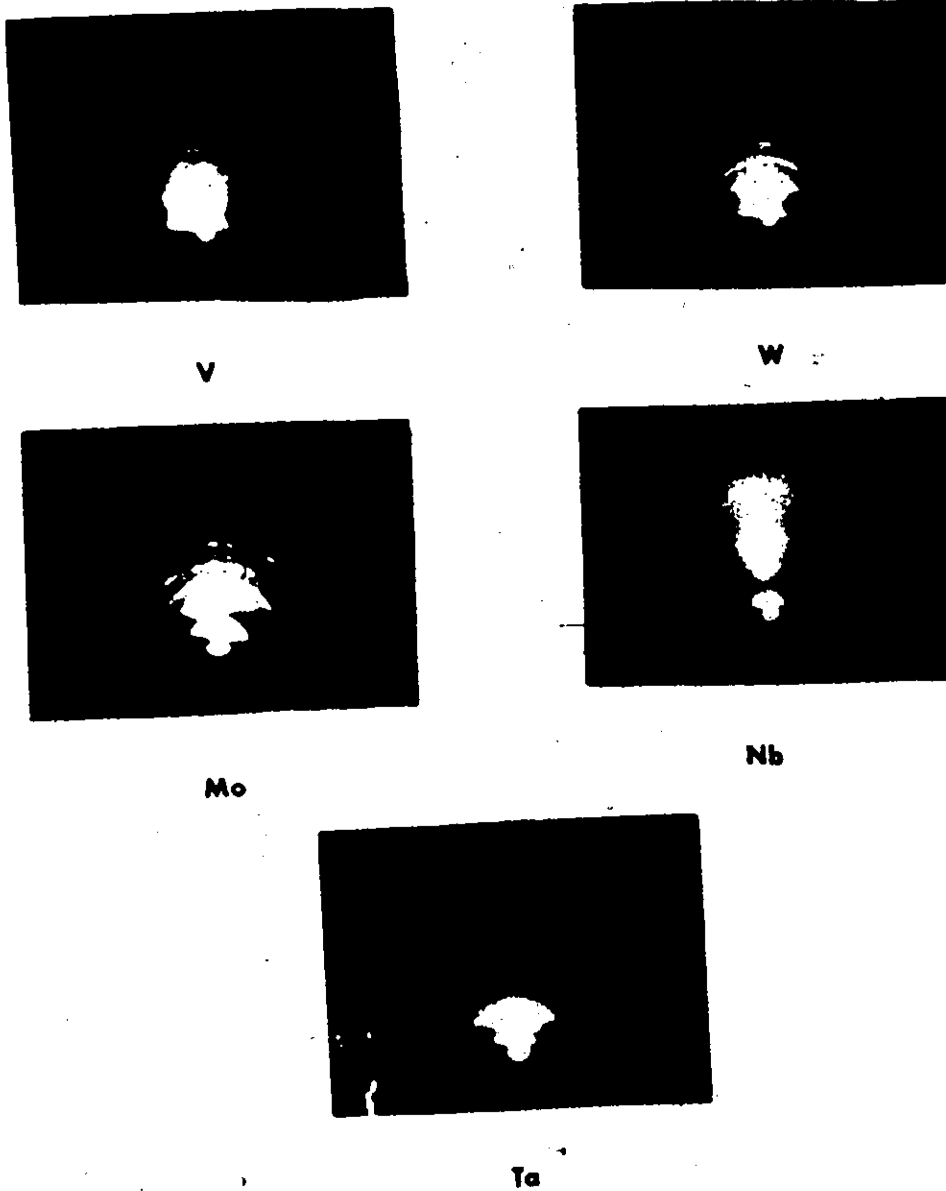

Fig. 5-2 Reflection-Electron-Diffraction Patterns of as-formed Thin Anodic Films($\lesssim 200 Å$)

on W in the 130-160 Å range were crystalline in nature. The diffraction patterns obtained for V, Mo, W and Ta were analyzed with results as given in Tables 5-2 to 5-5, and show that the films on Mo, W and Ta mainly consisted of MoO_3, WO_3, and β-Ta_2O_5. With V, no final decision could be reached though of all the available data, the pattern obtained for V corresponded best with Vanadium Hydrogen Oxide ($H_6V_4O_{12}$).

Vermilyea (1955), in his work with field-induced crystallization of anodic films on Ta, found that the thickness of a crystalline anodic film formed at a given voltage is much greater than the corresponding thickness of an amorphous film, i.e., the field required for the growth of a crystalline anodic film is much smaller. Such a behaviour may be explained either by assuming that the crystalline films permit the ionic motion more easily or by assuming that the ionic current is given by the relation

$$i = i_o \exp\left(\frac{qaVK}{kTx}\right)$$

where K is similar to $\left(\frac{\varepsilon+2}{3}\right)$, and ε is the dielectric constant, and depends on the nature of anodic films; K is apparently larger for crystalline films than for amorphous films if the example of Al_2O_3 is typical*. The latter argument implies the validity of Lorentz field within the film rather than the

*According to Young (1961), n of crystalline Al_2O_3 is 1.76 while that of anodic Al_2O_3 is 1.64; ε of crystalline Al_2O_3 should also be correspondingly greater than that of anodic Al_2O_3.

Table 5-2

Electron Diffraction Data for As-Formed Anodized V (6 volts)

Experimental		$(H_6V_4O_{12}$ (ASTM 13-163)	
I/I$_o$*	d,Å	d,Å	I/I$_o$
–	–	6.04	4
–	–	4.80	100
–	–	4.73	4
–	–	4.05	50
–	–	3.87	48
w	3.51	3.51	12
–	–	3.18	2
m	3.03	3.02	25
–	–	2.91	4
wm	2.72	2.74	6
wm	2.36 (doublet)	2.44	25
–	–	2.39	4
–	–	2.22	4
w	2.14	2.12	4
–	–	2.071	4
–	–	2.010	4
m	1.91	1.959	18
–	–	1.878	4
wm	1.75	1.815	12
–	–	1.788	4
–	–	1.686	6
–	–	1.662	4

*w = weak; m = medium; s = strong

Table 5-3

Electron Diffraction Data for As-Formed Anodized Mo (6 volts)

Experimental		MoO_3 (ASTM 5-0508)	
I/I_o	d,Å	d,Å	I/I_o
-	-	6.93	34
-	-	3.81	82
-	-	3.46	61
ms	3.30	3.26	100
w	3.00	3.006	13
-	-	2.702	19
-	-	2.655	35
-	-	2.607	6
m	2.50	2.527	12
w	2.39	2.332	12
wm	2.27	2.309	31
		2.271	18
w	2.09	2.131	9
wm	1.965	1.996	4
		1.982	13
		1.960	17
wm	1.875	1.849	21
		1.821	11
w	1.745	1.771	5
		1.756	5
		1.733	17
m	1.67	1.693	8
		1.663	13
		1.631	13

Table 5-4

Electron Diffraction Data for As-Formed Anodized W (6 volts)

Experimental		Monoclinic WO_3 (ASTM 5-0363)	
I/I_o	d, Å	d, Å	I/I_o
-	-	3.835	100
-	-	3.762	95
-	-	3.642	100
ms	3.40	3.408	5
		3.339	50
w	3.10	3.106	50
		3.073	50
s	2.58	2.681	75
		2.659	60
		2.615	90
w	2.14	2.170	50
		2.147	60
m	1.98	1.989	35
		1.964	30
w	1.90	1.916	50
		1.877	50
wm	1.765	1.818	75
		1.805	40
		1.791	50
w	1.665	1.705	60
		1.686	55
		1.645	25

Table 5-5

Electron Diffraction Data for As-Formed Anodized Ta (10 volts)

Experimental I/I$_o$	Experimental d,Å	β-Ta_2O_5 (ASTM 8-255) d,Å	β-Ta_2O_5 (ASTM 8-255) I/I$_o$
-	-	3.87	90
-	-	3.36	10
s	3.17	3.15	100
		3.09	50
w	2.53	2.55	20
		2.46	100
-	-	2.43	60
-	-	2.36	20
w	2.17	2.11	10
s	1.96	2.02	30
		1.95	50
-	-	1.83	40
-	-	1.80	40
m	1.71	1.76	20
		1.71	10
		1.68	10
		1.661	100
-	-	1.655	40
-	-	1.632	30
w	1.55	1.582	30
		1.551	30

Maxwell field, and is essentially equivalent to that successfully employed in explaining the kinetic data in terms of how doping affects $\frac{dV}{dt}$ (section 3.5.4). Thus, a larger value of K for crystalline films, with all the other factors being fixed, leads to a larger value of x for a given current. If one accepts the results of Vermilyea to be rather general, then the initially larger slopes in the thin-film region for V, Mo, W and Ta are quite consistent with these films being crystalline. With Nb, however, even thin films showed halos and no distinction between the thin and thick film patterns could be detected. But a closer examination of the discontinuity with Nb shows that the change of slope is only marginal, being in fact nearly undetectable (Table 5.1). The behaviour of all five metals is thus remarkably consistent.

5.3.3 Thermally Crystallized Films in Air: Since the anodic films formed on Nb and Ta have already been studied in great detail, they were not studied beyond what has been given in section 5.3.2. In continued work with V, Mo and W, the as-formed thick films were thermally crystallized in air, and then observed under reflection electron diffraction. The heatings were in all cases with the films still on the metal substrates and were carried out for 10 minutes, with crystallization temperatures as given in Table 5-6. The diffraction patterns observed for air heatings are shown in fig. 5-3. These patterns were analysed, with results as given in Tables

TABLE 5-6

Crystallization Temperatures of Anodic Films on V, Mo and W

Metal	Crystallization Temperatures, °C air	Vacuum
V	∿400	∿300
Mo	∿325	∿300
W	∿450	∿425

5-7 to 5-9, and show that the crystallized films can be identified as V_2O_5, MoO_3, and WO_3. There is apparently thus good agreement with the results obtained in the previous chapter based on the metal-removal and film-formation thicknesses (Table 4-3). We would emphasize that the agreement is only "apparent", since as will be discussed subsequently, air-heating will have an obvious tendency to oxidize films.

All the above information was obtained by operating the Philips electron microscope EM300 at 80 to 100 keV. The penetration of electrons at such energies is limited and the information obtained is only from a surface layer of about 100 Å thick. Therefore, the conclusions about the nature of these films are not only in doubt because of possible oxidation during the air heating but are also limited only to a surface layer.

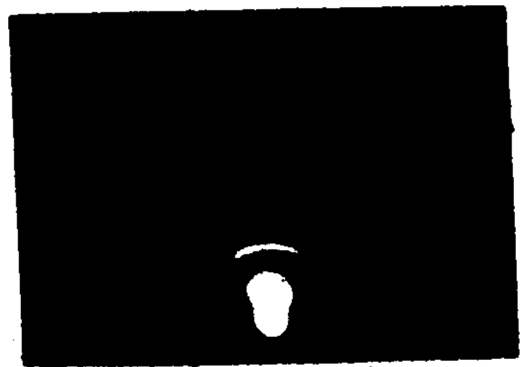

V

Mo

W

Fig. 5-3 Reflection-electron-diffraction patterns of air-heated anodic films

Table 5-7

Air-Heating of Anodic Film on V at 425°C

Experimental		V_2O_5 (ASTM 9-387)	
I/I$_o$	d,Å	d,Å	I/I$_o$
	–	5.76	40
	–[a]	4.38	100
	–[a]	4.09	35
s	3.26	3.40	90
m	3.11		
m	2.83	2.88	65
		2.76	35
ms	2.68	2.687	15
		2.61	40
w	2.39	2.492	7
		2.405	7
wm	2.22	2.185	17
		2.147	11
w	2.01	1.992	17
	–	1.919	25
		1.900	17
w	1.83	1.864	13
		1.84	5
wm	1.78	1.78	3
		1.76	30
w	1.65	1.65	11
		1.63	7

(continued)

Table 5-7 (continued)

Experimental		V_2O_5 (ASTM 9-387)	
I/I$_o$	d,Å	d,Å	I/I$_o$
wm	1.52	1.58	9
		1.56	11
		1.54	9
m	1.47	1.51	17
		1.49	17
w	1.45	1.44	7
		1.41	7

[a]Not observable with the equipment available due to the direct beam.

Table 5-8

Air-Heating of Anodic Film on Mo at 400°C

Experimental		MoO_3 (ASTM 5-0339)	
I/I_o	d,Å	d,Å	I/I_o
	–[a]	6.93	34
ms	3.80	3.81	82
	–	3.46	61
s	3.26	3.26	100
	3.08	3.006	13
m	2.67	2.702	19
		2.655	25
		2.607	6
	–	2.52	12
m	2.35	2.332	12
		2.309	31
		2.271	18
w	2.18	2.13	9
wm	2.01	1.996	4
		1.982	13
		1.960	17
w	1.88	1.849	21
m	1.78	1.821	11
		1.771	5
		1.756	5
		1.733	

(continued)

Table 5-8 (continued)

Experimental		MoO_3 (ASTM 5-0339)	
I/I_o	d,Å	d,Å	I/I_o
		1.693	8
		1.663	13
m	1.63	1.631	13
		1.597	15
		1.587	6
		1.569	16
w	1.52	1.504	5

[a]Not observable with the equipment available due to the direct beam.

Table 5-9

Air-Heating of Anodic Film on W at 425°C

Experimental		Monoclinic WO_3 (ASTM 5-0363)		WO_3 (Lieberman et al., 1969)	
I/I_o	d,Å	d,Å	I/I_o	d,Å	I/I_o
	–[a]	3.835	100	3.829	82
s	3.69	3.762	95	3.658	100
		3.642	100		
	–	3.411	5	–	–
m	3.33	3.342	50	3.35	4
wm	3.14	3.109	50	3.077	18
		3.076	50		
m	2.68	2.684	75	2.626	40
		2.661	60		
		2.617	90		
	–	2.528	35	–	–
	–	2.509	40		
s	2.24	2.172	50	2.15	14
		2.149	60		
	–	2.098	10		
m	2.03	2.038	40	1.975	4
		2.020	30		
		2.011	25		
		1.991	35		
		1.966	30		
–		1.917	50	1.912	4
ms	1.85	1.879	50	1.824	10
		1.82	50		
		1.807	75		
		1.793	40	1.794	8

(continued)

Table 5-9 (continued)

Experimental		Monoclinic WO_3 (ASTM-50363)		WO_3 Lieberman et al. (1969)	
I/I_o	d,Å	d,Å	I/I_o	d,Å	I/I_o
		1.707	60		
		1.687	55		
m	1.69	1.654	50	1.69	5
		1.646	40		
		1.638	25	1.64	11
		1.593	10		
wm	1.54	1.580	10	1.504	4
		1.554	30		

[a]Not observable with the equipment available due to the direct beam.

In fact, one does not really expect the anodic films to be totally uniform throughout their thicknesses due to the possibility of minor variations in stoichiometry. For example, Vermilyea (1965) found that when as little as 0.01% H_2O_2 is added to dilute acids (e.g. 1% HNO_3 or 1% H_2SO_4), the electronic conductivity of anodic films on Nb and Ta decreases by several orders of magnitude. This effect follows naturally from a slight non-stoichiometry due to a deficiency of anions, such that the presence of H_2O_2 oxidizes the films to the pentavalent state. Similar results were also obtained by Harvey and Wilman (1961), who crystallized the anodic films on Ta in air as well as in vacuum to conclude that the structures obtained corresponded to a non-stoichiometric composition close to Ta_2O_5.

5.3.4 Thermally Crystallized Films in Vacuum: We have already intimated that it is quite possible for the air-heating of anodic films formed on V, Mo and W to have caused slightly non-stoichiometric films to reach their highest oxidation state. This is demonstrated thermodynamically by reactions (i) for V, Mo, and W in Table 5-10 - i.e., the oxygen pressure over V_2O_5, MoO_3, and WO_3 at the temperatures used for crystallization are negligibly small. To circumvent this problem, experiments on thermal crystallization were also carried out in a vacuum of about 10^{-6} torr at the lowest possible crystallization temperatures. The results are shown in Fig. 5-4 and are analyzed

Table 5-10

Thermodynamic Calculations of Possible Oxidation/Reduction Processes

(JANAF Tables, 1970; Kubaschewski et al., 1967)

V Possible reactions when anodized V is heated in vacuum are as follows:

(i) Reduction to $VO_2(s)$

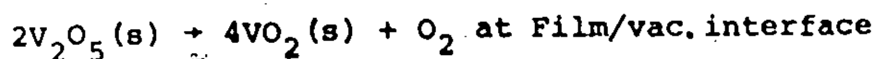

$$2V_2O_5(s) \rightarrow 4VO_2(s) + O_2 \text{ at Film/vac. interface}$$

$$-RT\ell n p_{O_2} = 64{,}480 - 45.6\ T$$

which means that at $T = 573°K$, one needs a vacuum of $\sim 10^{-11}$ torr. Direct reduction to $VO_2(s)$ will therefore not occur.

(ii) Oxidation to $V_2O_5(s)$

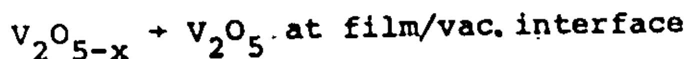

$$V_2O_{5-x} \rightarrow V_2O_5 \text{ at film/vac. interface}$$

While oxidation to $V_2O_5(s)$ is thermodynamically expected, it may not be kinetically possible. The relevant relation is "atoms colliding per unit area" = $\frac{1}{4}$ N<v>t [Dushman and Lafferty, 1962] which has a value of $\sim$ 100 atomic layers for 1×10^{-6} torr and 10 minutes. Since the relation $\frac{1}{4}$ N<v>t gives the upper limit to oxygen uptake, one concludes that oxidation to $V_2O_5(s)$ is just barely possible from a kinetic point of view.

(iii) $xV_2O_5 + y \cdot V \rightarrow zV_6O_{13}$ or zVO_2 at film/metal interface

This reaction is possible at all temperatures, being further supported by the fact that the exchange of isotopically enriched oxygen with V_2O_5 is fairly rapid

(continued)

at 500°C (Jiru and Novákovà, 1963). The overall conclusion is that heating anodized V in vacuum would more likely lead to reduction by process (iii) than oxidation by process (ii).

Mo Again, possible reactions for vacuum heated anodized Mo are as follows:

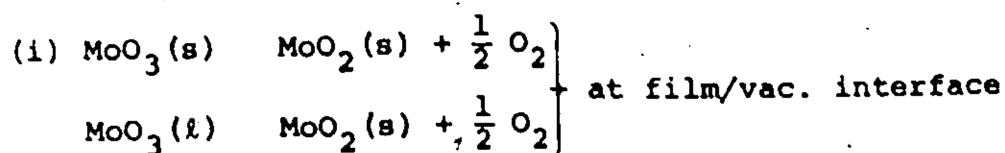

(i) $MoO_3(s) \quad MoO_2(s) + \frac{1}{2} O_2$ } at film/vac. interface
$MoO_3(\ell) \quad MoO_2(s) + \frac{1}{2} O_2$

where thermodynamic values of liquid phase are assumed to correspond to an amorphous structure.

From Janaf tables, one finds that at 600°K, a vacuum of $\sim 10^{-14}$ torr is required for $MoO_3(s)$ and a vacuum of $\sim 10^{-13}$ torr for $MoO_3(\ell)$. Clearly, a direct reduction to $MoO_2(s)$ will not occur.

(ii) $MoO_{3-x} \rightarrow MoO_3$

Again kinetically speaking, this reaction will occur to some extent, the upper limit to which is $\sim$ 100 atom layers. It is therefore just barely possible.

(iii) $Mo + 2MoO_3 \rightarrow 3MoO_2$

Thermodynamically, this reaction is possible at all temperatures and once again the exchange of isotopically enriched oxygen with MoO_3 is fairly rapid at 550°C (Jiru and Norákovà, 1964). Thus, a likely fate for anodized Mo heated at 10^{-6} torr is reaction (iii).

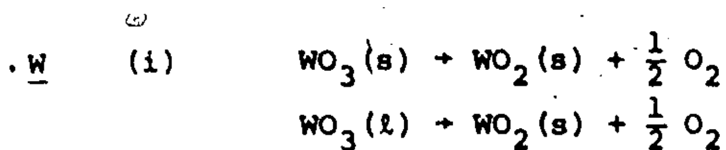

W (i) $$WO_3(s) \rightarrow WO_2(s) + \frac{1}{2} O_2$$
$$WO_3(\ell) \rightarrow WO_2(s) + \frac{1}{2} O_2$$

At 700°K, one requires a vacuum of $\sim 10^{-27}$ torr for $WO_3(s)$ and $\sim 10^{-22}$ torr for $WO_3(\ell)$ for reduction to occur. The above reactions are therefore not favourable for the conditions of temperature and pressure used.

(ii) $$WO_{3-x} \rightarrow WO_3$$

Again, kinetically speaking, this reaction is just barely possible.

(iii) $$W + 2WO_3 \rightarrow 3WO_2$$

Thermodynamically, this reaction is possible at all temperatures but due to the high melting points of WO_3 (1473°C) and thus low inferred oxygen mobility plus a low oxygen exchange rate at 700°C (hence a direct confirmation of low oxygen mobility) it will probably not occur to any great extent.

V

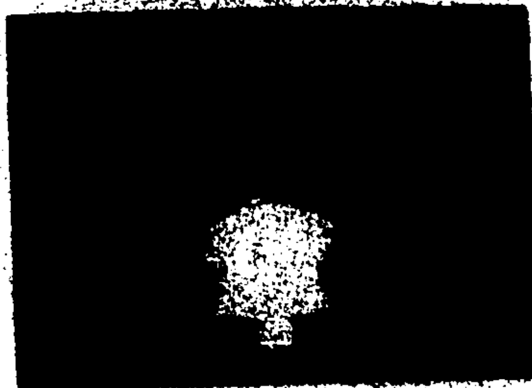

Mo

W

Fig. 5-4 Reflection-electron-diffraction patterns of vacuum-heated anodic films

in Tables 5-11 to 5-13. The pattern obtained with W is again found to be WO_3, whereas with V and Mo, the patterns obtained corresponded closely to the lower oxides V_6O_{13} and MoO_2 respectively. On the basis of thermodynamic calculations in Table 5-10, one concludes that the vacuum heating was probably prevented kinetically from oxidizing the anodic films but that with V and Mo reactions of the type oxide+metal → lower oxide were possible. This means that the films on W are almost certainly WO_3 whereas the films on V and Mo have stoichiometries which are undefined in a crystallization experiment. The arguments based on thickness calibrations are, however, not limited in this way and in fact suggest that the films on V and Mo are V_2O_5 and MoO_3 respectively.

5.4 On the Occurrence of V_6O_{13} and MoO_2

When the anodic films on V and Mo were heated to about 300-450°C in vacuum, the films were found to be V_6O_{13} and MoO_2 respectively. When these films were next heated in air to about 425°C, they became V_2O_5 and MoO_3, and this transition between V_6O_{13} and V_2O_5 on one hand and MoO_2 and MoO_3 on the other could be carried on repeatedly by a suitable choice of heating medium. Two conclusions follow. Firstly, it is implied that there is no stable structure either between V_6O_{13} and V_2O_5 or between MoO_2 and MoO_3 at 300-450°C even though V_3O_7 has been detected by some workers (Anderson et al., 1970; Kosuge, 1967; Sata, 1968). Secondly, it is shown that

Table 5-11

Vacuum Heating of Anodic Film on V at 300°C

Experimental		V_6O_{13} (Theobold et al. (1968))	
I/I_o	d,Å	d,Å	I/I_o
-	-[a]	5.85	20
m-s	3.52	3.52	100
w-m	2.96	2.96	20
m	2.64	2.67	30
m	2.00	1.99	60
m-s	1.84	1.85	80
m	1.67	-	-
m	1.55	1.56	10
		1.55	30
m	1.43		
m	1.35		

[a]Not observable with the equipment available due to the direct beam.

Table 5-12

Vacuum Heating of Anodic Film on Mo at 300°C

Experimental		MoO_2 (ASTM-0452)	
I/I_o	d,Å	d,Å	I/I_o
	–[a]	4.78	20
	–[a]	3.41	100
m	2.86	2.804	30
s	2.47	2.433	50
		2.420	85
		2.405	40
		2.397	50
w	2.21	2.176	30
		2.171	10
ms	2.09	2.147	30
w	1.825	1.833	35
wm	1.69	1.718	55
		1.704	80
		1.692	50
m	1.605	1.597	10
s	1.485	1.540	25
		1.530	40
		1.522	35
		1.463	25

[a]Not observable with the equipment available due to the direct beam.

Table 5-13

Vacuum Heating of Anodic Film on W at 425°C

Experimental		WO_3 (Lieberman, 1969)		Monoclinic WO_3 (ASTM 5-0363)	
I/I_o	d, Å	d, Å	I/I_o	d, Å	I/I_o
s	3.84	3.829	82	3.835	100
	–	–	–	3.762	95
s	3.63	3.658	100	3.642	100
	–	–	–	3.411	5
w	3.37	3.35	4	3.342	50
w	3.11	3.077	18	3.109	50
				3.076	50
ms	2.68	2.626	40	2.684	75
				2.661	60
				2.617	90
w	2.50	–	–	2.528	35
				2.509	40
w	2.16	2.15	14	2.172	50
				2.149	60
w	2.06	–	–	2.098	10
	–	1.975	4	2.039	40
				2.020	30
				2.011	25
				1.991	35
				1.966	30
m	1.87	1.912	4	1.917	50
				1.879	50

(continued next page)

Table 5-13 (continued)

Experimental		WO_3 (Lieberman, 1969)		Monoclinic WO_3 (ASTM 5-0363)	
I/I$_o$	d,Å	d,Å	I/I$_o$	d,Å	I/I$_o$
		1.824	10	1.82	50
				1.807	75
		1.794	8	1.793	40
				1.707	60
				1.687	55
ms	1.70	1.69	5	1.654	50
				1.646	40
				1.638	25
		1.64	5	1.593	10
				1.580	10
wm	1.56	1.504	4	1.554	30

V_6O_{13} and MoO_2 are stable in the temperature range of 300-450°C.

One might also add that V_6O_{13} is largely unstudied from an electrical point of view, and the present work suggests a simple and direct method of preparing it.

5.5 Summary

Reflection-electron-diffraction studies have been carried out with the anodic films on V, Mo and W, and to a limited extent with Nb and Ta. The as-formed films on V, Mo, W and Ta are found to be crystallized when thin (< 200 Å) whereas all thick films, as well as thin films on Nb, are amorphous in nature. When thermally crystallized in air, the anodic films on V, Mo and W can be identified as V_2O_5, MoO_3 and WO_3 respectively; vacuum crystallization shows that films on W are still WO_3 while those on V and Mo are now V_6O_{13} and MoO_2. This suggests that the film on W is indeed WO_3 but leaves undefined the stoichiometry of the film on Mo and V. Reduction of V_2O_5 to V_6O_{13} and MoO_3 to MoO_2 can be adequately explained on the basis of thermodynamic calculations such that oxidation (governed kinetically by the well-known relation $\frac{1}{4} N\langle v\rangle t$) is less favourable than reduction of the type OXIDE+METAL = LOWER OXIDE (shown kinetically possible by the known tendency for oxygen exchange). The uncertainty with V and Mo is largely removed by the results obtained in the thickness-calibration experiments, with the stoichiometries here shown to be V_2O_5 and MoO_3.

With a proper choice of atmosphere, V_6O_{13} and V_2O_5 on one hand and MoO_2 and MoO_3 on the other could be converted into each other repeatedly. Since V_6O_{13} has not been studied extensively from the electronic point of view, the present method suggests a direct method of formation, making such studies possible.

CHAPTER 6

RANGE PROFILES - BACKGROUND

6.1 Potential Applications of Anodic Sectioning:

In the preceding chapters, the anodic sectioning of V, Mo, Nb, Ta and W has been described with both the metal-removal and film-formation thicknesses established as a function of anodizing voltage. These sectioning procedures enable uniform films, as thin as 10-15 Å in thickness, to be removed from the surfaces of metals. Such methods have found application in various fields. For example, in ion-implantation work, only a method as sensitive and reproducible as anodic sectioning may be employed in determinining range profiles. Further, as described in the introduction, certain bcc metals have been found to show anomalous self-diffusion behaviour, whereas near-surface diffusion anomalies have been discovered in the case of the noble metals. Again extremely sensitive methods are needed and only anodic sectioning meets the requirements.

Another important application of anodic sectioning may be visualized in the study of damage produced during bombardment. As will be described in Chapter 8, some targets show stoichiometry changes upon ion bombardment, while others are known toamorphize. Stoichiometry changes or amorphization

may be studied as a function of depth either using dissolution techniques based on anodic sectioning (Reid and Kelly, 1973), or using electron microscopy such that the specimen is inspected before and after sectioning (for references, see Lam and Kelly, 1972), or by using electrical measurements where again measurements are made before and after each sectioning.

Technological applications also exist such as in any situation where either erosion (turbines, space-craft, high-speed fluid flow) or corrosion (fluid flow in general) or radiation damage (nuclear reactors, fusion reactors) occurs with the thicknesses involved being much smaller than one micron. Then perhaps the only convenient method available to measure the effect is one based on anodic sectioning. This was done to measure metal loss during the formation of a protective oxide film on tin (Giani and Kelly, 1974).

Of the various potential applications of anodic sectioning, only range profiles and sputtering have been studied as a part of this investigation. It will be shown that ranges in polycrystalline specimens of these five metals have contributions both from random stopping and channeling and that the range profiles as obtained can be expressed in analytical form as a sum of two exponential terms. In the case of sputtering, which has been described only in connection with anodic films on V, ion bombardment leads to changes in surface stoichiochemistry such that $V_2O_5 \rightarrow V_2O_3 \rightarrow VO$ as bombardment progresses. Simultaneously, the sputtering coefficient varies with dose

such that it may be as high as about 44±9 atoms/ion initially but then decreases gradually to about 12 atoms/ion at the saturation dose. But before going into the details of experimental results, theoretical background and a brief survey of previous results on range profiles will be presented (this chapter). Only then will the present results on ranges and sputtering be considered (Chapters 7 and 8).

6.2 Range Profiles

6.2.1 General: A great deal of attention has been devoted in the last few years to studying range profiles of energetic charged particles in solids. One reason for this is the recent upsurge in ion-implantation work, where solids are bombarded with energetic ions, usually in the keV to MeV energy range, in order to bring about changes in electrical properties. Another reason is that a knowledge of range profiles provides new insight into interpreting radiation damage and sputtering phenomenon. At McMaster University, range profiles are used to help understand work in which ion bombardment is used to cause stoichiometry changes accompanied by dramatic changes in the electrical conductivity (Naguib and Kelly, 1972; Parker and Kelly, 1973). A variant on the conventional range profile is one showing channeling, which has been much used in the study of atom location, lattice disorder, and surface contamination. Finally, a fundamental reason for studying ranges also exists, in that they provide accurate experimental data to test theories of atomic collision.

6.2.2 Advantages and Disadvantages of Ion Implantation:

From an engineering point of view, the most important aspect of range profiles is in ion implantation. This method of introducing dopants into solids has various advantages as compared with the more conventional thermal diffusion method such as the following:

(i) A wider variety of dopants may be introduced into the solid. Thus, the ordinary solubility limits of low temperatures are not applicable, and any concentration of dopants up to a few atomic percent may be implanted.

(ii) The number of dopants and their range profiles may be independently controlled, whereas in thermal diffusion these two quantities are interrelated.

(iii) The shape and the size of an implanted area can be more effectively controlled since in thermal diffusion the dopant may penetrate in all directions as well as along dislocations.

(iv) The precision achieved with ion-implantation, especially concerning the total number of dopants, is an order of magnitude better than by the normal diffusion techniques (Davies, 1972).

(v) The depth profile decreases more slowly with thermal diffusion whereas in the case of ion implantation, it can in principle be varied at will by changing the ion energy.

There are, however, severe disadvantages too. Perhaps the major one is the radiation damage caused by the ions. For example, when 40-keV Al ions are introduced into a silicon crystal, each Al ion displaces about 8000 silicon atoms along its trajectory and even after subsequent high-temperature annealing, perhaps ∿ 0.1% disorder still remains corresponding to about 8 displaced silicon atoms for each Al ion. If any of these residual damage centers are electrically active, they may completely mask the behaviour of the implanted dopants. Keeping this limitation in mind, one could say that the successful application of ion implantation raises the following three problems (Davies, 1972):

(1) what is the range profile of the ions,

(2) how much and what kind of damage occurs, and

(3) on what type of lattice sites do the ions come to rest.

It is not easy to answer such questions. As has been mentioned earlier, due to the experimental difficulties, range profiles of energetic ions are known only for a limited number of targets (namely Al, Si, Au and W). In the absence of such measurements, the most generally accepted procedure of obtaining range data is by means of the theoretical treatment of Lindhard, Scharff, and Schiøtt (1963), to be referred to hereafter as LSS theory. This approach is, however, of limited value if the target is crystalline due to the often large role played by channeling, as will be discussed below.

6.3 LSS Theory

6.3.1 General:

This treatment is based on a model in which the energy loss occurs by nuclear and electronic stopping (treated as independent and additive) and where the arrangement of atoms in the target is assumed to be random. Because the role of crystal structure is ignored, the results apply strictly only to amorphous targets, and not to crystalline materials, whether polycrystalline or single-crystalline. The discrepancy, which is always in one direction, can be enormous.

6.3.2 Stopping Processes:

When energetic ions are injected into a solid, there are two main competing energy-loss processes. These are elastic collisions between the incident ions and the target nuclei, also called nuclear stopping, and inelastic collisions between the incident ions and the target electrons, also called electronic stopping.

Nuclear Stopping: In general, nuclear stopping depends on the cumulative effect of a succession of statistically independent elastic scattering events between the incident particles and the target atoms. The momentum imparted to the struck atoms is generally sufficient to permanently displace them from their equilibrium positions. As seen in fig. 6-1, the stopping cross-section for nuclear collisions is large for low ion energies and therefore nuclear stopping can be expected to be the dominant stopping process near the end of the incoming ion's range regardless of its initial energy.

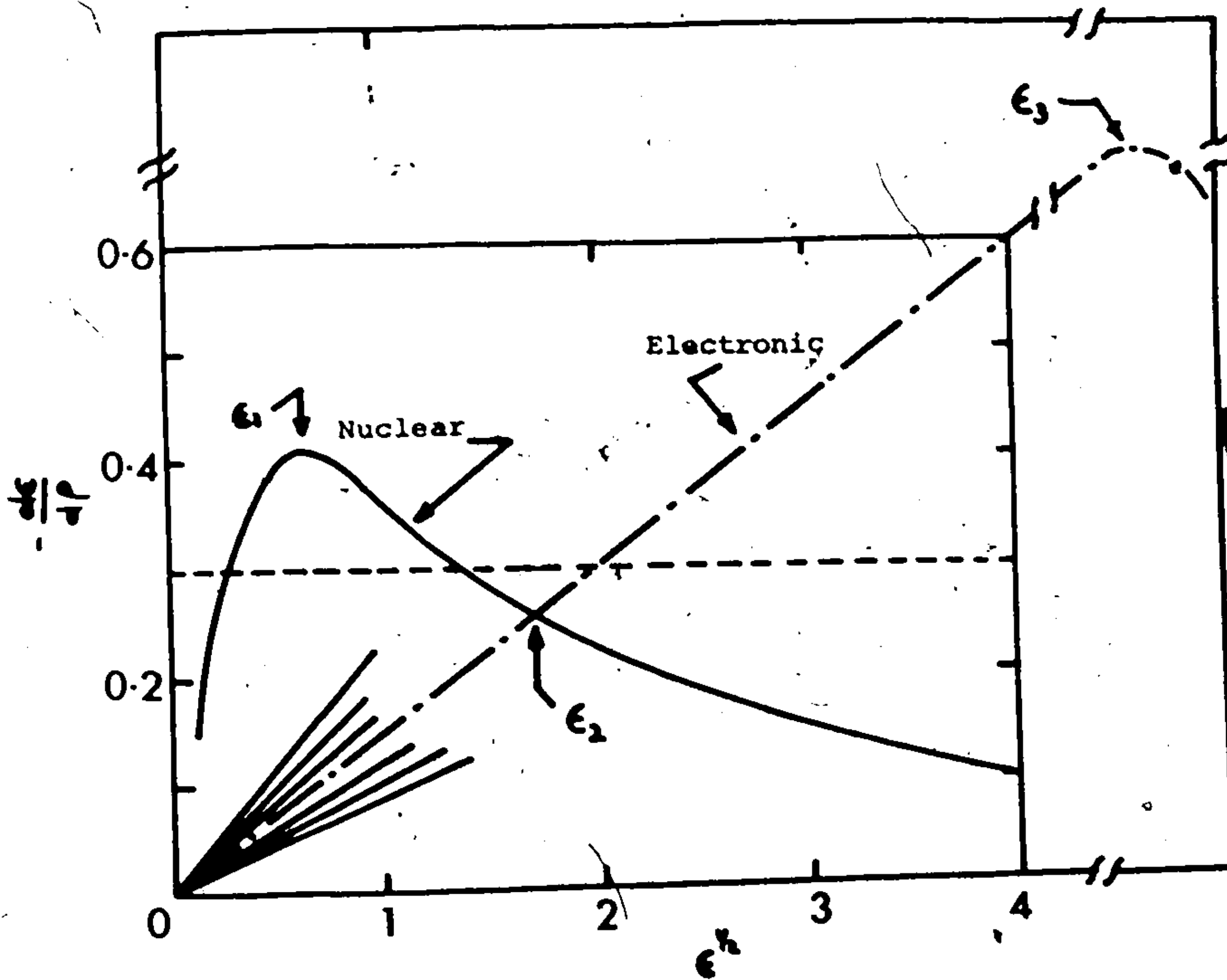

Fig. 6-1 Theoretical nuclear and electronic stopping-power curves based on the LSS theory.

Electronic Stopping: The injected ions may also lose energy by ionizing or exciting electrons. This process is important when the ion velocity v exceeds that corresponding to ε_2 that the incident ions and the target electrons have similar velocities. Electronic stopping is therefore most significant for light and fast moving ions during their initial slowing down, though is never negligible (as sometimes thought). This is shown by the results of Table 6-1 (K. B. Winterbon, private communication), in which the mean projected range for Kr in Si is calculated with and without inclusion of electronic stopping.

Table 6-1

Projected Ranges With and Without Electronic Stopping

Ion Energy keV	$\langle R_p \rangle$, $\mu g/cm^2$ Without electronic stopping	With electronic Stopping
10	2.27	2.17
20	3.77	3.56
30	5.12	4.80
40	6.42	5.98
50	7.70	7.13

6.3.3 Range Concepts:

The Total Range: The total range, R, is defined simply as the sum of the path lengths between successive collisions.

Owing to the statistical nature of the collision processes, there is a distribution in total ranges, though an average total range $\langle R \rangle$ may be defined as the arithmetic average as would be observed with a large number of incident ions.

<u>The Projected Range:</u> $\langle R_p \rangle$ is the average penetration depth as projected along the normal to the target surface. It is $\langle R_p \rangle$ rather than $\langle R \rangle$ which is observed experimentally.

<u>The Most Probable Range:</u> $R_{prob.}$ is the most probable projected penetration depth, i.e., the peak if any in the differential range profile.

<u>The Median Range:</u> R_m is the median projected penetration depth, i.e., the range within which 50% ions come to rest. R_m is more readily measured than $\langle R_p \rangle$ due to experimental profiles being integral rather than differential.

<u>The Maximum Range:</u> R_{max} is the upper limit for ion penetration as observed for the small fraction of ions which suffer no nuclear collisions due to their motion in crystallographically open directions (i.e. due to channeling). This range is observed only in crystalline targets and even then only in very careful experiments.

In amorphous substances, the range profiles closely resemble a Gaussian distribution, so that $\langle R_p \rangle$, $R_{prob.}$ and R_m are nearly equivalent (to within about 20%) and such departure from Gaussian behaviour as occurs normally being in the form of a skewness "to the right" (Fig. 6-2a). The occurrence of channeling in crystalline solids causes the profile to broaden

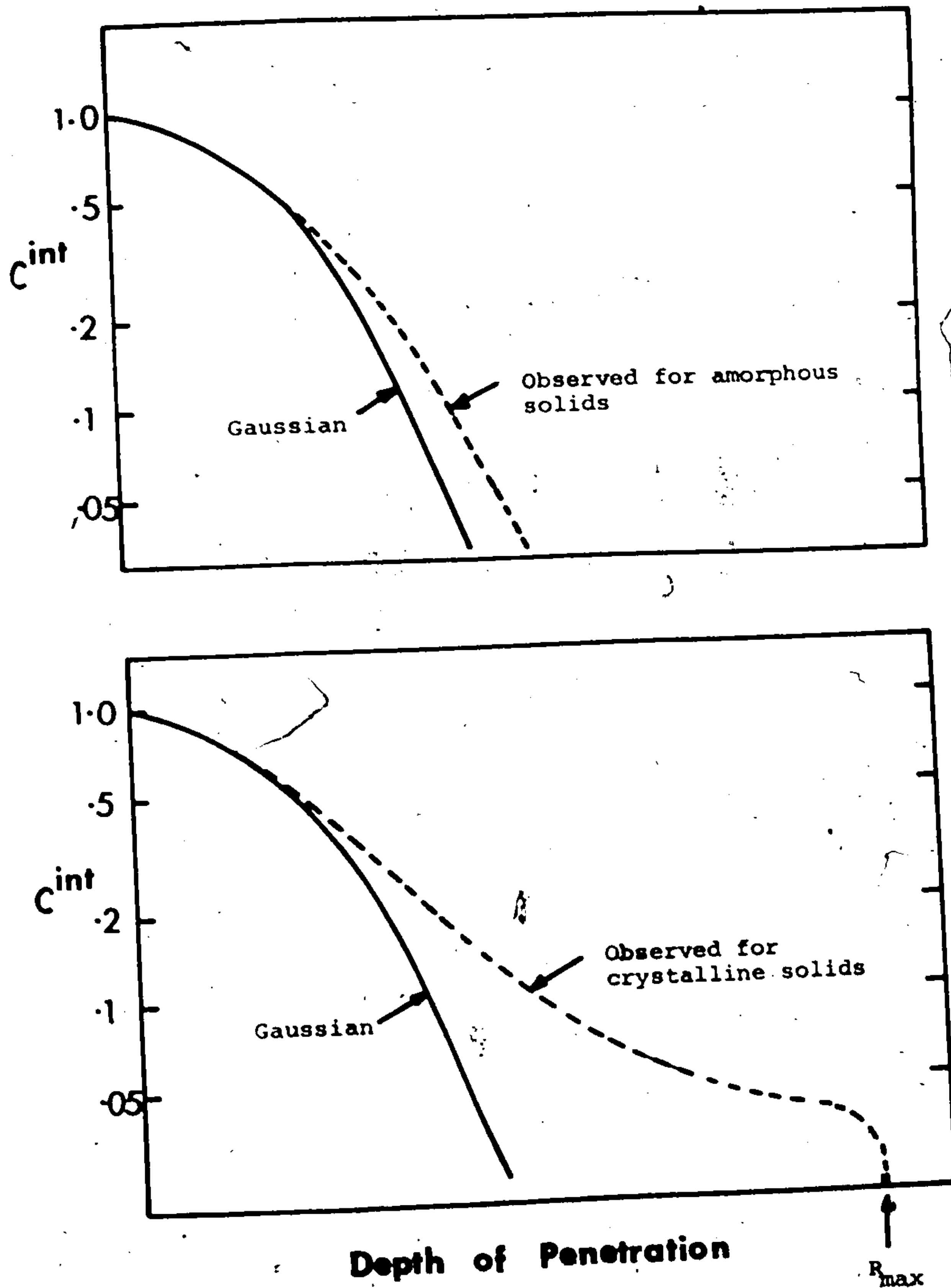

Fig. 6-2 Typical range profiles. Solid: Gaussian. Dashed: (a) as observed for amorphous solids, and (b) as observed for crystalline solids.

markedly towards deeper penetration (i.e., towards R_{max}), and significant deviations between the three types of ranges then arise (Fig. 6-2b). In general, range estimates derived from the work of LSS are thus meaningfully used only with amorphous targets.

6.3.4 Outline of LSS Theory: This theory assumes the collisions to be two-bodied, classical and non-relativistic, and employs a Thomas-Fermi interaction potential for predicting the energy-loss during collisions. The energy loss per unit path length for a moving ion, in accordance with what has been said before, can be approximately split up into two contributions:

$$\frac{dE}{dx} = \left(\frac{dE}{dx}\right)_e + \left(\frac{dE}{dx}\right)_n \qquad (6\text{-}1)$$

$$\equiv -N[S_e(E) + S_n(E)] \qquad (6\text{-}2)$$

where $S_e(E)$ = stopping cross-section for energy loss to electrons

$S_n(E)$ = stopping cross-section for energy transformed to nuclear motion

N = number density of atoms in the target.

The quantity $S_n(E)$ is in turn related to $d\sigma$, the differential scattering cross-section, by the integral:

$$S_n(E) = \int_0^{\Lambda E_1} T d\sigma \qquad (6\text{-}2a)$$

where T = transferred energy ; $0 \leq T \leq \Lambda E_1$

$$\Lambda = \frac{4M_1M_2}{(M_1+M_2)^2}$$

E_1 = energy of the incident ion.

M_1, M_2 = mass of incident ion and of target respectively.

This description by stopping and scattering-cross-sections is adequate for random media, i.e., when crystal lattice effects (channeling) can be ignored. It then leads immediately to a direct estimate of the mean total range for a random medium.

$$\langle R\rangle = \int_0^{E_1} \frac{-\,dE}{(\frac{dE}{dx})_e + (\frac{dE}{dx})_n} \qquad (6\text{-}3)$$

which takes on a particularly simple form in the limits of low and high energy.

At Low Energy: In LSS theory, the electronic energy loss is considered to be proportional to ion velocity so that we have

$$(\frac{dE}{dx})_e = -KE^{1/2} \quad . \qquad (6\text{-}4)$$

Since this term is quite small compared to the nuclear stopping at low enough energy (cf. also fig. 6-1), $\langle R\rangle$ follows as

$$\langle R\rangle = \int_0^{E_1} \frac{dE}{NS_n(E)} \quad . \qquad (6\text{-}5)$$

For screened Coulomb interaction between an ion and an atom (or between two atoms), Lindhard et al. (1968) derived the following approximate form of the differential cross-section

$$d\sigma = CE^{-m}\, T^{-1-m}\, dT \qquad (6\text{-}6)$$

where

$$C = \frac{\pi}{2}\lambda_m a^2 \left(\frac{M_1}{M_2}\right)^m \left(\frac{2Z_1Z_2e^2}{a}\right)^{2m}$$

$$= \frac{\pi}{2}\lambda_m a^2 \left(\frac{E}{\varepsilon}\right)^{2m} \Lambda^m$$

$$\lambda_{1/3} = 1.309; \quad \lambda_{1/2} = 0.327; \quad \lambda_1 = 0.50$$

$$a = \text{screening distance}$$

$$= 0.8853\, a_o [Z_1^{2/3} + Z_2^{2/3}]^{1/2}$$

$$a_o = \frac{\hbar^2}{me^2} = 0.529\ \text{Å}$$

$$\varepsilon = \left(\frac{M_2E_1}{M_1+M_2}\right)\left(\frac{Z_1Z_2e^2}{a}\right)^{-1} \qquad (6\text{-}8)$$

The nuclear stopping cross-section may accordingly be written as

$$S_n(E) = \int_0^{\Lambda E_1} T d\sigma$$

$$= \frac{C}{1-m}\Lambda^{1-m}E^{1-2m} \qquad (6\text{-}9)$$

Substitution of eqn. 6-9 into 6-5 yields

$$\langle R \rangle = \frac{(1-m)E^{2m}}{2mC\Lambda^{1-m}N} \qquad (6\text{-}10)$$

while multiplying both sides by $(\frac{\rho}{R})$, where ρ is defined below, gives

$$\rho = \frac{(1-m)\varepsilon^{2m}}{2mC\ \Lambda^{1-m}\ N}\left(\frac{\rho}{R}\right)\left(\frac{E}{\varepsilon}\right)^{2m}$$

and so,

$$\rho = \frac{(1-m)}{m\ \lambda_m}\varepsilon^{2m} \qquad (6\text{-}11)$$

This is a result of remarkable simplicity considering the complexity of its origin. Here, ρ and ε are the dimensionless range parameters of LS6, namely,

$$\rho = R \cdot \frac{NM_2 \, 4\pi \, a^2 M_1}{(M_1+M_2)^2}$$

$$\varepsilon = E \cdot \frac{a \, M_2}{Z_1 Z_2 \, e^2 (M_1+M_2)} \quad . \tag{6-12}$$

The significance of ρ-ε notation is seen clearly in eqn. 6-11, in that all parameters restricted to a particular ion or target have cancelled out, leaving a result which is essentially universal. For $m = \frac{1}{2}$, eqn. 6-11 becomes the well known universal range-energy equation of Nielsen (1956)

$$\rho = 3.06 \; \varepsilon \tag{6-13}$$

<u>At Very High Energy</u>: In this energy range, electronic stopping tends to dominate over nuclear stopping so that one can write

$$\langle R \rangle \approx \int_0^{E_1} \frac{dE}{NS_e(E)}$$

$$= \int_0^{E_1} \frac{dE}{KE^{1/2}}$$

$$\langle R \rangle = \frac{2E^{1/2}}{K} \quad . \tag{6-14}$$

In ρ-ε units, eqn. 6-14 becomes

$$\rho = \frac{2\varepsilon^{1/2}}{k} \tag{6-15}$$

where

$$k = \xi_e \cdot \frac{0.0793\, Z_1^{2/3} Z_2^{1/2} (M_1+M_2)^{3/2}}{(Z_1^{2/3}+Z_2^{2/3})^{3/4} M_1^{3/2} M_2^{1/2}} \qquad (6\text{-}16)$$

$$\xi_e \approx Z_1^{1/6}.$$

Winterbon (1968) has tabulated ρ, ε and k, a part of which is reproduced in Table 6-2. Note that eqn. 6-15 is not quite universal since it depends upon k and so on Z_1 and Z_2. Except for values of $Z_1 << Z_2$, k takes up values less than unity and generally between 0.1 and 0.2.

General Case: At intermediate energies, where both types of stoppings are important, one must write

$$\rho = -\int_0^{\varepsilon} \frac{d\varepsilon}{(\frac{d\varepsilon}{d\rho})_n + (\frac{d\varepsilon}{d\rho})_e} = \rho(\varepsilon, k) \qquad (6\text{-}17)$$

and ρ is accordingly neither universal nor has a simple form. Eqn. 6-17 has been tabulated extensively by Winterbon (1968) for a Thomas-Fermi differential scattering cross-section.

6.3.5 Corrections:

In deriving accurate range-energy relationships to predict the range profiles in amorphous media, the following correction factors are necessary:

(a) Since the experimentally measured quantity is $\langle R_p \rangle$ rather than $\langle R \rangle$, Lindhard et al. (1963) have given an approximate relation between $\langle R \rangle$ and $\langle R_p \rangle$ for pure nuclear stopping governed by a power-law differential cross-section with $m = \frac{1}{2}$, namely

Table 6-2

Values of ε, ρ and k for incident Kr^{85}

Target	M_2	ε/E*	ρ/R**	k
Li	7	0.00636113	0.12848919	0.09318515
O	16	0.00463559	0.09287578	0.10439931
Al	27	0.00413422	0.06850111	0.11118309
Ti	48	0.00342332	0.04256084	0.12712325
Nb	93	0.00241217	0.01955108	0.16676703
Ta	181	0.00157873	0.00708706	0.24656639

*E in keV

**R in $\mu g/cm^2$

$$\frac{\langle R \rangle}{\langle R_p \rangle} \simeq 1 + \frac{M_2}{3M_1} \qquad (6\text{-}18)$$

which is valid at low energies for $\frac{M_2}{M_1} \lesssim 2$.

(b) Polyatomic Targets: Complications arise when the target consists of two (or more) different atomic species, such as oxide targets. Schiøtt (1970) has given a simple interpolation rule to determine projected ranges for mixed substances

$$\frac{1}{\langle R_p \rangle} = \sum_i \frac{X_i}{\langle R_p^i \rangle} \qquad (6\text{-}19)$$

where X_i is the fraction of the total mass constituted by the ith component and $\langle R_p^i \rangle$ is the projected range (in mass units per cm^2) in the ith component. This formula is readily derived from eqn. 6-5 by assuming the same energy dependence of stopping powers (eqn. 6-9) in the various substances in the compound.

(c) Z_1 oscillations in $(\frac{d\varepsilon}{d\rho})_e$: The use of Thomas-Fermi statistical concepts in the LSS treatment lead to an electronic stopping power that increases monotonically with Z_1 for a given Z_2 and ion velocity. Experimental results [Ormrod et al. 1963, 1965; Fastrup, 1965, 1968] have shown that the electronic stopping has a periodic dependence on Z_1, with oscillations of up to 50% on either side of the LSS relationship (eqn. 6-15). A similar effect occurs also with channeled ions though to a different extent.

6.3.6 <u>Range-Straggling:</u> In ion implantation studies, one is interested in the entire range-profile which, in a random target, is approximately Gaussian in shape. One therefore requires at least one extra parameter besides the projected range, namely, the average standard deviation $\langle\Delta R_p\rangle$ in the projected range. Again, LSS have developed a useful theoretical framework for treating this problem. Provided $\frac{M_2}{M_1} < 1$, the difference between $\frac{\langle\Delta R\rangle}{\langle R\rangle}$ and $\frac{\langle\Delta R_p\rangle}{\langle R_p\rangle}$ is rather small. In such cases, for $\varepsilon < 3$, LSS find that the predicted range straggling, expressed in terms of the reduced parameter

$$\frac{\langle\Delta R_p\rangle}{\langle R_p\rangle} \cdot \frac{1}{\Lambda^{1/2}}$$

approaches an almost constant value of 0.35,which is characteristic of power-law scattering. Winterbon, Sigmund and Sanders (1970) have computer-calculated the range parameters as functions of mass ratio $\frac{M_2}{M_1}$ and a part of their results are reproduced in fig. 6-3. Large values of $\frac{\langle\Delta R_p\rangle}{\langle R_p\rangle}$ for light ions might be anticipated from the fact that $\langle R_p\rangle$ is now much smaller than $\langle R\rangle$. The decrease in $\frac{\langle\Delta R_p\rangle}{\langle R_p\rangle}$ with increasing energy is due to the increased contribution of electronic stopping.

The range profile may be constructed with successively increasing accuracy by the use of Edgeworth's expansion and the method generally followed is discussed in the next section.

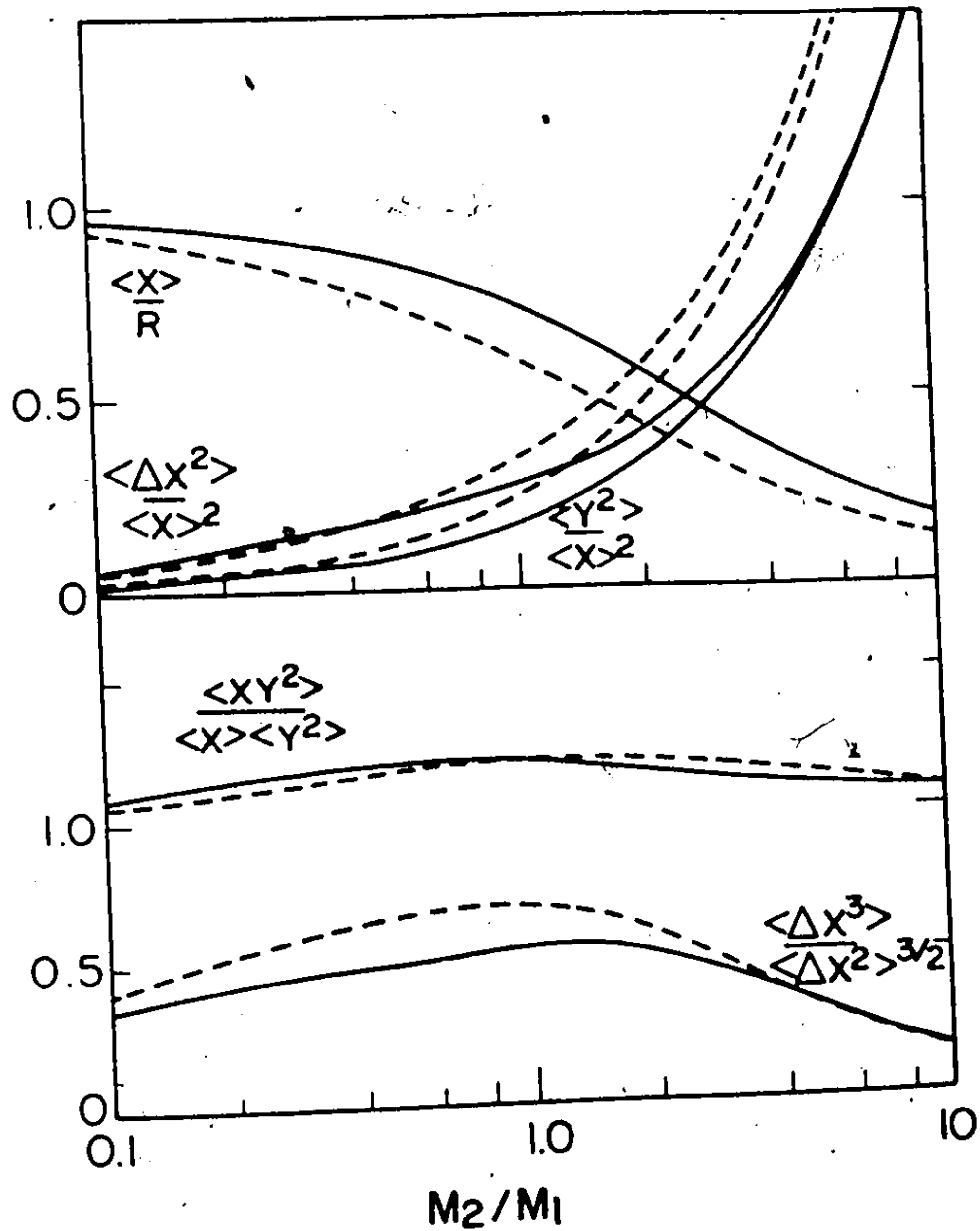

Fig. 6-3 Range parameter as functions of mass ratio M_2/M_1 (after Winterbon et al., 1970)

6.4 Constructing Range Profiles:

6.4.1 Differential Profiles: We outline here the method currently used, based on Edgeworth's expansion, for constructing differential range profiles. Define $C^{diff.}(x)dx$ such that it is the probability for a projectile to come to rest in a layer of thickness dx at a depth x from the surface. In calculating $C^{diff.}(x)dx$, it is assumed that it can be approximated with successively increasing accuracy by the use of Edgeworth's expansion in terms of spatial moments over the true range distribution. This expansion converges best when the distribution under consideration is similar to a Gaussian, which is the case for amorphous targets with $M_2 > M_1$. In other cases, the convergence can be quite poor (Winterbon et al, 1970) and one has to use other expansions.

Define a dimensionless parameter ξ where

$$\xi = \frac{x-\langle R_p\rangle}{\mu_2^{1/2}} \qquad (6\text{-}20)$$

with

$$\mu_n = \langle (x-\langle R_p\rangle)^n\rangle, \quad n = 2,3,4 \ldots.$$

Here $\mu_2^{1/2}$ is the same as $\langle \Delta R_p\rangle$, the mean projected standard deviation. Then $C^{diff.}(\xi)$ is given by an infinite number of terms in Edgeworth's expansion, and can be approximated by N terms:

$$C^{diff.}(\xi) = \sum_{n=2}^{N} \bar{a}_n(\xi)$$

where
$$a_2(\xi) = \frac{1}{\sqrt{2\pi}} \exp(-\frac{\xi^2}{2})$$
$$a_3(\xi) = -\frac{\mu_3}{6\sqrt{2\pi}\cdot\mu_2^{3/2}} (3\xi-\xi^3)\exp(-\frac{\xi^2}{2})$$

and the general term is discussed by Sigmund (1968). Taking N=4 in eqn. (6-20), the distribution function becomes

$$C^{diff.}(\xi) = \frac{1}{\sqrt{2\pi}} \exp(-\frac{\xi^2}{2})\cdot f(\xi) \qquad (6\text{-}21)$$

$$= (\text{Gaussian distribution})\cdot(\text{correction term})$$

where the correction term is given by

$$f(\xi) = 1 - (\frac{\mu_3}{6\mu_2^{3/2}})(3\xi-\xi^3) + \frac{1}{24}(\frac{\mu_4}{\mu_2^2} - 3)(3-6\xi^2+\xi^4) - (\frac{\mu_3^2}{72\mu_2^3})(15-45\xi^2 + 15\xi^4 - \xi^6)$$

Eqn. (6-21) gives the theoretical differential ion concentration profile to be used in what follows.

6.4.2 Integral Profiles:- Integral profiles, which are normally obtained experimentally, are described in terms of the integral concentration, $C^{int.}(x)$:

$$C^{int.}(x) = \frac{1}{A}\int_x^{\infty} C^{diff.}(x)dx$$

where the factor A serves as normalization:

$$A = \int_0^{\infty} C^{diff.}(x)dx \,.$$

Fig. 6-4 Theoretical differential and integral range profiles of Kr^{85} in amorphous Mo in linear scale

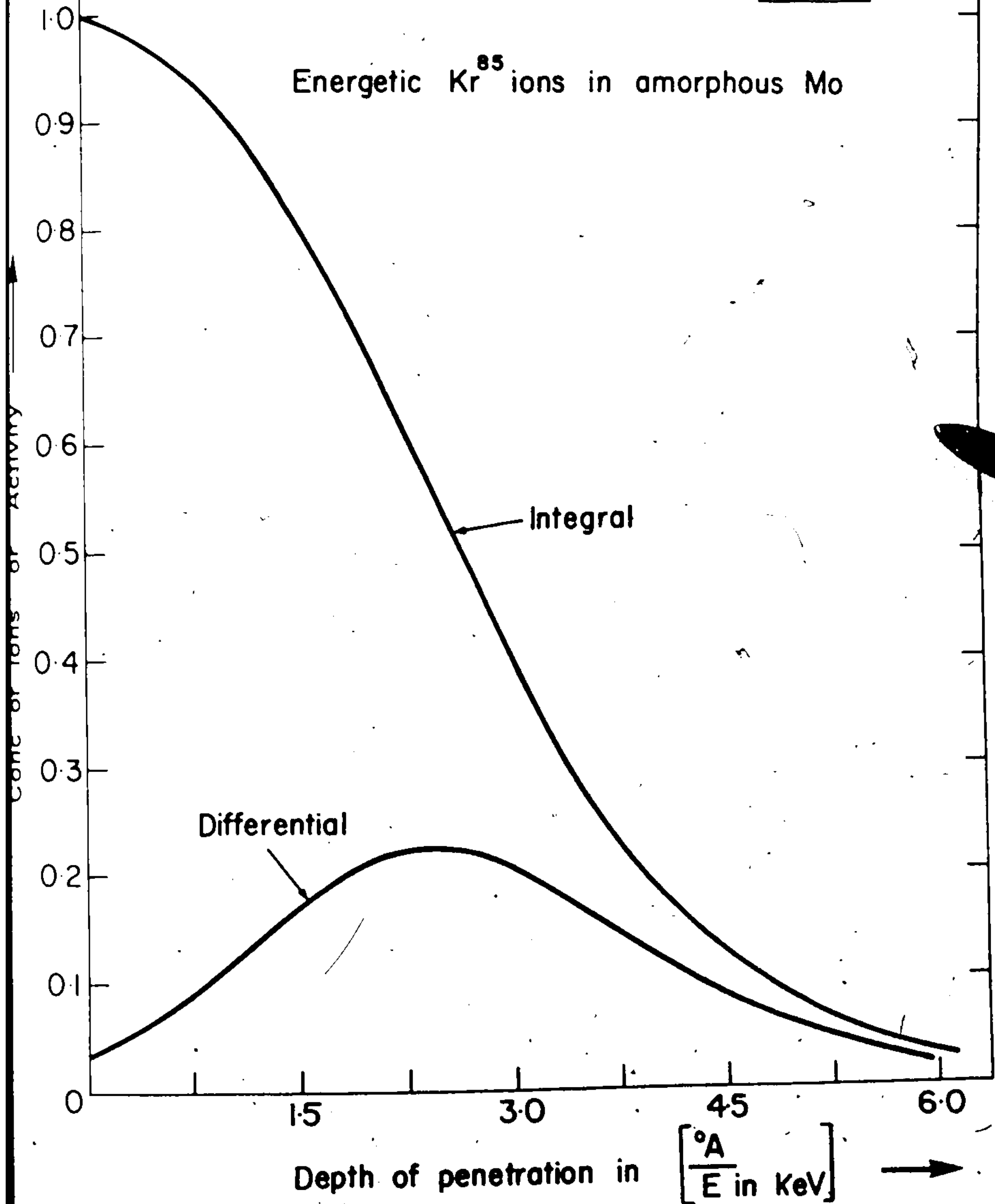
Theoretical Differential and Integral Concentration Profiles.
Energetic Kr85 ions in amorphous Mo
Integral
Differential
1·0
0·9
0·8
0·7
0·6
0·5
0·4
0·3
0·2
0·1
0
1·5
3·0
4·5
6·0
Depth of penetration in [°A / E in KeV]

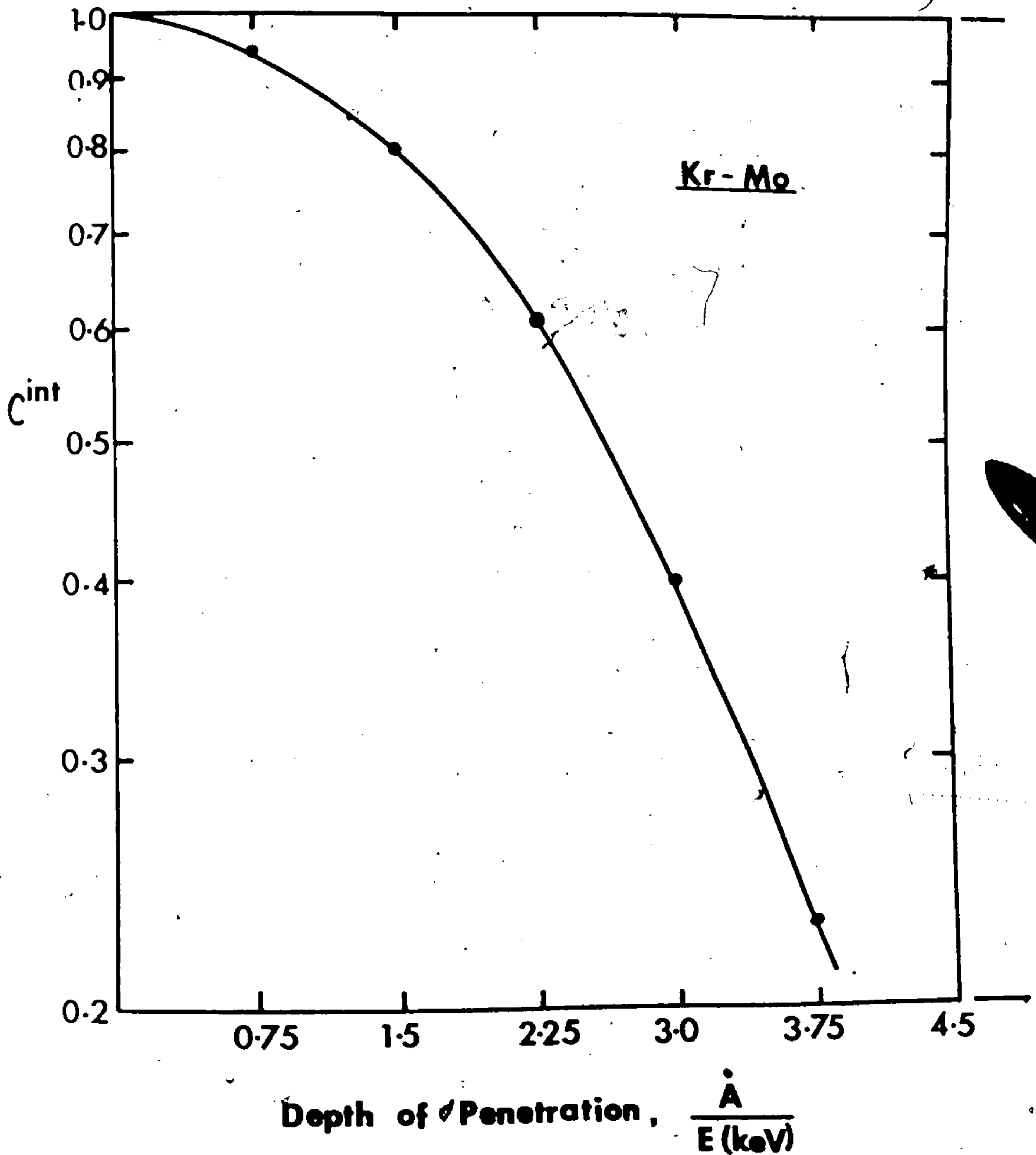

Fig. 6-5 Theoretical integral range profile of Kr^{85} in amorphous Mo in the usual logarithmic form

The form corresponding to eqn. (6-21) is given by

$$C^{int.}(x) \approx \frac{1}{2} \operatorname{erfc}\left(\frac{\xi}{\sqrt{2}}\right) \cdot g(\xi) \qquad (6\text{-}22)$$

where the correction term is

$$g(\xi) = 1 - \left(\frac{2}{\pi}\right)^{1/2} \exp\left(-\frac{\xi^2}{2}\right)\left[\operatorname{erfc}\left(\frac{\xi}{2^{1/2}}\right)\right]^{-1}$$
$$\times \left\{ \left(\frac{\mu_3}{6\mu_2^{3/2}}\right)(1-\xi^2) + \frac{1}{24}\left(\frac{\mu_4}{\mu_2^2} - 3\right)(3\xi-\xi^3)\right.$$
$$\left. - \left(\frac{\mu_3^2}{72\mu_2^3}\right)(\text{[illegible]}0\xi^3+\xi^5)+\ldots\right\}$$

The correctness of $g(\xi)$ can, if desired, be verified by differentiation. Fig. (6-4) shows the differential and integral profiles in linear form obtained for Kr^{85} in amorphous Mo, while fig. (6-5) shows integral profiles in the more usual logarithmic form.

6.5 Crystal Lattice Effects on Ranges:

6.5.1 General: The LSS treatment outlined in section 6.3 was based on the slowing down of particles in a series of independent collisions with a random arrangement of atoms. On the whole, the experimental results obtained with amorphous solids agree with the predictions based on this framework. However, in crystalline solids, the arrangement of atoms is periodic rather than random and this periodic lattice causes, to some extent, correlated rather than independent collisions. The possible influence of the crystal lattice on the range profiles is now discussed.

In amorphous solids, the penetration profile exhibits, as we have seen, an approximately Gaussian form; when polycrystalline specimens are used, however, the range profiles exhibit a skewness with a deeply penetrating tail (fig. 6-2) as found by Davies et al. (1960). At about the same time, Rol et al. (1959) and Almèn and Bruce (1961) found anisotropic behaviour for the sputtering coefficient of Cu, such that the sputtering coefficient had a minimum along a low index crystal direction. Such behaviour could not be adequately explained by the transparency model, which assumed that the low index directions in crystals were relatively transparent (open) and so presented fewer atoms to the incident ions. Later, Robinson and Oen (1963) used a high-speed digital computer to study range profiles and observed exceptionally long trajectories which apparently resulted from steering by a succession of glancing collisions with the channel walls. That is, since some ions undergo only glancing collisions, the energy loss per unit path length will be considerably reduced. This phenomenon has come to be called channeling. Soon after the work of Robinson and Oen (1963), Lutz and Sizmann (1963), Nelson and Thompson (1963) and Piercy et al. (1964), all working independently, provided conclusive experimental evidence in support of the channeling phenomenon.

6.5.2 Channeling: The concept of channeling is not really new. As Davies (1972) points out, it was first postulated by Bragg

(for reference, see Von Laue, 1952) in order to explain X-ray diffraction patterns. In fact, Stark (1912) actually proposed a channeling experiment involving a beam of protons in a single crystal and predicted the phenomenon very accurately. Thus, when an energetic ion enters a crystal within a certain critical angle of a low index axis, then each time it approaches one of the aligned rows of lattice atoms, the gradually increasing repulsion between the screened Coulomb (i.e. Thomas-Fermi) fields of the ion and the lattice row is sufficient to steer the ion away again, thereby preventing violent nuclear collisions from occurring. Lindhard (1965) has formulated a theoretical framework which enables reasonable estimates to be made of the critical angle within which channeling occurs. For heavy ions at the keV energies, the channeling criterion for an ion of energy E_1 and the angle of incidence ψ relative to row of atoms is given by:

$$\psi \lesssim \psi_2 \equiv \left[\left(\frac{a}{d}\right)\psi_1\right]^{1/2}$$

where

$$\psi_1 = \left(\frac{2Z_1Z_2e^2}{E_1 d}\right)^{1/2}$$

where a, as before, is the Thomas-Fermi screening distance with a magnitude of 0.1-0.2 Å, and d is the atomic spacing along the aligned row. For energies less than a few hundred keV, ψ_2 is between 3° and 5° along <110> or <111> axes.

One consequence of channeling is that all processes requiring small impact parameters such as nuclear collisions are completely prohibited for a channeled beam and related processes such as radiation damage or sputtering are greatly reduced.

Ion trajectories of interest for axial channeling are shown schematically in fig. 6-6, in which the crystal lattice is depicted as a set of atomic "strings" of radius'a'. In fig 6-6a, the ion A enters at a large angle, $\psi > \psi_2$, and

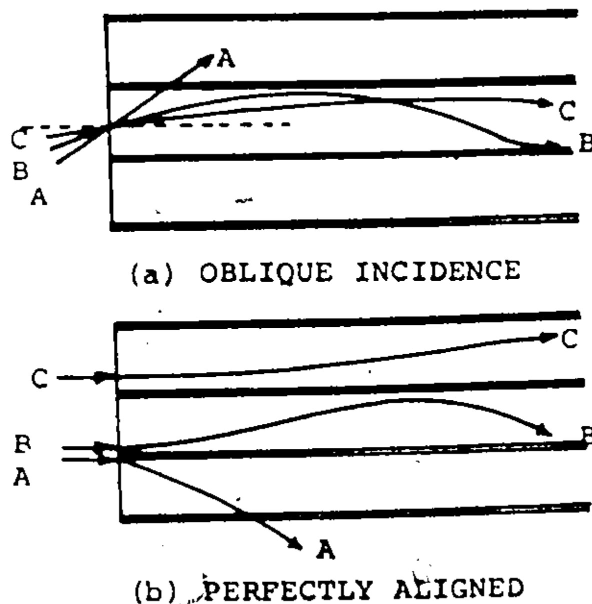

Fig. 6-6 Schematic representation of ion trajectories for axial channeling, with crystal lattice depicted as a set of atomic "strings" (a) variation in trajectories with angle of incidence, and (b) with impact position.

will not be steered by the lattice rows. It thus has approximately the same range profile as in an amorphous target. Ion B, incident near mid-channel, with an angle $\psi < \psi_2$, will oscillate between strings without undergoing any large-energy-loss nuclear collisions; its path, however, has wider amplitude oscillations than ion C with smaller ψ. Even in case of a perfectly aligned beam of incident ions (fig. 6-6b), one still observes three different types of collisions, since the initial

impact position of an ion also influences its trajectory. That is, ions entering the crystal close to an atomic row are scattered immediately through an angle sufficiently large that they do not become channeled (trajectory A) in spite of the angle ψ being initially small. It is convenient, therefore, to divide the incident ions into three broad categories (Davies, 1972) corresponding to the trajectories shown in fig. 6-6:

Group A,	those particles that do not "feel" the lattice and so have a range distribution similar to that in an amorphous material.
Group B,	those particles that start with large oscillations and which probably get scattered (de-channeled) well before they are stopped, and
Group C,	those particles that start out "well-channeled" and thus have a better chance of remaining in the channel throughout their slowing down process.

Fig. 6-7 illustrates the type of range profile obtained when a heavy-ion beam is implanted into a well-aligned W crystal. Tungsten presents a rather attractive and perhaps "ideal"

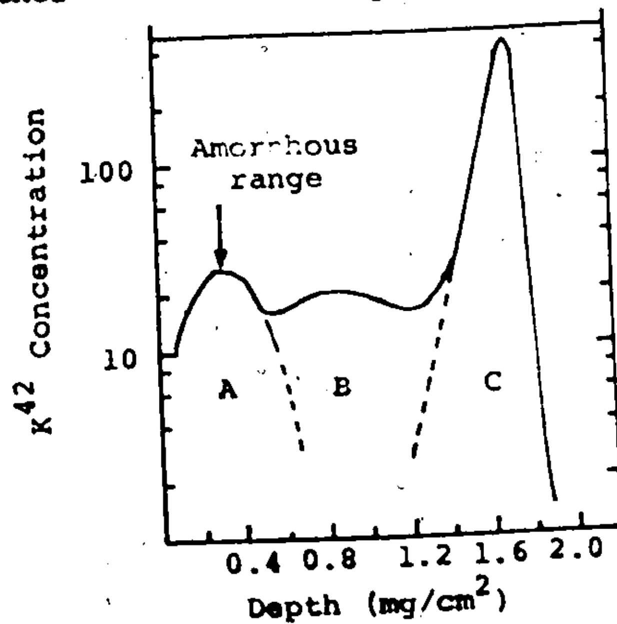

Fig. 6-7 The experimental range profile of 500-keV K^{42} ions injected at 27°C along the <111> direction in W (after Ericksson, 1967)

choice owing to the small lattice vibrations observed at room temperature and thus a minimum of de-channeling effects. Three clearly divided regions are indeed observed which may be roughly identified with the three types of trajectories shown in fig. 6-6. The two peaks A and C correspond respectively to random and well-channeled ions. The latter is characterized by a sharp cut-off, this cut-off being defined as the maximum range, R_{max}. In general, de-channeling is quite prominent at room temperature and the range profile generally obtained is as shown by dashed lines (fig. 6-2).

6.5.3 Factors Affecting Channeling:- Various factors affect the range profiles of channeled ions such as the temperature, dose, beam misalignment, surface disorder, etc., some of which are discussed below.

(a) Dependence on Temperature: The effect of lattice vibrations is shown in fig. 6-8a for 500-keV ions injected into W along the <111> direction. At 250°C, the number of ions appearing in the channeled peak C is a factor of 2-3 less than at 25°C, presumably due to the increased scattering arising from the larger mean vibrational amplitude.

(b) Dependence on Bombardment Dose: Incident ions create damage along their trajectories and hence destroy the lattice structure necessary for channeling, this effect being particularly pronounced for substances such as Si and Ge, which tend to amorphize when bombarded at room temperature. This behaviour is clearly seen in fig. 6-8b which shows the in-

Fig. 6-8 (a) Effect of target temperature on the range profile of 500-keV K^{42} injected along the <111> direction in W (after Ericksson, 1967).

(b) Range profiles of P^{32} implanted into Si at 40-keV along the <110> direction (after Dearnaley et al., 1968)

(c) Effect of misalignment and surface disorder on the range profile of 40-keV Xe^{125} implanted into <110> Si at 25°C (after Davies et al., 1964)

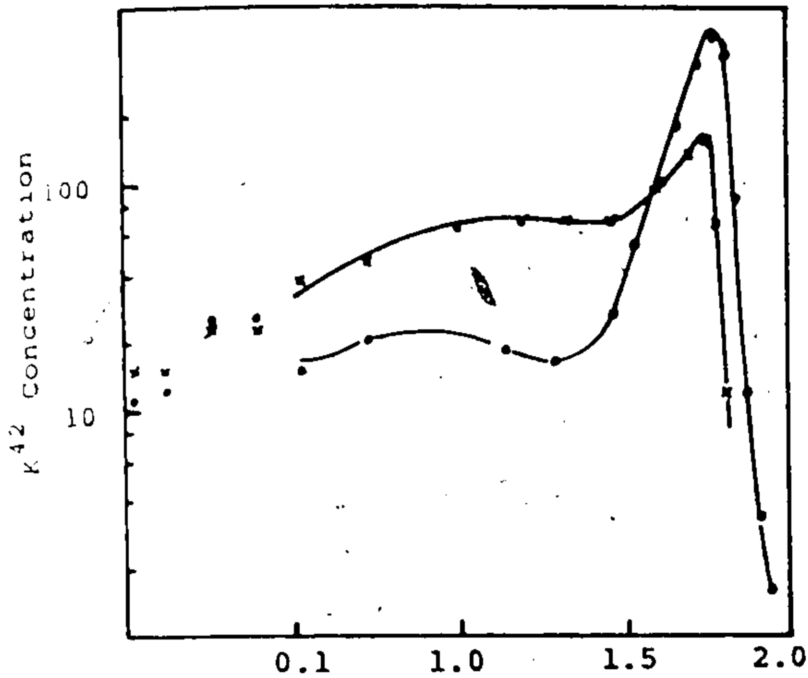

(a)

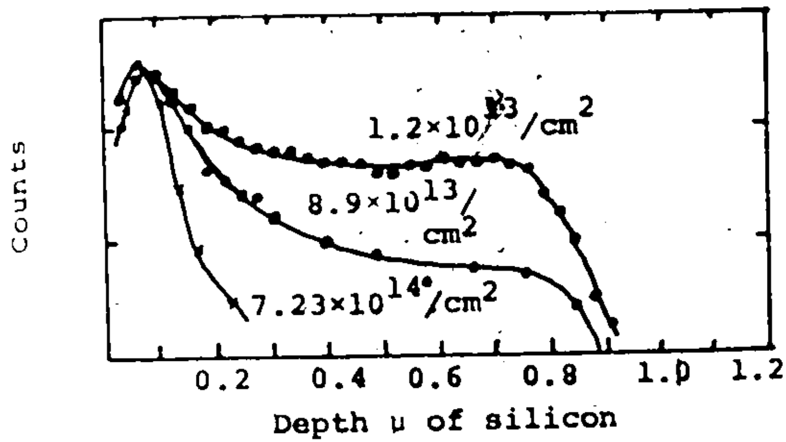

(b)

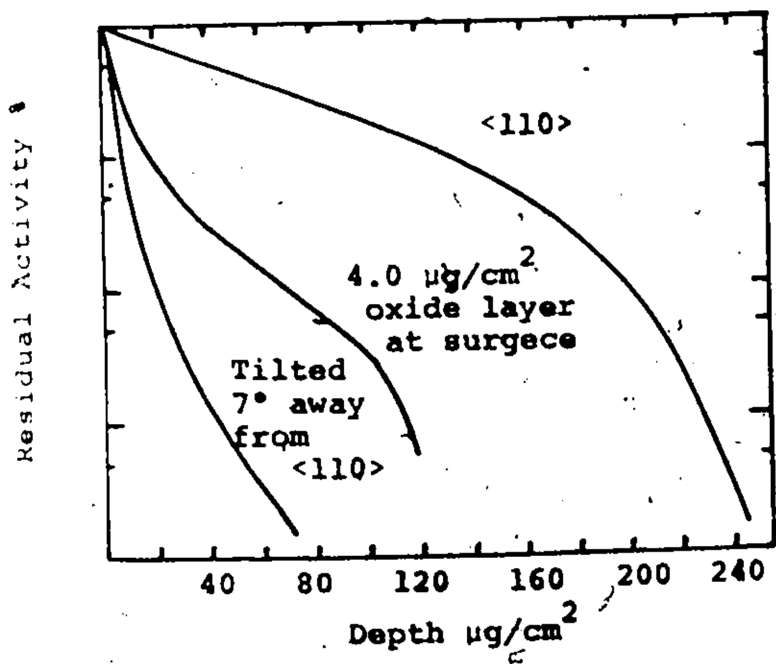

(c)

fluence of dose on the distribution of 40-keV P^{32} ions in Si for implantation along the <110> direction. The concentration profiles shown here have been normalized to the same random peak height to show how the relative number of channeled ions decreases with increasing dose. It should be noted that this sensitivity to ion dose occurs to different extents in different crystals. For example, in W, dose levels in excess of 10^{16} ions/cm^2 at 25°C are required to cause drastic changes in range profiles, whereas in Si, only $\leq 10^{13}$ ions/cm^2 are enough. This is reasonable when it is remembered that Si, but not W, amorphizes under ion impact.

(c) Dependence on Misalignment and Surface Disorder: Both of these factors influence the range profile in a similar fashion. Fig.6-8c shows the effect of a misalignment (by 7°) and of a surface oxide layer (∿ 200 Å thick) on the profile of Xe^{125} in a <110> Si crystal. Thus, even a small beam misalignment or the presence of a small amount of surface oxide would affect significantly the shape of a channeled range profile.

These factors all tend to cause uncertainties in the range profiles with targets which are subject to channeling. The most reproducible experimental parameter for characterizing range profiles in single crystals is therefore the maximum range, $R_{max.}$, since the factors mentioned above affect only the total number of ions approaching $R_{max.}$ and not the maximum range itself. A knowledge of $R_{max.}$ immediately leads to the

estimation of electronic stopping powers and such estimates, when plotted against $E^{1/2}$ (fig. 6-9) yield a linear plot down to very low energies of a few keV. This shows that for a well-

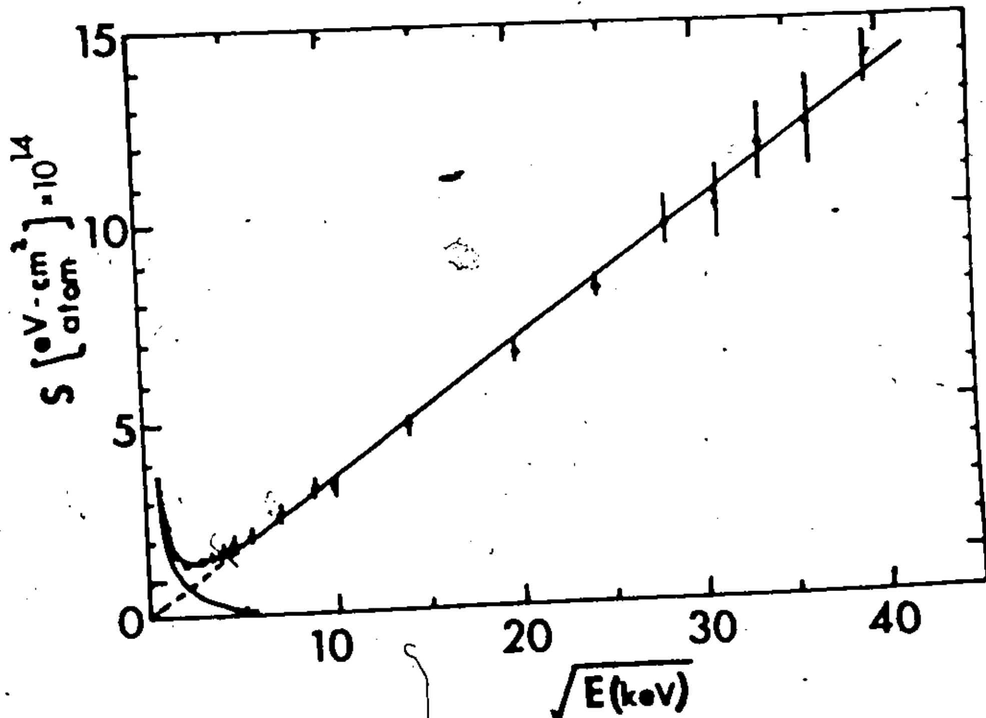

Fig. 6-9

Plot of total stopping cross-section S vs $E^{1/2}$ for well-channelled Xe ions injected into W along the <100> direction. (After Ericksson et al.,1967)

channeled ion, electronic stopping is generally the dominant mechanism of energy loss at $E \gtrsim$ 10-keV for Xe in W. By contrast, LSS theory predicts, for a non-channeled beam of Xe in W, that electronic stopping would begin to dominate at about 2.7 MeV and one thus has a rather striking example of the failure of LSS theory in crystalline solids. This fact of electronic stopping dominance leads to a smaller stopping power for well-channeled heavier ions than for well-channeled light ions at the same incident energy due to their low velocity. The heavier ions therefore penetrate more deeply, completely contrary to what is obtained for a non-channeled beam.

6.5.4 Supertails: Since a well-channeled ion does not create any damage along its trajectory, it has the possibility of coming to rest as an interstitial ion in a completely undamaged region of the crystal. Such an ion may diffuse rather deeply into the crystal at room temperature due to the low activation energy of interstitial motion. When experiments were carried out with W, about 0.5% of the ions implanted at room temperature did indeed penetrate to an anomalous depth (5-10 μ) and such penetration has been called a "supertail". Davies and Jespersgaard (1966) inferred that this supertail was caused by interstitial diffusion arising from almost perfectly channeled ions that had come to rest without producing damage in the surrounding lattice. Hermann et al. (1966) confirmed this with elegant experiments in which they implanted Kr ions along <100> W channels at -196°C and found supertails after warming to room temperature. When, before warming, W specimen was subjected to an He ion bombardment which caused defect production beyond the previously implanted Kr, subsequent warming showed the absence of a supertail. That is, Kr ions are unable to move at -196°C and the vacancies induced by the bombardment prevented their migration during warm up.

From a theoretical consideration of the slowing-down behaviour of well-channeled ions, Andersen and Sigmund (1965) predict that for $Z_1 > Z_2$, even perfectly channeled ions can initiate collision cascades and thus become trapped at the end of their trajectory. Their criterion for the observation of a

supertail thus is that Z_1 be smaller than Z_2. The conclusion that for $Z_1 > Z_2$ no supertail should be observed has been tentatively confirmed when Rn^{222} was implanted into W (Domeij et al., 1965). However, due to its complicated decay scheme, radon does not present the ideal choice in verifying the criterion of Anderson and Sigmund. Mo and Nb would perhaps be the best targets for such a study, for, due to their mid-way position in the periodic table, a variety of ion masses, greater and smaller than Z_2, would be available.

6.5.5 <u>Z_1 Oscillations:</u> There is another important consequence of channeling. As was seen earlier (section 6.3.5), the electronic stopping behaviour departed from the theoretical predictions by up to ± 50%. Such departures in the case of well-channeled ions are not only dramatically enhanced but they also exhibit oscillations about a monotonically increasing Z_1 dependence. Such effects of Z_1 oscillations have been observed for W (Ericksson, 1967) and Si (Eisen, 1968) when experiments were carried out for various incident ions of a constant velocity (fig. 6-10). The theoretical curve labeled "Firsov" is calculated from a velocity-proportional stopping power equation derived by Firsov (1959), where $S_e(E)$ is postulated to depend on the impact parameter. His treatment is seen to predict reasonably well the "average" attenuation in $S_e(E)$ though is not successful as far as Z_1 oscillations are concerned. Recently, several groups [Bhalla, 1968; Cheshire, 1968; El-Hoshy, 1968; Harrison, 1968; Winterbon, 1968] have tackled this problem and have

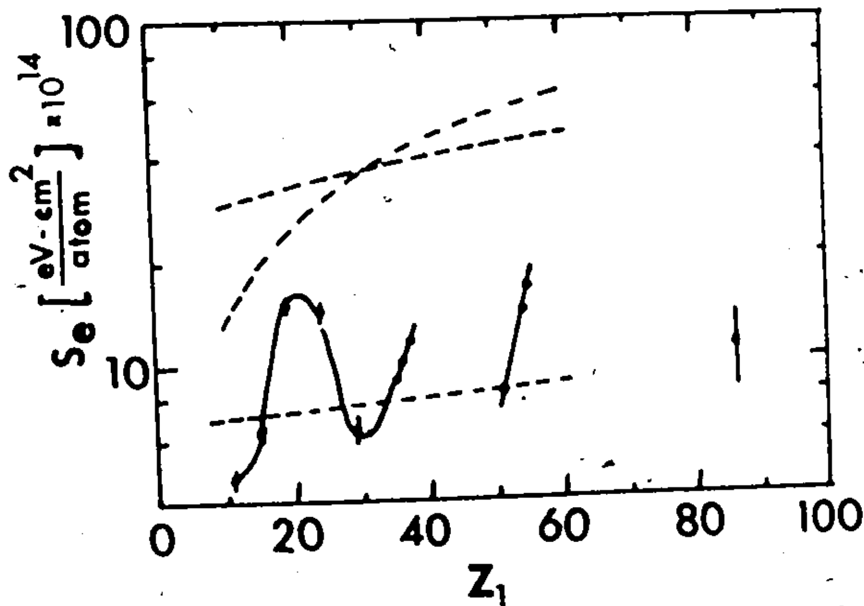

Fig. 6-10 Z_1 dependence of the electronic stopping power, S_e, in W for well-channeled ions injected at a constant velocity of 1.5×10^8 cm/sec along 100 direction (after Ericksson et al. 1967)

correlated the positions of maxima and minima roughly with the ion size. Lindhard and Finnemann (1968) are reported to have developed a quite different theoretical approach that also appears to fit reasonably well with the observed positions of the maxima and the minima. However, none of these theoretical approaches is yet able to accurately predict either the magnitude of the oscillations or their dependence on energy or on channel size (Mayer et al. 1970).

Recently, Whitton (1973) has studied the electronic stopping cross-section of K^{42} in different target materials. He has found that $S_e(E)$ for bcc metals is about five times as large as for fcc metals. This result was attributed to the nature of electron density which is different for bcc and fcc metals. It would appear that the electronic shell effect is the same whether or not the atom is moving (Z_1) or bound in the lattice (Z_2). As pointed out by Whitton (1973), a practical significance of these results lies in the formation of electrical junctions by deliberately channeling energetic ions to their maximum range. Differences in depth of a factor of about 40 to 60 may thus be achieved by a proper choice of the incident ions (Z_1) and of the target (Z_2).

6.6 Summary:

The theoretical framework of LSS, based on the assumption of an amorphous medium and the use of the Thomas-Fermi interatomic potential, is described and shown to predict range profiles to be Gaussian in nature. The agreement with experimental

results for amorphous solids is reasonably good. With crystalline solids, however, deeply penetrating tails have been observed which can be attributed to crystal-lattice effects such that some of the incident ions get into the open spaces between atomic rows (channels) and penetrate deep into the solid without encountering as many random collisions as the other ions. This effect is called channeling.

When energetic ions are implanted into well-aligned single crystals, two separate peaks of ion concentration are sometimes observed which correspond to ions either undergoing random collisions or being well-channeled. These well-channeled ions, when $Z_1 < Z_2$, may end up at interstitial sites without causing lattice damage in their immediate neighbourhood and may then diffuse interstitially at room temperature to cause "supertails", with a depth of about 5-10 μ having been observed for Xe into W. Various factors tend to dechannel incident ions but the maximum range observed with well-channeled ions remains unaffected. The measurement of this $R_{max.}$ directly leads to the estimates of the electronic stopping power and Z_1 oscillations are found to occur; similar oscillations due to Z_2 have also been observed and it is concluded that the oscillations are perhaps caused by the details of the electron density. With a proper choice of the incident ion and the target material, $R_{max.}$ may be varied by a factor as large as 40 to 60, an effect which may prove to be of great practical significance in the formation of electrical junctions.

CHAPTER 7

APPLICATIONS OF ANODIC SECTIONING (PART I): RANGE PROFILES

7.1 General:

It has been mentioned earlier that ranges of energetic heavy ions of keV energies in solids involve extremely small thicknesses and their experimental determination requires an extremely sensitive technique such as anodic sectioning. Since anodic sectioning is possible only for a limited number of substances, most of the work on range profiles has been restricted to these materials only. In the absence of experimental methods, LSS theory, as briefly described in the previous chapter, is employed to predict range profiles. This theory, however, assumes a random arrangement of atoms in the target and predicts well the stopping behaviour only for amorphous materials. For crystalline solids, channeling plays an important role and various experimental conditions such as the total ion dose, target temperature, beam misalignment, surface disorder etc. seriously affect the range profiles. Thus, the most reliable procedure of obtaining range profiles in crystalline solids lies in experimentally determining them by using anodic sectioning. In Chapters 3 and 4, the anodic sectioning behaviour of five metals, V, Mo, Nb, Ta and W has been described. These methods have been utilized in determining the range pro-

files of energetic Kr^{85} with results as described below.

7.2 Experimental

7.2.1 General: In brief, the experimental method of determining the depth distributions of implanted ions in solids consists of:

(a) surface preparation of the target,

(b) bombardment of the target with radioactive ions of chosen energy and dose,

(c) removal of successive layers from the surface of the target by anodic sectioning, and

(d) counting the target activity both initially and after each sectioning.

7.2.2 Surface Preparation: Polycrystalline specimens (cold-rolled) with dimensions of 15×20×0.1 mm, and with a purity claimed to be 99.8%, were used. V, Mo and W were cleaned using a sequence of petroleum ether, dilute nitric acid, and distilled water and were then anodically sectioned at least 4 times at 50 volts. Nb and Ta were first chemically polished using the solution as suggested by Tegart (1959) and then anodically sectioned at least twice at 50 volts. This treatment may be assumed, by analogy with Al (Davies, 1960), to provide a reproducibly flat surface of constant area for thickness calibration and subsequent range-profile measurements.

7.2.3 <u>Bombardment and Counting Techniques</u>: The bombardments were carried out using an accelerator fitted with a radio-frequency (77 mega-hertz) ion source and operated at energies up to 40-keV. This accelerator has no mass separation or electro-static deflection of the beam, though this problem is to some extent compensated by the exclusive use of heavy ions, since impurities would be of low mass, and would create less damage than one predicts from their abundance. Fig. 7-1 shows the target arrangement. A Faraday cup, floating at -800 volts with respect to the target, is used to prevent secondary electrons from leaving the target, as otherwise current readings are too high by a factor of 2 to 3 (an electron leaving the target is electrically indistinguishable from a positive ion striking it). The target is connected to the terminal of a high tension power supply.

The amount of radioactive material in the target was measured using a conventional G.M. counting system. The particular GM probe had a halogen gas as quenching agent and a mica end-window with a thickness of 3.5-4.0 mg/cm^2. Corrections for decay or absorption are not necessary with Kr^{85}.

7.3 Results and Discussion:

Specimens of polycrystalline V and Mo were bombarded at energies ranging from 5- to 40-keV to a dose of about 5×10^{15} ions/cm^2 and the range profiles determined. The results are shown in figs. 7-2 and 7-3, while Table 7-1 enables a comparison

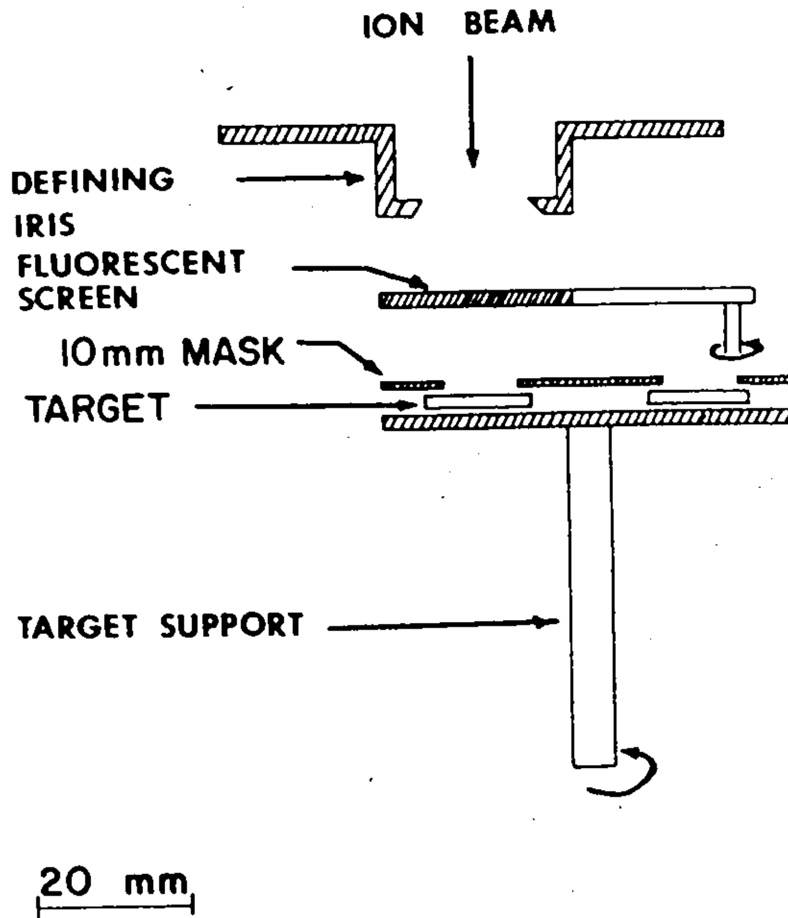

Target Arrangement

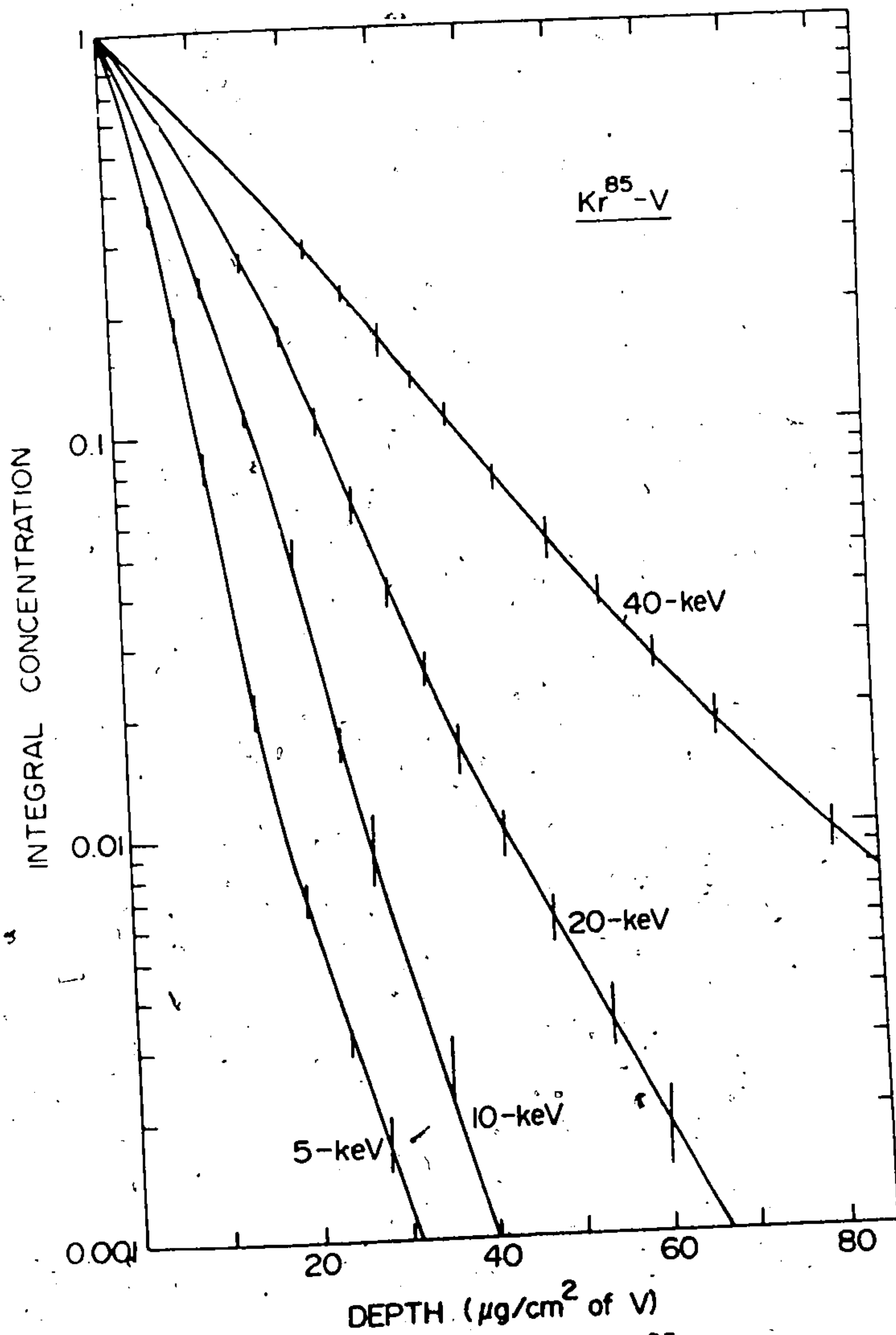

Fig. 7-2 Range profiles of Kr^{85} in polycrystalline V at various energies

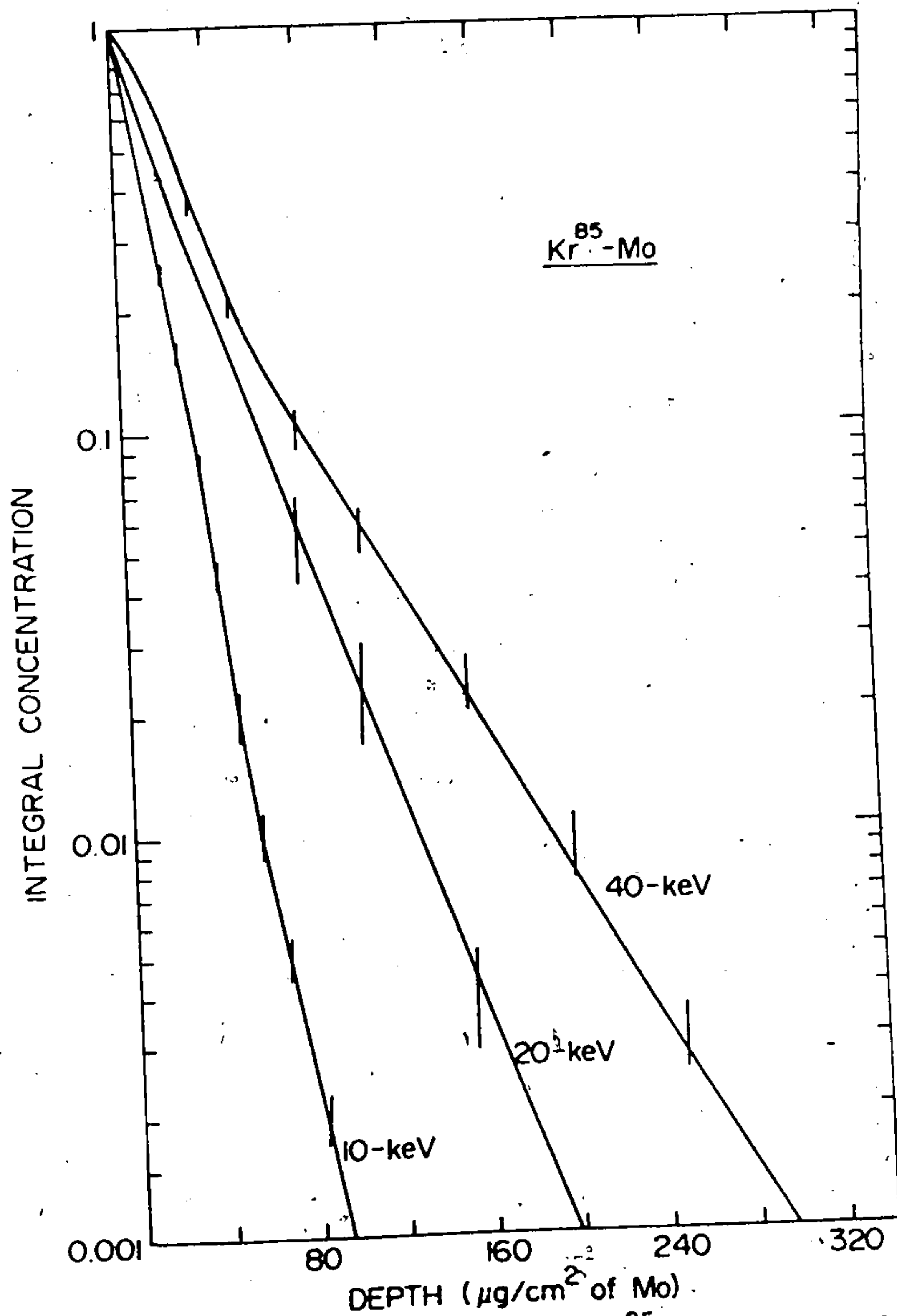

Fig. 7-3 Range profiles of Kr^{85} in polycrystalline Mo at various energies

Table 7-1

Comparison Between Experimental Median Projected Range, R_m, and the Expected Mean Projected Range, $\langle R_p \rangle_{LSS}$

Energy (keV)	R_m, $\mu g/cm^2$		$\langle R_p \rangle_{LSS}$, $\mu g/cm^2$		$R_m/\langle R_p \rangle_{LSS}$	
	V	Mo	V	Mo	V	Mo
5	3.5	-	1.8	-	1.94	-
10	5.4	10.0	2.85	3.75	1.89	2.67
20	8.4	17.0	4.7	6.1	1.79	2.79
40	12.5	26.0	8.0	10.25	1.56	2.53

to be made between the experimental median projected range, R_m, and the expected mean projected range $\langle R_p \rangle$ based on the LSS theory. A large discrepancy is observed between the predicted and the experimental ranges. Similar experiments were also carried out with Nb, Ta and W at 10- and 30-keV at a dose of 5×10^{15} ions/cm^2, with results shown in figs. 7-4 to 7-6 and summarized in Table 7-2. It is seen that the predicted and the experimental ranges agree rather well in the case of Nb, whereas again a

Table 7-2

Comparison of Experimental Median Projected Range, R_m, and the Expected Mean Projected Range $\langle R_p \rangle_{LSS}$

Energy (keV)	R_m, $\mu g/cm^2$			$\langle R_p \rangle_{LSS}$, $\mu g/cm^2$			$R_m/\langle R_p \rangle_{LSS}$		
	Nb	Ta	W	Nb	Ta	W	Nb	Ta	W
10	4.4	9.7	13.0	3.7	5.3	5.35	1.19	1.83	2.43
30	8.2	20.8	38.4	8.2	11.6	11.65	1.0	1.80	3.30

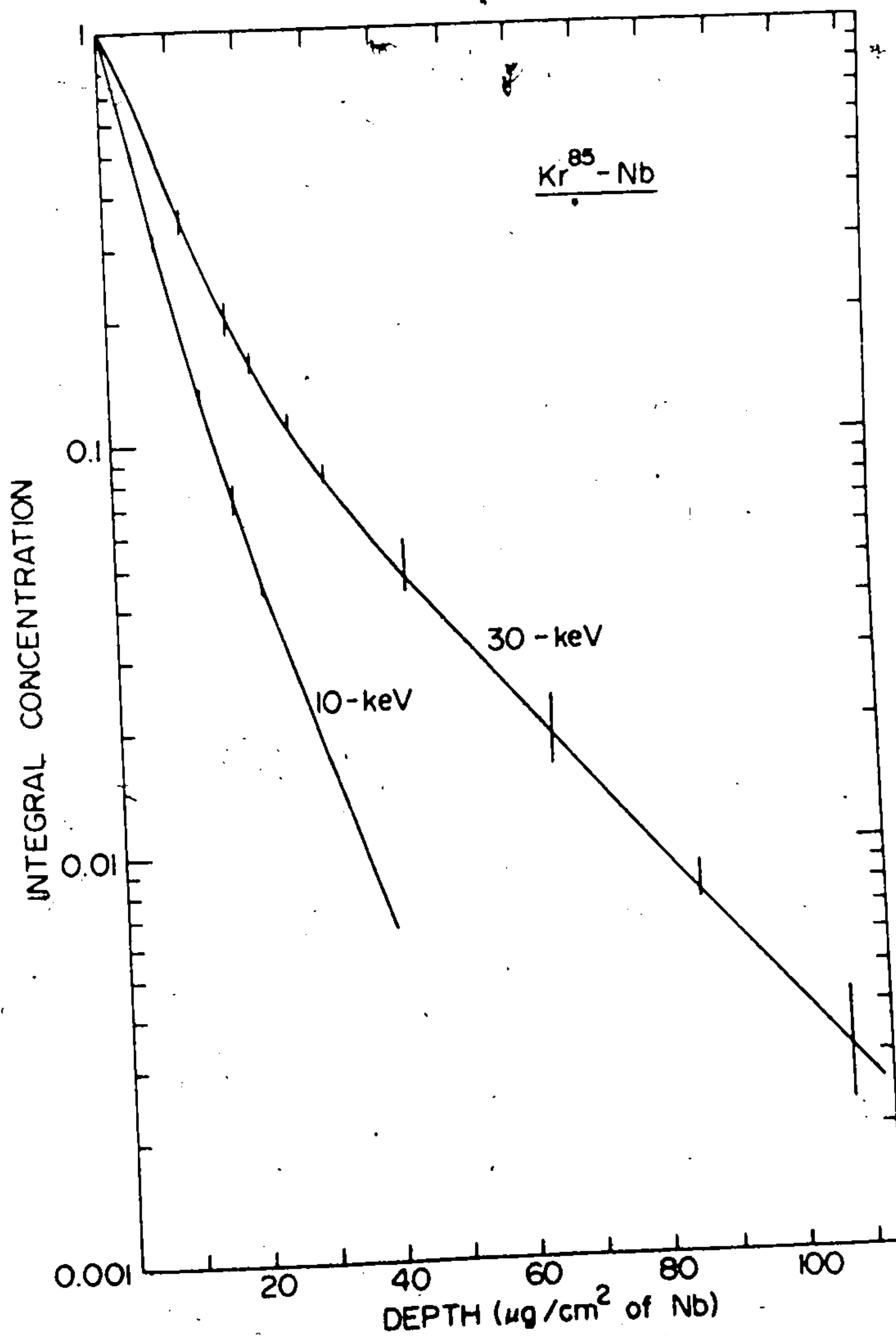

Fig. 7-4 Range profiles of Kr^{85} in polycrystalline Nb at 10- and 30-keV

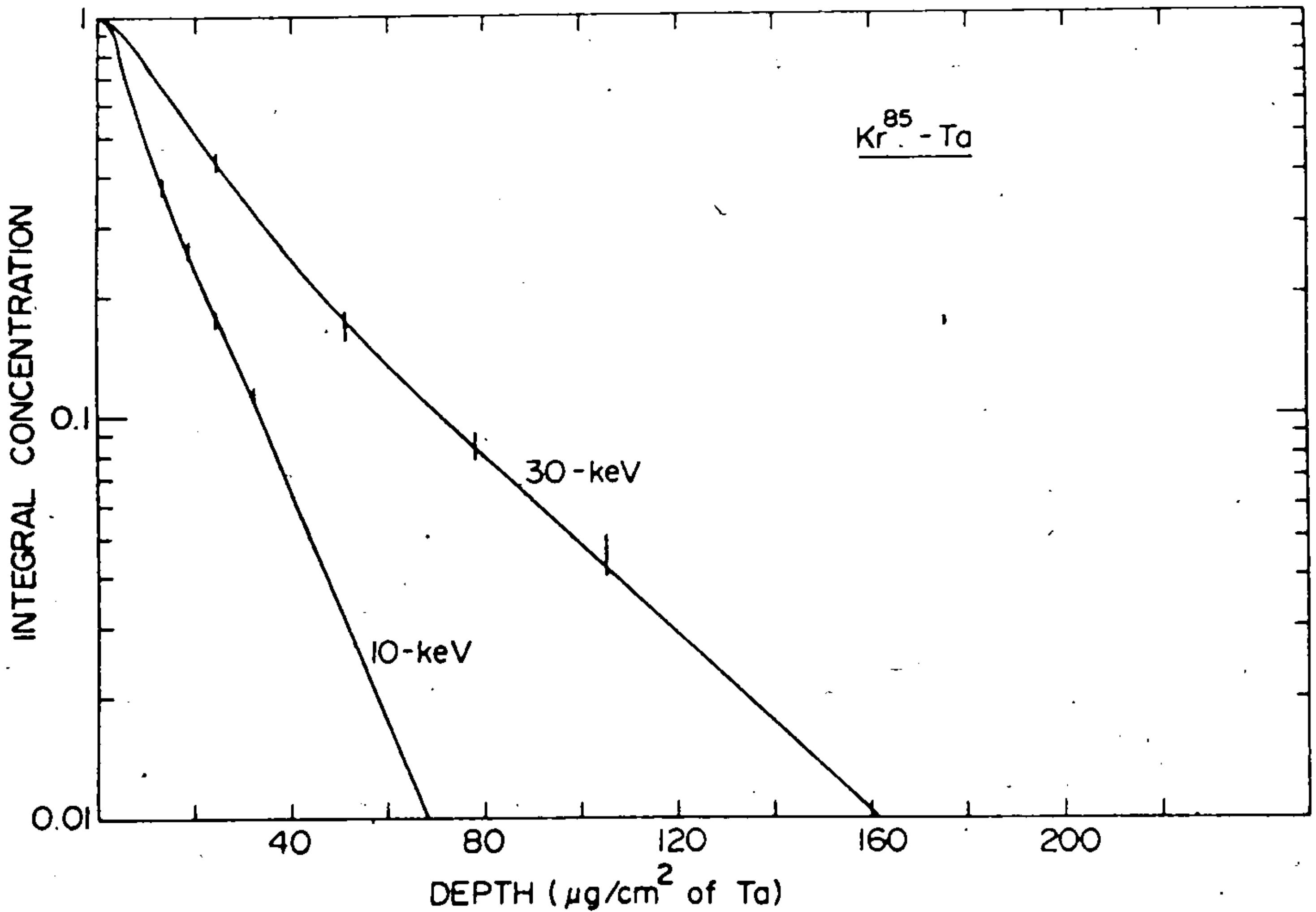

Fig. 7-5 Range profiles of Kr^{85} in polycrystalline Ta at 10- and 30-keV

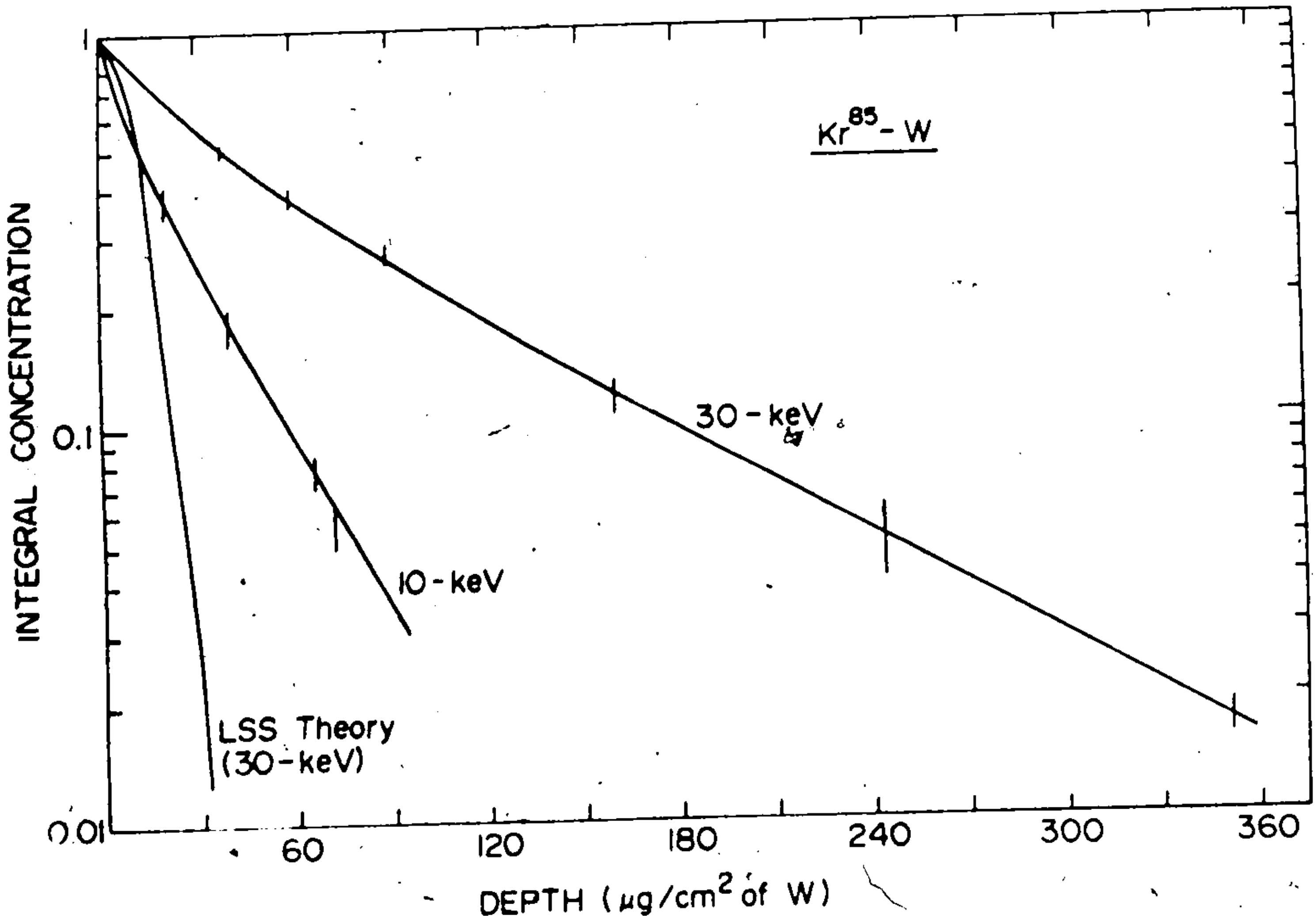

<u>Fig. 7-6</u> Range profiles of Kr^{85} in polycrystalline W at 10- and 30-keV

discrepancy is present for Ta and W. Similar differences have also been observed by other workers, and the results for Al and W, as obtained previously by Davies et al.(1960,1963) are summarized in Table 7-3 along with the present results.

Table 7-3

Summary of Comparison Between R_m and $\langle R_p \rangle_{LSS}$

Energy keV	Metal	R_m μg/cm^2	$\langle R_p \rangle_{LSS}$ μg/cm^2	$R_m / \langle R_p \rangle_{LSS}$	Reference
20	Al	4.5	3.67	1.23	Davies (1960)
20	W	20.0	8.65	2.32	Davies (1963)
20	V	8.4	4.7	1.79	Present
20	Mo	17.0	6.1	2.79	Present
30	Nb	8.2	8.2	1.0	Present
30	Ta	20.8	11.6	1.80	Present
30	W	38.4	11.65	3.30	Present

The theoretical ranges are based, as was discussed in chapter 6, on the assumption that the target is amorphous. The large differences between the experimental and theoretical ranges are therefore readily attributed to the crystal-lattice effects. The fact that the $R_m/\langle R_p \rangle_{LSS}$ for Nb is near unity should not be taken as meaning that channeling is absent. Rather, channeling is a major effect, as is shown clearly by the non-Gaussian appearance of fig. 7-4. It appears, however, that the proportion of channeling is small with the particular Nb specimens used so that R_m is largely unaffected.

7.4 Evidence for Channeling:

Channeling is already a well established effect so it will not be discussed further except with regard to whether the present evidence for channeling is spurious.

7.4.1 Effect of Radiation Damage: We ask first of all whether the supposed channeling is simply an artefact of the anodic sectioning procedure being damage sensitive. Thus, supposedly large ranges could indicate a reduction in the amount of metal removed for a given anodizing voltage. This problem has been considered previously (section 4.5), where the thickness calibrations were found to be generally independent of the bombardment dose, except perhaps at very high doses ($\geq 10^{17}$ ions/cm^2). We take this result as confirming that the large ranges observed in crystalline V, Ta, Mo and W are indeed due to channeling.

7.4.2 Use of Amorphous Targets: A second approach to verifying the validity of the present results is to determine range profiles in amorphous materials and again compare the results with the predictions based on the LSS theory. The discrepancy should now be minimal.

As shown in Chapter 5, thick anodic films formed on V are amorphous as formed. Implantations were therefore carried out at 20- and 40-keV to various doses after forming known thicknesses of anodic films on V, and the range profiles were then determined using the conventional transmission technique. A problem arose in these experiments that when the dose exceeded about 10^{15} ions/cm^2, some sputtering of the anodic films was

observed. Only about 10^{14} ions/cm^2 were accordingly implanted in the anodized specimens. The profiles thus obtained are shown in fig. 7-7, where the dashed curves correspond to the LSS predictions (using Edgeworth's expansion with terms up to that including the fourth central moment) and the solid curves are the experimental results. The agreement between theory and experiments is, in general, excellent and we again conclude that the discrepancies with the crystalline targets were due to channeling.

7.4.3 Dose Effect: It has been argued above that when energetic ions are incident upon a crystalline target, they will partly undergo nuclear collisions and will partly get into channels and penetrate deeply into the target. Ions incident at a low dose obviously have a higher probability of finding open channels since the target is initially devoid of angstrom-scale disorder. High doses, however, cause some of the target atoms to be displaced and there should then be a smaller probability of channeling. An effect related to dose was therefore sought by carrying out the following two types of experiments.

In the first experiment, crystalline Mo targets were implanted with Kr^{85} ions at 10-keV and doses varying from about 4×10^{13} ions/cm^2 to 4×10^{16} ions/cm^2. The resulting profiles are shown in fig. 7-8, where the predicted profile based on LSS theory is also shown. Table 7-4 enables a comparison to be made between the experimental median projected range, R_m, and the expected mean value $\langle R_p \rangle_{LSS}$ which is taken here as

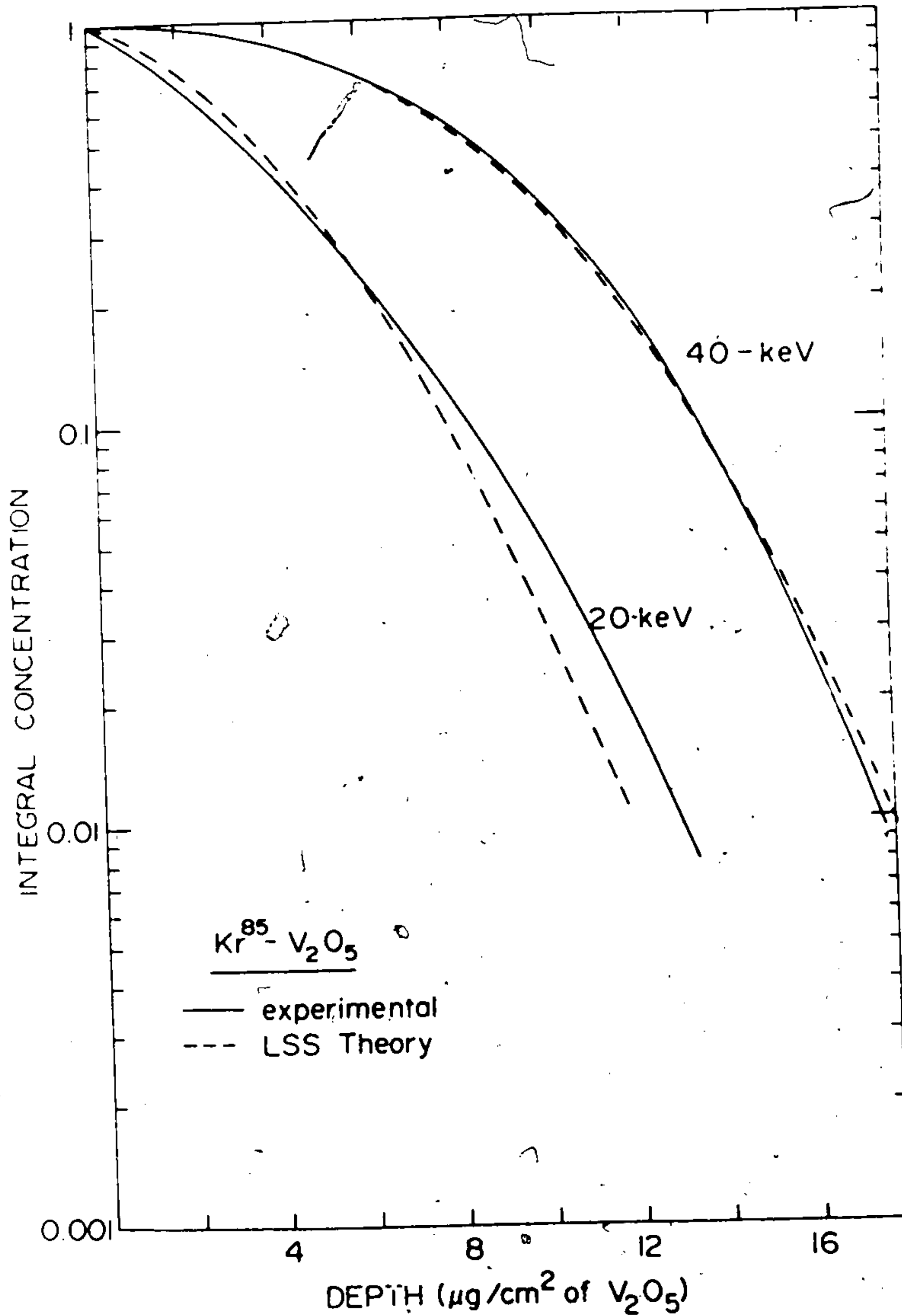

Fig. 7-7 Range profiles of Kr^{85} in anodized V at 20- and 40-keV. Solid: experimental curves. Dashed: curves based on LSS theory

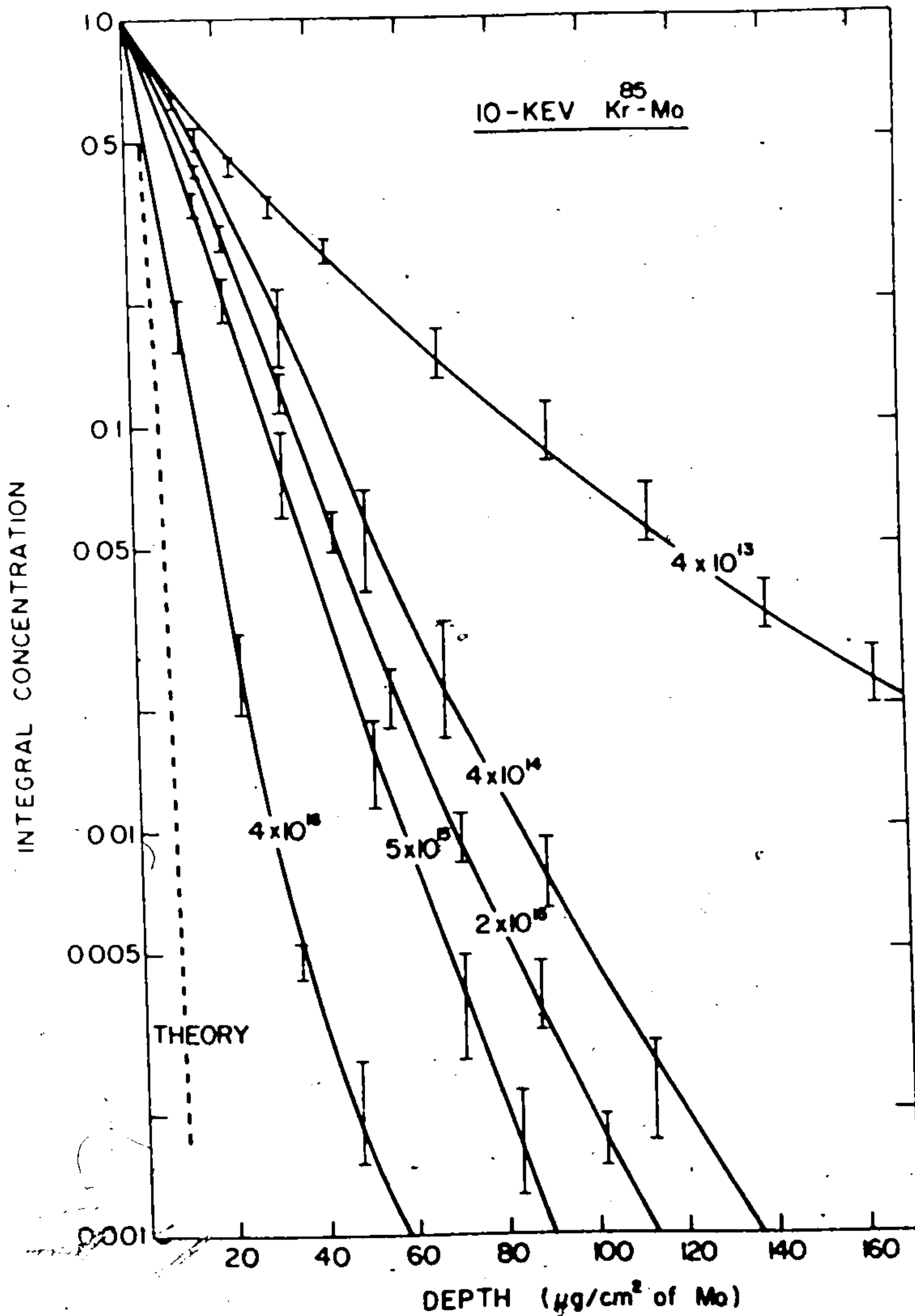

Fig. 7-8 Effect of varying ion dose on range profiles of Kr^{85} in polycrystalline Mo at 10-keV. Solid: experimental curves. Dashed: LSS theory

3.7 μg/cm^2 (LSS theory). R_m is seen to be a factor of 5.4

Table 7-4

Comparison of R_m and $\langle R_p \rangle_{LSS}$ for Mo for Various Doses at 10-keV

Kr^{85} dose ions/cm^2	R_m μg/cm^2 of Mo	$\langle R_p \rangle_{LSS}$ μg/cm^2 of Mo	$\frac{R_m}{\langle R_p \rangle_{LSS}}$
4×10^{13}	20.0	3.7	5.4
4×10^{14}	15.5	3.7	4.2
2×10^{15}	12.5	3.7	3.4
5×10^{15}	10.0	3.7	2.7
4×10^{16}	4.0	3.7	1.1

larger than $\langle R_p \rangle_{LSS}$ at the lowest dose (4×10^{13} ions/cm^2). By comparison, for polycrystalline W, at low doses, Davies et al. (1963) found $R_m/\langle R_p \rangle_{LSS}$ to have an average value of 2.3, while for single-crystalline W with <111> or <100> orientations, Kornelsen et al. (1964) found the ratio to be 10 to 12.

R_m decreases with increasing dose such that for a dose of about 4×10^{16} ions/cm^2, it is comparable to the theoretical value. This is the expected result if channeling plays a role.

In the second experiment, specimens were bombarded with 10-keV radioactive Kr^{85} ions to a dose of 5×10^{15} ions/cm^2 and the range profile was determined. Then the same specimens were first prebombarded with inactive 10- or 40-keV Kr ions to doses of 5×10^{15}, 5×10^{16} and 5×10^{17} ions/cm^2 so as to create

defects, and finally with radioactive 10-keV Kr^{85} ions (5×10^{15} ions/cm^2). The results are given in fig. 7-9 and reveal that prebombardment moves the experimental curve towards the predicted LSS curve. Again, the result is consistent with channeling.

7.5 Estimation of Corrosion Rates:

Knowing the range profiles of energetic Kr^{85} in polycrystalline V, Nb, Ta, Mo and W, it becomes possible to estimate the rate of metal dissolution in any solvent, for example, the film-dissolving solutions as used for sectioning. One then implants Kr^{85} into the metals and exposes them to the dissolving reagent directly and determines the loss of activity as a function of time. This loss of activity can be, knowing the range profiles, converted into the total amounts of metal dissolved. One could, on the other hand, use the data of the type shown in fig. 4-1 and then estimate the rate of metal dissolution (i.e. the corrosion rate). Final results are given in Table 7-5.

Table 7-5

Rate of Metal Corrosion in Saturated KOH Solution

Metal	Dissolution Rate Å/min
V	$\lesssim 0.3$
Nb	$\lesssim 3.0$
Mo	$\lesssim 0.3$
Ta	$\lesssim 0.3$
W	$\lesssim 0.4$

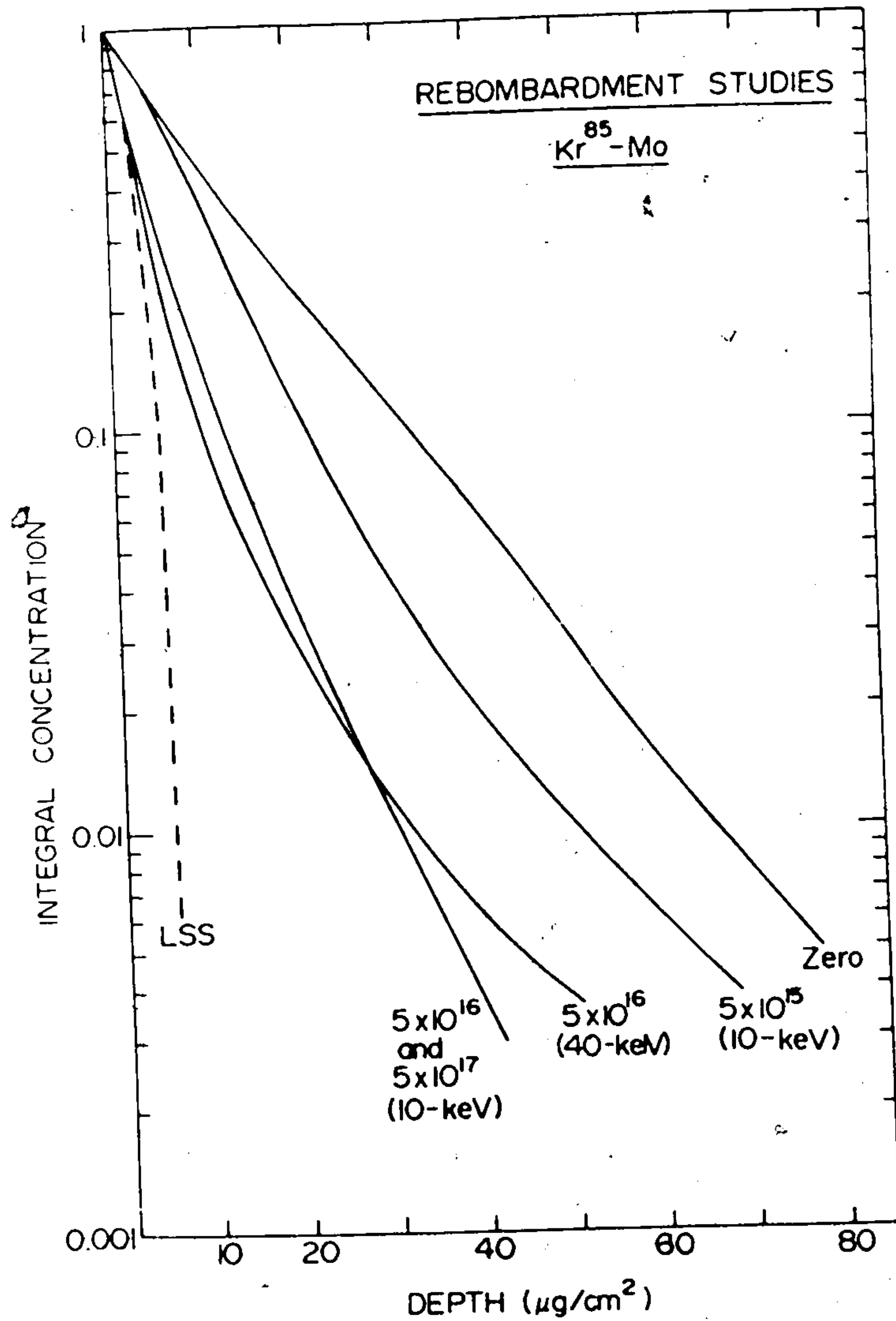

Fig. 7-9 Effect of prebombardment on range profiles of Kr^{85} in polycrystalline Mo

7.6 Analytical Forms for Range Profiles:

The range profiles obtained in the energy interval 5-40 keV for Kr^{85} in the five metals under investigation have the common feature that the profiles tend to become exponential in their tails. Attempts were therefore made to fit the experimental profiles to the convenient analytical form,

$$C^{int.} = A \exp(-\frac{x}{B}) + C \exp(-\frac{x}{D}) \qquad (7-1)$$

where x is the depth in $\mu g/cm^2$ in metal, and A, B, C and D are constants. $C^{int.}$ is, as usual, the fraction of ions not yet stopped for depth x and the results of curve fitting are given as follows for energies of 20- to 40-keV.

Metal	Ion Energy (keV)	Expression for $C^{int.}$
V	40	$0.53 \exp(-\frac{x}{14.3}) + 0.47 \exp(-\frac{x}{20.8})$
Nb	30	$0.72 \exp(-\frac{x}{6.9}) + 0.28 \exp(-\frac{x}{23.8})$
Ta	30 (for $x \geq 10 \frac{\mu g}{cm^2}$)	$0.37 \exp(-\frac{x}{16.6}) + 0.63 \exp(-\frac{x}{40.0})$
	(for $x < 10 \frac{\mu g}{cm^2}$)	$0.46 \exp(-\frac{x}{16.6}) + 0.63 \exp(-\frac{x}{40.0})$
Mo	20	$0.23 \exp(-\frac{x}{14.5}) + 0.77 \exp(-\frac{x}{29.4})$
	40	$0.47 \exp(-\frac{x}{23.2}) + 0.53 \exp(-\frac{x}{50.0})$
W	30	$0.38 \exp(-\frac{x}{25.0}) + 0.62 \exp(-\frac{x}{9.8})$

One could, if desired, identify the first term in eqn. (7-1) with random stopping and the second term with channeling.

We do not regard this as correct because the random and the channeled behaviour are not independent of each other. Rather, the analytical expressions should be taken at their face value, namely, as empirical descriptions of the range profiles. Their main use is foreseen to be in providing a simple means of evaluating erosion or corrosion as discussed in Section 7.5.

7.7 Summary:

Experimental range profiles have been obtained for energetic Kr^{85} ions in the energy range 5-40 keV for V, Mo, Nb, Ta and W. The ranges thus obtained in polycrystalline specimens differ considerably from those predicted on the basis of the LSS theory which, in its formulation, assumes an amorphous target. Such differences were not observed when measurements were made using amorphous anodic films formed on V. Likewise, the range profiles approached the LSS profiles when either the dose was increased or the target was prebombarded with inactive Kr ions. The differences observed with polycrystalline specimens were therefore attributed to crystal-lattice effects. The knowledge of the range profiles was subsequently used to estimate the corrosion rates of the five metals in sat. KOH with values lying in the region 0.3 to 3 Å/min.

Finally, the range profiles obtained in the energy interval 20-40 keV have been fitted to an analytical expression of the form,

$$C^{int.} = A \exp(-\frac{x}{B}) + C \exp(-\frac{x}{D})$$

and the constants A, B, C and D obtained for all five metals

being considered here. It is emphasized that this expression should not be interpreted as involving one term for randomly stopped ions and one for channeled ions.

In the present chapter, only the penetration behaviour of the implanted ions is considered. Other related effects of ion-bombardment may also occur during the slowing down process of energetic ions. For example, during high-dose ion implantation, some target atoms may be ejected from the surface. This phenomenon is known as "sputtering" and will be discussed in the next chapter.

CHAPTER 8

APPLICATIONS OF ANODIC SECTIONING (PART II): SPUTTERING

8.1 General:

In studies of ion implantation, energetic ions, in the keV energy range, are made incident upon the target. These ions penetrate the surface of the target and gradually lose their energy through a series of collisions with the target atoms. These collisions are called the "primary collisions", and when the incident ions are radioactive in nature, these primary collisions lead to an experimentally measurable range profile such as described in the previous chapter.

However, the above picture of the slowing down of incident ions has other important aspects. During primary collisions, the ions impart a large amount of energy to the target atoms. Whenever this imparted energy exceeds a particular threshold energy, roughly 25 eV, the atoms involved in the collision are removed a sufficient distance from their original site that they remain permanently displaced (unless, of course, thermal motion is possible). In addition, provided the target atoms recoil with a high enough energy they propagate the collisions to other target atoms, thereby creating a volume of recoiling atoms having dimensions similar to

$<\Delta R_p>\cdot<y^2>$, where $<y^2>$ is the mean square projected straggling perpendicular to the ion beam. To some extent the incident momentum carried by the ions will always become reversed so that target atoms will be ejected from the surface over a wide range of angles and energies. This process of atomic ejection during bombardment is called "sputtering" and a sputtering coefficient "S" can be defined as the number of atoms ejected per incident ion. A simplified scheme of collisions leading to the sputtering process is shown in fig. 8-1. Sputtering must be considered in any study of ion implantation, for it can lead to significant changes in the target surface.

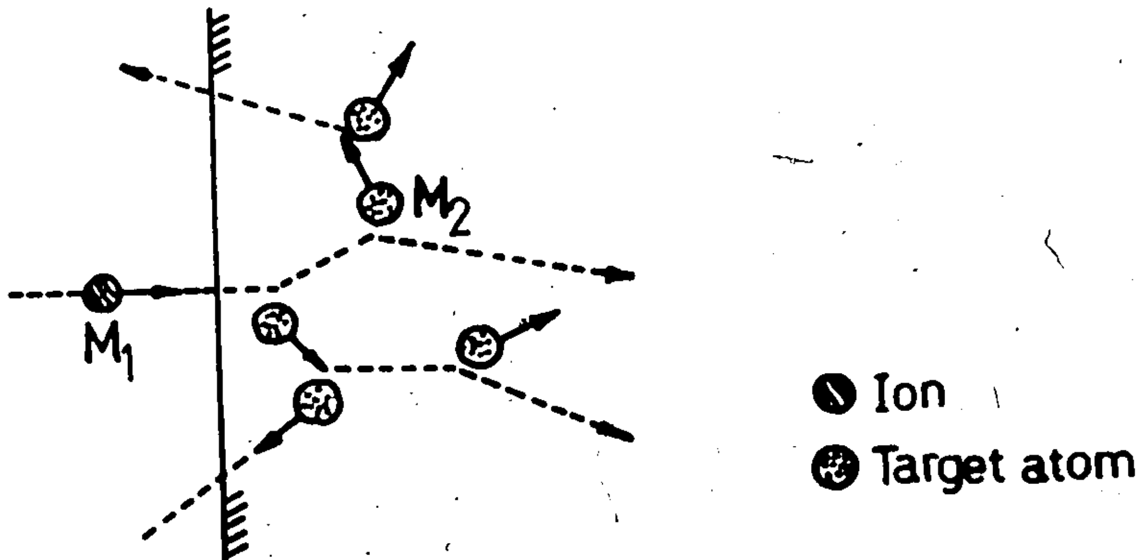

Fig. 8-1 Collisions leading to sputtering process

Thompson (1968) has determined the energy distribution of atoms sputtered from Au and Cu and has established that a peak occurs at very small energies (∿ 5 eV). During slowing down, there is evidently a distribution of energies such

that the lower energies predominate. Moreover, since atoms moving with low energies have atomically small ranges, they can be sputtered only if originally located within a few atomic layers from the target surface.

We will here describe experiments in which the anodic sectioning of V led to an unintentional study of sputtering behaviour. Our original objective was to measure, as part of chapter 7, range profiles by the transmission method where anodic films of various thicknesses are first grown on metals and only then labeled with radioactive Kr^{85}. The activity is then counted before and after dissolving the film to yield the range profiles in amorphous anodic films. The present results followed as an accident which are, as already implied, unintentional in the sense that studying sputtering was not one of the original aims of this research. They are, however, important enough to discuss in detail, for it will emerge that we have succeeded in measuring 'S' as a function of dose with perhaps more sensitivity than in any preceding work.

8.2 Factors Affecting a Sputtering Coefficient:

The sputtering coefficient, S, i.e. the number of ejected atoms per incident ion, has been found to depend on several factors such as the nature of the ions and target, the ion energy, the angle of incidence, etc., some of which will now be discussed briefly.

8.2.1 Ion Energy: The sputtering coefficient 'S' increases with ion energy as shown in figure 8-2. Thus, S initially

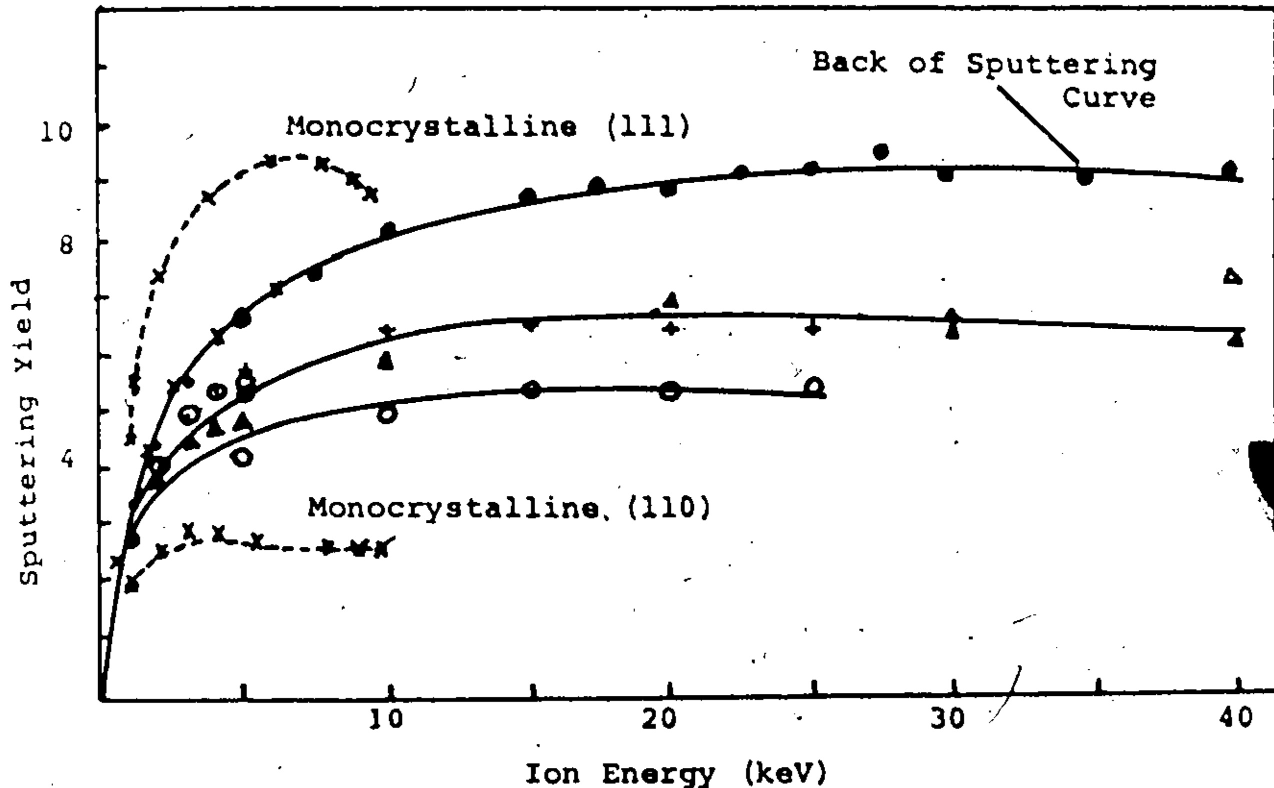

Fig. 8-2 Variation of the sputtering yield with ion energy

increases rather rapidly, reaches a broad maximum and then, at high energies, decreases again. The initial increase is understandable, in a qualitative sense, as arising from the increasing value of $(\frac{dE}{dx})_n$ [see fig. 6-1). Likewise, the decrease is reasonable either on the grounds that the ions penetrate deeply before interacting, or more correctly because $(\frac{dE}{dx})_n$ decreases for very high energies.

8.2.2 Target Material: Laegried and Wehner (1961) and Rosenberg and Wehner (1962) determined the sputtering yield for various target materials with noble gases as incident ions at 400-eV. Their results for noble gas ions are shown in fig. 8-3 and can be successfully correlated with the state of electron concentrations in the "d" shells. Later, Almén and Bruce (1961) used 45-keV Kr ions and found essentially similar behaviour. These correlations with 'd' shell electrons were attributed to the fact that ranges are supposedly larger in targets with more open electronic structure, an effect which would tend to lower the sputtering yield for such materials. In more modern terms, the correlations would be justified in terms of surface binding energies (section 8.3.2) since these have a similar periodicity to the electron structure.

8.2.3 Incident Ion: Almén and Bruce (1960) determined the sputtering yield of Cu, Ta, and Ag at 45-keV for various incident ions and their results are shown in fig. 8-4. Yields

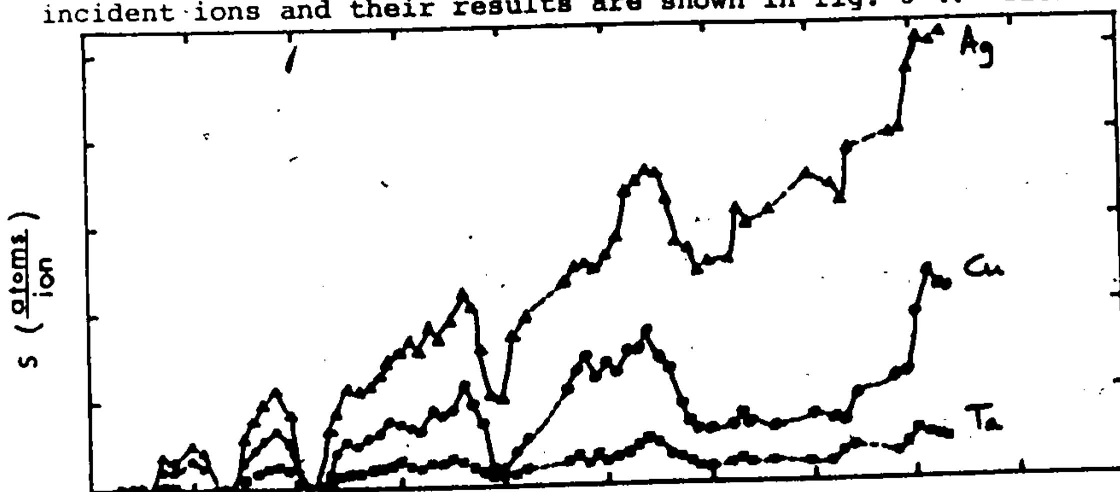

Fig. 8-4 Variation of the sputtering yield with atomic number of the incident ions at 45 keV for Cu, Ag and Ta. After Almén and Bruce, 1960)

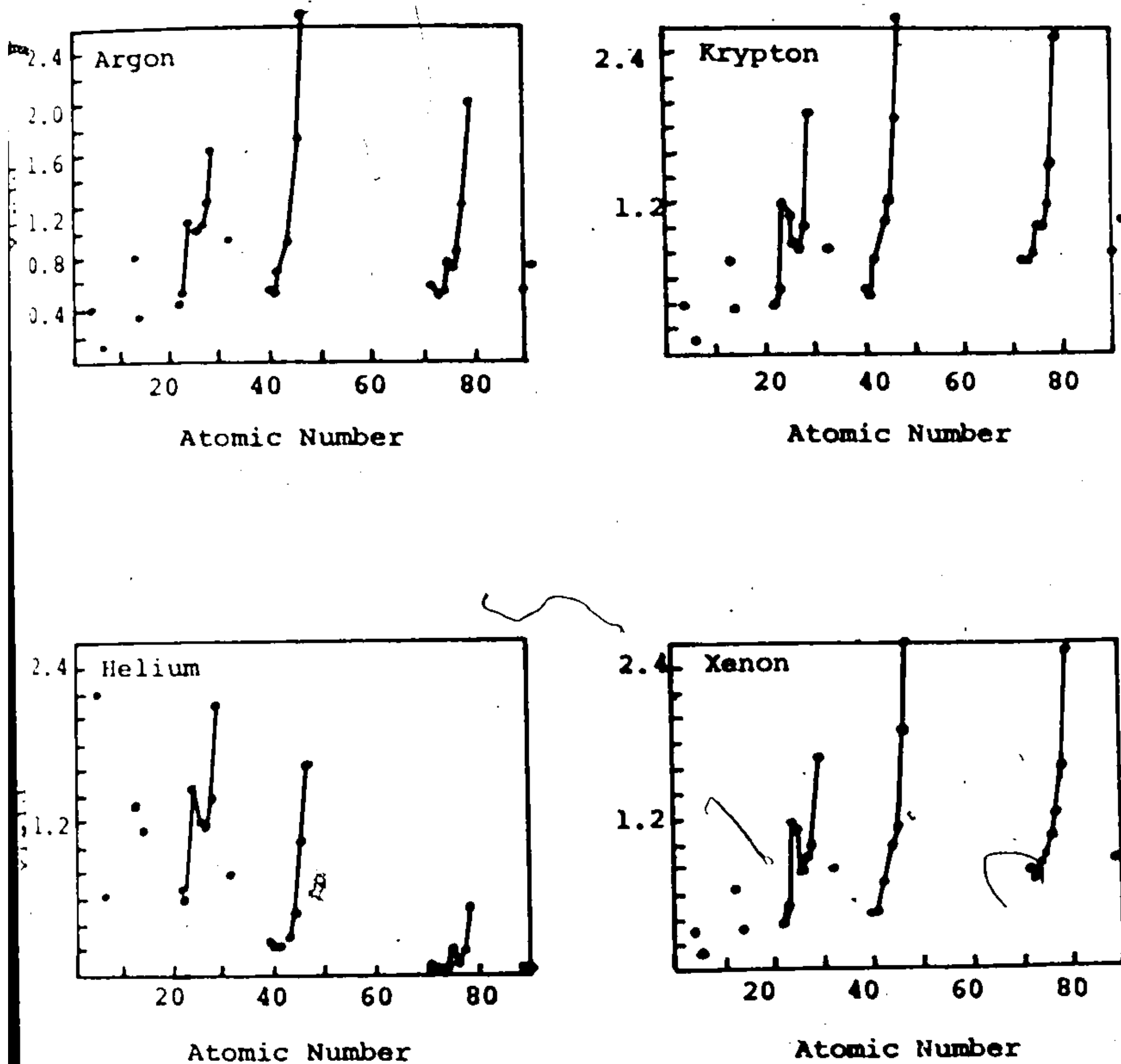

Fig. 8-3 Variation of the sputtering yield with atomic number of the target for 400 eV noble gas ions. (After Laegried, 1961; Rosenburg, 1962).

are found to vary periodically, with the maxima occurring for inert gas. Rol et al. (1960a) found similar results at lower energies (5-25 keV). It is not clear how such results can be justified in "modern" terms, as surface binding energies are not relevant here and there is in fact recent evidence (Anderson et al. 1972) that "Z_1 oscillations" are experimental artifacts due to the beam current being too low.

8.2.4 Ion Dose: Ideally speaking, sputtering experiments should involve very low doses (< 10^{14} ions/cm^2) so that the targets remain undamaged. When high doses are employed, the ions entering the target at later stages of the experiment encounter not only trapped ions but also the damage caused by them. Thus, the sputtering coefficient is in principle dependent on the dose. This is particularly true in the case of alloy- or oxide-targets since the various components of the target may have different sputtering yields, thereby causing not only a change in damage with dose but also a change in composition (Gillam, 1959; Naguib and Kelly, 1972). This factor will be further discussed later.

Most results are, by necessity, obtained using prolonged bombardment so that the concepts of low dose and an undamaged surface are not valid. In addition, channeling has a pronounced influence on the sputtering yield, and is itself strongly dose dependent. Therefore, one must consider carefully the effects of dose when comparing experimental results with the calculated yields based on theoretical considerations.

Several theoretical treatments of the sputtering process have been developed in recent years but only two, those of Rol et al. (1960b,1960c) and of Sigmund (1968,1969), will be discussed here. Both theories use the concept of momentum transfer from the incident ions to the target atoms and assume an amorphous target. That is, they exclude the anisotropy of the energy transfer within a crystal lattice.

8.3 Theories of Sputtering:

8.3.1 Theory of Rol, Fluit and Kistemaker:

Rol et al. (1960b, 1960c) proposed that only the collisions between ions and lattice atoms which occur near the target surface are responsible for sputtering. The sputtering coefficient is then proportional to the average energy dissipated by the incident ion in the first few atomic layers by nuclear scattering events. Since the probability that a collision will occur near the surface is inversely proportional to the mean free path, λ, of the ion, the sputtering coefficient may be expressed as

$$S = \frac{K}{\lambda \cos\phi} \quad \frac{M_1 M_2}{(M_1+M_2)^2} \cdot E \qquad (8\text{-}1)$$

where ϕ is the angle of incidence and K is an empirical constant depending on the target. Almén and Bruce (1961) examined their results on sputtering yields in terms of this theory for 10- to 65-keV Ne^+, Ar^+, and Xe^+ ions and reached the conclusion that

$$K = A \exp[-BM_1^{1/2}E_b/(M_1+M_2)] \qquad (8\text{-}2)$$

where A and B are constants and E_b is the surface binding energy of the target atoms. For amorphous and polycrystalline materials, and at low energies, the theoretical estimates are in fairly good agreement with the experimental results. However, Rol et al. have calculated λ from a hard-sphere approximation so that the agreement must be considered in part fortuitous. In addition, the effects of electronic excitation in the high energy region and of anisotropy of the energy transfer within the crystal lattice have been ignored. The theory may, however, be improved either by using a power-law approximation to calculate λ or better still by using experimental values of ion ranges in place of λ (Lam, 1971). In the latter case, crystallographic effects are in part allowed for. Nevertheless, the theory always retains one crucial weakness - the constant K is empirical and absolute sputtering coefficients are therefore not deducible.

8.3.2 Sigmund's Theory: Sigmund (1968,1969) has recently formulated a completely analytical approach to the estimation of sputtering coefficients using the methods of transport theory and considering a random target with a plane surface. A Boltzmann-type equation was employed together with the power-law approximation to the Thomas-Fermi cross-section and a planar-potential barrier at the surface.

This approach consists of four steps:

(1) determining the amount of energy deposited by energetic particles (ion and recoil atoms) near the surface;

(2) deducing how many low-energy recoil atoms will arise;

(3) determining how many of these atoms come to the very surface; and

(4) selecting those atoms that have sufficient energy to overcome the surface binding forces.

The essential quantities required are the scattering cross-sections for low-energy atoms and ions near the end of their trajectories, the scattering cross-sections for high-energy atoms and ions, and the surface binding energy. Two main stages of the collision cascade are distinguished - one at high energies consisting of the primary ion and all recoil atoms of comparable energies, and second, the creation and slowing down of low-energy recoils that constitute the major part of all atoms set in motion. High-energy collisions are characterized by a Thomas-Fermi (whence power law) type of cross-section, while a Born-Mayer type of cross-section is used for low-energy atoms. Electronic stopping is included whenever needed for high energy scattering. Following this approach, Sigmund obtained the following analytical expression for the sputtering coefficient:

$$S = 0.042 \frac{\alpha \cdot S_n(E) \cdot 10^{16}}{E_b} \qquad (8.3)$$

where α depends on m and $\frac{M_1}{M_2}$ as shown in Fig. 8-5, E_b is the surface binding energy in eV, and $S_n(E)$ is the nuclear stopping power in erg/cm given, as in section 6.2.3, by

$$S_n(E) = \frac{C}{1-m} \Lambda^{1-m} E^{1-2m} \qquad (8\text{-}4a)$$

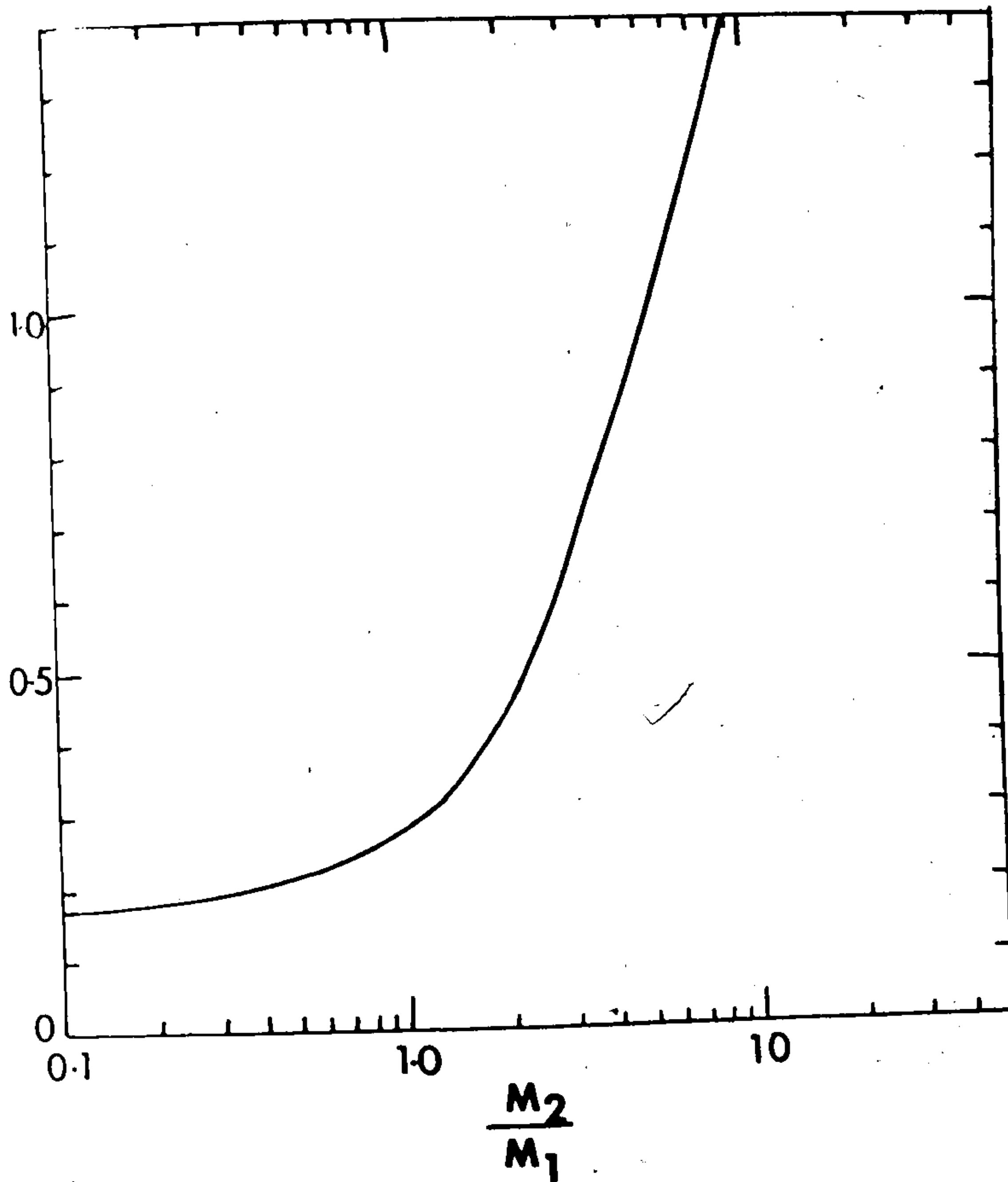

Fig. 8-5 Variation of α with mass ratio in the elastic collision region (after Sigmund, 1968)

for power-law scattering. $S_n(E)$ can also be written as

$$S_n(E) = \frac{(\rho/R)\ s_n(\epsilon)}{(\epsilon/E)\cdot N} = \frac{4\pi Z_1 Z_2 e^2 a M_1}{(M_1+M_2)} s_n(\epsilon) \qquad (8-4b)$$

where $s_n(E)$ is the reduced nuclear stopping cross-section, which is a universal function tabulated by Lindhard et al. (1968) and here reproduced in Table 8-1. By combining eq. (8-3) and (8-4b) we obtain an expression for S in reduced units:

$$S = \frac{\alpha M_2(\rho/R) s_n(E)}{1.42(\epsilon/E)E_b} \qquad (8-5)$$

Table 8-1

Reduced Nuclear Stopping Cross-Section $s_n(\epsilon)$ (After Lindhard et al. 1963)

ϵ	$s_n(\epsilon)$
0.002	0.120
0.004	0.154
0.01	0.211
0.02	0.261
0.04	0.311
0.10	0.372
0.15	0.393
0.20	0.403
0.40	0.405
1.0	0.356
2.0	0.291
4.0	0.214
10.0	0.128
20.0	0.0813
40.0	0.0493

where R is in $\mu g/cm^2$, E is in keV, and E_b is still in eV. The ratios ρ/R and ϵ/E are tabulated by Winterbon (1968) with selected values reproduced in Table 6-2.

The main advantage of Sigmund's theory is that the calculation of S does not require a computer, being possible over a wide range of ion energies using only a Table (Table 8-1) and a graph (fig. 8-5).

8.4 Experimental Results and Discussion:

8.4.1 General: As was mentioned earlier (section 8.2.4), the ion dose may play a vital role in the numerical values of a sputtering coefficient. With binary materials, this will be due in part to the fact that, due to differential sputtering, the various components may have somewhat different sputtering yields, thereby causing a change in the target stoichiometry as the bombardment progresses. For example, when Naguib and Kelly (1972) bombarded crystalline pellets of V_2O_5 and MoO_3 with Kr ions the final structures obtained were found to be V_2O_3 and MoO_2 respectively, associated with marked increases in the electrical conductivity. Similar results will now be described with anodic films on V.

8.4.2 Variable Dissolution Rates: In the previous chapter, range profiles in various metals were described and the effects of varying the total ion dose studied. Similar work was also initiated with the amorphous anodic films formed on V. It was found, however, that the effects of varying the total ion dose could not be studied in the latter case for two reasons.

Firstly the bombarded anodic film showed variable dissolution behaviour such that at high doses ($\geq 8\times10^{15}$ ions/cm^2), the films could not be completely removed. This result is in sharp contrast with those described earlier with unbombarded films (section 4.2.2), where the films were found to be completely dissolved in about 30 seconds. Secondly, severe sputtering as evidenced by changes in the interference colours occurred.

Knowing the total film thickness and time of film dissolution, average dissolution rates could be determined as a function of ion dose, with results as given for 12-volt films implanted with 40-keV Kr^{85} ions in Table 8-2. At low doses ($\sim 4\times10^{13}$ ions/cm^2), the dissolution rate is almost unaffected but as the total dose is increased, the average dissolution rate decreases until at high doses ($\geq 8\times10^{15}$ ions/cm^2), the film could not be completely removed. At very high doses ($\sim 3.2\times10^{16}$ ions/cm^2), the films hardly dissolved at all, indicating that the structure had markedly changed and a structural investigation was thus found necessary.

8.4.3 Structural Investigation: The ion bombardment experiments described above were repeated and a correlation between the dissolution behaviour and the film structure was attempted using reflection electron diffraction (RED). The results are shown in figs. 8-6 (a-d). It is seen that up to a dose of about 4×10^{15} ions/cm^2, the film was amorphous (fig. 8-6a) as expected. At higher doses of 8×10^{15} and 1.6×10^{16} ions/cm^2, however, the amorphous halos were somewhat sharper (fig. 8-6b),

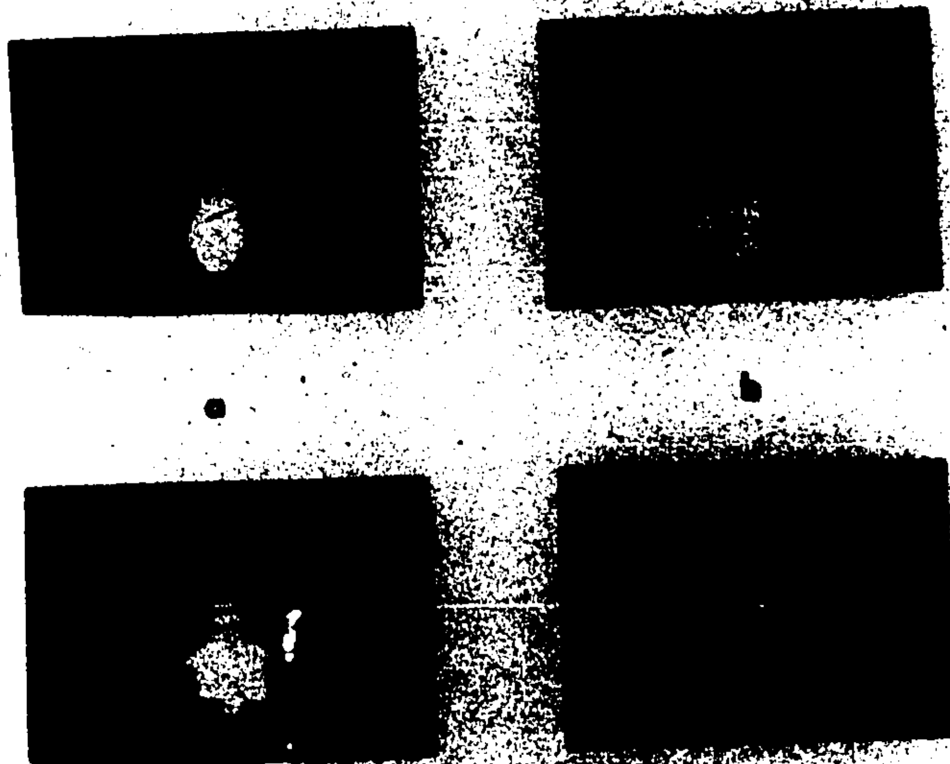

Fig. 8-6 Effect of 40-keV Kr Ion Bombardment on Anodic Films of V at various Doses; a: upto ~ 4×10^{15} ions cm^{-2}, b: at ~ 1.6×10^{16} ions cm^{-2}, c: at ~ 3.2×10^{16} ions cm^{-2}, d: at ~ 6.4×10^{16} ions cm^{-2}.

Table 8-2

Dissolution Rate as a function of Ion Dose

Dose ions/cm^2	Dissolution Time min.	Average Dissolution Rate, μg/cm^2 per min.	Remarks
4×10^{13}	$\sim\frac{1}{4}$	~64	Film completely dissolved
2×10^{14}	~ 1	~16	Film completely dissolved
4×10^{14}	~ 3	~5.3	Film completely dissolved
1×10^{15}	~ 6	~2.3	Film completely dissolved
2×10^{15}	~10	~1.32	Film completely dissolved
4×10^{15}	~11	~1.10	Film completely dissolved
8×10^{15}	~20	~0.47	Film only partly dissolved
1.6×10^{16}	~20	~0.38	Film only partly dissolved
$\geq3.2\times10^{16}$	-	-	Film hardly dissolved

indicating that an ordering was taking place. At still higher doses of 3.2×10^{16} ions/cm^2, the film was found to be crystalline (fig.8-6c) and could be identified as V_2O_3 (Table 8-3). When the ion dose was further increased to $\geq6.4\times10^{16}$ ions/cm^2, the film was still crystalline but with a different pattern (fig.8-6d) and it could now be identified as VO (Table 8-4). Thus, whereas bombardment of thick crystalline V_2O_5 pellets yields

Table 8-3

Electron Diffraction Data for V_2O_3

V_2O_3 ASTM 1-1293 I/I_o	d,Å	As Observed d,Å	Intensity*
		-	-
		-	-
60	3.65		
		2.75	s
80	2.70		
		2.50	ms
60	2.47		
		-	-
2	2.32		
		2.16	wm
20	2.18		
		-	-
2	2.03		
		1.82	m
25	1.83		
		1.735	s
100	1.69		

*s=strong; m=medium; w=weak

Table 8-4

Electron Diffraction Data for VO

VO ASTM 10-313 I/I_o	d,Å	As Observed d,Å	Intensity
		-	-
30	2.36		
		2.03	ms
80	2.06		
		1.47	s
100	1.45		
		1.24	m
60	1.24		
		1.21	m
60	1.19		
		1.05	wm
50	1.03		
		0.93	m
50	0.944		
70	0.92		

V_2O_3, thin anodic V_2O_5 films yield VO as the final product.

The result is in general consistent with the mechanism currently proposed for differential oxygen loss. In one group of mechanisms, differential sputtering is assumed to occur at the surface and an altered layer to develop by in-diffusion of V_o or M_i. Such in-diffusion would be more effective with a thin film, as the metal would act as a sink for V_o or M_i. In another group of mechanisms, differential internal precipitation is assumed. Again, the precipitation would be more effective with thin films due to the metal acting as a sink.

Further discussion of the differential sputtering or internal precipitation is quite beyond the scope of this thesis. For details on the subject, see recent work by Kelly (1974) and Sigmund (1974).

8.4.4 Estimation of Sputtering Coefficients: The same experiments as used to determine dissolution rates could also be used to estimate the sputtering coefficients. It will be recalled that in these experiments, specimens of V were first anodized to 12 volts, then labeled with 40-keV Kr^{85} to various doses, and finally exposed to 1% KOH. The results are shown in fig. 8-7. A knowledge of the range profile for 40-keV Kr^{85} ions in the amorphous anodized V (fig. 7-7) permits the estimation of the thickness removed by sputtering and this finally leads to values for the average sputtering coefficient.

An important correction to the range profiles is, however, first necessary; the range profiles evolve continuously

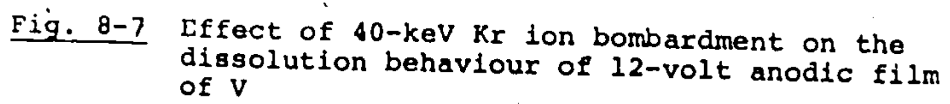

Fig. 8-7 Effect of 40-keV Kr ion bombardment on the dissolution behaviour of 12-volt anodic film of V

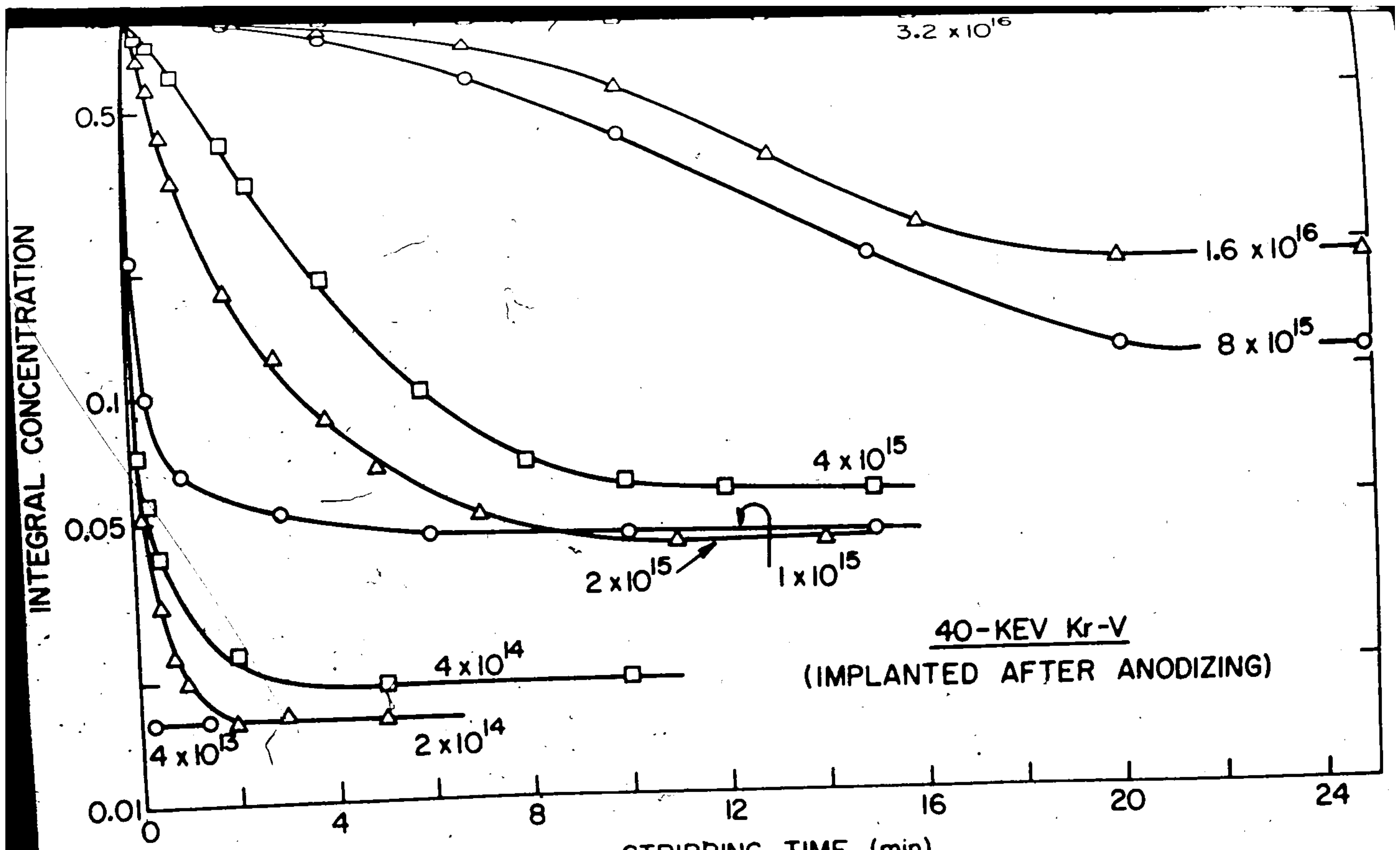
3.2 x 10^16
1.6 x 10^16
8 x 10^15
4 x 10^15
2 x 10^15
1 x 10^15
4 x 10^14
2 x 10^14
4 x 10^13
40-KEV Kr-V
(IMPLANTED AFTER ANODIZING)
INTEGRAL CONCENTRATION
0.5
0.1
0.05
0.01
STRIPPING TIME (min)
0
4
8
12
16
20
24

during ion bombardment due to sputtering. Therefore, the 'S' values were determined using the integral concentration profiles as determined for a moving surface boundary. Thus, in absence of sputtering, mean projected range $\langle R_p \rangle$ is defined with respect to the surface x=0. This would be true at time t=0 for the case of surface sputtering, such that at any point x_1 we have,

$$C^{diff.}(x_1,0) = \frac{1}{\sqrt{2\pi}\cdot\langle\Delta R_p\rangle} \exp\{-[\frac{(x_1 - \langle R_p\rangle)^2}{2\langle\Delta R_p^2\rangle}]\} . \quad (8\text{-}6)$$

However, at any time t>0, the newly formed differential profile will have moved toward target interior such that at the same point x_1, we have

$$C^{diff.}(x_1,t) = \frac{1}{\sqrt{2\pi}\cdot\langle\Delta R_p\rangle} \exp\{-[\frac{(x_1 - vt - \langle R_p\rangle)^2}{2\langle\Delta R_p^2\rangle}]\} \quad (8\text{-}7)$$

where v is the velocity of the moving surface as defined by the sputtering rate and given by $\frac{BS}{N}$ with B being the ion beam current density. Hence, at any point x_1, the total differential concentration will be the sum of all the profiles generated in the specific time interval t=0 to t=T:

$$C^{diff.}(x_1,T)_{total} = A\int_0^T \exp-[\frac{(x_1 - vt - \langle R_p\rangle)^2}{2\langle\Delta R_p^2\rangle}]dt$$

$$= A[\operatorname{erfc}(\frac{x_1 - vT - \langle R_p\rangle}{\sqrt{2}\ \langle\Delta R_p\rangle}) - \operatorname{erfc}(\frac{x_1 - \langle R_p\rangle}{\sqrt{2}\ \langle\Delta R_p\rangle})] \quad (8\text{-}8)$$

where A is the normalizing factor.

Then, one gets by integration

$$C^{int.}(x_1,T) = A \int_x^{\infty} [\text{erfc}(\frac{x_1 - vT - \langle R_p \rangle}{\sqrt{2}\ \langle \Delta R_p \rangle}) - \text{erfc}(\frac{x_1 - \langle R_p \rangle}{\sqrt{2}\ \langle \Delta R_p \rangle}) dx$$

$$C^{int.}(x_1,T) = A\{\text{ierfc}(\frac{x - \langle R_p \rangle}{\sqrt{2}\ \langle \Delta R_p \rangle}) - \text{ierfc}(\frac{x + vT - \langle R_p \rangle}{\sqrt{2} \cdot \langle \Delta R_p \rangle})\} \qquad (8-9)$$

where (x+vT) has been substituted for x_1 with x being the distance measured from the instantaneous surface.

Results of such calculations are given in Table 8-5. It is seen that the average sputtering coefficient varies from

Table 8-5

Sputtering Coefficients for Anodized V as a Function of Dose

12 Volt Films Implanted with 40-keV Kr^{85}				
Dose ions/cm^2	Observed $C^{int.}$	Corresponding Film Thickness from eqn. 8-9 μg/cm^2	Loss of Film Thickness μg/cm^2	S* atoms/ion
4×10^{13}	0.016	16.0	-	-
2×10^{14}	0.016	16.0	-	-
4×10^{14}	0.0194	15.4	0.6	35
1×10^{15}	0.043	13.7	2.3	53
2×10^{15}	0.043	13.2	2.8	32
4×10^{15}	0.054	12.0	4.0	23
8×10^{15}	0.11	9.4	6.6	19
1.6×10^{16}	0.19	7.7	8.3	12
$\geq 3.2\times10^{16}$	∼0.90	-	-	-

*S is deduced from the relation $S = \frac{N}{Bt} \cdot x = \frac{N_o}{\bar{M}} \cdot \frac{x}{Bt} \times 10^{-6}$ where x is thickness removed in μg/cm^2, N_o is Avagadro's number, $\bar{M}$ is mean molecular weight of the target and Bt is the ion dose in ions/cm^2.

a maximum of 44±9 atoms/ion to about 12 atoms/ion. The qualitative features of the results are unmistakable and a marked variation in S with ion dose is demonstrated. This variation can, moreover, be correlated directly with the changes in film stoichiometry: high 'S' for V_2O_5 and low 'S' for V_2O_3 and VO. Since most of the previous work on sputtering has involved the conventional method of using extremely high doses without associated work on structure or stoichiometry, some of this work, especially that done on materials which are susceptible to a structure or stoichiometry change on ion bombardment must be questioned.

8.5 Summary:

The experiments described here were in the first instance intended to be a simple extension of those of chapter 7 in which range profiles were obtained in anodic V_2O_5 films by the conventional transmission technique. The films were found, however, to exhibit catastrophic property changes on ion bombardment. For example, the average film dissolution rates and average sputtering coefficients varied with ion dose, and these changes could be correlated with changes in the film structure and stoichiometry. Thus, the initially amorphous V_2O_5 films evolved to crystalline V_2O_3 and then to crystalline VO, as revealed by reflection electron diffraction. One obvious conclusion to draw from this work is that experiments with materials which are susceptible to property changes on ion bombardment must be interpreted carefully since

the final product may be quite different from the initial material. One could say, perhaps with justification, that structural investigations must accompany all ion bombardment studies to show explicitly either the presence or the absence of structural modifications.

More specifically, the previous data on sputtering coefficients in Nb_2O_5, WO_3 and TiO_2 [(Lam, 1970,1971); Kelly (1968b)] must be regarded as suspect. No structural work was carried out in connection with the experiments and yet these oxides are now known to evolve during bombardment to lower stoichiometries, namely NbO, $W_{18}O_{49}$, and Ti_2O_3.

CHAPTER 9

SUMMARY AND SUGGESTIONS FOR FURTHER RESEARCH

9.1 Summary:

1. It has been demonstrated for the first time that Mo can be anodized such that thick, protective films are formed. The key lies in the use of non-aqueous electrolytes based on acetic acid.

2. The anodic behaviour of V, Mo, and W has been studied in an electrolyte containing 1 mole of water and 0.02 moles of $Na_2B_4O_7 \cdot 10H_2O$ in acetic acid. At low formation currents (< 1.0 mA/cm^2), V and Mo show induction periods such that voltage does not rise with time. These induction periods become more pronounced at lower currents or with stirring, and are apparently caused by dissolution during film formation. Even when formed at higher currents, the films on V and Mo are quite unstable and have to be stabilized by drying them immediately after withdrawal from the electrolyte. Neither induction periods nor film stability are observed with W.

3. Due to the low conductivity of the acetic-acid-based electrolyte, constant voltage conditions are necessary to obtain uniform anodic films. Minor experimental details such as electrode spacing, stirring, etc. also play an important role. The effects of these details on film for-

mation were studied and optimum anodizing conditions were found to include the use of 2.0 mA/cm^2 as the initial current, 0.8-1.0 cm as the electrode spacing, and a total anodizing time of six minutes at 25±1°C, with no stirring of the electrolyte.

4. Current efficiencies were determined under conditions of constant current and when both current and voltage are preset. At constant current, the efficiency increases with current from about 0.6 at 0.25 mA/cm^2 to about 0.97-0.98 at 4.0 mA/cm^2. When both the current and the voltage are preset, the efficiency varies between 0.8 to 1.0, with lower values being applicable to V and higher to Mo and W.

5. Use of a dilute aqueous solution of KOH permits rapid dissolution of anodic films formed on V, Mo and W without undue attack on the substrates. For example, anodic V_2O_5 dissolves at the rate of ∿ 2000 Å/min whereas V dissolves at ∿ 0.3 Å/min. A combination of the acetic-acid-based electrolyte and dilute KOH as dissolving reagent thus permits anodic sectioning of V, Mo and W.

6. Anodization of Nb and Ta has been studied with a view to anodic sectioning. Of the various electrolytes and dissolving reagents studied, only a combination of a non-aqueous electrolyte containing 25% H_2SO_4 in diethyl sulphate and saturated KOH solution as the stripping reagent permits satisfactory sectioning. The important detail here seems

to be the significant doping of the films formed in the sulphate-based electrolyte, which enhances the film dissolution in saturated KOH.

7. Doped nature of the anodic films was studied using the direct and conventional gravimetric method and the indirect but more sensitive method of observing the constant current kinetics in aqueous and non-aqueous electrolytes. Results show that films formed on Ta in non-aqueous electrolyte are very much doped in nature, with those on Nb somewhat less but still significantly doped. Similar studies with W showed its anodic films only slightly, if at all, doped whereas no conclusions are possible with V and Mo due both to dissolution during film formation as well as there being only one electrolyte available that permits anodization.

8. Calibrations for thick films, corresponding to $\geq$ 10-15 volts, were obtained using the conventional gravimetric method, with separate results being obtained for the film formation and metal-removal thicknesses. These results, when analyzed, enable the film stoichiometries to be deduced as V_2O_5, MoO_3, WO_3, Nb_2O_5, and Ta_2O_5. These conclusions are not necessarily trivial as lower oxides have been proposed for the anodic films on V as VO_2 by Keil and Salomon (1968) and on W as (WO_2 + $WO_{2.9}$) by Brandon et al. (1969) and Aladjem et al. (1970).

9. Thicknesses of thin films were obtained using range profiles. Metal-removal thicknesses of thin films were expressed as a

proportion of those for thick films. For thickness determinations of anodic films, rather than of metal-removal, this method in principle presents an attractive alternative to ellipsometry, particularly when the optical constants of the anodic films and/or of the substrate are not available. In the present case, this method fails for film thickness determinations due to the unexpected changes in the nature of the film but such behaviour will also influence the ellipsometry equally.

10. Reflection electron diffraction studies with as-formed anodic films show that thin films, formed at $\lesssim$ 7-8 volts, are crystalline in the case of V, Mo, W, and Ta. Thin anodic films on Nb as well as thick films were, on the other hand, found to be amorphous in nature.

11. When thermally heated in air for ten minutes, films on V, Mo and W crystallized at about 425, 400 and 400°C to V_2O_5, MoO_3, and WO_3 respectively. Vacuum heating, at $\sim 10^{-6}$ torr, leads to crystallization at lower temperatures of 300, 300 and 370°C respectively for V, Mo, and W, with the final products now being V_6O_{13}, MoO_2, and WO_3. Cyclic heating in air and a vacuum of 10^{-6} torr leads to a corresponding transition between V_2O_5 and V_6O_{13} at about 425°C, demonstrating that V_6O_{13} is thermodynamically stable.

12. Range profiles in the 5-40 keV energy interval have been determined in polycrystalline V, Mo, W, Nb and Ta, and

the experimental profiles shown to differ considerably from the predicted profiles based on LSS theory (which assumes amorphous targets). Related experiments using amorphous targets, high doses and pre-bombardment show that the observed discrepancy is due to the channeling phenomenon and is therefore reasonable.

13. Effects of radiation damage on the anodic behaviour (i.e., thickness calibrations) were studied for V and Mo and the results showed that except at very high does of $\sim 10^{17}$ ions/cm^2, damage had no noticeable effect.

14. The experimentally obtained range profiles in crystalline specimens have been shown to fit the analytical expression

$$C^{int.} = A \exp(-\frac{x}{B}) + C \exp(-\frac{x}{D}).$$

It is emphasized that this expression must not be interpreted as involving one term for random stopping and another for channeled stopping.

15. Heavy-ion bombardment of anodic films on V leads to a change in film dissolution rate as a function of ion dose. This behaviour has been correlated with a change in film stoichiometry from V_2O_5 to V_2O_3 and finally to VO using reflection electron diffraction, and subsequently, values of the

sputtering coefficient, S, at various doses have been estimated to vary between 44±9 atoms/ion for V_2O_5 and about 12 atoms/ion for V_2O_3 and VO. The sputtering coefficients were obtained using range profiles, an approach which is effective even at low doses, an area where other methods are not possible.

16. The above result of structural transformation induced by heavy-ion bombardment, namely $V_2O_5 \rightarrow V_2O_3 \rightarrow VO$, is slightly different from the result previously obtained by Naguib and Kelly (1972) where bulk crystalline V_2O_5 was found to finally evolve to V_2O_3. The difference is suggested to lie in the presence or absence of the oxide-metal interface which acts as a sink for V_o or M_i.

17. Above results tend to make suspect some of the previous data available on 'S' as well as on range profiles for various materials. This is particularly true for WO_3, Nb_2O_5 and Ti_2O_3 which are now known to evolve to $W_{18}O_{49}$, NbO and Ti_2O_3 on ion bombardment. The correct approach would seem to combine 'S' determinations with structural work so as to show clearly either the presence or absence of any structural transformations.

9.2 Future Work:

1. Anodic sectioning should be developed for Zr, Fe, and Be, with the principle of doping and use of non-aqueous electrolytes in mind. Here, Zr and Fe are important as nuclear fuel

cladding, while Be is of interest as the lightest possible target for ion impact work.

2. With the anodic sectioning of V, Mo and Nb now possible, the concept of the "supertail" may be studied in greater detail and the criterion of Anderson and Sigmund (1965) of $Z_1 < Z_2$ for the presence of a supertail examined. The point is that V, Mo and Nb have a position nearly in the middle of the periodic table and it is therefore possible to explore both $Z_1 < Z_2$ and $Z_1 > Z_2$.
3. Ion impact studies, similar to those carried out with the anodic film on V, should also be carried out for the films on Mo and W, and structural transformations, if any, examined. Use should also be made of the possibility of determining 'S' at low doses using range profiles.
4. Work on 'S' determinations in the cases of Nb_2O_5, Ta_2O_5, and TiO_2 should be repeated, this time with associated structural examination.
5. Studies on anomalous self-diffusion behaviour may now be extended to Mo, Nb and Ta.
6. Anomalous near-surface diffusion behaviour may be studied with bcc metals, it being noted that all the previous work involved only noble metals.

References*

Aladjem, A. (1968) J. Mater. Sci. 3, 328.

Aladjem, A., Brandon, D.G., Yahalom, J., and Zahavi, J. (1970) Electrochim. Acta 15, 663.

Almén, O. and Bruce, G. (1960) "Electromagnetic Separation of Radioactive Isotopes", Vienna, Springer-Verlag, p. 227.

Almén, O. and Bruce, G. (1961a) Nucl. Instr. Methods 11, 257.

Almén, O. and Bruce, G. (1961b) ibid. 11, 279.

Ammar, I.A., and Kamal, I. (1971) Electrochim. Acta 16, 1539.

Ammar, I.A. and Salim, R. (1971) Cor. Sci. 11, 591.

Amsel, G. and Samuel, D. (1962) J. Phys. Chem. Sol. 23, 1707.

Amsel, G., Cherki, C., Feuillade, G. and Nadai, J.P. ibid. 30, 2117.

Andersen, H.H. and Sigmund, P. (1965) Nucl. Inst. Methods 38, 238.

Andersen, T. and Sørensen, G. (1969) Rad. Effects 2, 111.

Anderson, S., Galy, J. and Wilhelmi, Kar-Axel (1970) Acta Chem. Scand. 24 (4), 23.

Arora, M.R. and Kelly, R. (1972) J. Electrochem. Soc. 119, 270.

Arora, M.R. and Kelly, R. (1973) ibid. 120, 128.

Arora, M.R. and Kelly, R. (1974) Electrochim. Acta To be published.

Bean, C.P., Fisher, J.C. and Vermilyea, D.A. (1956) Phys. Rev. 105, 551.

Becker, E. and Hilberg, H. (1925) Z.f. Electrochem. 31, 31.

Bernard, W.J. and Randall, J.J. Jr. (1961) J. Electrochem. Soc. 108, 822.

---

*For extra references, see page 260.

Bøgh, E. (1968) Can. J. Phys. 46, 653.

Boosz, H.J. (1957) Metall. 11, 511.

Cabrera, N. and Mott, N.F. (1948-9) Repts. Prog. Physics 12, 163.

Calbrick, C.J. and Schwartz, N. (1962) Trans. 9th Nat. Vac. Symp. p 81, McMillan, N.Y.

Calvert, L.D. and Draper, P.H.G. (1962) Can. J. Chem. 40, 1943.

Charlesby, A. (1951) Atomic Energy Research Establishment U.K. Rept. M/R 714.

Cheseldine, D.M. (1964) J. Electrochem. Soc. 111, 1128.

Christov, S.G. (1963) Z. Elektrochem. 67, 117.

Christov, S.G. and Ikonopisov, S. (1969) J. Electrochem. Soc. 116, 56.

Croset, M., Petreanu, E., Samuel, D., Amsel, G. and Nádai, J.P. (1971) ibid. 118, 717.

Davies, J.A., Friesen, J. and McIntyre, J.D. (1960) Can. J. Chem. 38, 1526.

Davies, J.A., Domeij, B. and Uhler, J. (1963) Arkiv för Fysik 24 (27), 377.

Davies, J.A., Ball, G.C., Brown, F. and Domeij, B. (1964) Can. J. Phys. 42, 1070.

Davies, J.A., Domeij, B., Pringle, J.P.S. and Brown, F. (1965) J. Electrochem. Soc. 112, 675.

Davies, J.A. and Jespersgaard, P. (1966) Can. J. Phys. 44, 1631.

Davies, J.A. (1972) AECL Rept. 4335. Int. Atomic Energy Agency, Vienna.

Dearnaley, G. (1970) Harwell (U.K.) Rept. AERE-R6559.

Despić, A.R. and Bockris, J. O'M. (1960) J. Chem. Phys. 32, 389.

Dewald, J.F. (1955) J. Electrochem. Soc. 102, 1.

Dewald, J.F. (1957a) ibid. 104, 244.

Dewald, J.F. (1957b) J. Phys. Chem. Sol. 2, 55.

Dignam, M.J. (1964) Can. J. Chem. 42, 1155.

Dignam, M.J., Goad, D. and Sole, M. (1965) ibid. 43, 800.

Dignam, M.J. (1965) J. Electrochem. Soc. 112, 729.

Dignam, M.J. (1972) "Oxides and Oxide Films" Ed. John Diggle, p. 91, Marcel-Dekker Inc. New York.

Domeij, B. and Erickson, L. (1965) Unpublished results.

Draper, P.H.G. (1963a) Electrochim. Acta 8, 847.

Draper, P.H.G. (1963b) Acta Met. 11, 1061.

Draper, P.H.G. and Harvey, J. (1963c) ibid. 11, 873.

Dreiner, R. (1964) J. Electrochem. Soc. 112, 729.

Dubrovskii, L.A., Mel'nik, V.G. and Odynets, L.L. (1962) Russ. J. Phys. Chem. 36, 1183.

Eisen, F.H. (1968) Can. J. Phys. 46, 561.

Ericksson, L. (1967) Phys. Rev. 161, 235.

Ericksson, L., Davies, J.A. and Jespersgaard, P. (1967) ibid. 161, 219.

Evans, U.R. (1971) Electrochim. Acta 16, 1825.

Fastrup, B., Hvelplund, P. and Sautter, C.A. (1965) Nucl. Inst. Methods 38, 260; (1966) Kgl. Dan. Viedenskab. Selskab. Mat. Fys. Medd. 35 (10).

Fastrup, B., Borup, A. and Hvelplund, P. (1968) Can. J. Phys. 46, 489 and Phys. Rev. 165, 408.

Fetz, V.M. and Oechsner, H. (1960) Zeit Angew. Phys. 12, 250.

Firsov, O.B. (1959) Sov. Phys.-JETP (English Trans.) 9, 1076.

Giani, E. (1971) M.Sc. Thesis, McMaster University.

Giani, E. and Kelly, R. (1974) J. Electrochem. Soc. To be published.

Güentherschulze, A. and Betz, H. (1937) "Electrolytkondensatoren" Krayn, Berlin.

Harvey, J. and Wilman, H. (1961) Acta Cryst. 14,1278.

Hermann, H., Lutz, H. and Sizmann, R. (1966) Z. Naturforsch. 21a, 365.

Hoar, T.P. (1959) "Modern Aspects of Electrochemistry", p. 262, vol. 2, Academic Press, N.Y.

Hoar, T.P. (1970) J. Electrochem. Soc. 117, 17C.

Ibl, N. (1967) Electrochim. Acta 12, 1043.

Ikonopisov, S. (1972-73) Electrodeposition and Surface Treatment 1, 305.

Ikonopisov, S. (1972) J. Electroanaly. Chem. 35, App. 1.

Janaf Thermochemical Tables (1971) 2nd Ed., D. R. Stull and H. Prophet.

Janninck, R.F. and Whitmore, D.H. (1962) J. Chem. Phys. 37, 2750.

Johansen, H.A., Adams, G.B. and Rysselberghe, P. van (1957) J. Electrochem. Soc. 104, 339.

Johnson, W.S. and Gibbons, J.F. (1970) "Projected Range Statistics in Semiconductors", Stanford University Bookstore.

Kawamura, H. and Azuma, K. (1953) J. Phys. Soc. Japan 8, 797.

Keil, R.G. and Salomon, R.E. (1965) J. Electrochem. Soc. 112, 643.

Keil, R.G. and Salomon, R.E. (1968) ibid. 115, 628.

Keil, R.G. and Ludwig, K. (1971) ibid. 118, 864.

Kelly, R. (1968a) J. Appl. Phys. 39, 5298.

Kelly, R. (1968b) Can. J. Phys. 46, 473.

Kornelsen, E.V., Brown, F., Davies, J.A., Domeij, B. and Piercy, G. R. (1964) Phys. Rev. 136 (3A), A849.

Kosuge, K. (1967) J. Phys. Chem. Sol. 28, 1613.

Kover, F. and Musselin, M.J. (1968) Thin Solid Films 2, 211.

Kuessner, H. (1910) Z.f. Elekrochem. 16, 754.

Laegried, N. and Wehner, G.K. (1961) J. Appl. Phys. 32, 365.

Lakhiani, D.M. and Shrier, L.L. (1960) Nature 188, 49.

Lam, N.Q. and Kelly, R. (1970) Can. J. Phys. 48, 137.

Lam, N.Q. (1971) Ph.D. Thesis, McMaster University.

Lam, N.Q., Rothman, S.J. and Nowicki, L.J. (1972a) J. Electrochem. Soc. 119, 715.

Lam, N.Q., Rothman, S.J. and Nowicki, L.J. (1972b) ibid. 119, 1344.

van Laue, M. (1952) "Historical Introduction to International Tables for X-ray Crystallography" 1, Kynoch Press.

Lavrenko, V.A. and Pen'kov, A.A. (1963) Russ. J. Phys. Chem. (English Trans.) 37, 551.

LeClaire, A.D. (1965) "Diffusion in bcc Metals", p. 3., American Society for Metals, MetalsPark, Ohio, U.S.A.

Lewis, J.E. and Plumb, R.C. (1958) J. Electrochem. Soc. 105, 496.

Lieberman, M.L. and Madrud, R.C. (1969) ibid. 116, 242.

Lindhard, J., Scharff, M. and Schiøtt, H.E., (1963) Kgl. Dan. Videnskab. Selskab. Mat-Fys. Medd. 33 (14).

Lindhard, J. (1965) ibid. 34 (14).

Lindhard, J., Nielsen, V. and Scharff, M. (1968) ibid. 36 (10).

Lutz, H. O. and Sizmann, R. (1963) Phys. Lett. 5, 113.

McCargo, M., Davies, J.A. and Brown, F. (1963) Can. J. Phys. 41, 1231.

McLean, D.A. (1960) Proc. Nat. Electronics Conf. U.S.A. p. 206.

Masing, G. and Röth, G. (1952) Werkstoffe u. Korrosion 3, 176, 253.

Masing, L. and Young, L. (1962) Can. J. Chem. 40, 903.

Maurer, R.J. (1941) J. Chem. Phys. 9, 579.

Mayer, J.W., Ericksson, L. and Davies, J.A. (1970) "Ion Implantation in Semiconductors", Academic Press, N.Y.

Menzies, I.A., Marshall, G.W. and Griffin, G.B. (1969) Cor. Sci. 9, 287.

Moak, D.D., Reese, H., Jr. and Good, W.M. (1951) Nucleonics, 9, 18.

Kihara-Morishita, H., Takamura, T. and Takeda, T. (1970) Thin Solid Films, R29-31.

Mortlock, A.J. (1969) J. Austr. Inst. Metals 14, 98.

Mott, N.F. (1947) Trans. Faraday Soc. 43, 429.

Naguib, H.M. and Kelly, R. (1972) J. Phys. Chem. Sol. 33, 1751.

Nelson, R.S. and Thompson, M.W. (1963) Phil. Mag. 8, 1677.

Nielsen, K.O. (1956) "Electromagnetically Enriched Isotopes and Mass Spectroscopy", Academic Press, N.Y., Butterworth and Co., London, p. 68-81.

Ormrod, J.H. and Duckworth, H.E. (1963) Can. J. Phys. 41, 1424.

Ormrod, J.H., MacDonald, J.R. and Duckworth, H.E. (1965) ibid. 43, 275.

Parker, T. and Kelly, R. (1973) Proc. 3rd Int. Conf. on Ion Implantation in Semiconductors and other Materials, Yorktown Heights, N.Y.

Pawel, R.E. (1964) Rev. Sci. Inst. 35, 1066.

Pawel, R.E. and Campbell, J.J. (1964) J. Electrochem. Soc. 111, 1230.

Pawel, R.E. and Lundy, T.S. (1965) J.Phys. Chem. Sol. 26, 937.

Piercy, G.R. (1964) AECL Annual Report, April 1 - June 30.

Piercy, G.R., McCargo, M., Brown, F. and Davies, J.A. (1964) Can. J. Phys. 42, 1116.

Plumb, R.C. (1958) J. Electrochem. Soc. 105, 497.

Pringle, J.P.S. (1972) ibid. 119, 482.

Pringle, J.P.S. (1973) ibid. 120, 398.

Randall, J.J.Jr., Bernard, W.J. and Wilkinson, R.R. (1965) Electrochim. Acta 10, 183.

Reid, I. and Kelly, R. (1973) Rad. Effects 17, 253.

Robinson, M.T. and Oen, O.S. (1963) Appl. Phys. Lett. 2, 30.

Rogers, G.T., Draper, P.H.G. and Wood, S.S. (1968) Electrochim. Acta 13, 251.

Rol, P.K., Fluit, J.M., Viehbock, F.P. and DeJong, M. (1959) Proc. IVth Int. Conf. Ion Phenomena in Gases, Uppsala, p. 257.

Rol, P.K., Fluit, J.M. and Kistemaker (1960a) "Electromagnetic Separation of Radioactive Isotopes", Vienna, Springer-Verlag, p. 207.

Rol, P.K., Fluit, J.M. and Kistemaker (1960b) Physica 26, 1000.

Rol, P.K., Fluit, J.M. and Kistemaker (1960c) ibid. 26, 1009.

Rosenburg, D. and Wehner, G.K. (1962) J. Appl. Phys. 32, 365.

Rowe, C. (1970) Private Communication.

Sata, T., Komada, E. and Ito, Y. (1968) Kogyo Kagaku Zasshi 71 (5), 643.

Sato, T. and Ito, Y. (1968) ibid. 71 (5), 647.

Schiøtt, H.E. (1970) Rad. Effects 6, 107.

Schmidt, P.F. and Michel, W. (1957) J. Electrochem. Soc. 104, 230.

Schmidt, P.F. and Owen, A.E. (1964) ibid. 111, 682.

Sigmund, P. (1968) Phys. Rev. 184, 383.

Sigmund, P. (1969) Bull. Am. Phys. Soc. 13, 1445.

Smyth, D.M., Tripp, T.B. and Shirn, G.A. (1966) J. Electrochem. Soc. 113, 100.

Stark, J. (1912) Phys. Z. 13, 973.

Stull, D.R. and Prophet, H. (1971) JANAF Thermochemical Tables (U.S. Dept. of Commerce, Washington).

Takamura, T., Kihara-Morishita, H. and Moriyana, U. (1970) Thin Solid Films 6, R17-R19.

Theóbald, F., Cabala, R. and Bernard, I. (1968) C.R. Acad. Sc. Paris 266, 1534.

Thompson, M.W. (1968) Phil. Mag. 18, 377.

Verkerk, B., Winkel, P. and deGroot, D.G. (1958) Philips Res. Reports 13, 506.

Vermilyea, D.A. (1953) Acta Met. 1, 282.

Vermilyea, D.A. (1954) ibid. 2, 482.

Vermilyea, D.A. (1955) J. Electrochem. Soc. 102, 207.

Vermilyea, D.A. (1957) ibid. 104, 427.

Vermilyea, D.A. (1963) "Advances in Electrochemistry" Vol. 3, p. 211, Ed. P. Delahay, Interscience Publishers Inc., N.Y.

Vermilyea, D.A. (1965) J. Electrochem. Soc. 112, 1232.

Verwey, E.J.W. (1935) Physica 2, 1059.

Wales, R.D. (1963) J. Electrochem. Soc. 110, 914.

Whitton, J.L. and Davies, J.A. (1964) ibid. 111, 1347..

Whitton, J.L. (1965) J. Appl. Phys. 36, 3917.

Whitton, J.L. (1969) Proc. Roy. Soc. A311, 63.

Whitton, J.L. (1973) Unpublished Results.

Wilcock, W.L., Emerson, D.L., and Weekly, B. (1960) Inst. Radio Engrs. Trans. Nucl. Science NS-7, 126.

Wilkins, M.A. (1968) Harwell (U.K.) Rept. AERE-R5875.

Winterbon, K.B. (1968) AECL Rept.-3194, Chalk River, Canada.

Winterbon, K.B., Sigmund, P. and Sanders, J.B. (1970) Mat. Fys. Medd. Dan. Vid. Selsk. 37 (14).

Wood, G.C. and Pearson, C. (1967) Cor. Sci. 7, 119.

Yahalom, J. and Zahavi, J. (1971) Electrochim. Acta 16, 603.

Yahalom, J. (1973) Proc. Symp. "Oxide-Electrolyte Interfaces" Ed. by R. S. Alwitt, J. Electrochem. Soc., Inc. Princeton, p. 289.

Young, L. (1956) Trans. Faraday Soc. 52, 502.

Young, L. (1959) Can. J. Chem. 37, 276,

Young, L. (1960) Proc. Roy. Soc. A258, 496

Young, L. (1961) "Anodic Oxide Films", Academic Press, N.Y.

Young, L. (1961a) Proc. Roy. Soc. A263, 395.

Young, L. (1963) J. Electrochem. Soc. 110, 589.

Young, L. and Zobel, F.G.R. (1966) ibid. 113, 277.

Zwerdling, S. and Sheff, S. (1960) ibid. 107, 338.

Hass, G. (1947) Z. anorg. u. allgem. Chem. 254, 96.

Hass, G. and Bradford, A.P. (1957) J. Optical Soc. America 47, (2) 125.

Kelly, R. (1974) To be published.

Landolt-Börnstein (1962) Eigenschaften der Materie in ihren Aggregatziständen, Band II, Teil 8, Springer-Verlag, Berlin.

Sigmund, P. (1974) To be published.